

*Development of  
low-diffusion techniques  
for a high pressure xenon  
electroluminescent TPC*

DOCTORADO EN FÍSICA

Ryan Felkai

*Directores:* Francesc Monrabal Capilla  
Neus López March

*Tutor:* José Díaz Medina



VNIVERSITAT  
E VALÈNCIA

Departamento de Física Atómica, Molecular y Nuclear

Abril de 2022

The work in this thesis has been carried out at the *Instituto de Física Corpuscular* (IFIC), affiliated with the Universitat de València and CSIC.

© Ryan Felkai, April 2022

# DECLARACIÓN

**Neus López March**, Profesora Ayudante Doctor Universitat de Valencia,

**Francesc Monrabal Capilla**, Ikerbasque Research Associate del Donostia International Physics Center,

CERTIFICAN:

Que la presente memoria titulada, "*Development of low-diffusion techniques for a high pressure xenon electroluminescent TPC*", ha sido realizada bajo su dirección en el Instituto de Física Corpuscular (centro mixto Universitat de València - CSIC) por **Ryan Felkai** y constituye su Tesis para optar al título de Doctor por la Universitat de València una vez cursados los estudios en el Doctorado en Física.

Y para que conste, en cumplimiento de la legislación vigente, firmamos el presente certificado a 16 de abril de 2022.



Neus López March



Francesc Monrabal Capilla

*Le courage, c'est d'aimer la vie et de regarder la mort  
d'un regard tranquille ; c'est d'aller à l'idéal et de  
comprendre le réel.*

— Jean Jaurès, *Discours à la jeunesse, Albi, 1903*

# Remerciements

Mes premiers remerciements vont à ceux qui ont rendu possible cette thèse, qui m'ont fait venir et accueilli à Valencia : Juanjo et Michel. Ensuite à Francesc et Neus pour avoir été mes patients directeur et directrice de thèse. Je n'oublierai jamais les deux semaines à Canfranc au début de l'année 2017 pendant lesquelles Francesc m'a expliqué en détail et en direct les arcanes du détecteur NEXT-White pendant ces longues journées dans la montagne ; ces deux semaines ont eu un impact décisif sur cette thèse. Je n'oublierai pas non plus les mois d'excitations à construire DEMO++ en équipe avec Neus et les *ingenier@s* : Sara, Alberto, Marc, Vicente, Javi, Raül...

J'ai aussi eu la chance, grâce à Lior, d'avoir pratiqué pendant ces deux dernières années l'intensité de la vie en Israël. Merci aussi aux *nexters*, d'Arlington à Be'er Sheva en passant par Valencia, qui ont partagé un *office* avec moi : Jose Maria, Carmencita, Yair, Mirta, Gonzalo, Brais, Alberto, Leslie... Je remercie aussi particulièrement Adam pour avoir relu ce manuscrit et Ander pour son aide.

À Valencia j'ai eu la chance et le bonheur de rencontrer des gens qui venaient très souvent d'ailleurs, comme moi, et de m'en faire des amis. Certains n'étaient que de passage, d'autres sont restés et finalement c'est moi qui suis parti. Les amitiés construites entre personnes qui bougent se distendent très souvent, c'est parfois injuste, mais c'est la vie. On finira par se retrouver comme si on ne s'était jamais quitté. Certains viennent de NEXT comme Andrew, Josh, Paola, Marija, d'autres plus généralement de l'IFIC comme Louis, Susy, Sam, Chris, Daniele. Quant à mes grandes amies Ichika et Vicky, nos légendaires fêtes nocturnes à la plage resteront dans les mémoires !

Et puis il y a ceux avec qui j'ai eu le bonheur de partager la *puerta ocho* au 3, *Calle Música Hipólito Martínez* dans mon fief de

Benimaclet : Ania, Yoan, Paula, Asja, Sophie... Et Emma, une des plus belles personnes qu'il m'ait été donné de rencontrer.

En Israël j'ai fait la connaissance de beaucoup de gens avec qui j'ai partagé la galère de vivre sous les roquettes pendant la crise israélo-palestinienne de 2021 ainsi que la pandémie du COVID en étant à l'étranger, forcé à rester loin de ma famille pendant aussi longtemps. Pour ça, j'ai une pensée toute particulière pour Jenny, Oskar, Boško, Nenad, Zach, Guru, Ganesh, les colloqs Piotr et Paweł, Johan, Fabian, Christian, Avi, Laura, Franziska... Mais aussi Lou et ma grande copine Louise, avec qui le *gerushim* s'éternise ! Les amis du *Language Exchange* : Eyal, Shimon, Karin, Lucero, Tamar, Roe, Keren, Adib, Annan, Yasha, Dana... Et enfin Yaniv, *ach sheli*, sans qui Israël n'aurait pas été un endroit aussi accueillant.

Je veux remercier une institution en particulier : l'Éducation nationale française, laïque et gratuite, à laquelle je donne le visage de mes profs de prépa au Lycée Condorcet, Monsieur Barnier et Monsieur Bertrand. Merci pour m'avoir formé l'esprit. Je veux aussi ajouter le nom de mes amis d'enfance dont je suis fier d'avoir conservé l'amitié depuis ce temps-là : Alice, Augustin, Jonathan, Nicolas, Quentin et Raphaël. Et il y a aussi Zhibin et Nelly que je remercie pour leur constant soutien émotionnel et leurs encouragements.

Cette thèse et tout ce qui l'a précédée n'aurait pas été possible sans le soutien de ma famille. Je veux principalement remercier Ali, Jamina, feu David et feu Driss, dont j'ai l'honneur de porter aussi le nom. Auxquels s'ajoutent naturellement ma deuxième mère Aïcha et ma sœur-de-cœur Soukaïna. Comme de la famille, je veux aussi remercier les amis de mes parents qui sont restés fidèle à mon père en étant fidèle à ma mère ces douze dernières années. Je ne peux pas égrener de noms, mais pour en nommer un pour tous : le parrain José.

Merci enfin à mon frère Andy et à ma sœur Inès, que j'aime et qui doivent savoir que leur grand frère est fier d'eux. Ma mère, pour laquelle je ne peux pas avoir assez de reconnaissance pour son amour et son soutien absolument inconditionnel. Sans ses efforts titanesques pour tenir la barre dans la tempête rien n'aurait été possible. Et finalement, ceux qui ne sont plus là et qui devraient vraiment en être. Ma grand-mère, ma Henna à laquelle je veux faire honneur en me montrant à la hauteur des sacrifices et des choix courageux qu'elle a su faire. Et à mon père : merci pour **TOUT**.

# Contents

|   |           |
|---|-----------|
| <b>Resumen</b>  | <b>7</b>  |
| <b>Summary</b>  | <b>19</b> |
| <b>1 The nature of neutrinos</b>                                | <b>31</b> |
| 1.1 Towards the neutrino discovery . . . . .                    | 31        |
| 1.1.1 Early days . . . . .                                      | 31        |
| 1.1.2 Reines and Cowan experiment . . . . .                     | 33        |
| 1.1.3 Csikai and Szalay experiment . . . . .                    | 35        |
| 1.1.4 Discovery of the muon and tau neutrinos . . . . .         | 36        |
| 1.2 Neutrino mixing . . . . .                                   | 36        |
| 1.2.1 The solar neutrino problem . . . . .                      | 36        |
| 1.2.2 PMNS matrix . . . . .                                     | 40        |
| 1.3 Neutrino mass . . . . .                                     | 42        |
| 1.4 Majorana or Dirac . . . . .                                 | 44        |
| 1.4.1 The origin of neutrino mass . . . . .                     | 45        |
| 1.4.2 See-saw mechanism . . . . .                               | 46        |
| 1.5 Summary . . . . .   | 47        |
| <b>2 Neutrinoless Double Beta Decay</b>                         | <b>49</b> |
| 2.1 Decay modes . . . . .                                       | 49        |
| 2.1.1 Two-neutrino mode . . . . .                               | 49        |
| 2.1.2 Zero-neutrino mode . . . . .                              | 52        |
| 2.1.3 Other decays . . . . .                                    | 52        |
| 2.1.4 Quadruple neutrinoless beta decay . . . . .               | 53        |
| 2.2 Inner mechanisms . . . . .                                  | 54        |
| 2.2.1 The black box theorem . . . . .                           | 54        |
| 2.2.2 The standard mechanism: light neutrino exchange . . . . . | 54        |

|          |  |            |
|----------|--|------------|
| 2.2.3    | Other processes . . . . .  | 57         |
| 2.3      | General considerations for neutrinoless double beta decay experiments . . . . .          | 58         |
| 2.3.1    | Target mass and isotope choice . . . . .   | 60         |
| 2.3.2    | Energy resolution . . . . .  | 62         |
| 2.3.3    | Background rate . . . . .  | 62         |
| 2.4      | Landscape of neutrinoless double beta decay experiments                                  | 63         |
| 2.4.1    | Recent and current experiments . . . . .   | 63         |
| 2.4.2    | Other experiments . . . . .  | 71         |
| 2.4.3    | Upcoming tonne-scale experiments . . . . .   | 73         |
| 2.5      | Summary . . . . .  | 75         |
| <b>3</b> | <b>The NEXT experiment</b>   | <b>77</b>  |
| 3.1      | The SOFT concept . . . . .   | 77         |
| 3.2      | Gaseous xenon as a detector medium for a TPC . . . . .                                   | 79         |
| 3.2.1    | Primary interaction: ionization and excitation .   | 80         |
| 3.2.2    | Secondary processes leading to detected signals: drift and electroluminescence . . . . . | 82         |
| 3.3      | The NEXT detectors . . . . .   | 85         |
| 3.3.1    | NEXT-DEMO . . . . .  | 87         |
| 3.3.2    | NEXT-DBDM . . . . .  | 89         |
| 3.3.3    | NEXT-White . . . . .   | 90         |
| 3.3.4    | NEXT-100 . . . . .   | 95         |
| 3.4      | Towards the tonne scale: NEXT-HD and NEXT BOLD .   | 103        |
| 3.4.1    | NEXT-HD . . . . .  | 103        |
| 3.4.2    | NEXT-BOLD . . . . .  | 105        |
| 3.5      | Summary . . . . .  | 108        |
| <b>4</b> | <b>Low-diffusion mixtures</b>  | <b>109</b> |
| 4.1      | Microphysics of electron transport . . . . .   | 110        |
| 4.1.1    | Transverse and longitudinal diffusion . . . . .  | 110        |
| 4.1.2    | MagBoltz and PyBoltz . . . . .   | 112        |
| 4.1.3    | Degrad . . . . .   | 114        |
| 4.1.4    | Garfield++ . . . . .   | 114        |
| 4.2      | Pure xenon . . . . .   | 115        |
| 4.2.1    | Data production . . . . .  | 116        |
| 4.2.2    | Data selection and reconstruction . . . . .  | 117        |
| 4.2.3    | Drift velocity . . . . .   | 119        |



|          |   |            |
|----------|---|------------|
| 4.2.4    | Longitudinal diffusion . . . . .                                  | 120        |
| 4.2.5    | Transverse diffusion . . . . .                                    | 121        |
| 4.3      | Molecular gas admixtures . . . . .                                | 121        |
| 4.3.1    | Molecule additive impact on electron drift in EL<br>TPC . . . . . | 121        |
| 4.3.2    | Molecules tested by the NEXT Collaboration . .                    | 123        |
| 4.4      | Helium-Xenon mixtures . . . . .                                   | 124        |
| 4.4.1    | Diffusion and drift velocity . . . . .                            | 125        |
| 4.4.2    | Energy Resolution . . . . .                                       | 128        |
| 4.4.3    | Primary scintillation . . . . .                                   | 137        |
| 4.4.4    | Photosensors and helium atmosphere . . . . .                      | 138        |
| 4.5      | HeXe mixtures at constant target mass . . . . .                   | 141        |
| 4.6      | Summary . . . . .   | 143        |
| <b>5</b> | <b>The NEXT-DEMO++ detector</b>                                   | <b>147</b> |
| 5.1      | Gas system and pressure vessel . . . . .                          | 147        |
| 5.1.1    | Pressure vessel . . . . .   | 147        |
| 5.1.2    | Gas system . . . . .  | 148        |
| 5.2      | TPC main components . . . . .                                     | 151        |
| 5.2.1    | Field cage . . . . .  | 151        |
| 5.2.2    | Cathode . . . . .   | 152        |
| 5.2.3    | Gate and anode . . . . .  | 153        |
| 5.2.4    | High voltage feedthroughs . . . . .                               | 155        |
| 5.2.5    | Light tube . . . . .  | 156        |
| 5.3      | Energy plane . . . . .  | 158        |
| 5.3.1    | Description and mechanical design . . . . .                       | 158        |
| 5.3.2    | Electronics . . . . .   | 159        |
| 5.4      | Tracking plane . . . . .  | 160        |
| 5.4.1    | Description . . . . .   | 160        |
| 5.4.2    | Electronics . . . . .   | 161        |
| 5.5      | Data Acquisition System . . . . .                                 | 162        |
| 5.5.1    | Hardware . . . . .  | 162        |
| 5.5.2    | Software . . . . .  | 163        |
| 5.6      | Sensors calibration . . . . .                                     | 164        |
| 5.6.1    | PMTs . . . . .  | 164        |
| 5.6.2    | SiPMs . . . . .   | 165        |
| 5.6.3    | Calibration database . . . . .                                    | 166        |
| 5.7      | Slow controls . . . . .   | 167        |

|          |   |            |
|----------|---|------------|
| 5.8      | Geant4 simulation of NEXT-DEMO++ . . . . .        | 167        |
| 5.9      | Summary of NEXT-DEMO++ operation . . . . .        | 169        |
| 5.9.1    | Helium-xenon separation challenge . . . . .       | 169        |
| <b>6</b> | <b>Characterization of a Helium-Xenon mixture</b> | <b>173</b> |
| 6.1      | Datasets and data selection . . . . .             | 173        |
| 6.1.1    | Datasets and run conditions . . . . .             | 173        |
| 6.1.2    | Data reconstruction and selection . . . . .       | 175        |
| 6.2      | <i>SI</i> comparison . . . . .                    | 178        |
| 6.3      | Drift velocity . . . . .                          | 180        |
| 6.4      | Energy resolution . . . . .                       | 183        |
| 6.4.1    | Lifetime correction . . . . .                     | 183        |
| 6.5      | Longitudinal diffusion . . . . .                  | 185        |
| 6.6      | Transverse diffusion . . . . .                    | 189        |
| 6.6.1    | Point Spread Functions . . . . .                  | 189        |
| 6.6.2    | Transverse coefficient measurement . . . . .      | 190        |
| 6.7      | Summary . . . . .                                 | 193        |
| <b>7</b> | <b>Conclusions and prospects</b>                  | <b>195</b> |
|          | <b>Bibliography</b>                               | <b>199</b> |

# Resumen

El neutrino es una partícula que ha suscitado un gran interés en las últimas décadas. Su existencia fue conjeturada por W. Pauli en 1930 para explicar el espectro continuo de la desintegración  $\beta$ . Enseguida pasó a formar parte de la teoría de la desintegración  $\beta$  de Fermi. El neutrino siguió siendo una partícula hipotética hasta su descubrimiento en 1956 por Reines y Cowan. Durante décadas se pensó que no era más que una partícula sin masa y sin carga, a pesar de la desconcertante observación de una discrepancia entre el flujo detectado de neutrinos procedentes del Sol y el esperado por los modelos solares más avanzados. Por otra parte, si los neutrinos fueran masivos, el llamado problema de los neutrinos solares podría explicarse por la oscilación entre los diferentes sabores de los neutrinos, un fenómeno que surge de la propagación de tres estados de masa de neutrinos diferentes, dos de los cuales al menos deben ser no nulos. El descubrimiento inequívoco de la oscilación de neutrinos en 1998 demostró que los neutrinos tienen una masa no evanescente.

Por tanto, es necesario acomodar un neutrino masivo en la teoría ampliando el Modelo Estándar y eso puede hacerse de dos maneras diferentes. La primera consiste en tener un neutrino de Dirac, es decir, un neutrino que obtiene su masa por el mismo mecanismo que los demás fermiones: el mecanismo de Higgs. El segundo supone que el neutrino es una partícula de Majorana, que se define como un fermión que es su propia antipartícula. El mecanismo que da masa a un neutrino de Majorana podría explicar la leptogénesis primordial y parte de la asimetría materia-antimateria observada en el universo primitivo.

Otra implicación de la naturaleza Majorana del neutrino sería que se permiten los procesos que violan el número de leptones en dos

unidades. Esto tiene una implicación experimental importante: la desintegración doble beta tendría un modo en el que se produce sin emisión de neutrinos:

$$(Z, A) \rightarrow (Z + 2, A) + 2e^- + Q_{\beta\beta} \quad (1)$$

En este modo, la totalidad de la energía de desintegración disponible,  $Q_{\beta\beta}$ , sería entonces transportada por los dos electrones. Esta desintegración, en su modo normal (que emite dos antineutrinos junto a los electrones), es una desintegración rara que sólo es posible para un conjunto reducido de núcleos, con vidas medias del orden de  $10^{19}$ - $10^{21}$  años. La observación de una desintegración doble beta sin neutrinos establecería definitivamente que el neutrino es una partícula de Majorana.

La amplitud de este proceso es una suma sobre la contribución de los tres estados de masa del neutrino ligero  $\nu_i$  ( $i = 1, 2, 3$ ) por lo que se puede definir la masa efectiva del neutrino Majorana,  $m_{\beta\beta}$ , como

$$m_{\beta\beta} = \left| \sum_{i=1}^3 U_{ei}^2 m_i^2 \right| \quad (2)$$

donde los  $U_{ei}$  son los elementos de la matriz PMNS que parametriza la oscilación del neutrino. En el caso de que el proceso subyacente que gobierna la desintegración doble beta sin neutrinos es el llamado intercambio de neutrinos ligeros, la masa efectiva de Majorana estaría relacionada con la vida media de la desintegración,  $T_{1/2}^{0\nu}$  que es el principal observable accesible experimentalmente. Esta relación se escribiría

$$(T_{1/2}^{0\nu})^{-1} = G^{0\nu} |M^{0\nu}|^2 \left( \frac{m_{\beta\beta}}{m_e} \right)^2 \quad (3)$$

donde  $G^{0\nu}$  es un factor de espacio de fase que depende del valor  $Q_{\beta\beta}$  de la desintegración así como del número atómico  $Z$ , y  $M^{0\nu}$  es el elemento matriz nuclear (NME). Por tanto, una tasa observada para esta desintegración proporcionaría una restricción en la escala de masa absoluta del neutrino.

El campo de la búsqueda de desintegración doble beta sin neutrinos es, por tanto, muy activo y ha dado la oportunidad a muchos experimentos diferentes de buscar, por diferentes medios y en diferentes isótopos, la misma propiedad fundamental del neutrino. Para

observar esta desintegración es importante caracterizar su firma característica. Como he comentado más arriba, la principal diferencia de este modo con respecto al de dos neutrinos es que en este, los dos electrones se llevan la energía total,  $Q_{\beta\beta}$ , disponible en el sistema que es específica del isótopo considerado. Dado que las energías en juego son de unos pocos MeV, la radiactividad natural es la principal fuente de fondo. Los detectores construidos para las búsquedas de doble beta sin neutrinos tienen sus materiales cuidadosamente seleccionados para maximizar su radiopureza. También se utilizan blindajes pasivos y activos para reducir aún más el índice de fondo. Algunos experimentos desarrollan otras técnicas para contar el número de electrones emitidos y para marcar los núcleos hijos de un evento para alcanzar un régimen casi libre de fondo.

La sensibilidad a una vida media determinada que puede alcanzarse tras un tiempo de funcionamiento  $t$  es función del número de emisores  $\beta\beta$  (relacionado con su "masa objetivo"  $M_{\beta\beta}$ ), la resolución energética  $\Delta E$  que permite separar el modo de dos neutrinos del modo de neutrino cero y la actividad de fondo que cae dentro de la región energética de interés  $c$ , expresado en recuentos/(keV kg años). Esto se resume en la siguiente fórmula donde  $\epsilon$  es la eficiencia de detección:

$$S(T_{1/2}^{0\nu}) \propto \sqrt{1/\epsilon} \left( \frac{c\Delta E}{M_{\beta\beta}t} \right)^{1/4} \quad (4)$$

A pesar del gran esfuerzo realizado por las diferentes colaboraciones y del excelente rendimiento de sus detectores, aún no se ha encontrado una señal positiva a este proceso. Sin embargo si que hemos conseguido seguir mejorando el límite inferior a la vida media del proceso sin neutrinos. A fin de mejorar la sensibilidad y observar este proceso, el campo está diseñando nuevos detectores en la escala de la tonelada. Los mejores límites de las vidas medias han sido fijados por GERDA para  $^{76}\text{Ge}$  en  $1.8 \times 10^{26}$  años, KamKAND-Zen para  $^{136}\text{Xe}$  en  $2.3 \times 10^{26}$  años, EXO-200 también para  $^{136}\text{Xe}$  en  $3.5 \times 10^{25}$  años y CUORE para  $^{130}\text{Te}$  en  $3.2 \times 10^{25}$  años.

Para hacer frente a este reto, la colaboración NEXT ha estado desarrollando Time Projection Chambers (TPC, Cámara de Proyección Temporal) electroluminiscentes de alta presión durante la última década para buscar la desintegración doble beta sin neutrinos usando el

xenón-136, donde el volumen de detección está constituido por dicho isótopo. Una TPC es un tipo de detector que puede medir la energía depositada por la radiación primaria dentro de su volumen. La radiación incidente ioniza y excita los átomos del medio de detección. En el volumen activo se crea un campo eléctrico para evitar la recombinación de los pares electrón-ión y conseguir mover los electrones hacia una etapa de amplificación diseñada para producir una señal detectable. Para una partícula produciendo ionización mínima, el número de electrones secundarios producidos por la ionización es proporcional a la energía depositada. La gran ventaja de la TPC es que puede reconstruir los eventos que suceden dentro del volumen fiduciario usando un solo plano de lectura. Para hacerlo, este plano lee información ordenada por tiempo, luego, suponiendo un conocimiento previo de la velocidad de los electrones en el gas, el tiempo puede transformarse a una tercera coordenada (a menudo denominada  $z$ ), proyectando así el tiempo información en una coordenada espacial, de ahí el nombre Cámara de Proyección Temporal.

El experimento NEXT utiliza un proceso de amplificación lineal, la electroluminiscencia, con fluctuaciones despreciables para explotar la buena resolución energética intrínseca del gas xenón (alrededor del 0.3% anchura a media altura, FWHM, en  $Q_{\beta\beta}$ ) con el fin de maximizar la sensibilidad del experimento, como se muestra en la ecuación 4. Por otro lado, en un gas a alta presión las trazas dejadas por los electrones emitidos por la desintegración doble beta se extienden a unos pocos centímetros, lo que permite determinar sus características topológicas. Una clasificación de los eventos basada en su topología permite realizar un paso adicional de rechazo del ruido fondo.

Justo después de su inicio, la colaboración construyó dos demostradores: NEXT-DEMO y NEXT-DBDM. Estos prototipos funcionan con aproximadamente 1-2 kg de xenón y sirvieron para validar la prueba de concepto de la TPC electroluminiscente de alta presión para las búsquedas de la desintegración doble beta sin neutrinos. Desde entonces, la colaboración ha operado con notable éxito el detector NEXT-White desde 2016 hasta 2021. Consiguió demostrar con 10 kg de xenón enriquecido su objetivo nominal de una resolución energética por debajo del porcentaje en 2.6 MeV, así como la capacidad de rechazo de fondo basado en la topología. Fue sensible al modo de dos neutrinos, estableciendo su propia medida en su vida media. El

sucesor de NEXT-White, NEXT-100, está en construcción y operará con 100 kg de xenón enriquecido para establecer un límite competitivo en la vida media de la desintegración doble beta sin neutrinos.

La generación de detectores NEXT a escala de la tonelada sigue un enfoque incremental. El diseño del primer módulo a escala de la tonelada, NEXT- HD, está en marcha. Consistirá en una TPC simétrica cuyo volumen activo será un cilindro de 3 m de longitud por 2.2 m de diámetro. Le seguirá un segundo módulo, NEXT-BOLD, cuyo objetivo será alcanzar el régimen libre de fondo mediante la implementación de un sistema capaz de detectar al vuelo el núcleo hijo emitido por una desintegración doble beta.

### *Mezclas de baja difusión*

A escalas de la tonelada, la difusión de los electrones secundarios moviéndose en el gas xenón se convierte en un problema ya que la gran difusión de estos limita la correcta reconstrucción de las trazas originales. Se han realizado un conjunto de mediciones de las propiedades de transporte de los electrones en el xenón a alta presión utilizando el detector NEXT-White. Los valores medidos concuerdan con los calculados por el software de simulación de microfísica más avanzado utilizado para los detectores gaseosos. La difusión surge principalmente de la agitación térmica de los electrones en la deriva. Por lo tanto, la alta difusión de los electrones de deriva en el xenón se debe a la ineficacia de la transferencia de energía a través de colisiones elásticas entre los electrones y los átomos de xenón. Esto tiende a difuminar las características de la señal topológica en la que se basa el rechazo del fondo topológico.

Por lo tanto, encontrar una solución a este problema ha sido una línea de búsqueda activa dentro de la colaboración. Se han realizado amplios estudios, tanto numéricos como experimentales, de una serie de mezclas en las que se añade al xenón una minúscula concentración de un gas molecular. Estos estudios muestran una drástica reducción de la difusión que va acompañada, en la mayoría de los casos, de una degradación de la resolución energética.

La propuesta de utilizar un gas noble, el helio, como adición al xenón es el tema central de la presente tesis. Por un lado, la transferencia de energía a través de colisiones elásticas entre electrones y átomos

de helio es aproximadamente dos órdenes de magnitud más eficiente que la que se produce entre electrones y átomos de xenón. Por otro lado, en la escala de energía de los electrones de deriva, las colisiones elásticas electrón-helio dominan a las de electrón-xenón. Estas consideraciones, en conjunto, apuntan a una reducción considerable de la difusión térmica en las mezclas de helio y xenón (HeXe).

Las mezclas de HeXe se estudiaron primero numéricamente para evaluar su potencial. Las simulaciones de las propiedades de transporte de los electrones muestran, en efecto, que se prevé un factor de reducción de la difusión transversal de aproximadamente 3 para las mezclas que contienen un 15% de helio a 15 bares. Puede reducirse aún más con rendimientos decrecientes al aumentar la fracción de helio. La difusión longitudinal tiene un comportamiento diferente al de la difusión transversal y depende en gran medida de la distribución de energía de los electrones a la deriva. Las simulaciones muestran que a 15 bar y bajo los campos de deriva típicos, la difusión longitudinal en las mezclas de HeXe es muy cercana a la del xenón puro.

Para evaluar el impacto de la adición de helio en la electroluminiscencia en términos de rendimiento lumínico y de la varianza del proceso, se realizó un conjunto de simulaciones. Un estudio con elementos finitos produjo los mapas de campo eléctrico. Estos se utilizan como entrada para simular la evolución de los electrones a la deriva dentro de una etapa de amplificación. Esta evolución se calcula mediante integración Monte-Carlo. La naturaleza de la colisión electrón-átomo se decide estocásticamente; se supone que el número de fotones emitidos es igual al número de excitaciones de átomos. Este sencillo modelo de centelleo ha sido validado experimentalmente. Estas simulaciones muestran que la electroluminiscencia en mezclas de helio y xenón es extremadamente similar a la del xenón puro en términos de rendimiento lumínico y de las fluctuaciones del rendimiento lumínico. Este comportamiento se debe a que a las energías de los electrones que pasan por la etapa de amplificación de la TPC, dominan las colisiones electrón-xenón. Las simulaciones nos dicen que tienen lugar también colisiones entre los electrones y los átomos de helio, los cuales afectan a la producción de luz en la zona de producción de electroluminiscencia por reducir el número de colisiones con átomos de xenón. Pues con menor número de colisiones entre electrones y átomos de xenón, menos fotones producidos, así como mayor umbral de campo eléc-



trico necesario para que se produzca electroluminiscencia. El campo necesario es directamente proporcional a la presión parcial del helio y el número de fotones producidos inversamente proporcional a ella.

La conclusión es que, a diferencia de las mezclas de gases moleculares, el helio reduce la difusión sin sacrificar la resolución energética del xenón puro. Sin embargo, aún faltaba resolver un problema, aislar los fotomultiplicadores de la atmosfera de Helio. Una propuesta para proteger estos fotomultiplicadores consiste en utilizar una ventana cristalina junto con selladores metálicos.

Se realizó un conjunto adicional de simulaciones para evaluar cómo evolucionan las propiedades de las mezclas de HeXe cuando se mantiene la presión parcial del xenón a 15 bares. La ventaja es que la masa del emisor doble beta se mantendría sin cambios, lo que conllevaría pequeñas mejoras en el rendimiento lumínico y en la difusión.

### *El detector NEXT-DEMO++*

A la luz de las entusiastas predicciones sobre las mezclas de helio-xenón (HeXe), la colaboración NEXT construyó y puso en marcha el prototipo NEXT-DEMO++. Este detector es una TPC construida siguiendo opciones de diseño que fueron una mezcla entre las realizadas para NEXT-White y las que se implementaron para NEXT-100.

NEXT-DEMO++ está construido siguiendo el concepto SOFT (Separated-Optimized Functions TPC). Un conjunto de fotomultiplicadores (PMT) se encarga de detectar el centelleo primario y de realizar la medida de la energía que se realiza recogiendo la emisión secundaria de luz emitida en la región de amplificación. El montaje final implementó sin problemas la propuesta de diseño que garantiza un funcionamiento seguro de los fotomultiplicadores sensibles al helio para las mezclas que contienen una cantidad considerable de helio. La elección de los PMT se debe a su bajo ruido y alta ganancia. La reconstrucción de trazas se realiza mediante una densa matriz de fotomultiplicadores de silicio (SiPM). Los sensores utilizados inicialmente eran los mismos que los utilizados en NEXT-White. El sistema de adquisición de datos instalado para NEXT-DEMO++ era una versión reducida del de NEXT-White.

El recipiente de presión de NEXT-DEMO++ es el mismo que se utilizó para el primer demostrador, NEXT-DEMO. Los principales componentes de la TPC son los electrodos de formación del campo eléctrico. La jaula de campo (field cage) permite aplicar un campo uniforme a través del volumen activo para derivar los electrones secundarios hacia la zona de amplificación. Se ha diseñado de forma que pueda ampliarse fácilmente para NEXT-100. En la parte interior de la jaula de campo se ha montado un conjunto de paneles de teflón revestidos con un cambiador de longitudes de onda para aumentar la eficacia de los sensores a la luz.

El cátodo limita el volumen activo en el lado opuesto de la etapa de amplificación, está formado por una rejilla de hilos de acero inoxidable tensados sobre un marco de acero. Durante la toma de datos se notaba que el campo eléctrico del cátodo se extendía hasta el volumen activo del detector con una forma diferente de lo esperado. Usando una simulación por elementos finitos pudimos estudiar la forma del campo con más detalle y así calcular de forma precisa el campo presente en el volumen activo. Esa predicción es necesaria para poder usar Monte Carlo en el estudio de los parámetros de transporte de los electrones los cuales son muy sensibles a cambios en el campo eléctrico. Sin entender la forma e intensidad del campo cerca del cátodo, el estudio de estas propiedades fundamentales es imposible, particularmente en detectores más grandes donde el correcto posicionamiento de las interacciones en el eje  $z$  tiene importantes implicaciones a la hora de rechazar sucesos ruidosos procedentes del cátodo o detrás de él.

El otro lado del volumen activo está materializado por una malla de acero inoxidable, que da la entrada a la zona de amplificación. Esta malla forma, junto con una placa de vidrio recubierta con una capa conductora, la región de amplificación del detector, donde un campo eléctrico más alto acelera los electrones secundarios para producir el centelleo secundario. Dos puertos de alimentación de alto voltaje llevan la tensión a la malla y al cátodo, siguiendo un diseño implementado para el detector NEXT-White.

Construido principalmente con el objetivo de probar mezclas de HeXe, NEXT-DEMO++ también fue pensado de forma más general como banco de pruebas para NEXT-100. NEXT-DEMO++ ha probado diferentes configuraciones de sensores de reconstrucción de la señal topológica y debería probar diferentes etapas de amplificación posi-

bles para NEXT-100. La operación del detector tuvo éxito al operar con seguridad una mezcla de HeXe, pero reveló una fuente de dificultad en cuanto a la separación de helio y xenón por criorecuperación. Se esperaba que la diferencia entre el punto de ebullición del helio y del xenón permitiera una clara separación a la temperatura del nitrógeno líquido. Pero tras el primer intento, se observó que la presión residual en el detector era mucho mayor de lo esperado (1 bar). Algunas pruebas iniciales indicaban que el aumento de la superficie a la temperatura del nitrógeno líquido mejoraba la recuperación del xenón en la botella de criogenia, sin embargo no se consiguió recuperar por completo el gas del detector, haciendo que el coste de operación fuese demasiado alto. En la actualidad se están explorando alternativas para superar este problema.

### *Caracterización de una mezcla de Helio-Xenón*

Se tomaron datos utilizando NEXT-DEMO++ para comparar una mezcla de HeXe al 15% con una mezcla de xenón puro de referencia. Para caracterizar las dos mezclas, se utilizó la misma fuente de calibración. Esta fuente radiactiva produce  $^{83m}\text{Kr}$  que se distribuyen en el volumen activo antes de decaer, dejando depósitos de energía puntuales que son especialmente útiles para caracterizar las propiedades de transporte de electrones.

El detector cuenta con dos conjuntos de sensores que trabajan conjuntamente: los fotomultiplicadores (PMTs) utilizados para determinar el inicio de la adquisición de los eventos y realizar la medición de energía; y los fotomultiplicadores de silicio (SiPMs), utilizados para la reconstrucción 2D, midiéndose la tercera dimensión como la duración entre la interacción primaria y la ampliación de la señal.

Los datos en bruto recogidos por los sensores se registran y procesan mediante una maquinaria de software desarrollada internamente en el marco de la colaboración NEXT. Cada evento se registra en última instancia como una colección de características tales como su posición reconstruida en 3D, su correspondiente luz de centelleo primaria y secundaria recogida, etc. Un análisis de estos datos permite caracterizar la mezcla de HeXe en relación con la referencia de xenón. Es necesario aplicar una selección a los datos para retener sólo los eventos de interés inducidos por la fuente de calibración, una fuente de  $^{83m}\text{Kr}$ .

Una comparación entre las características de la luz detectada como centelleo primario sugiere que el centelleo primario en las mezclas de HeXe no difiere, como se esperaba, de los del xenón puro. Dado que los eventos de  $^{83m}\text{Kr}$  se utilizan normalmente como herramienta de calibración continua para los detectores de tipo NEXT, este resultado confirma la viabilidad de las mezclas de HeXe según los estándares del experimento NEXT.

Dado que los eventos de  $^{83m}\text{Kr}$  liberan una deposición de energía monocromática, es posible medir la resolución energética del detector a 41.56 keV con cada mezcla, ya que la energía es proporcional a la luz detectada. Tras la corrección de la señal para tener en cuenta las pérdidas de electrones debido a impurezas, la resolución energética que se mide es  $7.42 \pm 0.04$  % FWHM en HeXe y en  $4.99 \pm 0.02$  % FWHM en xenón puro. Esta menor cantidad de luz en el HeXe está en consonancia con la que predicen las simulaciones numéricas correspondientes a un campo de amplificación bastante cercano al umbral electroluminiscente. La aparente degradación de la resolución energética se debe a la menor cantidad de luz detectada en el HeXe con respecto al xenón puro, que era esperable según las simulaciones.

Como estaba previsto, también se evaluaron los parámetros de transporte de electrones. La velocidad de deriva se calculó midiendo el tiempo de deriva de los electrones procedentes del cátodo que corresponde al tiempo de deriva máximo. La velocidad de deriva medida fue de  $0.950 \pm 0.006$  mm/ $\mu\text{s}$  en xenón puro y de  $3.012 \pm 0.020$  mm/ $\mu\text{s}$  en HeXe. De nuevo, estos resultados son compatibles con los calculados por los métodos numéricos.

El coeficiente de difusión a lo largo de una dimensión, representado por la letra  $D$ , se define como:

$$\sigma^2(t_{drift}) \propto 2Dt_{drift} \quad (5)$$

donde  $\sigma^2$  es la dispersión media a lo largo de la misma dimensión, observada después de un tiempo de deriva  $t_{drift}$ .

El coeficiente de difusión longitudinal se midió a través de su efecto sobre la dispersión del pulso de centelleo secundario registrado por los PMT. Se midió un coeficiente de difusión de  $40.915 \pm 0.896$  cm<sup>2</sup>/s en xenón puro y de  $214.188 \pm 6.660$  cm<sup>2</sup>/s en HeXe. Dado que la difusión longitudinal se ve muy afectada por las condiciones de trabajo,

el mayor valor de su coeficiente en HeXe no es preocupante y era de esperar. Una mezcla de HeXe al 15% operada a la presión nominal de un detector NEXT: 15 bar o incluso 17.65 bar tendría una difusión longitudinal mucho menor. El valor medido en xenón es compatible con las mediciones anteriores, a pesar de la discrepancia con las expectativas numéricas.

Por último, se midió por primera vez el coeficiente de difusión transversal en una mezcla de helio y xenón a alta presión a través de su efecto en las Funciones de Dispersión de Puntos (PSF en sus siglas en inglés). Éstas se calcularon para diferentes tiempos de deriva. La PSF calculada para cada corte temporal es en realidad la media calculada usando todos los eventos en el correspondiente corte temporal. Se midió un coeficiente de difusión de  $687.935 \pm 0.596 \text{ cm}^2/\text{s}$  en el xenón puro y de  $303.749 \pm 3.028 \text{ cm}^2/\text{s}$  en el HeXe. El valor medido en xenón puro se ajusta a las expectativas numéricas. La medición de la difusión transversal en HeXe parece menos consistente, lo que puede explicarse en parte por la menor cantidad de luz recogida por el plano de seguimiento, afectando así a su correcta reconstrucción y estimación.

No obstante, se ha confirmado experimentalmente que la difusión transversal se reduce en un factor de entre 2 y 3 en HeXe. Esto demuestra que el helio puede utilizarse como mezcla con xenón para obtener una mezcla de baja difusión para una TPC electroluminiscente. El primer módulo a escala de una tonelada que construirá la colaboración NEXT, NEXT-HD, se diseñará de forma que pueda funcionar con una mezcla de baja difusión de HeXe.

Esta tesis presenta estudios dirigidos a entender las propiedades de transporte de electrones en mezclas de gases con particular interés en la combinación de xenón y helio, la cual podría mejorar varios parámetros del experimento NEXT. Se interesa por todos los aspectos experimentales: desde el cálculo numérico para asesorar el impacto de una mezcla en el detector hasta el estudio de las soluciones técnicas necesarias para operar TPCs con aditivos moleculares o helio. Entre las soluciones propuestas se cuenta con la de aislar los PMTs del volumen de gas mediante ventanas de zafiro. Por último, se llevó a cabo una prueba experimental exitosa de una mezcla de helio-xenón con el prototipo NEXT-DEMO++ que se construyó con ese fin.



# Summary

The neutrino is a particle that has seen a surge of interest in the past decades. Its existence was conjectured by W. Pauli in 1930 to explain the continuous spectrum of the  $\beta$  decay. It was promptly integrated as a part of the Fermi's theory of  $\beta$  decay. The neutrino remained hypothetical until its discovery in 1956 by Reines and Cowan. And it was thought for decades to be nothing more than a massless and chargeless particle, despite the puzzling observation of a discrepancy between the detected flux of neutrinos coming from the Sun and that flux expected by the state of the art solar models. It was predicted that if neutrinos were massive, the so-called solar neutrino problem could be explained by neutrino oscillation, a phenomenon arising from the propagation of three different neutrino mass states, two of which at least must be non zero. The unambiguous discovery of neutrino oscillation in 1998 proved that neutrinos have a non vanishing mass.

It is therefore necessary to accommodate a massive neutrino in the theory by expanding the Standard Model and that can be done in two different ways. The first consists of having a Dirac neutrino, that is a neutrino that gets its mass through the same mechanism as the other fermions: the Higgs mechanism. The second assumes that the neutrino is a Majorana particle, which is defined as a fermion being its own antiparticle. The mechanism giving its mass to a Majorana neutrino could explain the leptogenesis and part of the matter-antimatter asymmetry observed in the early universe.

Another implication of a Majorana neutrino is that processes violating the lepton number by two units become allowed. This has a major experimental implication: the double beta decay would have a

mode in which it does not emit neutrinos:

$$(Z, A) \rightarrow (Z + 2, A) + 2e^- + Q_{\beta\beta} \quad (6)$$

The entirety of the available decay energy,  $Q_{\beta\beta}$ , would then be carried by the two electrons. This decay, in its normal mode (which emits two antineutrinos alongside the electrons), is a rare decay that is possible only for a handful nuclides, with half-lives of the order of  $10^{19}$ - $10^{21}$  years. Seeing an unambiguous neutrinoless double beta decay would definitively establish that the neutrino is a Majorana particle.

The amplitude of this process is a summation over the contribution of the three light neutrino mass states  $\nu_i$  ( $i = 1, 2, 3$ ) so one can define the effective neutrino Majorana mass,  $m_{\beta\beta}$ , as:

$$m_{\beta\beta} = \left| \sum_{i=1}^3 U_{ei}^2 m_i^2 \right| \quad (7)$$

where the  $U_{ei}$  are the elements of the PMNS matrix parametrizing the neutrino oscillation. In the case where the underlying process governing the neutrinoless double beta decay is the so-called light neutrino exchange, the effective Majorana mass would be related to the half-life of the decay,  $T_{1/2}^{0\nu}$  which is the main observable experimentally accessible. This relation would be written:

$$(T_{1/2}^{0\nu})^{-1} = G^{0\nu} |M^{0\nu}|^2 \left( \frac{m_{\beta\beta}}{m_e} \right)^2 \quad (8)$$

where  $G^{0\nu}$  is a phase-space factor that depends on the Q-value of the decay as well as the atomic number  $Z$ , and  $M^{0\nu}$  is the nuclear matrix element (NME). As such an observed rate for this decay would provide a constraint on the absolute mass scale of the neutrino.

The field of neutrinoless double beta decay searches is therefore very active and gave an opportunity for a lot of different experiments to search for the same fundamental property of the neutrino through different means and on different isotopes. The aim of all the experiments is to detect the signature of a neutrinoless double beta decay, which is the emission of two electrons carrying a total energy  $Q_{\beta\beta}$  specific to the isotope considered. Because the energies at play are



about a few MeV, natural radioactivity is the main background source. Detectors built for neutrinoless double beta searches have their materials carefully selected so as to maximize their radiopurity. Passive and active shielding are also used to further reduce the background index. Some experiments develop other techniques to count the number of electrons emitted and to tag the daughter nuclei of the decay in order to reach a quasi background-free regime.

The sensitivity to a given half-life that can be achieved after a running time  $t$  is a function of the number of  $\beta\beta$  emitters (related to its "target mass"  $M_{\beta\beta}$ ), the energy resolution  $\Delta E$  that allows separation of the two neutrinos mode from the zero neutrino mode and the background count falling within the energetic region of interest  $c$ , expressed in counts/(keV kg years). This is summarised in the following formula where  $\epsilon$  is the detection efficiency:

$$\mathcal{S}(T_{1/2}^{0\nu}) \propto \sqrt{1/\epsilon} \left( \frac{c\Delta E}{M_{\beta\beta}t} \right)^{1/4} \quad (9)$$

Despite the great effort made by the different collaborations and the excellent performance of their detectors, a positive signal to this process has not yet been found. However, these experiments managed to further improve the lower limit on the half-life of the neutrinoless process. The best limits on the half-lives have been set by GERDA for  $^{76}\text{Ge}$  at  $1.8 \times 10^{26}$  years, KamKAND-Zen for  $^{136}\text{Xe}$  at  $2.3 \times 10^{26}$  years, EXO-200 also for  $^{136}\text{Xe}$  at  $3.5 \times 10^{25}$  years and CUORE for  $^{130}\text{Te}$  at  $3.2 \times 10^{25}$  years. In order to improve the sensitivity and observe this process, the field is designing new detectors on the tonne scale.

To meet this challenge, the NEXT collaboration has been developing high pressure electroluminescent Time Projection Chambers (TPCs) over the past decade to search for the neutrinoless double beta decay in xenon-136 where the detection volume is constituted of the target isotope. A TPC is a type of detector that can measure the energy deposited by a primary radiation within its volume. The incident radiation ionizes and excites the atoms of the detection medium. An electric field is applied to prevent the recombination of the electron-ion pairs and drift the electrons towards an amplification stage designed to produce a detectable signal. For a minimum ionizing particle, the number of secondary electrons produced by ionization is proportional to the energy deposited. The great advantage of the TPC is that it

can reconstruct the events happening within the fiducial volume using a single readout plane. In order to do so, this plane reads information ordered by time, then, assuming prior knowledge of the electron velocity in the gas, the time can be transformed to a third coordinate (often noted  $z$ ), thus projecting the time information into a spatial coordinate, hence the name Time Projection Chamber.

The NEXT experiment uses a linear amplification process, electroluminescence, with negligible fluctuations to exploit the good intrinsic energy resolution of the xenon gas (around 0.3% FWHM at  $Q_{\beta\beta}$ ) in order to maximize the sensitivity of the experiment, as shown in Equation 9. On the other hand, operating on a gas at high pressure extends the tracks left by the electrons emitted by double beta decay to a few centimeters which turns their fine topological features into accessible information. A classification of events based on their topology allows performance of an extra step of background rejection.

Right after its inception, the collaboration has built two demonstrators: NEXT-DEMO and NEXT-DBDM. These prototypes operate about 1-2 kg of xenon and validated the proof of concept of high pressure electroluminescent TPC for neutrinoless double beta searches. Since then, the collaboration has operated with acclaimed success the detector NEXT-White from 2016 until 2021. It managed to demonstrate with 10 kg of enriched xenon its nominal goal of a sub-percent energy resolution at 2.6 MeV as well as the efficiency of the topological-based background rejection. It was sensitive to the two-neutrino mode, setting its own measurement on its half-life. The successor of NEXT-White, NEXT-100, is under construction and will operate 100 kg of enriched xenon in order to set a competitive limit on the half-life of the neutrinoless double beta decay.

The tonne-scale generation of NEXT detectors follows an incremental approach. The design of the first tonne-scale module, NEXT-HD, is underway. It will be a symmetric TPC whose active volume will be a cylinder of 3 m long with a 2.2 m diameter. A second module, NEXT-BOLD, following that, will aim to reach the background-free regime by implementing a system capable of tagging on the fly the daughter nucleus emitted by a double beta decay.

*Low-diffusion mixtures*

In view of scaling the experiment to the tonne scale, the diffusion of the drifting secondary electrons in the xenon gas becomes problematic. A set of measurements of the electron transport properties were made in high pressure xenon using NEXT-White. The measured values are in good agreement with those computed by the state of the art microphysics simulation software used for gaseous detectors. The diffusion arises mainly from the thermal agitation of the drifting electrons. Therefore, the high diffusion of drifting electrons in xenon is due to the inefficiency of the energy transfer through elastic collisions between electrons and xenon atoms. It tends to blur the features on which the topological-based background rejection is based.

Thus, finding a solution to this issue has been an active line of research within the collaboration. Extensive studies were performed, both numerical and experimental, of a number of mixtures where a minute concentration of a molecular gas is added to xenon. These studies show a drastic reduction of the diffusion that is accompanied, in most cases, with a degradation of the energy resolution.

The proposal to use a noble gas, helium, as an admixture to xenon is the central subject of the present thesis. On the one hand the energy transfer through elastic collisions between electrons and helium atoms is about two orders of magnitude more efficient than that between electrons and xenon atoms. On the other hand, at the energy scale of the drifting electrons, the elastic collisions of electron-helium dominate those of electron-xenon. Those considerations together hint for a sizeable reduction of the thermal diffusion in helium-xenon (HeXe) mixtures.

HeXe mixtures were first studied numerically to assess their potential. Simulations of the electron transport properties show indeed that a reduction factor of the transverse diffusion of about 3 is expected for mixtures containing 15% helium at 15 bar. It can be further reduced with diminishing returns by increasing the helium fraction. The longitudinal diffusion has a different behavior than the transverse diffusion and is heavily dependent on the drifting electrons' energy distribution. Simulations show that at 15 bar and under the typical drifting fields, the longitudinal diffusion in HeXe mixtures is very close to that of pure xenon.

For HeXe mixtures containing up to 20% of helium and according to the software simulating the primary interaction in a gaseous detector, the intrinsic energy resolution of xenon appears not to be changed in any relevant way. By studying the evolution of the population of excited atoms with the addition of helium, one can predict that the primary scintillation is expected also to remain nearly equal to that of pure xenon.

To evaluate the impact of helium addition on the electroluminescence in terms of light yield and of the variance of the process, a set of simulations were performed. A finite element solver produces the field maps. These are used as an input to simulate the evolution of drifting electrons inside an amplification stage. This evolution is computed by Monte-Carlo integration. The nature of the electron-atom collision is decided stochastically; the number of photons emitted is assumed to be equal to the number of atom excitations. This simple scintillation model has been validated experimentally. These simulations show that the electroluminescence in helium-xenon mixtures is extremely similar to that of pure xenon in terms of light yield and of the light yield fluctuations. This behavior stems from the fact that, at the energies of the electrons going through the amplification stage of the TPC, the electron-xenon collisions dominate. The simulations also indicate that part of the collisions happen with the helium atoms which also affects the light production along the electroluminescent process. It results in a small reduction of the light yield and a slightly larger electroluminescent field threshold. In particular, these effects are directly proportional to the helium partial pressure and are well understood: the more helium, the more electrons lose their energy through elastic collisions and, as a result the necessary field to excite xenon atoms becomes higher.

Overall the conclusion being that unlike molecular gas admixtures, helium lowers the diffusion without sacrificing the energy resolution of pure xenon. A proposal to protect the helium-sensitive photomultipliers from the helium-rich atmosphere consists of using a crystalline window along with metallic sealants.

An additional set of simulations were performed to evaluate how the properties of HeXe mixtures evolve when keeping the partial pressure of xenon at 15 bar. The advantage being that the target mass of the double beta emitter would be left unchanged which would come

with minor improvements regarding the light yield and the diffusion.

### *The NEXT-DEMO++ detector*

In light of the enthralling predictions concerning helium-xenon (HeXe) mixtures the NEXT collaboration built and commissioned the prototype NEXT-DEMO++. This detector is a TPC constructed following design choices that were a mix between those made for NEXT-White and those set to be implemented for NEXT-100.

NEXT-DEMO++ is built following the SOFT (Separately-Optimized Functions TPC) concept. An array of photomultipliers (PMTs) is responsible for detecting the primary scintillation and performing the energy measurement by collecting the secondary scintillation emitted from the amplification region. The final assembly notably implemented the design proposal that ensures a safe operation of the helium-sensitive photomultipliers for mixtures containing a sizeable amount of helium. The choice of PMTs is made due to their low noise and high gain. The tracking is done by a dense array of silicon photomultipliers (SiPMs). The sensors used initially were the same as those used in NEXT-White. The data acquisition system installed for NEXT-DEMO++ was a version scaled down of that of NEXT-White.

The pressure vessel of NEXT-DEMO++ is the same that was used for the demonstrator NEXT-DEMO. The main components of the TPC are the field shaping electrodes. The field cage ensures that a uniform field is applied through the active volume in order to drift the secondary electrons towards the amplification stage. It was designed in a way that can be easily scaled up for NEXT-100. On the inner part of the field cage are mounted a set of teflon panels coated with a wavelength shifter to increase the light collection efficiency.

The cathode limits the active volume on the opposite side of the amplification stage, it is made of a grid of stainless steel wires tensioned on a frame. It has been noted during the operation that, given the dimensions of the cathode grid, a notable field leakage was occurring in the active volume. An electrostatic finite element simulation confirmed this and gave a proper way to study the shape of the field in more detail and thus accurately calculate the field reigning in the active volume. Understanding this field leakage is fundamental for a proper comparison of the data with the Monte-Carlo estimations of

the electron transport parameters, which are very sensitive to changes in the electric field. Without understanding the shape and intensity of the field near the cathode, the study of these fundamental properties is impossible, particularly in larger detectors where the correct positioning of the interactions on the z-axis has important implications in rejecting noisy events from the cathode or behind it.

The other side of the active volume is materialized by a stainless steel mesh, the gate. The gate forms together with a glass plate coated with a conductive coating the amplification region of the detector, where a higher electric field accelerates the secondary electrons in order to yield the secondary scintillation. Two high-voltage feedthroughs bring the voltage to the gate and to the cathode, following a design implemented for NEXT-White.

Built primarily with the goal to test HeXe mixtures, NEXT-DEMO++ was also thought of more generally as a test bench for NEXT-100. NEXT-DEMO++ has tested different tracking sensor configurations and will test different possible amplification stages for NEXT-100.

The detector was successful at operating safely a HeXe mixture but revealed a source of difficulty regarding the separation of helium and xenon by cryo-recovery. It was expected that the difference between the boiling point of helium and xenon would allow for a clear separation at the temperature of liquid nitrogen. But after the first attempt, not all of the xenon was frozen in the cryo-bottle. Some initial tests hinted that increasing the surface at the temperature of liquid nitrogen improved the recovery of xenon in the cryo-bottle. Alternatives for overcoming this problem are currently being explored.

### *Characterization of a Helium-Xenon mixture*

Data were taken using NEXT-DEMO++ to compare a 15% HeXe mixture with a reference pure xenon mixture at 9.1 bar. In order to characterize the two mixtures, the same calibration source was used. This radioactive source produces  $^{83m}\text{Kr}$  that are distributed in the active volume before decaying, leaving point-like energy depositions which are especially useful to characterize the electron transport properties.

The detector has two sets of sensors working in conjunction: the photomultipliers (PMTs) used to trigger on the events and to perform the energy measurement; and the silicon photomultipliers (SiPMs),

used for the 2D reconstruction, the third dimension being measured as the duration between the primary interaction and the signal amplification.

Raw data collected from the sensors are recorded and processed through software machinery developed internally within the NEXT collaboration. Each event is ultimately recorded as a collection of characteristics such as its reconstructed 3D position, its corresponding primary and secondary scintillation light collected etc...

An analysis of these data allows characterization of the HeXe mixture relative to the xenon reference. A set of selection cuts need to be applied on the data in order to retain only the events of interest induced by the  $^{83m}\text{Kr}$  decay.

A comparison between the characteristics of the light detected as the primary scintillation suggests that the primary scintillation in HeXe mixtures does not differ, as expected, from those of pure xenon. Since the  $^{83m}\text{Kr}$  events are typically used as an on the fly calibration tool for NEXT-type detectors, this result confirms the viability of HeXe mixtures according to the standards of the NEXT experiment.

Because the  $^{83m}\text{Kr}$  events release a monochromatic energy deposition, it is possible to measure the energy resolution of the detector at 41.56 keV with each mixture as the energy is proportional to the light detected. After correction of the signal to account for the electron attachment to impurities, the energy resolution is measured at  $7.42 \pm 0.04$  % FWHM in HeXe and at  $4.99 \pm 0.02$  % FWHM in pure xenon. The apparent degradation of the energy resolution is due to the lower amount of light detected in HeXe with respect to pure xenon. This lower amount of light in HeXe is in line with the expectation coming from the numerical simulations corresponding to an amplification field fairly close to the electroluminescent threshold. This is consistent with the numerical simulations done regarding the light yield.

As intended, the electron transport parameters were also evaluated. The drift velocity was calculated by measuring the drift time of electrons originating from a known location within the detector, the cathode, which therefore corresponds to the maximum drift time. The drift velocity measured was  $0.950 \pm 0.006$  mm/ $\mu\text{s}$  in pure xenon and  $3.012 \pm 0.020$  mm/ $\mu\text{s}$  in HeXe. These results were observed to be in good agreement with the numerical estimations.

The diffusion coefficient along a dimension, noted  $D$ , is defined as

follows:

$$\sigma^2(t_{drift}) \propto 2Dt_{drift} \quad (10)$$

where  $\sigma^2$  is the mean spread along the same given dimension observed after a drift time  $t_{drift}$ .

The longitudinal diffusion coefficient was measured through its effect on the spread of the secondary scintillation pulse recorded by the PMTs. A diffusion coefficient of  $40.915 \pm 0.896 \text{ cm}^2/\text{s}$  was measured in pure xenon and of  $214.188 \pm 6.660 \text{ cm}^2/\text{s}$  in HeXe. Since the longitudinal diffusion is heavily affected by the working conditions, the higher value of its coefficient in HeXe is not worrisome and was expected. A 15% HeXe mixture operated at the nominal pressure of a NEXT detector: 15 bar or even 17.65 bar would have a much lower longitudinal diffusion. The value measured in xenon is compatible with previous measurements, despite a discrepancy with the numerical expectations.

Finally, the transverse diffusion coefficient was measured for the first time in a helium-xenon mixture at high pressure through its effect on the Point Spread Functions. Those were calculated for different drift times. The PSF of a given time slice is an average of the PSFs of all the events within that time slice. A diffusion coefficient of  $687.935 \pm 0.596 \text{ cm}^2/\text{s}$  was measured in pure xenon and of  $303.749 \pm 3.028 \text{ cm}^2/\text{s}$  in HeXe. The value measured in pure xenon is well in line with the numerical expectations. The measurement of the transverse diffusion in HeXe appears less consistent, which can be partly explained by the less amount of light collected by the tracking plane.

The transverse diffusion was nonetheless confirmed experimentally to be reduced by a factor between 2 and 3 in HeXe. This demonstrates that helium can be used as an admixture to xenon to make a low-diffusion mixture for an electroluminescent TPC. The first tonne-scale module that will be built by the NEXT collaboration, NEXT-HD, will be designed in a way that will allow it to be operated with a low-diffusion HeXe mixture.

This thesis presents studies aimed at understanding the electron transport properties in gas mixtures with particular interest in the combination of xenon and helium, which could improve several parameters of the NEXT experiment. It covered all relevant aspects related to these mixtures: from the numerical calculations to as-



sess their impact on a detector to the study of the technical solutions necessary for their implementation, among which is the proposal to isolate the PMTs using a crystalline sapphire window with metallic sealants. These steps paved the way for a successful experimental test of the performance of a helium-xenon mixture with the prototype NEXT-DEMO++ that was built for this purpose.



# The nature of neutrinos

# 1

The neutrino, denoted  $\nu$ , is an elementary particle of the standard model of particle physics. It is a neutral lepton so it can only interact by weak interaction. It is a particle that has long been around in particle physics, even though it was for a long time considered to be a bland, simple particle. But in the last two decades, there has been a surge of interest in them as they are a promising entry towards physics beyond the standard model.

## 1.1 Towards the neutrino discovery

### 1.1.1 Early days

The first studies of  $\beta$  radioactivity by James Chadwick in 1914 came with the surprising observation that the emitted electron energy spectrum was continuous between wide limits [1], which seemed sharply different from the more definite behaviour of  $\alpha$  and  $\gamma$  radiations. The controversy surrounding this observation was settled definitively by the experiment conducted by Ellis and Wooster in 1924, confirming that the  $\beta$  decay spectrum was continuous [2], the spectrum can be seen in Figure 1.1. Since no observational explanation arose by itself, the physicists at that time had to scratch their heads to find a solution to this puzzle.

It is only in 1930 that Wolfgang Pauli sent to his "radioactive" colleagues his famous letter [3] in which he calls for a "desperate remedy" to the puzzle of the continuous  $\beta$  spectrum. He makes the assumption that the missing energy is carried by a new, neutral particle that is extremely weakly interacting, so that no one has ever seen it before. It was the simplest alternative to the possibility of a violation

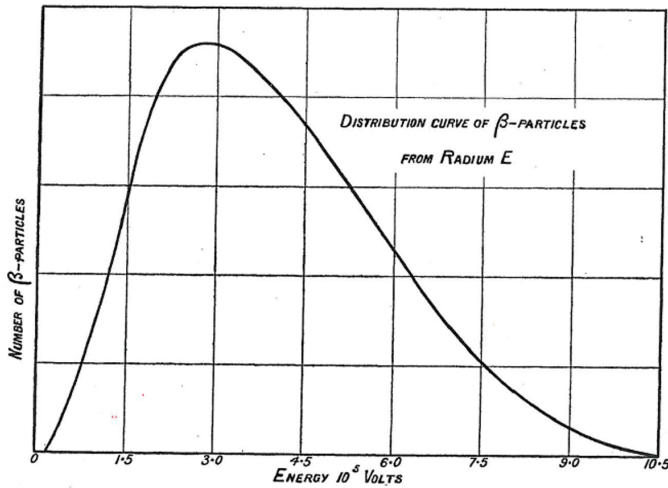


**Figure 1.1.** The continuous energy spectrum of the emitted electron in a  $\beta$  decay. Taken from [2].

of the energy conservation law inside the nucleus that was proposed by Niels Bohr.

The neutrino triggered Enrico Fermi to develop his theory of  $\beta$  decay as a four particle interaction (Figure 1.2). The original paper was published in Italian in 1933, a translated version can be found in [4]. This theory immediately appeared to be very robust as it accurately fit the data available at the time. It also could describe equally well a  $\beta$  decay where the electron would be replaced by the recently discovered positron, as it was observed for the first time in 1934 by F. Joliot and I. Curie [5].

Bethe and Peierls noted in the same year that Fermi's formalism should also allow the inverse- $\beta$  decay to exist: an existing neutrino interacts with a nucleus by transmuted it and emitting an electron or a positron. The detection of such phenomenon would be a direct proof of the neutrino's existence. They estimate the cross section of this process to be  $\sigma < 10^{-44} \text{cm}^2$  for the typical neutrinos produced in  $\beta$  decays. This result made them conclude that observing a neutrino was impossible [6].

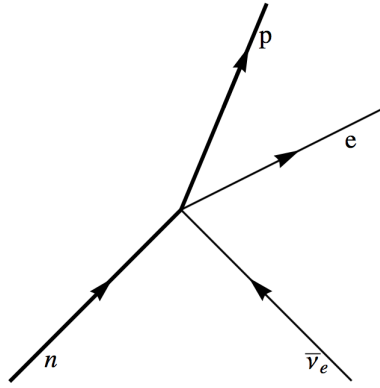
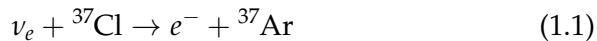


**Figure 1.2.** Four-fermion vertex in Fermi's  $\beta$  decay theory.

### 1.1.2 Reines and Cowan experiment

The progress made in nuclear physics, especially thanks to the Project Manhattan, changed the picture for neutrinos. Twelve years after the conclusion that neutrinos could never be observed due to their extremely low cross section with matter, Bruno Pontecorvo made a proposal to use the flux of neutrinos generated by the short lived fission products inside a nuclear reactor. This flux could balance out the low cross section of the neutrino-nucleus interactions and lead to a potential detection. The detection technique proposed by Pontecorvo was based on the famous chlorine-argon reaction occurring through inverse  $\beta$  decay [7]:



An attempt to detect the reactor antineutrinos with a chlorine-argon detector was made in 1954 by Davis but failed [8], suggesting that neutrinos and antineutrinos behave differently in their interaction with matter.

Reines and Cowan developed a design that they described as a "club sandwich" in order to detect the antineutrinos coming from a nuclear reactor. The targets ("the meat") are tanks filled with a water solution of cadmium chloride. The target cells are clustered between

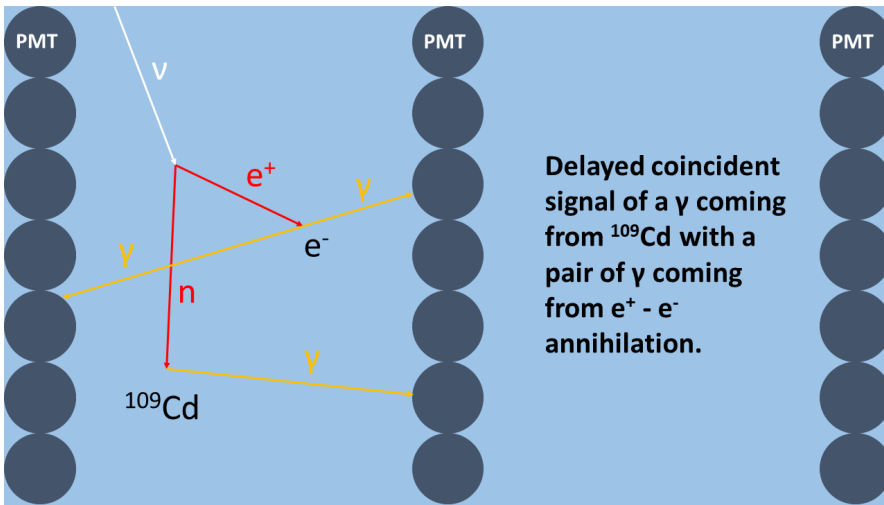


**Figure 1.3.** "Sandwich design" showing the experimental layout as well as a view of the processes taking place following a neutrino interaction in the water volume.

("the bread") liquid scintillators instrumented with photomultipliers. The interaction of an antineutrino with a hydrogen nucleus leads to the following inverse  $\beta$  reaction:



The positron annihilates and two back to back  $\gamma$  are emitted and detected in coincidence by the liquid scintillators. To unambiguously assess the primary neutrino interaction, the cadmium-108 in natural cadmium serves as a target for the produced neutron because of its high neutron absorption cross section. The neutron capture is promptly followed by a characteristic  $\gamma$  emission resulting from the de-excitation of the cadmium-109. A schematic view of the experiment can be seen in Figure 1.3.

In 1956 they ran their famous experiment near a nuclear reactor at the Savannah River nuclear site [9,10]. They observed a reactor-power-dependant signal of roughly 3 counts per hour, which corresponded to the calculated antineutrino flux's interaction frequency. Turning off the reactor did stop the signal accordingly. They ensured that the signal was also proportional to the number of proton targets in the

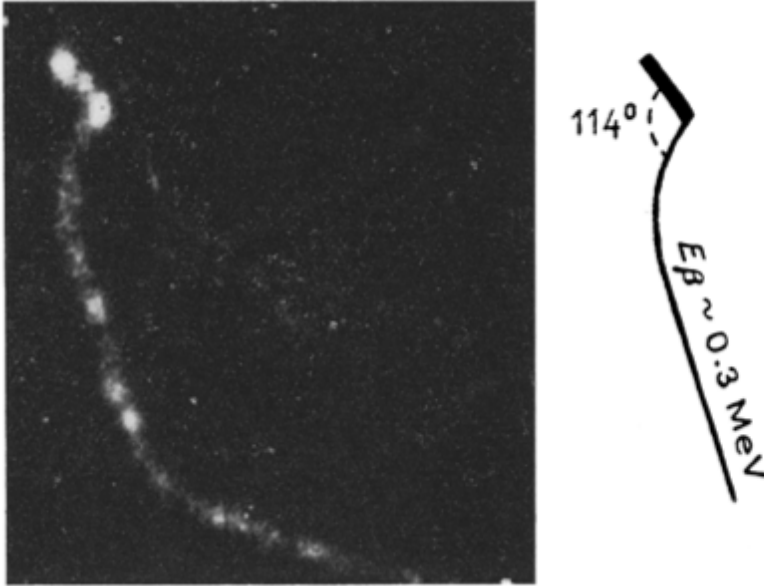


**Figure 1.4.** Cloud chamber photography of a  ${}^6\text{H}$   $\beta$  decay taken from [11]. The bright track corresponds to the recoil of the  ${}^6\text{Li}$  and the long one corresponds to the emitted electron.

detector by diluting the light water with heavy water, which reduced the single proton density by one half. The rate was then divided by two which confirmed that the inverse beta decay was generating the observed signal.

### 1.1.3 Csikai and Szalay experiment

Later in the year 1956, another experiment worth mentioning was successful at "showing" the neutrino. A month after the Soviet Army intervened in Budapest to repress the Hungarian uprising, J. Csikai and A. Szalay took the first photographic evidence of the missing momentum in a  $\beta$  decay by showing the recoil of a  ${}^6\text{Li}$  nucleus and the emitted electron [11]. They used a low pressure hydrogen cloud chamber and published their results in 1957. One of the pictures taken can be seen in Figure 1.4.

### 1.1.4 Discovery of the muon and tau neutrinos

The non-observation of the decay of a muon into an electron and a gamma suggested that the kind of neutrino coupling to the muon was of a different nature than the one coupling to the electron. The discovery of the muon neutrino was made possible by the amount of pions produced by collisions of a beam of accelerated protons in a beryllium target. Its discovery happened in 1962 [12] and it was notably the first neutrino experiment done with accelerators.

It came as a natural conclusion that the discovery of the tau lepton in 1975 was coming with its associated tau neutrino [13, 14]. It oddly came to the surprise of nobody that the DONUT experiment discovered the third neutrino in 2001 at Fermilab [15].

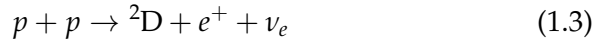
The LEP experiment ALEPH proved unambiguously that only three flavors of neutrinos are sensitive to the weak interaction [16].

## 1.2 Neutrino mixing

### 1.2.1 The solar neutrino problem

The development of solar models based on nuclear reactions led physicists to believe that, if those models fit reality, the Sun would be producing a sizable flux of neutrinos [17]. This potential flux was believed to provide experimentalists with a chance to discover the neutrino. That is what led to the first attempts to measure the solar neutrino flux.

The nuclear reactions occurring in the Sun involve  $\nu_e$  such as in the p-p reaction:



The chlorine-argon detector, which was proven not to be sensitive to antineutrinos coming from reactors, could however detect the neutrinos emitted by the Sun [8]. The models predicted that such a detector would be sensitive mostly to the neutrinos emitted by the  $\beta^+$  decay of  ${}^8\text{B}$  [17, 18]. Despite the very small flux of these neutrinos with respect to the dominant pp neutrinos, their higher average energy makes their cross section significantly larger.

These neutrinos were observed by Ray Davis and his collaborators with this chemical detector buried in the Homestake mine (4200 m of



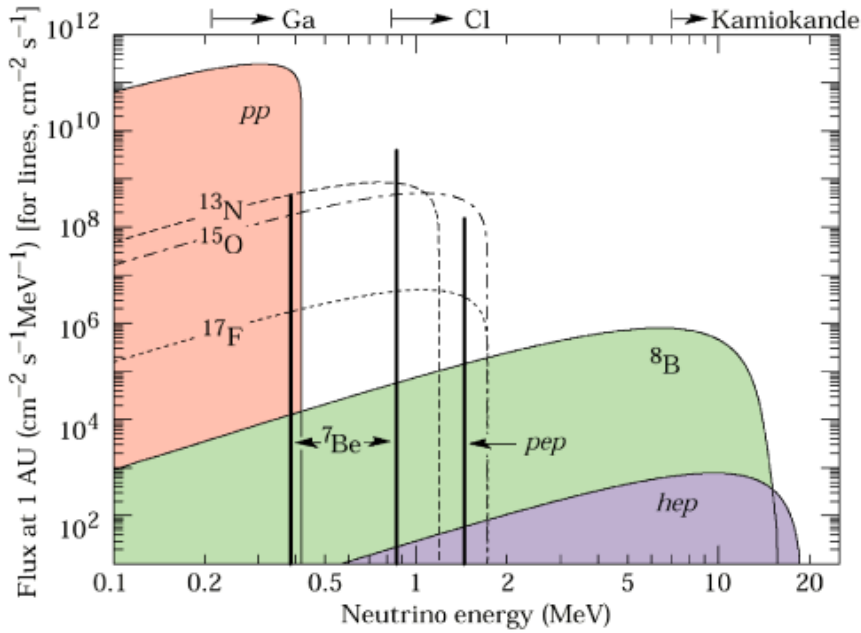


**Figure 1.5.** Predicted energy spectrum of solar neutrinos for the different nuclear reactions yielding neutrinos. The detection thresholds for the gallium-based, chlorine-based and KamiokaNDE experiments are displayed. This figure was taken from [24].

water equivalent) to prevent the background induced by cosmic rays. This famous experiment was not only a confirmation that neutrinos were indeed produced in the core of the Sun by nuclear reactions [19], it also measured a sizable deficit of those neutrinos detected with respect to the theory [20]. This deficit was referred to, in the next decades, as the solar neutrino problem and was confirmed by three other experiments: KamiokaNDE in 1989 [21], a water Cherenkov detector, and two gallium radiochemical experiments, GALLEX in 1992 [22] and SAGE in 1994 [23]. The energy spectrum of the solar neutrino can be seen in Figure 1.5.

The reason for this deficit is that the chemical detector of Davis was only sensitive to the charged currents involving the electron neutrino. As Gribov and Pontecorvo noted in 1969 [25], following earlier work

on the topic [26,27], if the neutrinos were not massless they could oscillate between their different flavors. The missing neutrinos would then have oscillated to muon and tau neutrinos.

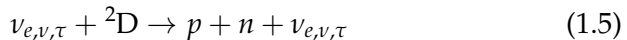
An accurate estimation of the disappearance of  $\nu_e$  in the solar neutrino flux could only be done once the so-called MSW effect was proposed. Lincoln Wolfenstein in 1978 realized that even if neutrinos were massless they could oscillate in matter by coherent forward scattering [28]. Mikheyev and Smirnov suggested in 1985 [29] that the main contribution may not be the oscillation of neutrinos in vacuum between the Sun and the Earth but rather that inside the Sun they cross a region where resonant oscillation happens due to the matter effect described by Wolfenstein. These deep oscillations would then be responsible for the electron neutrino deficit seen by chlorine-argon experiments.

The discovery of oscillation was made thanks to Super-Kamiokande (Super-Kamioka Neutrino Detection Experiment) [30]. The detector was a large water Cherenkov tank. It was sensitive to neutrinos with energies higher than 1 GeV which corresponds to the energy range of the so-called atmospheric neutrinos. They result from the decay of the light mesons and the muons in hadronic showers produced by cosmic rays hitting the atmosphere. Figure 1.6 shows the announcement of the neutrino oscillation discovery in 1998.

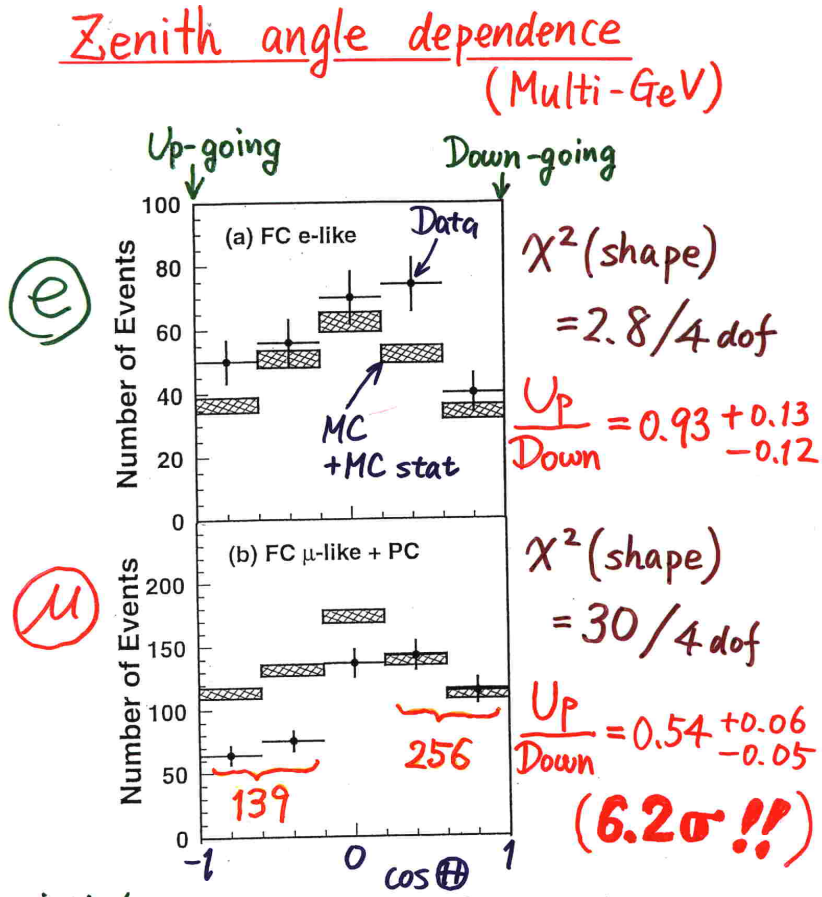
It is only after this discovery that the solar neutrino problem was definitively solved by the SNO experiment (Sudbury Neutrino Observatory). SNO is a detector functioning under the same general principle as Super-Kamiokande with one major difference: most of its detection volume was filled with heavy water. SNO was able to detect two separate reactions. The first one being the charged current interaction:



where the electron is detected by its Cherenkov effect. And the second being the neutral current interaction:



which is detected by the delayed  $\gamma$  emitted by the free neutron being absorbed afterwards (either by another deuterium nucleus, a dissolved



\* Up/Down syst. error for  $\mu$ -like

Prediction ( flux calculation .....  $\lesssim 1\%$   
 1km rock above SK ..... 1.5% ) 1.8%

Data ( Energy calib. for  $\uparrow\downarrow$  ..... 0.7%  
 Non  $\nu$  Background ..... < 2% ) 2.1%

**Figure 1.6.** Slide presented at the conference Neutrino 1998 [31]. It shows the observed numbers of  $\nu_\mu$  and  $\nu_e$  events for various zenith angles and the corresponding expected numbers under the no oscillation hypothesis. The data favored a scenario where up-going  $\nu_\mu$  were oscillating to  $\nu_\tau$ .

dopant or a  $^3\text{He}$  neutron counter). In addition, SNO could also observe neutrino interaction by elastic scattering which could involve all flavours albeit being dominated by electron neutrino.

It is by comparing the rate of these reactions that the first scientific result of the SNO experiment came out in 2001 [32,33]. It concluded that a fraction of the total neutrino flux coming from the  $^8\text{B}$  decay in the core of the Sun indeed changed flavor on its way to Earth. This observation was another proof of neutrino oscillation and finally solved the solar neutrino problem.

### 1.2.2 PMNS matrix

The neutrino oscillations result from the fact that in vacuum the neutrino mass eigenstates do not match the weak gauge eigenstates which correspond to the three flavors (electron, muon and tau). The formalism used to describe the neutrino mixing is then the same as for the quark mixing: a non-diagonal unitary matrix transforming an orthogonal basis into another one. In the case of neutrinos, the two bases are on the one hand the flavour eigenstates, denoted  $\nu_\alpha$  where  $\alpha = e, \mu, \tau$ , and on the other hand the mass eigenstates denoted  $\nu_i$  where  $i = 1, 2, 3$ . The elements of the mixing matrix are labeled  $U_{\alpha i}$  where again  $\alpha = e, \mu, \tau$  and  $i = 1, 2, 3$ . The transformation is written:

$$\begin{bmatrix} \nu_e \\ \nu_\mu \\ \nu_\tau \end{bmatrix} = \begin{pmatrix} U_{e1} & U_{e2} & U_{e3} \\ U_{\mu1} & U_{\mu2} & U_{\mu3} \\ U_{\tau1} & U_{\tau2} & U_{\tau3} \end{pmatrix} \begin{bmatrix} \nu_1 \\ \nu_2 \\ \nu_3 \end{bmatrix} \quad (1.6)$$

The  $3 \times 3$  matrix is the PMNS matrix and is named after the physicists who originally introduced the idea of neutrino mixing: Pontecorvo on one side (1957 for neutrino-antineutrino oscillation [34] and 1968 for flavour oscillation [27]) and Maki, Nakagawa and Sakata on the other side (1962 for flavour mixing [26]).

As a unitary  $3 \times 3$  matrix, the PMNS matrix can be parametrized by 3 mixing angles and 6 phases. However not all of these phases are physical because the lepton fields can be rephased to absorb some of them, it leaves a single real CP-violating phase  $\delta_{CP}$ . Following this and with the notation  $c_{ij} = \cos(\theta_{ij})$  and  $s_{ij} = \sin(\theta_{ij})$ , the PMNS matrix

can be written as follows:

$$\begin{pmatrix} c_{12}c_{13} & s_{12}c_{13} & s_{13}e^{-i\delta_{CP}} \\ -s_{12}c_{23} - c_{12}s_{13}s_{23}e^{i\delta_{CP}} & c_{12}c_{23} - s_{12}s_{13}s_{23}e^{i\delta_{CP}} & c_{13}s_{23} \\ s_{12}s_{23} - c_{12}s_{13}c_{23}e^{i\delta_{CP}} & -c_{12}s_{23} - s_{12}s_{13}c_{23}e^{i\delta_{CP}} & c_{13}c_{23} \end{pmatrix} P \quad (1.7)$$

where  $\theta_{ij}$  are the Euler mixing angles. It can also be rewritten in a way to highlight it as a product of three rotations:

$$\begin{pmatrix} 1 & 0 & 0 \\ 0 & c_{23} & s_{23} \\ 0 & -s_{23} & c_{23} \end{pmatrix} \begin{pmatrix} c_{13} & 0 & s_{13}e^{-i\delta_{CP}} \\ 0 & 1 & 0 \\ -s_{13}e^{i\delta_{CP}} & 0 & c_{13} \end{pmatrix} \begin{pmatrix} c_{12} & s_{12} & 0 \\ -s_{12} & c_{12} & 0 \\ 0 & 0 & 1 \end{pmatrix} P \quad (1.8)$$

The P matrix would be the identity matrix if neutrinos were Dirac particles or a diagonal matrix introducing two additional phases if neutrinos were Majorana particles.

The probability for a neutrino in a beam to oscillate from a flavour  $\alpha$  to a flavour  $\beta$  is:

$$\begin{aligned} P(\nu_\alpha \rightarrow \nu_\beta) = & \delta_{\alpha\beta} - 4 \sum_{i<j} \text{Re} \left[ U_{\alpha i} U_{\beta i}^* U_{\alpha j}^* U_{\beta j} \right] \sin^2 \left( \frac{\Delta m_{ij}^2 L}{4E} \right) \\ & + 2 \sum_{i<j} \text{Im} \left[ U_{\alpha i} U_{\beta i}^* U_{\alpha j}^* U_{\beta j} \right] \sin \left( \frac{\Delta m_{ij}^2 L}{2E} \right) \end{aligned} \quad (1.9)$$

where the parameters of the neutrino beam are E and L, the energy and the length traveled by the neutrinos respectively. The oscillations are governed by the mixing angles as well as the squared-mass differences  $\Delta m_{ij}^2 = m_i^2 - m_j^2$ .

In many experiments it turns out that the oscillation can be approximated to a two flavours mixing (particularly for the solar and atmospheric neutrinos experiments). Which makes it easier to identify the mixing angles of each sector separately. Typically the solar neutrinos probe the value of  $\theta_{12}$  and  $\Delta m_{21}^2$  while the atmospheric neutrinos probe  $\theta_{23}$  and  $|\Delta m_{32}^2| \simeq |\Delta m_{31}^2|$ . The remaining angle  $\theta_{13}$  was probed by nuclear reactor experiments at medium range (Daya Bay, Double Chooz, Reno).

The remaining parameters to determine are the mass hierarchy (Figure 1.7) and the phase describing the CP-violation. A summary compiling the data from all the experiments probing the different sector is provided by the global fit analysis [35]. The summary can be found in Table 1.1.

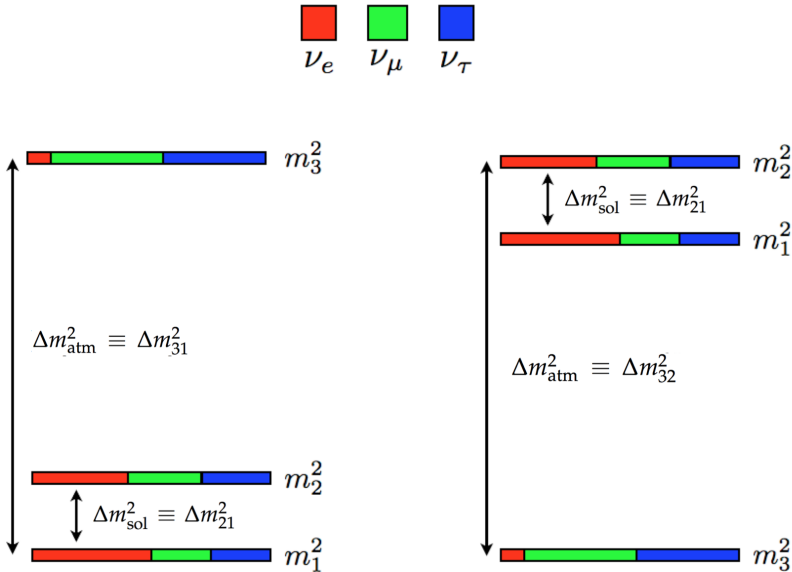


**Figure 1.7.** The two possible mass state orderings. The squared masses are separated by the known solar and atmospheric mass splitting. The colors represent the projection of each mass state  $\nu_{i=1,2,3}$  on the basis of the flavor states  $\nu_{\alpha=e,\mu,\tau}$ . This figure is extracted from [36]

It is to be noted that from oscillation experiments data alone, the global fit tends to favor a normal ordering at  $2\sigma$ .

### 1.3 Neutrino mass

The oscillation experiments can measure the gaps among the three neutrino masses which proves that at least two of them are not massless. But the absolute scale of the neutrino mass still eludes physicists since the oscillations are insensitive to it. In 1933 Francis Perrin, suggested that it was very likely for the neutrino to have a negligible mass with respect that of the electron given the energy distribution of the electron emitted in  $\beta$  decay [37].

Since then, there have been numerous attempts to measure the neutrino mass using different paths. The first one consists of exploiting

| parameter                                      | best fit $\pm 1\sigma$  |
|--|-------------------------|
| $\Delta m_{21}^2 [10^{-5} \text{eV}^2]$        | $7.50^{+0.22}_{-0.20}$  |
| $ \Delta m_{31}^2  [10^{-3} \text{eV}^2]$ (NO) | $2.55^{+0.02}_{-0.03}$  |
| $ \Delta m_{31}^2  [10^{-3} \text{eV}^2]$ (IO) | $2.45^{+0.02}_{-0.03}$  |
| $\theta_{12} [^\circ]$                         | $34.3 \pm 1.0$          |
| $\theta_{23} [^\circ]$ (NO)                    | $49.26 \pm 0.79$        |
| $\theta_{23} [^\circ]$ (IO)                    | $49.46^{+0.60}_{-0.97}$ |
| $\theta_{13} [^\circ]$ (NO)                    | $8.53^{+0.13}_{-0.12}$  |
| $\theta_{13} [^\circ]$ (IO)                    | $8.58^{+0.12}_{-0.14}$  |
| $\delta_{CP} [^\circ]$ (NO)                    | $194^{+24}_{-22}$       |
| $\delta_{CP} [^\circ]$ (IO)                    | $284^{+26}_{-28}$       |

**Table 1.1.** Neutrino oscillation parameters summary determined from the global analysis [35]. The ranges for inverted ordering refer to the local minimum for this neutrino mass ordering.

the kinematics of a  $\beta$  decay to measure the effective mass of the electron antineutrino:

$$m_{\nu_e}^2 = \sum_{i=1}^3 |U_{ei}|^2 m_i^2 \quad (1.10)$$

To pursue such experiment, tritium decay is the best candidate [38]. It has a short enough half life (12.32 years) that it provides good statistics as well as a very low energy endpoint (18.6 keV). This maximizes the effect of the neutrino mass on the shape of the tail of the energy spectrum of the emitted electron. The first experiments were conducted in 1947 and could set a limit of 10 keV [39, 40]. Many refinements done since then have brought this limit much lower [41–44]. As of today the best upper limit is set by the KATRIN experiment at 0.8 eV [45]. KATRIN is expected to achieve a sensitivity to a mass of 0.2 eV within a few years from now.

Similarly, experiments have been probing the effective mass of muon and tau neutrinos but the limits are obviously much higher and

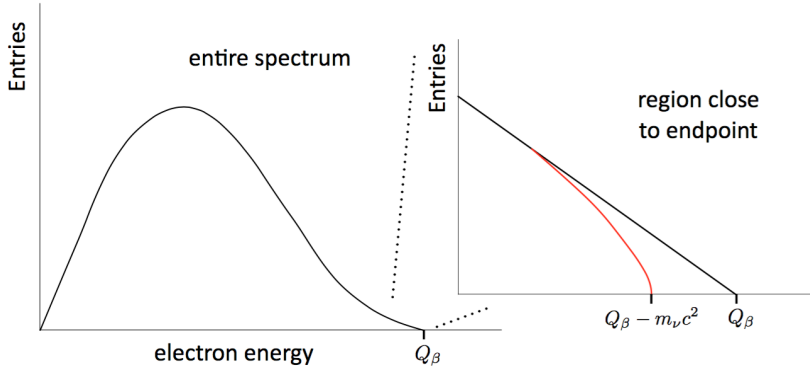


**Figure 1.8.** Energy spectrum of a  $\beta$  decay showing the endpoint region. The black line corresponds to zero neutrino mass and the red line to finite neutrino mass. Figure taken from [46].

less significant, 0.17 MeV [47] and 18 MeV [48] respectively.

Another way to measure the neutrino mass is to measure the arrival time difference of neutrinos emitted by a supernova. The analysis done with the data from SN 1987A gave limits in the range of 16 eV [49] or 5.7 eV [50] depending on the analysis performed.

By using cosmological observations an additional constraint could be put on the sum of the neutrino masses. The most recent observations using Planck data set this limit at 0.15 eV [51].

## 1.4 Majorana or Dirac

The existence of neutrino oscillations proves that neutrinos are not massless fermions. Therefore the Standard Model needs to be extended to somehow give mass to neutrinos. Additionally the current limit on the neutrino absolute mass scale raises another fundamental problem regarding the massive disparity between the neutrino masses and the other particles who get their mass from their interaction with the Higgs field.



### 1.4.1 The origin of neutrino mass

In the following paragraph negative (positive) chirality will be synonym of left-handed (right-handed) which is referred to with the subscript  $L$  ( $R$ ) in mathematical expressions.

In the Standard Model the mass of the fermions is introduced by the Dirac mass term. The Dirac mass term emerges from the Yukawa couplings to the Higgs doublet and thus couples the two chiralities of a fermion field. The contribution of the neutrino field to the Lagrangian would be written:

$$- \mathcal{L}_D = m_D (\bar{\nu}_L \nu_R + \bar{\nu}_R \nu_L) \quad (1.11)$$

Therefore, a massive neutrino would imply the existence of a right-handed neutrino field that would be *sterile*. This mechanism results in the neutrino and the antineutrino being two different particles. It has the disadvantage of not explaining why neutrinos are orders of magnitude lighter than their charged lepton counterparts.

Ettore Majorana has seen, in 1937 [52], that there is a way to generate a neutrino mass term using only the left-handed component of the neutrino field, effectively removing two degrees of freedom of a massive Dirac spinor. This is done by applying the Majorana condition, which can be formulated as identifying the right-handed component of the field with the charge conjugate of the left-handed component:

$$\nu_R = \nu_L^c \quad (1.12)$$

In this case the charge conjugate of the Majorana fermion field is itself, which means that a Majorana particle is its own antiparticle. The only particle that can possibly be a Majorana particle is the neutrino, being the only neutral fermion.

A mass term can be built for the left-handed component of the neutrino field in a similar fashion as that shown in Equation 1.11:

$$- \mathcal{L}_L = \frac{1}{2} m_L (\bar{\nu}_L \nu_L^c + \bar{\nu}_L^c \nu_L) \quad (1.13)$$

Likewise, a mass term for the right-handed neutrino can be written:

$$- \mathcal{L}_R = \frac{1}{2} M_R (\bar{\nu}_R \nu_R^c + \bar{\nu}_R^c \nu_R) \quad (1.14)$$

These Majorana mass terms are coupling particle to their own antiparticle, which allows lepton number violating (LNV) processes.

### 1.4.2 See-saw mechanism

There are a few ways to generate the Majorana mass term for the left-handed neutrino described above and explain the smallness of the neutrino masses, notably the see-saw mechanism.

The basic input is to add to the theory the right-handed neutrino field:  $N_R$  which is assumed to have a Majorana mass term,  $M_R$ , in the form of the Lagrangian  $\mathcal{L}_R$  given in Equation 1.14 as well as a Yukawa type coupling to the Standard Model lepton doublet  $L_L$ . The Lagrangian of the Standard Model can then be written with the additional term  $\delta\mathcal{L}$ :

$$-\delta\mathcal{L} = \overline{L}_L \lambda_\nu \tilde{\Phi} N_R + \frac{1}{2} N_R^T M_R N_R + h.c. \quad (1.15)$$

Upon symmetry breaking a Dirac mass term emerges, the Lagrangian can be written in the following way,:

$$-\delta\mathcal{L} = \frac{1}{2} \mathcal{N}^T \mathcal{M} \mathcal{N} \quad (1.16)$$

where  $\mathcal{M} = \begin{pmatrix} 0 & m_D \\ m_D & M_R \end{pmatrix}$  and  $\mathcal{N} = \begin{pmatrix} \nu_L \\ N_R \end{pmatrix}$  with  $m_D = \lambda v$ ,  $v = 174$  GeV being the vacuum expectation value of the Higgs doublet.

To get well defined mass states, the matrix  $\mathcal{M}$  must be diagonalized, which can be done at the perturbative level. Assuming that  $m_D \ll M_R$ , the diagonal matrix of the mass states is written:

$$\mathcal{U}^T \mathcal{M} \mathcal{U} = \begin{pmatrix} \frac{\lambda_\nu^2 v^2}{M_R} & 0 \\ 0 & M_R \end{pmatrix}, \quad \mathcal{U} = \begin{pmatrix} 1 & \frac{\lambda_\nu v}{M_R} \\ -\frac{\lambda_\nu v}{M_R} & 1 \end{pmatrix} \quad (1.17)$$

This gives two mass states:  $m_1 \simeq \frac{\lambda_\nu^2 v^2}{M_R}$  and  $m_2 \simeq M_R$ . Thus, if the right-handed component has a very large mass, a bit short of the scale of the GUT scale ( $10^{15}$  GeV), and the Yukawa coupling has a strength of the order of those already observed, the mass state  $m_1$  becomes extremely tiny and corresponds to that of a known light neutrino. A way to look at it from an experimental point of view is that the smallness of the neutrino mass scale is a hint of the aforementioned see-saw mechanism and its implications, which fits a satisfying pattern known in particle physics. Establishing the Majorana nature of the neutrino

would then give a very convenient way to explain the neutrino mass scale.

The mechanism predicting a heavy right-handed neutrino can also have a strong implication regarding leptogenesis scenarios. The heavy neutrinos can decay through the two following modes:

$$N_k \rightarrow l^- + H \quad (1.18)$$

$$N_k \rightarrow l^+ + H \quad (1.19)$$

Because the Yukawa coupling does not a priori conserve CP, it is possible for these two reactions to have different rates. In the early universe, once the temperature goes below that of the lightest heavy neutrino, the remaining decays would therefore induce a matter-antimatter asymmetry. These lepton asymmetries can turn into a baryon asymmetry through a sphaleron process [53].

## 1.5 Summary

The neutrino is a particle that has been in the spotlight since the early days of subatomic physics. Its spectacular prediction in 1930 and not less spectacular direct discovery in 1956 were, however, followed by decades of no major groundbreaking results. The solar neutrino problem has been for all this time foreshadowing the central place neutrino physics currently holds in particle physics.

The discovery of neutrino oscillations, despite confirming the solar models and allowing for a wide range of cleverly designed experiments to study this phenomenon, proved that the neutrinos are not massless particles. This consequently strengthens the motivation to measure the scale of their mass. But most notably opens the fundamental question of how they should be implemented in the theory: as Dirac or Majorana particles.

This question regarding the nature of neutrinos is, as of now, the main entry towards the new physics so called beyond the Standard Model. The neutrino being Majorana would make it possible to explain why the universe is as we see it, dominated by matter. In this case lepton number violating processes would be allowed, most notably the neutrinoless double beta decay, giving physicists a lever to probe the very nature of that elusive particle.



# Neutrinoless Double Beta Decay



Most of the phenomena associated with a Majorana neutrino are extremely subtle and very suppressed or would happen at energies that are not accessible to physicists. The double beta decay is the only process that has the potential to unveil the possible Majorana nature of the neutrino. As its name suggests, it consists of the simultaneous conversion of two neutrons into two protons associated with the emission of two electrons and two antineutrinos. But if neutrinos are Majorana particles, a lepton number violating mode of this decay is then allowed where the antineutrinos annihilate one another, leaving only two electrons emitted back to back. This specific decay is called the neutrinoless double beta decay ( $0\nu\beta\beta$  decay).

## 2.1 Decay modes

### 2.1.1 Two-neutrino mode

It has long been noted that some groups of isobar nuclei show a special feature in which some nuclei that are not at the global minimum of atomic mass are, however, at a local minimum. This means that they appear to be stable when it comes to  $\beta$  emission, because such decay would increase their atomic mass which is kinematically forbidden. But because they are not at the global minimum and are only two atomic numbers away from a more stable nucleus it is possible to imagine that by simultaneously undergoing two  $\beta$  emission it could bypass the forbidden  $\beta$  emission. This is summarized in Figure 2.1.

In 1935 Maria Goappert-Mayer [54], by using the Fermi theory of weak interaction, calculated the probability of the following process

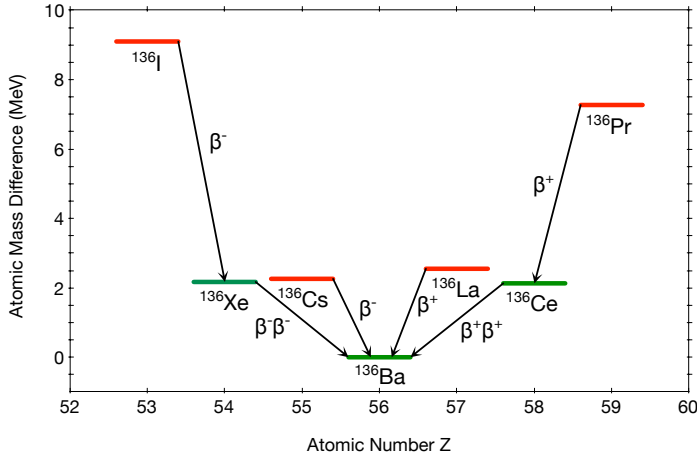


**Figure 2.1.** Diagram showing the mass differences between the isobars that have 136 nucleons with the red ones being odd-odd nuclides and the green ones being even-even nuclides. They are sorted by their atomic number  $Z$ . A kinematically allowed  $\beta$  transition can only go downward.

for a given nucleus of atomic number  $Z$  and atomic weight  $A$ :

$$(Z, A) \rightarrow (Z + 2, A) + 2e^- + 2\bar{\nu}_e + Q_{\beta\beta} \quad (2.1)$$

where  $Q_{\beta\beta}$  is the energy released. This decay is called the (two-neutrino) double beta decay and often noted  $2\nu\beta\beta$ . It is a second order weak interaction so it is extremely weak compared to the traditional  $\beta$  decay. Its Feynman diagram is shown in Figure 2.2. The double beta decay is obviously available to any  $\beta$  emitter whose daughter nucleus is also a  $\beta$  emitter. But due to the difference between the two decays half lives it is practically impossible to observe unambiguously a double beta decay for this type of nuclei.

Experimentally the only double beta emitters are those for which the single beta decay is forbidden or extremely suppressed, and that leaves 35 nuclei. These were long thought to be stable and only specific experiments could finally prove that this decay exists and measure its half life. The first evidence for various nuclei was gathered by radiochemical experiments from 1950 with a first estimation for  $^{130}\text{Te}$  [55]. After which the first direct observation of a double beta decay

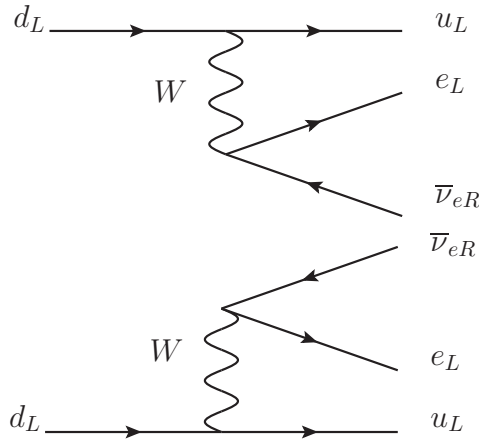


**Figure 2.2.** Feynman diagram of a  $2\nu\beta\beta$  decay.

| Isotope           | $T_{1/2}^{2\nu}$ ( $\times 10^{21}$ y) |
|-------------------|--|
| $^{48}\text{Ca}$  | $0.064^{+0.019}_{-0.015}$              |
| $^{76}\text{Ge}$  | $1.926 \pm 0.094$                      |
| $^{82}\text{Se}$  | $0.96 \pm 0.013$                       |
| $^{96}\text{Zr}$  | $0.0235 \pm 0.0030$                    |
| $^{100}\text{Mo}$ | $1.926 \pm 0.00004$                    |
| $^{116}\text{Cd}$ | $0.028 \pm 0.004$                      |
| $^{130}\text{Te}$ | $0.82 \pm 0.08$                        |
| $^{136}\text{Xe}$ | $2.165 \pm 0.045$                      |
| $^{150}\text{Nd}$ | $0.00911^{+0.00088}_{-0.00085}$        |
| $^{238}\text{U}$  | $2.0 \pm 0.6$                          |

**Table 2.1.** Measurements of the half-life of the  $2\nu\beta\beta$  decay as listed in page 768 of the reference [57] and respectively in [58] and [59] for the half lives of calcium-48 and tellurium-130.

occurred in 1987 for  $^{82}\text{Se}$ . The source was deposited in a thin Mylar foil embedded in a Time Projection Chamber [56]. Since then the  $2\nu\beta\beta$  has been directly confirmed and its lifetime measured for a grand total of nine nuclei, ten if we count uranium-238 (from a radiochemical measurement). They are listed in Table 2.1.

### 2.1.2 Zero-neutrino mode

In 1939, W. Furry noted that a Majorana neutrino would lead the double beta decay to have a mode in which no neutrino would be emitted [60]. The  $0\nu\beta\beta$  decay is written as:

$$(Z, A) \rightarrow (Z + 2, A) + 2e^- + Q_{\beta\beta} \quad (2.2)$$

Because in a  $0\nu\beta\beta$  decay the lepton number is not conserved by two units it is a transition forbidden by the Standard Model. Thus making it an unambiguous smoking gun for new physics, if ever seen.

The  $0\nu\beta\beta$  decay is very similar to the  $2\nu\beta\beta$  decay. In both modes the initial and final nuclei are in a  $0^+$  ground state but in some cases the final nucleus is allowed to end up in an excited  $0^+$  or  $2^+$  state, although these are suppressed by the smaller phase space available. Another important shared trait is that the recoil of the nucleus in the decay is negligible so the entirety of the energy is carried by the leptons emitted. The main outcome of this is the expected shape of the energy spectrum of the two electrons is continuous in the  $2\nu$  mode and monochromatic in the  $0\nu$  mode. In the latter case all the available energy,  $Q_{\beta\beta}$ , is carried by the two electrons emitted.

To this day the  $0\nu\beta\beta$  decay remains unobserved. Across the years multiple experiments have been able to set upper limits on the  $0\nu\beta\beta$  half-lives of the order of  $10^{25}$ - $10^{26}$  years for a wide set of isotopes that are listed in Table 2.3.

### 2.1.3 Other decays

There are three other nuclear decays that would exist in a  $0\nu$  mode if neutrinos were Majorana particles: the double positron emission, the positron emission with electron capture and the double electron capture respectively:

$$(Z, A) \rightarrow (Z - 2, A) + 2e^+ (+2\nu_e) \quad (2.3)$$

$$(Z, A) + e^- \rightarrow (Z - 2, A) + e^+ (+2\nu_e) \quad (2.4)$$

$$(Z, A) + 2e^- \rightarrow (Z - 2, A) + 2e^+ (+2\nu_e) \quad (2.5)$$

From an experimental point of view these processes are less accessible than a  $0\nu\beta\beta$  decay because their available phase space is smaller. It



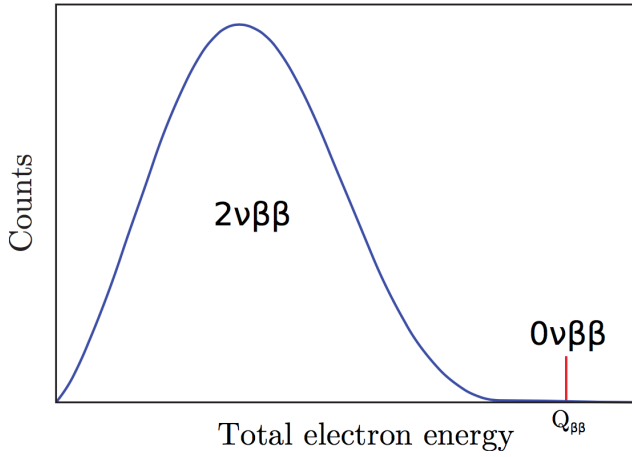


**Figure 2.3.** Illustration of the energy spectra of the  $2\nu$  mode (blue) and of the  $0\nu$  mode (red) of the double beta decay. The energy corresponds to the sum of the kinetic energy of the two emitted electrons. The relative amplitudes are arbitrary.

must be noted however that double electron capture has been seen in its  $2\nu$  mode only for three isotopes:  $^{78}\text{Kr}$ ,  $^{130}\text{Ba}$  and very recently in  $^{124}\text{Xe}$  [61].

#### 2.1.4 *Quadruple neutrinoless beta decay*

Another theoretical decay, similar to the  $0\nu\beta\beta$ , is the  $0\nu4\beta$  decay which would change the atomic number of a nucleus by four units:

$$(Z, A) \rightarrow (Z + 4, A) + 4e^- + Q_{4\beta} \quad (2.6)$$

But unlike the  $0\nu\beta\beta$  it does not require violation of conservation of the lepton number by two units so for a  $0\nu4\beta$  decay to happen neutrinos do not have to be a Majorana particle [62]. In fact it can be argued that a null  $0\nu\beta\beta$  accompanied by a  $0\nu4\beta$  detection would prove that at least one neutrino is a Dirac particle [63]. Only three nuclei have been identified as potential  $0\nu4\beta$  emitters: zirconium-96, xenon-136 and neodymium-150. This decay is not directly related to answering the Majorana neutrino question but it can be relevant for

experiments studying the aforementioned isotopes. A first limit has been set on  $^{150}\text{Nd}$  by the NEMO-3 Collaboration [64].

## 2.2 Inner mechanisms

### 2.2.1 The black box theorem

It has been said that should neutrinos be Majorana, the  $0\nu\beta\beta$  decay would be allowed. It is however tempting, to imagine a model that would not require a massive Majorana neutrino to give rise to the  $0\nu\beta\beta$  decay.

This possibility has been ruled out by J. Schechter and J. W. F. Valle [65, 66]. They showed that, a  $0\nu\beta\beta$  decay induces a transition of the type  $\nu_e \rightleftharpoons \bar{\nu}_e$ , which is described by a Majorana mass term irrespective of the underlying process. This is shown by calculating the non vanishing amplitude of the  $0\nu\beta\beta$  equivalent diagram shown in Figure 2.4 where the inner process is hidden in the "black box". This diagram gives rise to a nonzero Majorana mass term for the electron neutrino.

But it has also been noted that this mass term, generated at a four-loop level, is too small to account for the two mass splittings measured by oscillation experiments. As such a hypothetical observed rate of the decay may also be the result of other lepton number violating processes beyond the Standard Model. Therefore, while a positive signal may still prove that neutrinos have a non vanishing Majorana contribution, such signal could not necessarily be translated into information on the neutrino mass scale due to other processes governing it.

The next sections will discuss partially some mechanisms that are candidates to fit inside the black box.

### 2.2.2 The standard mechanism: light neutrino exchange

The simplest, most straightforward, and most studied mechanism for  $0\nu\beta\beta$  decay consists of the exchange of a light Majorana neutrino between two point-like Fermi vertices to produce the two electrons. In a nutshell at one vertex the electron is produced alongside an antineutrino which is mostly of positive helicity, only its negative helicity component, of the order of  $m_\nu/E$ , is absorbed on the other vertex to

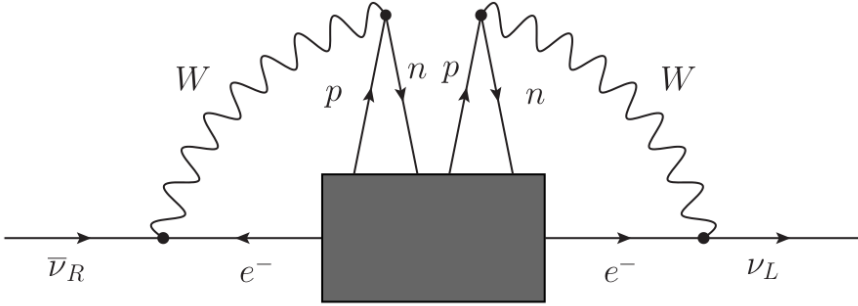


**Figure 2.4.** Diagram of a neutrinoless double beta decay where the underlying mechanism is hidden in a black box. The diagram shows that a transition from  $\bar{\nu}$  to  $\nu$  happens no matter the content of the black box, which translate to a Majorana mass term. This diagram was drawn originally in [65].

generate the other electron. The Feynman diagram of this mechanism is shown in Figure 2.5.

The amplitude of this process is a summation over the contribution of the three light neutrino mass states  $\nu_i$  and is proportional to  $U_{ei}^2$ , so the modulus of this amplitude must be proportional to the effective neutrino Majorana mass:

$$m_{\beta\beta} = \left| \sum_{i=1}^3 U_{ei}^2 m_i^2 \right| \quad (2.7)$$

If the case where the light neutrino exchange is the dominant process governing the  $0\nu\beta\beta$  decay, the inverse of the half-life of the decay can be written [67]:

$$(T_{1/2}^{0\nu})^{-1} = G^{0\nu} |M^{0\nu}|^2 \left( \frac{m_{\beta\beta}}{m_e} \right)^2 \quad (2.8)$$

where  $G^{0\nu}$  is a phase-space factor that depends on the Q-value of the decay as well as the atomic number  $Z$ , and  $M^{0\nu}$  is the nuclear matrix element (NME). The phase-space factor can be computed analytically very precisely (with an error estimate of about 1/1000) [68,69]. There are various nuclear models that can be used to evaluate the NME, and

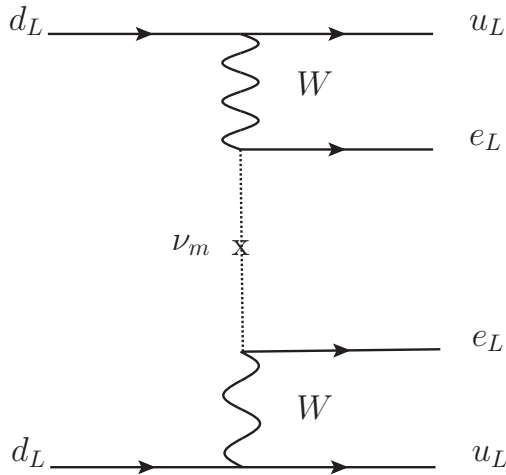


**Figure 2.5.** Feynman diagram of a  $0\nu\beta\beta$  decay with a light neutrino exchange.

the precision reached by these computations is pretty loose but has been improved in recent years. We can mention the Interacting Shell Model (ISM) [70], the Quasiparticle Random Phase Approximation (QRPA) [71, 72], the Interacting Boson Model (IBM-2) [73] and the Energy Density Functional Method (EDF) [74, 75]. Figure 2.7 shows the NME for various isotopes and different models.

But all in all we can see that, despite the uncertainty lying in nuclear physics calculations, and assuming a light neutrino exchange process for the  $0\nu\beta\beta$  decay, one can infer the effective neutrino Majorana mass  $m_{\beta\beta}$  from a nonzero  $0\nu\beta\beta$  decay rate. This also implies that a null signal for a given experiment can be interpreted as an upper limit set on  $m_{\beta\beta}$ .

As mentioned in Section 2.2.1, if the light neutrino exchange is the dominating process governing the  $0\nu\beta\beta$  decay, then the observable quantity  $m_{\beta\beta}$  is tied to the results of oscillation experiments as well as the absolute mass scale of the neutrino. Given the relation between  $m_{\beta\beta}$  and the three neutrino masses  $m_i$ , the former is affected by a number of things:

- the uncertainties in the matrix elements  $U_{ei}$  measured by oscilla-

tion experiments

- the mass ordering (whether  $m_1$  or  $m_3$  is the smallest mass)
- the unknown phases in the PMNS matrix (both Dirac and Majorana phases)

There is a panel that is very often displayed to show the link between  $m_{\beta\beta}$  and the lightest neutrino mass state,  $m_{min}$ , that can be seen in Figure 2.6. The two bands correspond to the two possible mass orderings, their widths are due to the unknown phases in the mixing matrix as well as the uncertainties on the measured value of the PMNS-matrix elements and the computed NME. Figure 2.6 also shows the upper limit on  $m_{\beta\beta}$  given by the cutting edge  $0\nu\beta\beta$  decay experiments while the upper limit on  $m_{min}$  comes from the cosmological constraints mentioned in Section 1.3.

On the other hand a discovery on the front of the  $\beta$  decay experiments described in Section 1.3 can lead to a better understanding of neutrino properties with respect to  $0\nu\beta\beta$  search as it would first and foremost set a constraint on  $m_{light}$ . As such a null  $0\nu\beta\beta$  signal over the possible  $m_{\beta\beta}$  values could imply that the neutrino is a Dirac particle. But in the case of a positive  $0\nu\beta\beta$  signal matching the constraint, it would then be possible to evaluate the Majorana phases  $\alpha_i$  in the neutrino mixing matrix. At last if the measured  $m_{\beta\beta}$  would appear to be significantly mismatching the value expected by the constraint set on  $m_{light}$  it could mean that other lepton number violating processes are at play in the  $0\nu\beta\beta$  decay.

### 2.2.3 Other processes

Other contributions can be added to expression 2.8 to account for other lepton number violating processes [76, 77]. These mechanisms can differ from the standard process described earlier in one or several aspects. One is the handedness of the current (involving right-handed or left-handed W bosons), the mass scale of the virtual particle exchanged like for example a heavy right-handed neutrino, and finally the number of particles in the final states. The latter could involve the emission of a majoron alongside the electrons, that is a light or massless particle that can couple to the neutrino. The presence of a

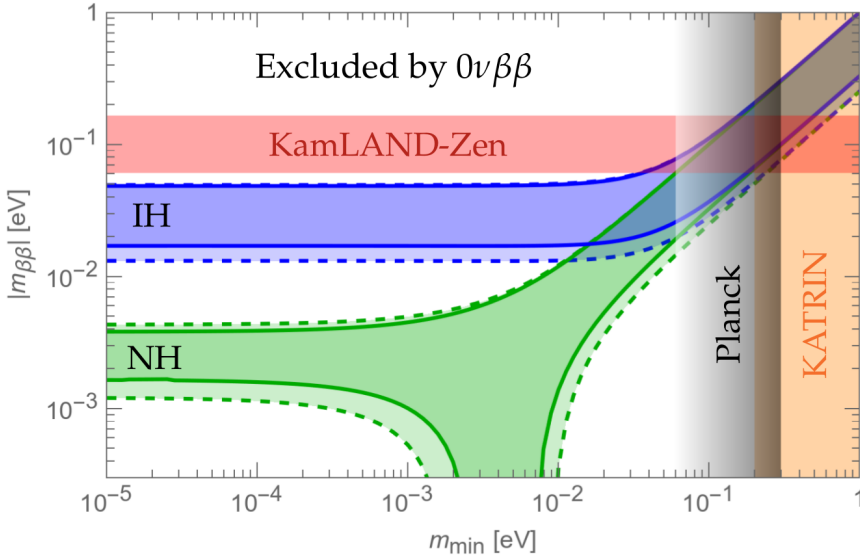


**Figure 2.6.** Allowed values for the effective Majorana mass,  $m_{\beta\beta}$  as a function of the lightest neutrino mass state,  $m_{min}$  for the two possible mass hierarchies. Is also shown in Figure the current best limit set on  $m_{\beta\beta}$  by the KamLAND-Zen experiment and the limits on  $m_{min}$  set directly by the KATRIN experiment or by the cosmological Planck data.

majoron in the final state would show as a continuous  $0\nu\beta\beta$  spectrum albeit distinguishable from the spectrum of the  $2\nu$  mode given a strong enough majoron-neutrino coupling.

Interference between all these mechanisms can also in principle contribute to the total rate of the decay, even though they are often ignored in the analysis if one mechanism is dominant.

### 2.3 General considerations for neutrinoless double beta decay experiments

It has been established that  $0\nu\beta\beta$  decay is a phenomenon whose observation would be a major milestone for particle physics and for our understanding of the Universe. But from an experimental point of view it turns out that building a detector capable of unambiguously

recognizing such an evanescent signal is a major feat. To begin with, the decay, if it exists, has a half-life that is many orders of magnitude longer than the age of the Universe. As an example an effective Majorana neutrino mass of 50 meV corresponds to half-lives in the range of  $10^{26}$  to  $10^{27}$  years. This implies that in order to achieve a possible detection in a reasonable time on a human scale, a large amount of  $\beta\beta$  emitter nuclei are required, enough to reach one event per year. The more the  $\beta\beta$  emitter mass the larger is the upper bound of half-lives that can be probed. But this would already raise the concern of isotopic purification of the large amount of the considered isotope and the funding required to achieve it.

To identify the fundamental figures of merit that one should have in mind when overviewing the different experiments, let us first take a look at the radioactive law. When the observation time  $t$  is much smaller than the half-life,  $T_{1/2}^{0\nu}$ , the number of detected decays expected to happen within  $t$ ,  $N_{0\nu\beta\beta}$ , can be approximated by:

$$N_{0\nu\beta\beta} = \log(2)\epsilon N_{\beta\beta} \frac{t}{T_{1/2}^{0\nu}} \quad (2.9)$$

where  $\epsilon$  is the detection efficiency and  $N_{\beta\beta}$  is the number of  $\beta\beta$  emitter nuclei. Assuming a perfect detection efficiency as well as a background free experiment, for an effective Majorana mass of 50 meV one would need a target mass of about 100 kg of  $\beta\beta$  emitter to see one decay per year.

By combining Equation 2.8 and Equation 2.9 one can link the effective Majorana neutrino mass  $m_{\beta\beta}$  to the exposure time and that can define the sensitivity reached by a specific  $0\nu\beta\beta$  decay experiment [78]:

$$m_{\beta\beta} = K_1 \sqrt{\frac{1}{\epsilon M_{\beta\beta} t}} \quad (2.10)$$

where  $M_{\beta\beta}$  is the target mass of the  $\beta\beta$  emitter and  $K_1$  is a constant that is specific to the isotope considered.

The case described above corresponds to a background-free experiment and it is a valid approximation as long as the background index is low enough. This quasi-background-free regime is what the cutting edge experiments are aiming for. But once the background becomes

noticeable, Equation 2.10 becomes:

$$m_{\beta\beta} = K_2 \sqrt{\frac{b^{1/2}}{\epsilon M_{\beta\beta} t}} \quad (2.11)$$

where  $K_2$  also depends of the isotope considered. If the background  $b$  is proportional to the exposure  $M_{\beta\beta} t$  and the width of the energy region of interest  $\Delta E$  then  $b$  becomes:

$$b = c M_{\beta\beta} t \Delta E \quad (2.12)$$

with  $c$  expressed in counts/(keV kg years). With this change, 2.11 becomes:

$$m_{\beta\beta} = K_2 \sqrt{1/\epsilon} \left( \frac{c \Delta E}{M_{\beta\beta} t} \right)^{1/4} \quad (2.13)$$

Equation 2.13 shows all the parameters that are affected by the design of a given experiment [79]. Control over these parameters is required when deciding the isotope and the technology an experiment will be using. Ultimately the goal is to minimize the  $m_{\beta\beta}$  value for a given running time.

### 2.3.1 Target mass and isotope choice

The choice of the isotope is the first and most crucial design choice. From a purely physical point of view the first difference between all the possible nuclei available is the  $Q_{\beta\beta}$  of the associated double beta decay. Since the phase-space factor Equation 2.8 goes in a power 5 of  $Q_{\beta\beta}$  [68], it follows that the highest  $Q_{\beta\beta}$ -values are favored. To improve the precision of the sensitivity an effort should be put in computing with higher accuracy the NME as it was mentioned in Section 2.2.2. The panel shown in Figure 2.7 shows the NME for a set of  $\beta\beta$  emitters. It displays the discrepancy between the different methods of computation.

Also from an experimental perspective a high  $Q_{\beta\beta}$ -value is preferred: it is associated with less background coming from ambient radioactivity. The chemical properties of the material can be either a hindrance or an opportunity for clever ideas design-wise. Lastly the natural purity and physical properties of the  $\beta\beta$  emitters defines if



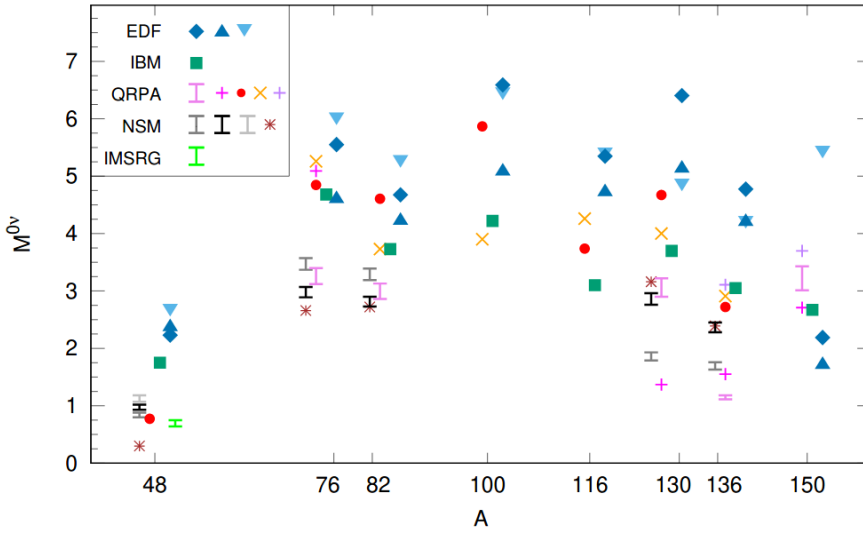


**Figure 2.7.** Nuclear matrix elements ( $M^{0\nu}$ ) for  $0\nu\beta\beta$  decay candidates given by their of mass number  $A$ . Taken from [80].

| Isotope           | Natural abundance (%) | $Q_{\beta\beta}$ (MeV) |
|-------------------|-----------------------|------------------------|
| $^{48}\text{Ca}$  | 0.187                 | 4.263                  |
| $^{76}\text{Ge}$  | 7.8                   | 2.039                  |
| $^{82}\text{Se}$  | 8.7                   | 2.998                  |
| $^{96}\text{Zr}$  | 2.8                   | 3.348                  |
| $^{100}\text{Mo}$ | 9.8                   | 3.035                  |
| $^{116}\text{Cd}$ | 7.5                   | 2.813                  |
| $^{130}\text{Te}$ | 34.08                 | 2.527                  |
| $^{136}\text{Xe}$ | 8.9                   | 2.459                  |
| $^{150}\text{Nd}$ | 5.6                   | 3.371                  |

**Table 2.2.** Characteristics of commonly used  $\beta\beta$  decay isotopes. The table has been extracted from [81].

enrichment is possible and to what extent. Table 2.2 contains a list of the isotopes with their respective abundance and  $Q_{\beta\beta}$ -value.

As seen in Section 2.2.3 a discovery of a positive signal would still not be the end of the  $0\nu\beta\beta$  decay search. Confirming the signal with other isotopes could shed light on physics that are beyond the Standard Model. This is why there is an interest to develop the technology for multiple isotopes simultaneously.

### 2.3.2 Energy resolution

The energy resolution is arguably the most fundamental parameter of any detector looking for  $0\nu\beta\beta$  decay. Because ultimately the only thing that differs between a  $2\nu\beta\beta$  decay and a  $0\nu\beta\beta$  decay is the energy of the emitted electrons, a positive signal would induce an excess of events at the high energy tail of the energy spectrum of the  $2\nu$  mode, around  $Q_{\beta\beta}$ . In that respect the  $2\nu$  mode is an inherent background and the signal to background ratio for it can be approximated by [79]:

$$\frac{S}{B} \propto \left( \frac{Q_{\beta\beta}}{\Delta E} \right)^6 \frac{T_{1/2}^{2\nu}}{T_{1/2}^{0\nu}} \quad (2.14)$$

A worse energy resolution would have to be compensated by an even lower background and higher exposure to reach a similar discovery potential. Because the material cost of an experiment grows faster than a linear function of the exposure, the energy resolution tends to become a parameter that can not be traded off.

### 2.3.3 Background rate

The first source of background as mentioned in the previous section is the  $2\nu$  mode of the double beta decay, which is completely indistinguishable from the  $0\nu$  mode when its energy falls within the ROI. Most other sources of background come from natural radioactivity. The main offenders are  $^{208}\text{Tl}$  from the thorium decay chain and  $^{214}\text{Bi}$  from the uranium decay chain. Those are primordial radioisotopes contaminating all the materials used. Even if shielding is necessary, it is also mandatory to make the detector itself as radiopure as possible, which requires an extensive screening campaign while choosing carefully the materials and suppliers.

Another source of contamination comes from  $^{222}\text{Rn}$ . Being a noble gas it is invasive and can end up within the active region of the detector. To alleviate these issues, a radon-free atmosphere is a requirement for rare events search laboratories. This can be achieved by using radon trap in the air purification system.

Cosmic rays, while largely suppressed by locating experiments in underground laboratories [82, 83], can still activate long-lived nuclei within the detector that can become a source of background thereafter as well as knocking neutrons into the active volume.

Beside the radiopurity and shielding, there are ways to reduce the background rate in the ROI. Either by reconstructing the topology of the event (so discriminating a two electrons emission from a single scattered electron), pulse shape discrimination and decay product identification [84]. The holy grail in rare events experiments is to reach the background-free regime, because then, as seen with Equation 2.10 and Equation 2.13, the sensitivity improves as a power of 1/2 of the exposure instead of a power 1/4.

## 2.4 Landscape of neutrinoless double beta decay experiments

### 2.4.1 Recent and current experiments

The most advanced recent experiments have probed half-lives that were as high as the order of  $10^{26}$  years. Table 2.3 lists the current best half-lives for each  $\beta\beta$  isotope. There is a wide variety of experiments in the  $0\nu\beta\beta$  research field. They cover a wide variety of detection techniques for an equally wide variety of isotopes. In this section the experiments will be sorted by the detection principle they use.

### Semiconductors

#### Gerda

The GERmanium Detector Array (GERDA) experiment is located at the Laboratori Nazionali del Gran Sasso (LNGS). The detector is made of high purity germanium (HPGe) diodes that are 86%-enriched in  $^{76}\text{Ge}$ . The strength of this design lies in the fact that HPGe detector is a very robust and mature technology. In the case of  $0\nu\beta\beta$  decay search the semiconductor diodes provide an energy resolution of 0.12%

| Isotope           | $T_{1/2}^{0\nu} (\times 10^{25} \text{ y})$ | $\langle m_{\beta\beta} \rangle (\text{eV})$ | Experiment            |
|-------------------|---|--|-----------------------|
| $^{48}\text{Ca}$  | $> 5.8 \times 10^{-3}$                      | $< 3.5 - 22$                                 | ELEGANT-IV            |
| $^{76}\text{Ge}$  | $> 18.0$                                    | $< 0.08 - 0.182$                             | GERDA                 |
|                   | $> 1.9$                                     | $< 0.24 - 0.52$                              | Majorana Demonstrator |
| $^{82}\text{Se}$  | $> 3.6 \times 10^{-2}$                      | $< 0.89 - 2.43$                              | NEMO-3                |
| $^{96}\text{Zr}$  | $> 9.2 \times 10^{-4}$                      | $< 7.2 - 19.5$                               | NEMO-3                |
| $^{100}\text{Mo}$ | $> 1.1 \times 10^{-1}$                      | $< 0.33 - 0.62$                              | NEMO-3                |
| $^{116}\text{Cd}$ | $> 1.0 \times 10^{-2}$                      | $< 1.4 - 2.5$                                | NEMO-3                |
| $^{128}\text{Te}$ | $> 1.1 \times 10^{-2}$                      | —  | —                     |
| $^{130}\text{Te}$ | $> 3.2$                                     | $< 0.075 - 0.35$                             | CUORE                 |
| $^{136}\text{Xe}$ | $> 10.7$                                    | $< 0.061 - 0.165$                            | KamLAND-Zen           |
|                   | $> 3.5$                                     | $< 0.078 - 0.239$                            | EXO-200               |
| $^{150}\text{Nd}$ | $> 2.0 \times 10^{-3}$                      | $< 1.6 - 5.3$                                | NEMO-3                |

**Table 2.3.**  $T_{1/2}^{0\nu}$  and  $\langle m_{\beta\beta} \rangle$  limits (90% C.L.) from recent measurements, sorted by the mass number. The table has been extracted from [81]. GERDA, CUORE and EXO-200 latest results were also included from respectively [85], [86] and [87].

(FWHM) at  $Q_{\beta\beta}$  and the process of scaling up the target mass is, at worse, linear by just adding more sensors. The detectors are immersed in a liquid argon cryostat which also helps minimizing the background contamination in the vicinity of the active volume and is used as an active veto against cosmic muons. A water tank surrounds the cryostat and provides passive shielding against external  $\gamma$ -rays and neutrons as well as an active shielding against cosmic muons by using their Cherenkov light detected by an array of photomultipliers as a veto. A schematic drawing of the detector can be seen on 2.8.

GERDA ran in two phases. The first one went from late-2011 to mid-2013 and used initially an enriched mass of 17.8 kg which was increased to 21.4 kg shortly after with the use of broad energy sensors (BEG) as they have a much better energy resolution. The main result of the first phase was to refute the controversial discovery claim made by the Heidelberg-Moscow experiment.

The second phase shipped major improvement with additional BEG as well as a LAr veto system that drastically improved the radioac-

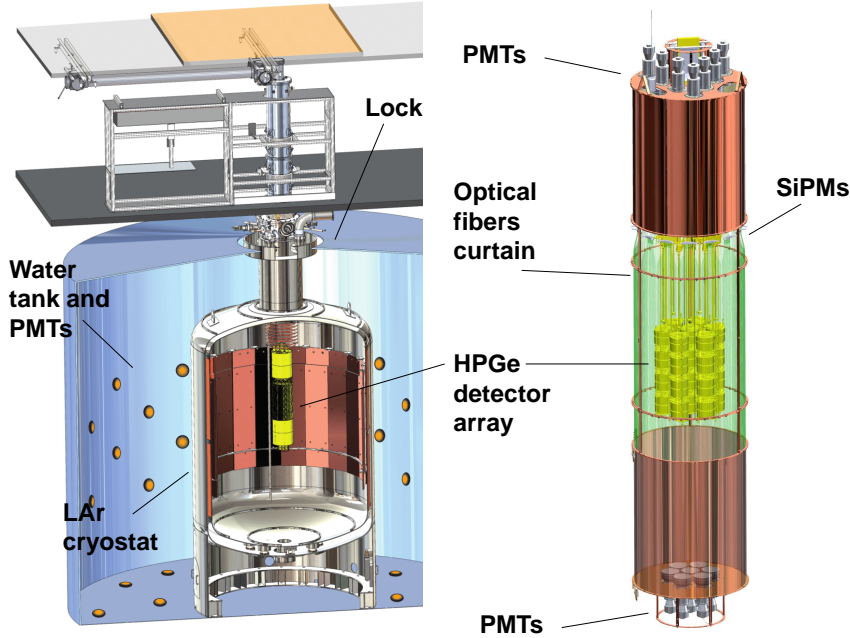


**Figure 2.8.** Schematic layout of the GERDA detector at LNGS. The right hand side of the picture is a zoom on the inner part of the setup. Taken from [88].

tive background and its rejection. It resulted to a very competitive background index of approximately  $5.2^{+1.6}_{-1.3} \times 10^{-4}$  counts/(keV kg years), on top of reaching a total enriched mass of 35.8 kg. Its ultimate data taking campaign added approximately 10 kg of inverted coaxial sensors. By combining all its data, GERDA reached a lower limit of  $T_{1/2}^{0\nu}$  at  $1.8 \times 10^{26}$  years at 90% CL [85].

#### Majorana demonstrator

The Majorana demonstrator (MJD) experiment was operating at Stanford Underground Research Facility. Unlike GERDA, MJD installed its detectors in two copper vacuum cryostats which were inside a shield made of layers of copper and lead and ultimately within a radon free environment. One of the most impressive feats of MJD is its ultra low background that could be achieved notably by using extremely radiopure materials. Among which features the copper used in the inner parts of the detector that has been electroformed

and machined directly underground to limit contamination and avoid cosmogenic activation [89].

MJD started taking data in 2015 as soon as its first cryostat was filled with the enriched sensors. The detector was finally fully assembled in 2017 and reached a background index of  $(4.7 \pm 0.08) \times 10^{-3}$  counts/(keV kg years). It could achieve a lower limit on  $T_{1/2}^{0\nu}$  of  $2.7 \times 10^{25}$  years at 90% CL [90].

## Bolometers

### CUORE

The Cryogenic Underground Observatory for Rare Events (CUORE) is also located at LNGS. It is using crystal bolometers made of  $\text{TeO}_2$ . They measure very accurately small temperature changes due to particle interactions within the crystals at a temperature of 10 mK. The crystals are  $5 \times 5 \times 5 \text{ cm}^3$  and are instrumented with a thermal sensor and a resistive heater. With this technology an energy resolution of 0.2% FWHM at  $Q_{\beta\beta}$  could be achieved.

The full detector is made of a series of towers that are sharing a total of 988  $\text{TeO}_2$  bolometers for a total of enriched mass of 206 kg. The towers are contained within a cryostat that can reach the temperature of 10 mK. The cryostat is shielded against incoming radiation with several layers of lead and copper. A schematic view is available in Figure 2.9.

For the  $^{130}\text{Te}$  isotope CUORE managed to report a background index of  $(1.38 \pm 0.07) \times 10^{-2}$  counts/(keV kg years) and a lower limit on  $T_{1/2}^{0\nu}$  of  $3.2 \times 10^{25}$  years at 90% CL [86].

## Time Projection Chambers

### EXO-200

The Enriched Xenon Observatory (EXO) is a Time Projection Chamber (TPC) using 200 kg of 80%-enriched  $^{136}\text{Xe}$  and located in the Waste Pilot Isolation Plant (WIPP) in New Mexico, USA. EXO-200 ran successfully in a two phase scientific program: the first run spanned from 2011 until 2014, and the second one following upgrades lasted from 2016 until 2018. Out of the total mass, about 175 kg were in liquid

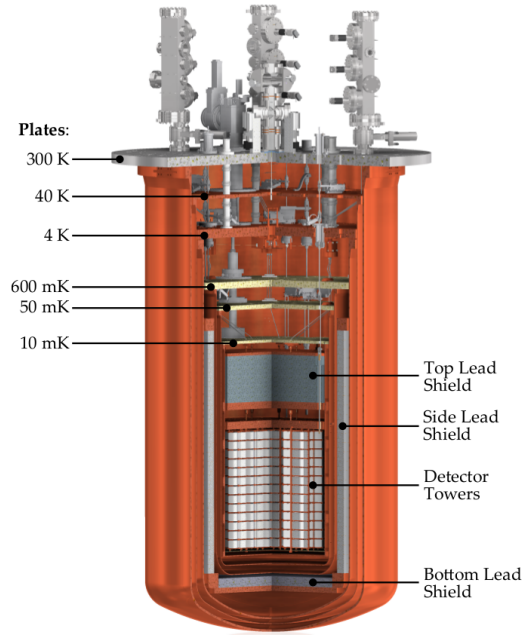


**Figure 2.9.** Schematic layout of the CUORE detector at LNGS. Taken from [91].

phase and that included the 110 kg inside the active volume of the TPC.

The detector, shown in 2.10, is a symmetrical TPC featuring a central transparent cathode where the ionization signal is readout at both anodes by two wire planes while the scintillation signal is read by two large-area photodiodes (LAAPDs). To improve background rejection the cryostat keeping the liquid xenon at 167 K was shielded with lead and surrounded by an active muon veto system made of plastic scintillators. By using xenon in its liquid phase EXO could achieve an energy resolution of  $(3.60 \pm 0.15)\%$  FWHM at  $Q_{\beta\beta}$  for single site events which are typically those involved in  $\beta\beta$  candidate events [92].

The EXO collaboration reported a background index at the level of  $(1.7 \pm 0.2) \times 10^{-3}$  counts/(keV kg years). The first result achieved by the EXO detector was to discover the  $2\nu$  mode of the double beta

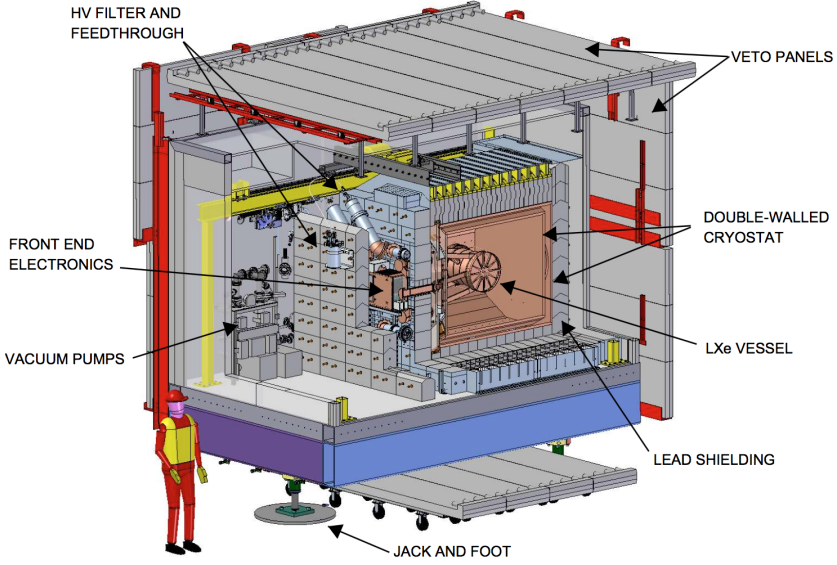


**Figure 2.10.** Drawing of the EXO-200 TPC detector. Taken from [96].

decay and measure its half-life:  $T_{1/2}^{2\nu}(^{136}\text{Xe}) = (2.165 \pm 0.016(\text{stat.}) \pm 0.059) \times 10^{21}$  years [93,94]. EXO-200 has been a very successful experiment alongside GERDA, setting a very competitive lower limit on  $T_{1/2}^{0\nu}$  of  $3.5 \times 10^{25}$  years at 90% CL [87]. It also probed the double beta decay that  $^{134}\text{Xe}$  is suspected to be prone to:  $T_{1/2}^{2\nu}(^{134}\text{Xe}) > 8.7 \times 10^{20}$  years and  $T_{1/2}^{0\nu}(^{134}\text{Xe}) > 1.1 \times 10^{23}$  years [95].

### NEXT-White

The detector NEXT-White is a detector built by the NEXT collaboration (Neutrino Experiment with a Xenon TPC) using roughly 10 kg of enriched xenon and located in the Laboratorio Subterráneo de Canfranc (LSC) in Spain. The major difference with EXO-200 is that in NEXT-White the xenon is in a gaseous phase, at 10 bar, which allows for a topology based background suppression and a better energy resolution. The collaboration reported an energy resolution of  $0.91\% \pm 0.12\%$  FWHM at 2.6 MeV. The operations of the detector NEXT-White and its results will be detailed more thoroughly in Section



3.3.3 of the next chapter.

A 100 kg detector, NEXT-100, is under construction and is expected to be assembled in 2022.

## Organic scintillators

### KamLAND-ZEN

The Kamioka Liquid Scintillator Antineutrino Detector Zero Neutrino is, as its name suggests, based in the famous mine of Kamioka in Japan. The experiment used the existing infrastructure of the KamLAND experiment used in the 00's to measure the "solar" sector of the neutrino mixing matrix by observing the disappearance channel of electron antineutrinos produced by nuclear reactors. The core of the detector is made of an inner spherical balloon of nylon (3 m diameter) filled with a xenon-loaded scintillator (Xe-LS). This inner balloon is installed inside an outer balloon (13 m diameter) filled with the scintillator. This assemblage is itself contained in a water tank that acts as a passive shield from external radiation as well as a traditional Cherenkov veto system against cosmic muons. A schematic view of the experiment can be seen in Figure 2.11.

The first data taking campaign started in October 2011 until June 2012 and was stopped due to a contamination of  $^{110m}\text{Ag}$  which was considered to be a fallout from the Fukushima reactors accident. This episode was followed by a period of 1.5 year of purifying the xenon loaded scintillator. During this first phase the energy resolution was 9.89% FWHM at  $Q_{\beta\beta}$ , for a total enriched mass of 320 kg of xenon-136. The second phase started in 2013 and lasted until 2015 for which the background has been considerably reduced and a total enriched mass of 380 kg was used. The second run had an energy resolution of 10.94% FWHM at  $Q_{\beta\beta}$ .

A combined analysis of both runs resulted to a background index of  $(1.0) \times 10^{-2}$  counts/(keV kg years) and a lower limit on  $T_{1/2}^{0\nu}$  of  $1.07 \times 10^{26}$  years at 90% CL for the decay of xenon-136 [97]. An upgraded version, KamLAND-ZEN 800, has been commissioned and started operation recently [98]. The first results were released [99] just before submission of this thesis: a lower limit on the half-life was established at  $2.3 \times 10^{26}$  years at 90% CL.

**SNO+**

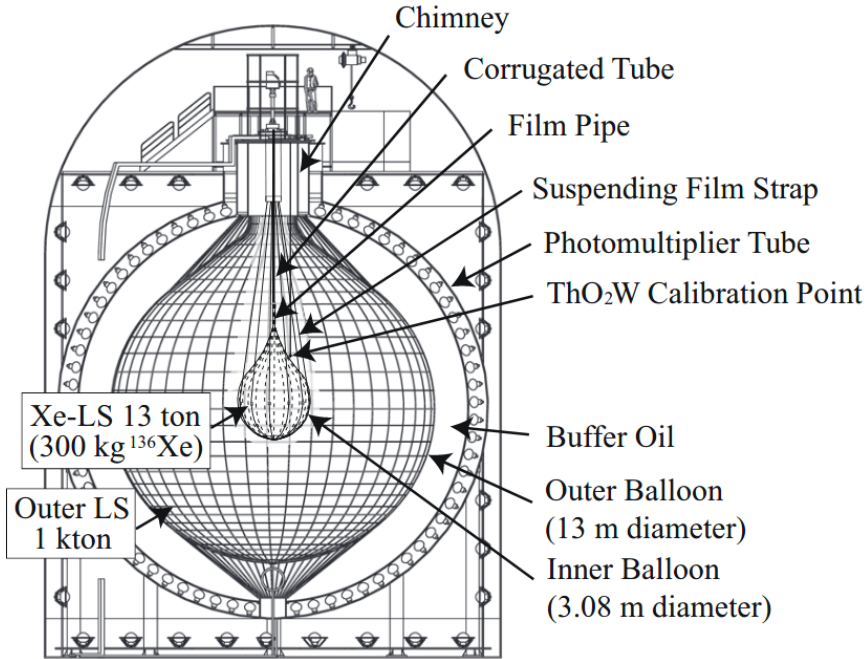
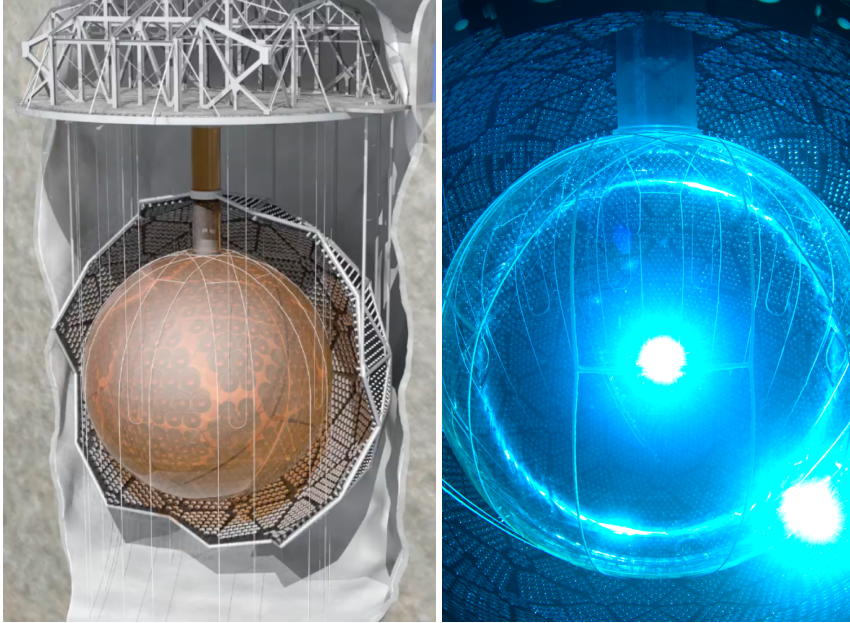


Figure 2.11. Drawing of the KamLAND-Zen detector. Taken from [100].

The Sudbury Neutrino Observatory located in SNO-LAB (Ontario, Canada), famous for its contribution to the discovery of neutrino oscillation and for solving definitely the solar neutrino problem. Like KamLAND-ZEN it has been revived for the purpose of  $0\nu\beta\beta$  decay search. The experiment consist of dissolving  $^{130}\text{Te}$  in the scintillator. By design the poor energy resolution is compensated by loading a large amount of  $\beta\beta$  emitter. The SNO+ has recently finished its "water phase" and will soon load its liquid scintillator to have access to lower its energy threshold. It is only its third phase that will involve its  $0\nu\beta\beta$  program by dissolving 3.9 tonnes of natural tellurium in the scintillator, which corresponds to 1.3 tonnes of  $^{130}\text{Te}$ ,  $\beta\beta$  emitter. Its expected sensitivity after 5 years is expected to reach  $T_{1/2}^{0\nu}$  of  $2.1 \times 10^{26}$  years at 90% CL [101].



**Figure 2.12.** Artistic drawing of the SNO+ detector (left). Photograph from inside the detector during its "water phase" (right). Taken from [101].

### 2.4.2 Other experiments

Despite the fact that the experiments mentioned in this section are not in line for the tonne scale they are worth mentioning because of some unique features they exhibit.

#### Inorganic scintillators

##### CANDLES

Calcium-48 has the advantage to have the highest  $Q_{\beta\beta}$  which suppresses most of the traditional radioactive background and because it is the lightest  $\beta\beta$  emitter, its NME are simple to compute. The main drawback is its very low natural enrichment of 0.187%. The CANDLES III experiment ended not far away from the best existing lower limit of the  $T_{1/2}^{0\nu}$  of  $^{48}\text{Ca}$  by using natural calcium [102]. But they mostly managed to demonstrate a background index comparable to the other current sensitive experiments. Associated with this

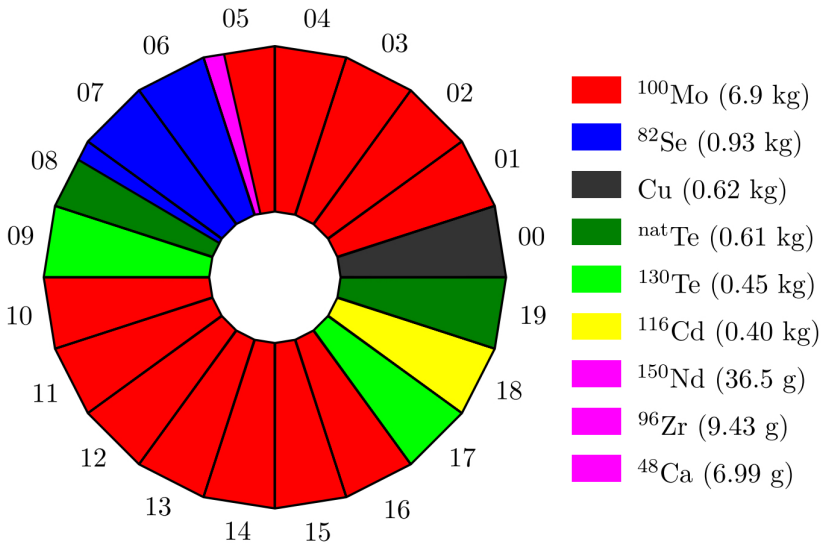


**Figure 2.13.** Source foils distribution in the NEMO3 detector.

effort is the development of novel enrichment techniques that would allow production of a high quantity of highly enriched  $^{48}\text{Ca}$  such as multi-channel counter-current electrophoresis (MCCCE) [103].

### Tracking calorimeters

#### NEMO-3

The Neutrino Ettore Majorana Observatory (NEMO) experiment was located in the Modane Underground Laboratory in France. The detector had a cylindrical shape and had a total of 20 segments of source foils containing a total of 10 kg of various  $\beta\beta$  isotopes. The source distribution and masses can be seen on the drawing 2.13. The detector was able to reconstruct the two electrons tracks coming from the sources in order to efficiently reject the background. It was taking data from 2003 until 2011 and while its design makes it hard to scale, it has been very successful at measuring the half life of seven  $\beta\beta$  emitters [81].

Following the success of NEMO-3, a successor detector is being assembled: SuperNEMO will be able to reach half-lives of the order

of  $10^{24}$  years. Thanks to its modular approach it can be also useful to probe systematically the  $2\nu$  mode of other isotopes [104].

### 2.4.3 Upcoming tonne-scale experiments

The next phase for  $0\nu\beta\beta$  decay search will aim to fully explore the  $m_{\beta\beta}$  band corresponding to the inverted mass hierarchy. To do so it is expected for experiment to use a target mass of the order of the tonne which raises a number of technical challenges. Because of the cost that such experiments will reach it is expected that only a handful of them will be able to carry on. In the fall of 2021 the effort seems to be shared by four experiments.

## LEGEND

The most mature, performing and promising technology will be set in motion by the LEGEND collaboration which results of the merging of the GERDA and Majorana collaborations. The road-map aims at reaching a sensitivity to half-life above  $10^{28}$  years for  $^{76}\text{Ge}$ .

The first phase of the experiment, LEGEND-200, is running at LNGS using the existing infrastructure of GERDA. It uses 200 kg of enriched germanium and after 5 years should be able to reach a sensitivity to half-life of the order of  $10^{27}$  years with a background index of  $(2.0) \times 10^{-4}$  counts/(keV kg years) [105]. The subsequent stage, LEGEND-1000, is designed in order to reduce the background by roughly another order of magnitude. It is aiming for a background index estimated to  $(9.1) \times 10^{-6}$  counts/(keV kg years), making the experiment practically background-free [106].

## CUPID

CUPID is the successor experiment of CUORE. Its name reflects this: CUORE with Particle Identification. It is planned to be installed at LNGS and to use scintillating bolometers. The scintillating bolometers will be made of  $\text{Li}_2\text{MoO}_4$  crystals with 95%-enriched molybdenum. These crystals will have 50 mm height and 50 mm diameter for a mass of 301 g each. The flat surfaces will be exposed to bolometric light detector fabricated from germanium wafers of 50 mm diameter and using an NTD germanium thermistor as a thermal sensor. These crystals will

be stacked on towers. With this design it will be 1500 crystals hosted within the cryostat, for about 250 kg of enriched mass. This experiment should reach of background index of  $10^{-4}$  counts/(keV kg years).

The CUPID collaboration is exploring two scenarios for a future upgrade: the first one consists of lowering the background by an order of magnitude in order to practically reach a background-free regime, while the second consists of scaling up the target mass in order to reach 1 tonne of enriched molybdenum. For the latter case the background index requirement would be of the order of  $5 \times 10^{-6}$  counts/(keV kg years) and the sensitivity reached after 10 years would be of the order of  $8 \times 10^{28}$  years [107].

### **nEXO**

The next Enriched Xenon Observatory (nEXO) is the iteration of the EXO-200 experiment. It will be a single phase liquid xenon TPC using 5 tons of enriched xenon-136. The density of the material and its quantity makes it possible to use the outer volume of the liquid xenon bulk to shield the inner active volume. This self-shielding added to external shielding, cosmic muon veto is expected to drastically improve the background index with respect to a smaller module. The detection technique will take advantage of both the ionization and the scintillation in order to improve the energy resolution with respect to EXO-200. The design foresees to use VUV-sensitive silicon photomultipliers installed behind the field shaping rings to also improve the light collection.

The nEXO collaboration estimates the sensitivity it could achieve under conservative assumptions to be of the order of  $5.7 \times 10^{27}$  years after ten years. Because of the necessity of self-shielding, the background index is very position-dependent, but assuming an active volume of 2 tons of liquid xenon, the nEXO collaboration predicts a background index of  $5.3 \times 10^{-6}$  counts/(keV kg years) [108].

### **NEXT-HD**

The NEXT collaboration is going through an intense R&D effort to make its technology ready for the tonne scale. The detector NEXT-HD will be a symmetrical TPC that will be built at the LSC starting in

2026. It will aim to reach a sensitivity to half-lives of the order of  $10^{27}$  years [109]. More information regarding the technical challenges and how the collaboration plans to tackle them will be given in Section 3.4.1 of the next chapter.

## 2.5 Summary

The importance of the nature of the neutrino has been highlighted in the previous chapter. Proving that the neutrino is a Majorana particle would be a very important milestone for particle physics. As such the attention of experimentalists for neutrinoless double beta decay has been increasing strongly over the past two decades.

Clever ideas have been tested and some were met with acclaimed success. The discovery of the two-neutrino mode of the double beta decay validated the idea to experimentally chase the zero-neutrino mode as a proof that the neutrino is a Majorana particle. A major effort has been made in the last ten years to run experiments using various isotopes with a target mass in the range of tenths of kilograms. They have established lower limits on the half-life of neutrinoless double beta decay of the order of  $10^{25}$ - $10^{26}$  years.

But despite these enthralling results, all experiments faced a null signal. In order to keep improving the sensitivity reached, the scale of the next generation experiments has to necessarily be increased by an order of magnitude. The most efficient, and realistic, way to scale up is to get as close as possible of the background-free regime.

But in order to probe the normal mass hierarchy the constraints on the technology selected might very well be harsher, notably due to the cost of the amount of enriched isotope needed. Such experiment would probably be required to be background-free as well as being readily scalable.





# The NEXT experiment

# 3

In the previous chapter we saw that the hunt for neutrinoless double beta decay is made extremely hard by the scale of its possible half-life. Should the effective Majorana mass lie beyond the values allowed for an inverted mass hierarchy, very few designs could be realistically scaled up to match the new requirements in terms of background index, energy resolution, and target mass.

The NEXT collaboration (Neutrino Experiment with a Xenon TPC) is aiming to demonstrate that a high pressure xenon Time Projection Chamber (HPXeTPC) is a design capable of probing the entire inverted mass hierarchy of allowed values for  $m_{\beta\beta}$ . It would also be able to go beyond that stage and be scaled up to a multi-tonne experiment for a more extensive search of the neutrinoless double beta decay.

The experimental approach consists of validating proofs of concepts with prototypes of increasing scale.

## 3.1 The SOFT concept

We have seen that looking for the  $0\nu\beta\beta$  decay requires optimizing a number of parameters, among which the energy resolution and the background index are typically the figures of merit impacting the sensitivity of an experiment. As such, a good design for a xenon-based detector would feature the best possible energy resolution combined with a way to track the two resulting electrons reliably in order to further reject background as done in the NEMO experiment. The Time Projection Chamber is a detector concept invented by Dave Nygren in the 70's [110,111]. This type of detector can do both tracking and calorimetry by using the properties of various possible gas mixtures.

A charged particle crossing a gaseous detector loses its energy by ionizing and exciting the atoms along its path leaving behind a track of ion-electron pairs. In a TPC these pairs are prevented from recombining by a uniform electric field. The excitation component of this primary interaction leads to a scintillation signal of the gas, in the VUV range of the spectrum for xenon (peaked at 172 nm). Because this signal comes directly from the primary interaction it is referred to as  $S1$ . The secondary electrons then drift along the field lines towards the anode of the detector where a zone with a higher uniform electric field amplifies these electrons to a detectable signal, the  $S2$ . A readout plane can then record the track in two dimensions. The coordinates on the third dimension, the one parallel to the electric field, is retrieved from the time difference between the prompt  $S1$  and the delayed  $S2$ , thus the *projection of the time coordinate*. So a TPC can reconstruct a track in three dimension while measuring the energy deposition locally as well as globally if the amplified signal is proportional to the primary signal. In the case of xenon-based  $0\nu\beta\beta$  decay searches it has been shown by the Gotthard experiment that the 3D reconstruction was effective at selecting candidates for  $\beta\beta$  events [112].

The designs that have been established by the NEXT collaboration rely on the Separately-Optimized Functions TPC (SOFT) concept. It consists of performing the tracking and calorimetry by two separate groups of sensors. Dave Nygren has noted that a high pressure xenon TPC can use advantageously the electroluminescence (EL) process to amplify the signal: it consists of accelerating the electrons just enough for them to excite the atoms of the medium without ionizing. The main advantage of using EL is that it is a process that has a very minimal variance compared to the amplification done by electron avalanche. The consequence being that the energy resolution of the detector is not crippled and can approach closely the intrinsic energy resolution. Because of this all the sensors used are light sensors, hence this class of detector is often named electroluminescent TPC (EL TPC).

In the SOFT concept the tracking function is performed by a dense array of silicon photomultipliers (SiPMs) located on the anode side of the detector while the calorimetry is done by a relatively small number of photomultiplier tubes (PMTs) on the cathode side of the detector. The former is referred to as the tracking plane and the latter as the energy plane. Because the PMTs can cover a large area for a minimal

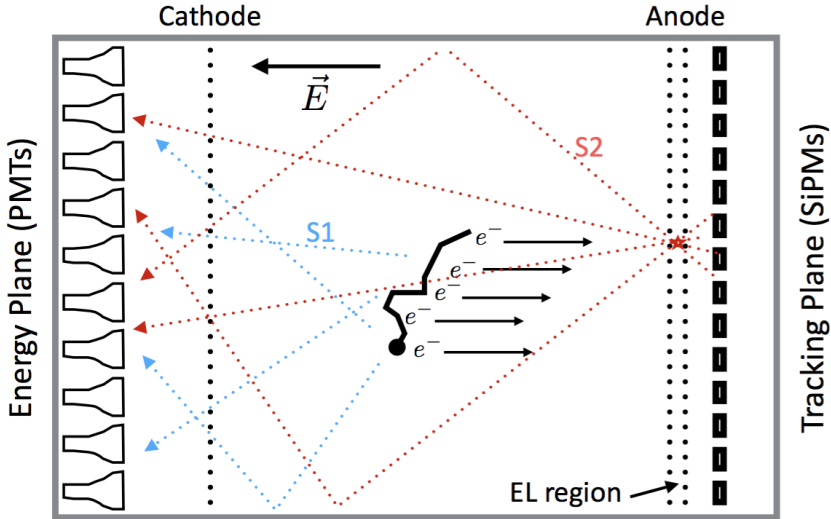


**Figure 3.1.** SOFT concept as presented in [113]. The S2 signal produced on the EL region is recorded simultaneously by the tracking plane at the anode for tracking and by the energy plane at the cathode for calorimetry. The latter also records the S1 used to reconstruct the z-coordinate.

number of channels and have a low noise and a high gain they are preferred for the energy measurement, while the high granularity that can be achieved with the SiPMs make them ideal for the tracking. Another important asset of this design choice is that the small first scintillation signal can be efficiently detected by the PMTs of the energy plane to provide the  $t_0$  required to reconstruct the z-coordinate. Figure 3.1 illustrates this paragraph.

### 3.2 Gaseous xenon as a detector medium for a TPC

Xenon is one of the few elements that has  $\beta\beta$  emitter isotopes. While its isotope 134 is suspected to undergo double beta decay, the favoured isotope for  $0\nu\beta\beta$  decay search is 136 due to its higher  $Q_{\beta\beta}$  value: 2457.83 keV [114]. With a natural abundance of 8.857% and being naturally a gas, it can be enriched at a relative low cost compared to

the other  $\beta\beta$  emitters by centrifugation.

The SOFT concept described in the previous section aims to take full advantage of the properties of xenon to achieve the best detector performances. When a  $^{136}\text{Xe}$  atom undergoes a  $0\nu\beta\beta$  decay it releases two electrons sharing a total energy equal to the  $Q_{\beta\beta}$ -value: 2.458 MeV. If we assume that these two electrons lose the entirety of their energy within the active region of the detector it is then possible to measure precisely their energy as well as to reconstruct the track of the two electrons to reject single electron background events. These single electron background events come essentially from Compton and photoelectric interactions of high energy  $\gamma$ -rays coming from the decay chain of  $^{208}\text{Tl}$  and  $^{214}\text{Bi}$ . For the energies considered in  $0\nu\beta\beta$  decay search, electrons can travel sufficiently in gaseous xenon (at around 10 bar) to behave like a minimum ionizing particles (MIP) for a part of their trajectories. Towards the end of their trajectories their  $dE/dx$  increases and they lose their remaining energy (approximately 300 keV) through multiple scatterings over a small region, a "blob". This topological feature is what helps recognize a two electron track from a single electron track.

While a description of the physical processes outlined in the description of the SOFT concept can be found in the following paragraphs, it is to be noted that these elements will be detailed more comprehensively in the Chapter 4.

### 3.2.1 Primary interaction: ionization and excitation

When a charged particle such as an electron resulting from a  $\beta\beta$  decay interacts within the gaseous xenon volume it loses its energy through heat, ionization and excitation. In the case of an excitation, one of the electrons from the inner shell of a xenon atom is raised to a higher energy level. In the case of an ionization the energy given is enough to fully knock the electron out of the atom resulting in the formation of an ion-electron pair. Atomic de-excitation and ion-electron recombination both lead to the emission of a photon through scintillation with a continuous spectrum peaking at 172 nm, in the VUV region for xenon. These processes are summarized in the schematic shown in Figure 3.2.

The Platzmann equation allows to quantify the share of energy lost

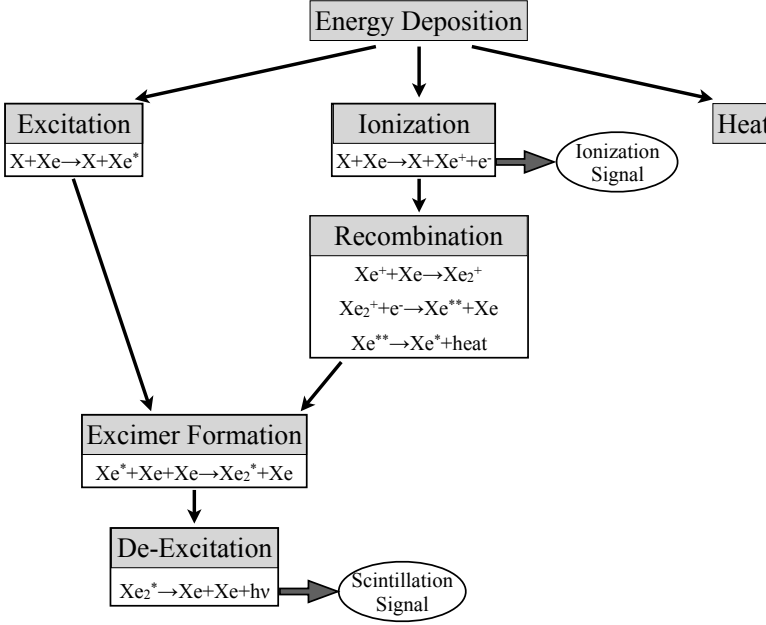


**Figure 3.2.** Diagram showing the different processes happening when a radiation (noted X in the diagram) deposits its energy in the detection medium. Taken from [115].

by an interacting ionizing radiation between these processes [116]:

$$E_{lost} = N_{ion} \langle E_{ion} \rangle + N_{exc} \langle E_{exc} \rangle + N_{ion} \langle \epsilon \rangle \quad (3.1)$$

where  $E_{lost}$  is the total energy lost by the primary particle (electron in the case of a  $\beta$ -like event),  $N_{ion}$  is the number of ion-electron pairs formed at an average energy expenditure  $\langle E_{ion} \rangle$ ,  $N_{exc}$  is the number of atoms left in an excited state at an average energy expenditure  $\langle E_{exc} \rangle$  and  $\langle \epsilon \rangle$  is the average kinetic energy of sub-excitation electrons, which is basically heat. The average energy spent in ionization/excitation is a useful quantity to characterize a detection medium, they are noted in this section respectively  $W_{ion}$  and  $W_{exc}$  and are written, following Equation 3.1, as:

$$W_{ion} = \frac{E_{lost}}{N_{ion}} = \langle E_{ion} \rangle + \langle E_{exc} \rangle \frac{N_{exc}}{N_{ion}} + \langle \epsilon \rangle \quad (3.2)$$

$$W_{exc} = \frac{E_{lost}}{N_{exc}} = \langle E_{ion} \rangle \frac{N_{ion}}{N_{exc}} + \langle E_{exc} \rangle + \langle \epsilon \rangle \frac{N_{ion}}{N_{exc}} \quad (3.3)$$

Regarding the notation, when the scintillation component is not included in the discussion (as will be the case in Chapter 4),  $W_{ion}$  will be simply referred to as the  $w$ -value.

### 3.2.2 Secondary processes leading to detected signals: drift and electroluminescence

Once the interaction has taken place in the bulk of the detection medium of the TPC, an applied electric field prevents the electron-ion pairs from recombining. To reach an optimum efficiency of the electron-ion pairs separation, a field above 200-250 V/cm is required at the typical working pressures of the TPC. The drift field is typically set between 350 and 450 V/cm. The ions drift slowly towards the cathode while the electrons drift towards the amplification stage near the anode. The details of the processes happening to the drifting electrons are provided in Section 4.1.

The first of these processes is the diffusion that is materialized by the electrons deviating from their trajectories. The second is attachment. Some electrons are lost during their drift by attaching to gas impurities, which is modeled by an exponential law:

$$N(t) = N_0 \exp(-t/\tau) \quad (3.4)$$

where  $N(t)$  is the number of drifting electrons after a drifting time  $t$ ,  $N_0$  is the initial number of secondary electrons produced and  $\tau$  is the electron lifetime. The dominant impurity responsible for these attachments is the  $O_2$  molecule. The tolerance on its concentration is set by the size of the drift region. For NEXT detectors typical values aimed for are less than 1 ppb (part per billion). These two processes lower the detector performance. Clever techniques to directly or indirectly minimize the diffusion can alleviate its effect on the topology reconstruction while the lifetime can be improved by constantly recirculating the gas through purifiers.

The primary ionization often does not produce a detectable signal by itself. This is why TPCs have an amplification stage, materialized by a higher electric field region. In the case of an electroluminescence

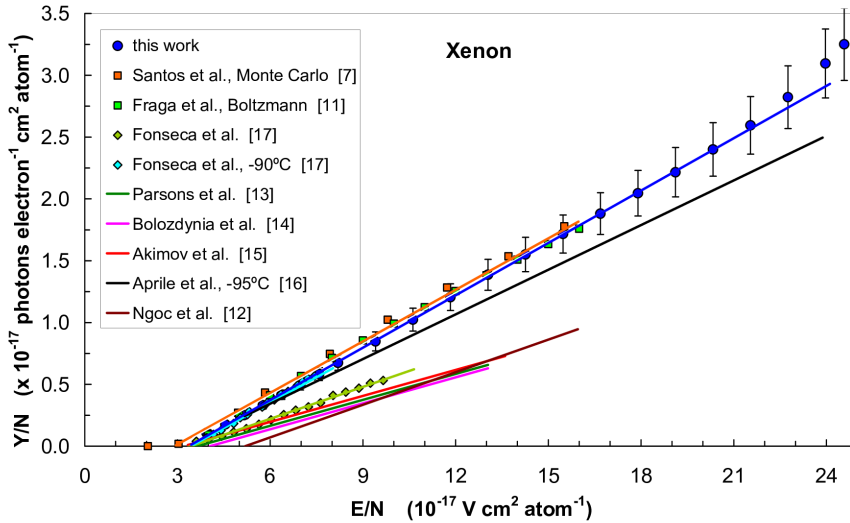


**Figure 3.3.** Panel summarizing different studies of the secondary scintillation yield in pure xenon. The reduced scintillation yield is the number of photons produced per secondary electron and per unit of pressure. It is a proportional quantity of the reduced electric field  $E/P$ . Taken from [118].

(EL) TPC this amplification stage accelerates the electrons to energies that are sufficient to excite the xenon atoms. The first excited state of xenon has an energy of 8.3 eV and its ionization potential is at 12.13 eV, thus an EL TPC aims to accelerate the electrons to an energy in-between these two values. The field required to achieve this is pressure dependent, the quantity of interest and quoted in the literature is therefore the reduced electric field, often noted  $E/P$ , and expressed in  $\text{kV cm}^{-1} \text{bar}^{-1}$ . The light yield is a linear function of this reduced field as long as the higher energy electrons do not accumulate enough energy to ionize the atoms. This linear dependency can be seen in Figure 3.3. In the case of fields above the ionization threshold, the light yield has an exponential growth. For NEXT-like detectors an amplification field between 1 and 3  $\text{kV cm}^{-1} \text{bar}^{-1}$  has been assessed as optimal [117].

These excitations are converted to a scintillation signal, the S2. The S2 is proportional to the number of secondary electrons [118] and its

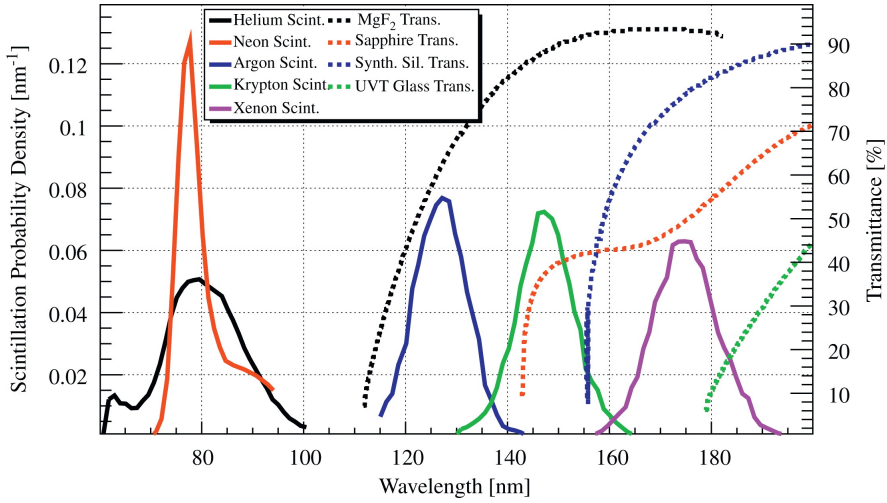


**Figure 3.4.** The solid lines show the scintillation spectra of the noble gases and the dashed lines show the percent transmittance some common optical materials. Taken from [120].

variance is extremely small, as seen in Section 3.1. Since the light is emitted in the VUV range (around 170 nm for xenon as can be seen in Figure 3.4), it is mostly absorbed by the materials of the detectors; and most sensors are not sensitive, or very poorly so, to these wavelengths. To circumvent this issue, the inner parts of the detector exposed to light are typically coated with tetraphenyl butadiene (TPB). It is a common wavelength shifter. Thin films of TPB are able to convert ultraviolet light into the visible spectrum [119]. The TPB coating does not only make light detection possible but it also increases greatly the light collection and therefore the detector performance.

### Energy resolution

In gaseous proportional counters the source for the energy measurement is the number  $N_{ion}$  of secondary electrons produced by ionization. The stochastic fluctuations in this number limits the energy resolution and is intrinsically tied to the Fano factor, noted  $F$ , and to the average energy required to create an ion-electron pair,  $W_{ion}$ . The variance in



the number of ionization is given by [121]:

$$\sigma_e^2 = FN_{ion} = \frac{FE_{lost}}{W_{ion}} \quad (3.5)$$

Which translates to the intrinsic energy resolution (FWHM):

$$\frac{\delta E}{E} = 2.35 \sqrt{\frac{FW_{ion}}{E}} \quad (3.6)$$

In the case of gaseous xenon the Fano factor has been measured between 0.13 and 0.17 [122–124]. Estimations of the Fano factor by Monte-Carlo simulations have been found to be in good agreement with these measured values [125]. On the other hand the value  $W_{ion}$  has been measured to be about 21.9 eV in gaseous xenon [125]. So a conservative value for the intrinsic energy resolution of gaseous xenon is around 0.5% FWHM.

The effective energy resolution of a detector also factors in the variance in the amplification process as well as the variance in the signal detection. All else being equal, Bolotnikov and Ramsey show [126] that the energy resolution of gaseous xenon is constant below a density threshold of 0.55 g/cm<sup>3</sup> and progressively degrades onwards towards the value in liquid xenon (Figure 3.5). This is possibly attributed to clusters of more than 10 xenon atoms generating a first exciton band. This exciton band would act as an added channel available for the primary radiation to lose its energy, consequently degrading the energy resolution [127].

### 3.3 The NEXT detectors

The NEXT collaboration has been operating HPXe TPCs for more than a decade in order to ultimately discover the  $0\nu\beta\beta$  decay of <sup>136</sup>Xe. During the first phase of the project (2009-2014) it developed two small scale prototypes: NEXT-DEMO and NEXT-DBDM. The goal of this initial stage was to prove the validity of the SOFT concept and to gain expertise in designing, building and operating this type of detector before moving to bigger prototypes. At this stage the amount of xenon used was of the order of 1 to 2 kg.

The second stage was to build and operate the medium-sized detector NEXT-White (NEW). This detector was operating with a mass

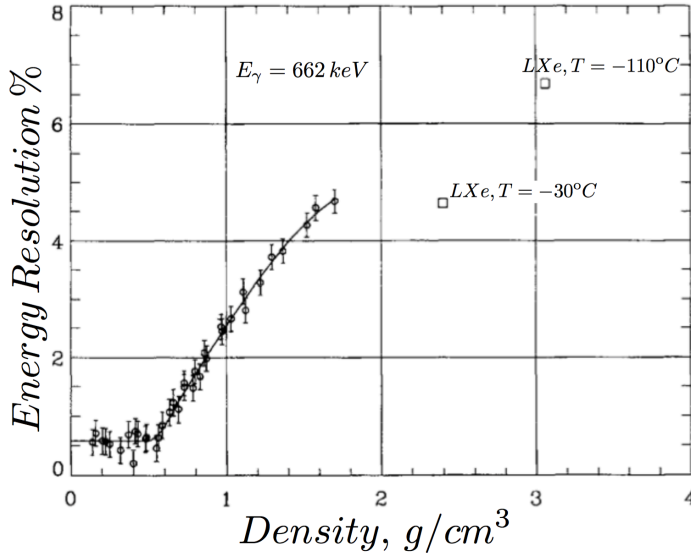


**Figure 3.5.** Evolution of the energy resolution with density in gaseous xenon using 662 keV  $\gamma$ -ray coming from a  $^{137}\text{Cs}$  source. Taken from [126].

of xenon of the order of 10 kg in a low background underground laboratory in the Spanish side of the Pyrenees: the Laboratorio Subterráneo de Canfranc (LSC). Its goal was to validate the background model, measure the  $2\nu$  half-life of  $^{136}\text{Xe}$  as well as validating the design choices made.

Currently the detector NEXT-100, that will operate with 100 kg of xenon at 15 bar is being built and is expected to start taking data in 2022. This detector will aim to prove further the scalability of the HPXe TPC and to be a testing bench for the technologies that will be used for the upcoming tonne-scale detector generation. On top of that it will aim to set a competitive limit on the neutrinoless double beta decay half-life.

### 3.3.1 NEXT-DEMO

The prototype NEXT-DEMO was built as the first proof-of-concept of the NEXT technology based on the SOFT concept. It was built in the Instituto de Física Corpuscular (IFIC) in Valencia, Spain. Because its goal did not require a low background environment, no specific concern about the radioactive budget was made and no shielding was established. It was assembled and operated inside a semi-clean room and was filled with natural xenon. The gas was circulating through a set of purifiers in order to avoid losing electrons to impurities.

NEXT-DEMO consisted of a stainless steel vessel able to withstand a gas at up to 15 bar. Its active volume, also known as the drift region, was 30 cm long with a diameter of 30 cm. In the drift region the electric field was set to 500 V/cm. Its EL stage, where the amplification takes place, was 5 mm long and was contained between two stainless steel wire grids. There the field was  $0.86 \text{ kV cm}^{-1} \text{ bar}^{-1}$ , high enough for the drifting electrons to excite the xenon atoms without ionizing them. A drawing of the NEXT-DEMO detector can be found on the top image of Figure 3.6.

Inside the field cage, a set of polytetrafluoroethylene (PTFE) panels surrounding the active volume were mounted to form an hexagonal tube in order to improve the light collection. This tube, called the "light tube", was coated with tetraphenylbutadiene (TPB) which is a wavelength shifter that is used in order to shift the VUV light to blue light that is detectable by the sensors used in the detector. A picture of the field cage can be seen on the bottom image of Figure 3.6.

The first operation of the detector made use of two identical sensor planes: one at the cathode for calorimetry and one at the anode for tracking. Each of these planes were made of 19 1-inch Hamamatsu R7378A PMTs [128]. The PMTs selected could work in an atmosphere of up to 20 bar, had a quantum efficiency for VUV of about 17% and of about 25% at the TPB re-emission wavelength. The PMTs of the tracking plane were used at a lower gain in order to avoid saturation.

In this first stage two configurations were tested, an ultraviolet configuration (UVC) where the light tube was not coated with TPB, and one where it was, the blue configuration (BC). On the one hand this run proved that the PMT tracking plane was not successful at reconstructing the tracks but was only merely able to gauge an average

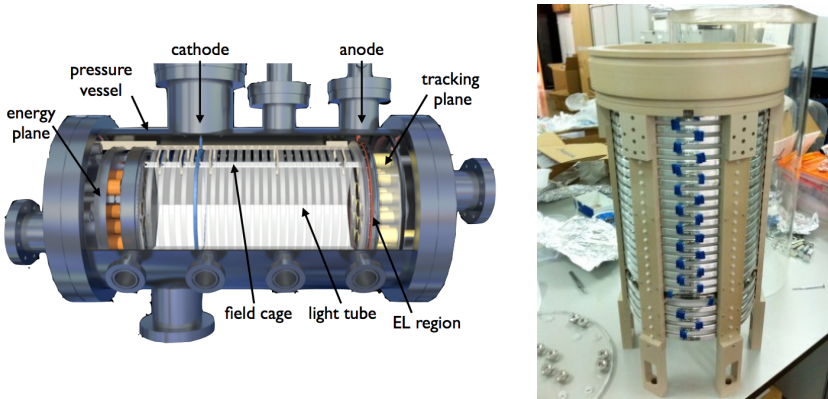


**Figure 3.6.** Drawing of the NEXT-DEMO detector (left). Picture of the field cage unmounted (right).

position of the event. On the other hand it demonstrated, by using the 511 keV back-to-back gammas from the  $\beta^+$  of a  $^{22}\text{Na}$  calibration source, that the energy resolution in the BC configuration was better (1.75% FWHM) than the UVC (2.89% FWHM) [129].

In the second stage of the lifespan of NEXT-DEMO, the tracking plane was replaced with one that was using 256 Hamamatsu S10362-11-050P SiPMs, with an active area of  $1\text{ mm}^2$  each [130]. They were distributed in four boards with each of them featuring a  $8 \times 8$  square grid of SiPMs with a pitch of 1 cm. Because these SiPMs are not sensitive to the VUV light they were coated with TPB.

The energy resolution was measured using the same  $^{22}\text{Na}$  source as before. Its value for the  $K_\alpha$  peak was measured at  $(5.691 \pm 0.003)\%$  FWHM; for the photopeak it was measured at  $(1.62 \pm 0.01)\%$  FWHM. These numbers translate to extrapolated energy resolutions at  $Q_{\beta\beta}$  of respectively 0.63% and 0.74% FWHM [131]. On the side of the track reconstruction, the change of tracking plane proved to be successful [132]. To evaluate the topology-based background rejection the collaboration used signal-like events (one track with two endpoints coming from electron-positron pair production from  $^{208}\text{Tl}$  high energy gammas) and single electron background events from the interaction of 1275 keV gammas from the  $^{22}\text{Na}$  source. An extra background rejection factor of  $24.3 \pm 1.4\%$  could be achieved while keeping an

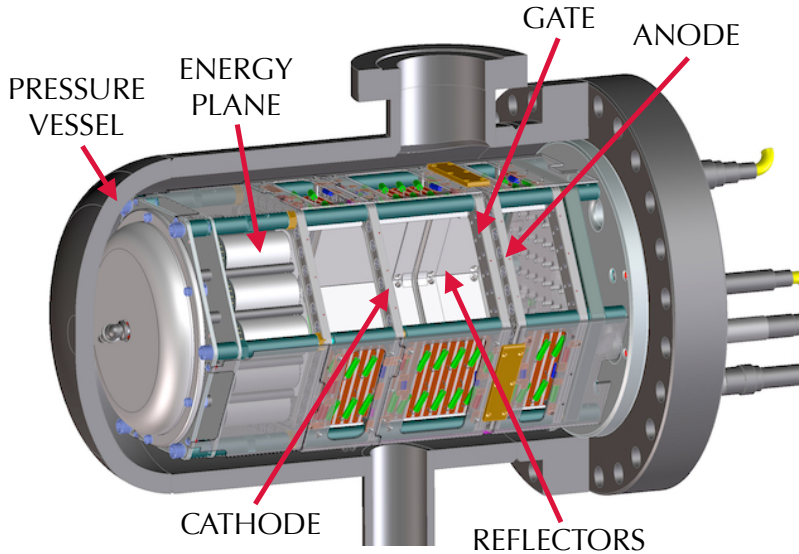


**Figure 3.7.** Drawing of the NEXT-DBDM detector.

efficiency of  $66.7 \pm 1.0\%$ .

### 3.3.2 NEXT-DBDM

The NEXT-DBDM prototype was built at the Lawrence Berkeley National Laboratory in the USA. It was operated with natural xenon between 2009 and 2014 and had the main goal to demonstrate the near-intrinsic energy resolution that could be achieved in high pressure xenon. It was made of a stainless steel vessel that was 33.5 cm long and had a diameter of 20 cm. Its drift region was 8 cm long while its EL stage was 5 mm long. Unlike NEXT-DEMO it had only an energy plane to perform the calorimetry. It was made of 19 1-inch Hamamatsu R7378A PMTs. The xenon was recirculating through a gas system that included a purification system. A view of the detector is shown in Figure 3.7.

The measurement of the energy resolution was made with the 662 keV gammas coming from a  $^{137}\text{Cs}$  source. The energy resolution measured was 1.1% FWHM at 10 bar and 1.0% FWHM at 15 bar, which extrapolate to approximately 0.5% FWHM at  $Q_{\beta\beta}$  [133].

### 3.3.3 NEXT-White

Originally named NEXT-10, it was renamed NEXT-White (NEW) in memory of James White. The detector was commissioned in the LSC, Spain and is the first radiopure NEXT detector. Built at the scale 1:2 of the following 100 kg class, it aimed to be a successful large scale validation of the technological and design choices made by the collaboration. A detailed overview of the detector can be found within the Reference [134].

On the physics front its goals were to assess the background model, measure the energy resolution directly at  $Q_{\beta\beta}$ , the characterization of the topological signature of signal-like events and the measurement of the  $2\nu$  mode of  $^{136}\text{Xe}$  half-life.

NEXT-White started its operations in October 2016, and finished completing its program in July 2021. A picture of the detector during operation can be seen in Figure 3.8. The detector was filled in the first place with the  $^{136}\text{Xe}$ -depleted gas in order to validate the background model and the radioactive screening campaign performed. Its first run (Run-I) was a technical one and lasted for just a few months. An inability to maintain a stable high enough voltage difference across the field cage required an intervention on the detector. Probing the behavior of the resistor chain of the field cage by replacing one of the end-caps of the vessel by an acrylic transparent end-cap allowed identification of the components at fault and replace them. Figure 3.9 shows the setup and the resistor chain. The change fixed the issue and the data taking campaign could restart in March 2017. Run-II lasted for over eight months and achieved stable conditions at 7.2 bar. Its purpose was to establish and validate the calibration procedure, notably based on the decay of  $^{83m}\text{Kr}$  [137]. It also allowed performance of a first measurement of the energy resolution, the electron drift parameters in high pressure xenon [138] and a measurement of the impact of  $^{222}\text{Rn}$  contamination on the radioactive budget [139]. It was followed by a short engineering run (Run-III) before the detector could be filled at 10.1 bar.

The following Run-IV was divided between a period of high-energy calibration campaign and a period of low-background data-taking. A procedure to continuously take data while simultaneously monitoring and calibrating the detector with  $^{83m}\text{Kr}$  data was imple-

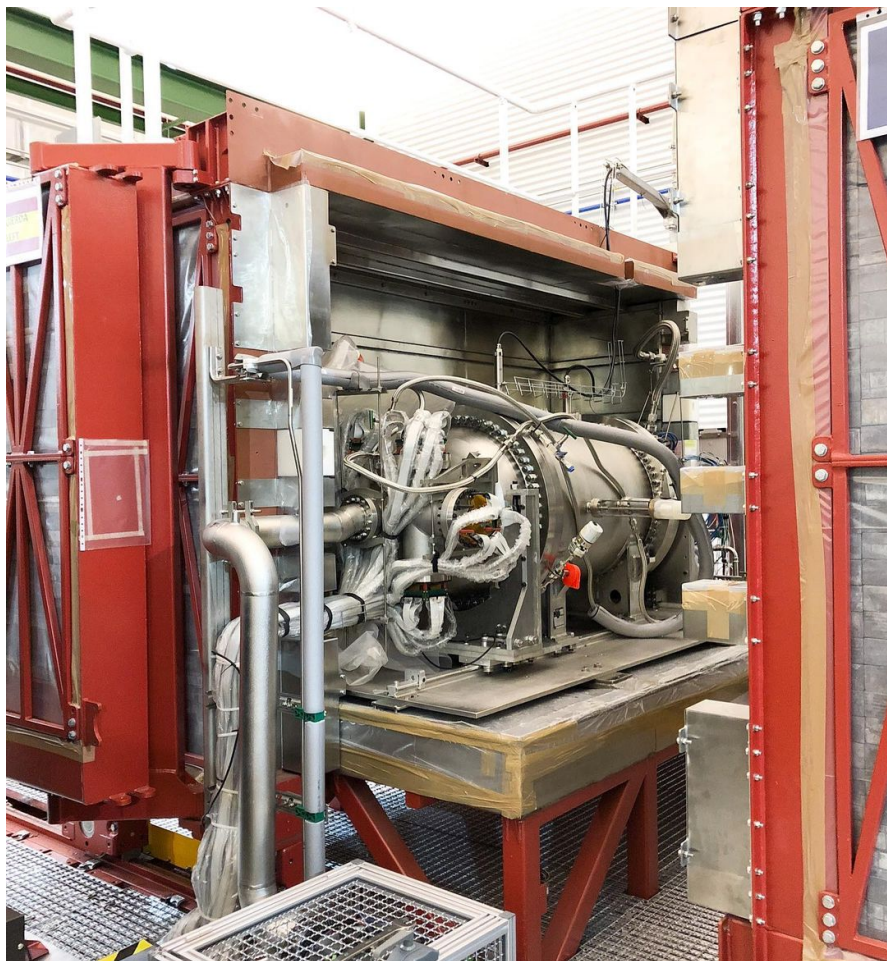


**Figure 3.8.** Picture of the detector Next-White sitting on its platform inside the LSC. The detector is seen from behind its tracking plane (anode side) with the lead castle used for shielding in its open position (painted in red). One can see the cables transmitting the SiPM signals to their specific front-end electronics. More details can be found on the electronics of the tracking plane in [135] and of the energy plane in [136].

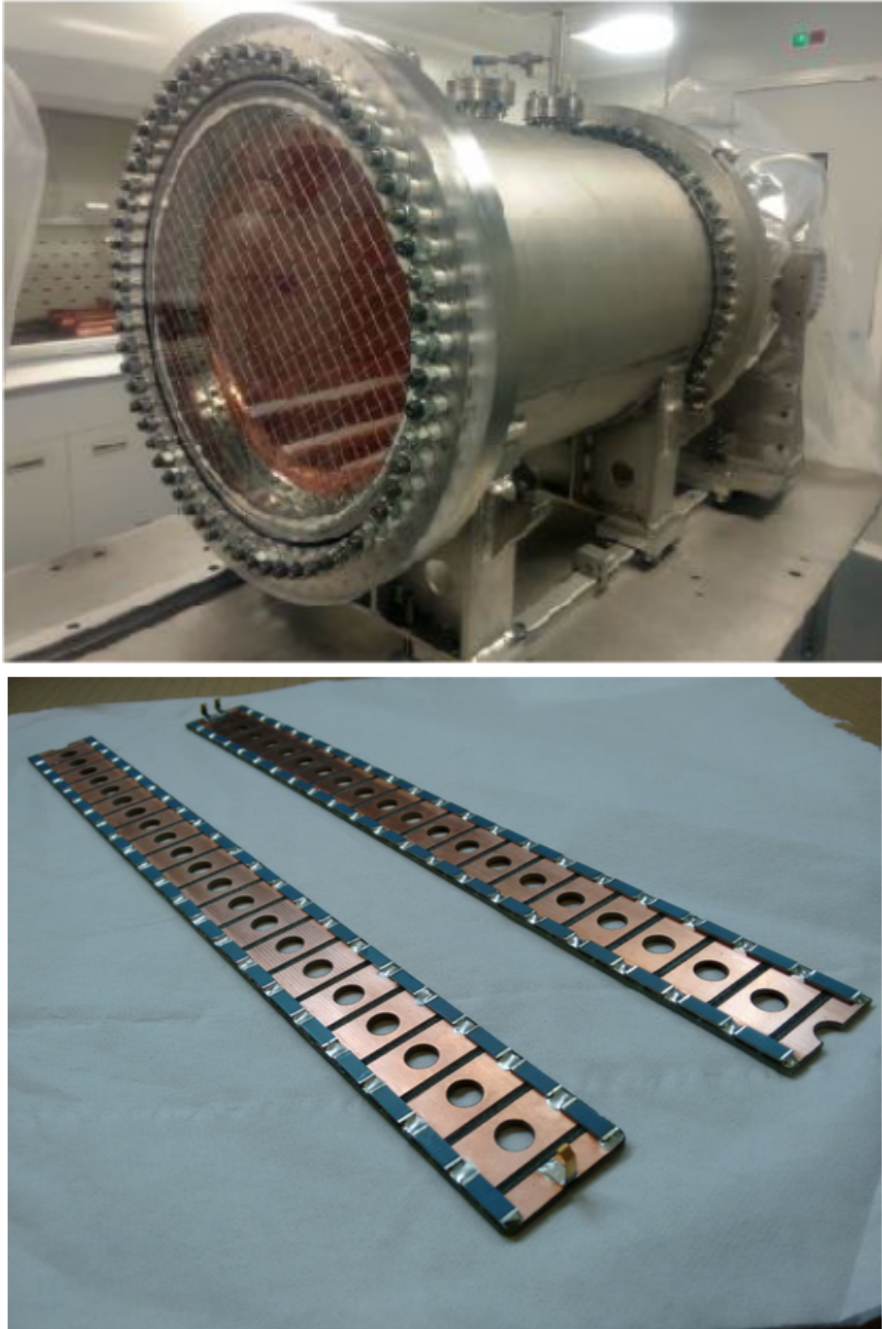


**Figure 3.9.** Acrylic end-cap built to troubleshoot the electrical components of the field cage under a 1.2 bar argon atmosphere (top). Resistor chain connecting the copper rings of the field cage together (bottom).



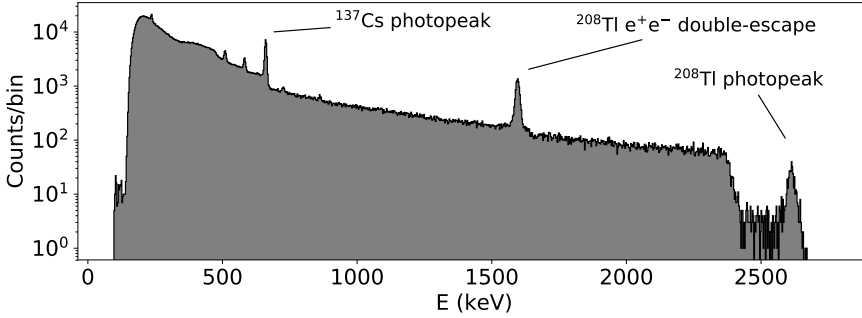


**Figure 3.10.** Full energy spectrum for calibration events provided by the  $^{137}\text{Cs}$  and  $^{228}\text{Th}$  sources. The spectrum is extracted from [140].

mented thanks to a dual trigger implemented in the Data Acquisition System (DAQ). Two sources were used for the high-energy calibration,  $^{228}\text{Th}$  placed in the upper part of the detector while lower energy calibration was performed with a more traditional source of  $^{137}\text{Cs}$ . The thorium sources provide gammas of 2.615 MeV which also give a double-escape peak resulting from a pair production ending with the two 511 keV gammas escaping the detector.

The detector was finally filled with the  $^{136}\text{Xe}$ -enriched gas (90%) on February 2019. In this last part that finished in July 2021 the detector took data to measure the half-life of the  $2\nu$  mode. In these last two runs the detector has shown an extremely good behavior with operating in a very stable state, with a low spark frequency and gas leak rate matching the expectations. In that respect it completely succeeded on the technical front.

On the side of performances NEXT-White achieved good results on three main areas. An energy resolution better than 1% FWHM at  $Q_{\beta\beta}$  was directly measured for the first time in a xenon-based detector [140], thanks to the fact that enough events at 2.6 MeV could be fully contained within the fiducial volume. The full spectrum recorded through the high-energy calibration campaign can be seen in Figure 3.10. The energy resolution at the energy of the thorium photopeak, 2.615 MeV, was measured to be  $0.91\% \pm 0.12\%$  FWHM.

The low-background run, which lasted 34.5 days, allowed comparison of the background rate measured against the predicted one

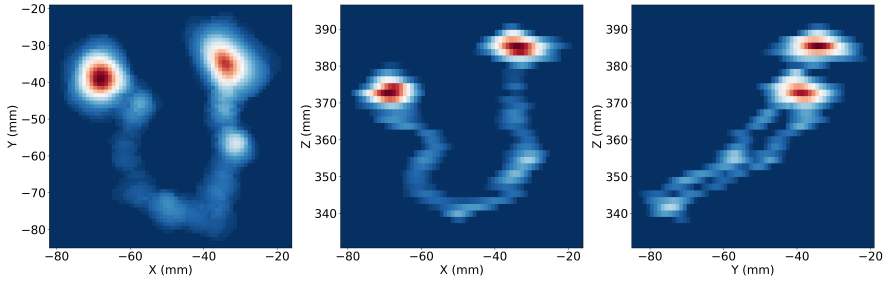


**Figure 3.11.** 2.0 MeV  $2\nu\beta\beta$  candidate after the Richardson-Lucy deconvolution. Data from NEXT-White [144].

that stemmed from a model which included four isotopes ( $^{40}\text{K}$ ,  $^{60}\text{Co}$ ,  $^{208}\text{Tl}$  and  $^{214}\text{Bi}$ ) and twenty-two detector volumes. The activity of each piece of the detector was simulated according to the radiopurity measurement campaign performed by the collaboration. Ultimately a good agreement between the data and the model was found [141]. The understanding of the background allowed the NEXT collaboration to measure the half-life of the  $2\nu$  mode via direct background subtraction [142]. The value reported is  $2.34^{+0.80}_{-0.46}(\text{stat})^{+0.30}_{-0.17}(\text{sys}) \times 10^{21}$  years. With a similar method the collaboration could obtain a lower limit on the half-life of the  $0\nu\beta\beta$  decay of  $5.8 \times 10^{23}$  years at 90% C.L. (preliminary result).

The last of the results of NEXT-White was to demonstrate the power of the background rejection based on the topological reconstruction [143]. To proceed, the signal-like events used were the 1.59 MeV double-escape peak of  $^{208}\text{Tl}$ , which was described in Section 3.3.1. On the other hand, the background events used were the Compton interactions of the 2.6 MeV gamma (also coming from  $^{208}\text{Tl}$ ) that had an energy of 1.59 MeV, the same energy as the double-escape peak aforementioned. By applying a Richardson-Lucy deconvolution algorithm the collaboration was able to achieve a very clean imaging of real  $2\nu\beta\beta$  candidate events [144]. An example of a  $2\nu\beta\beta$  candidate can be seen in Figure 3.11.

### 3.3.4 *NEXT-100*

The NEXT Collaboration is currently building the NEXT-100 which is the detector that will operate 100 kg of enriched xenon. The construction and commissioning of the detector was initially scheduled for the year 2021 but it has been delayed by several months due the COVID-19 crisis. An initial concept design report was published in 2011 [145]. It was followed a year later by a technical design report [146]. It has been mentioned that the detector will be roughly twice as big as NEXT-White, some parts can be directly reused or simply scaled up, but other parts need to be redesigned. In the following paragraphs the major changes with respect to NEXT-White will be outlined.

#### **Pressure vessel and passive shielding**

The pressure vessel has a cylindrical central section which is 160 cm long. Its inner diameter is 136 cm and its outer wall has a thickness of 1 cm. This central section is enclosed in two torispherical heads of 35 cm, inner diameter of 136 cm and wall thickness of 1 cm. The pressure vessel will feature a number of ports for the high voltage feedthroughs, calibration sources, gas inlets and outlets as well as for sensor connections.

An inner copper shield made of 40 bars of 12 cm thick radiopure copper will provide shielding of the inner volume against the radioactivity coming from the vessel. As for the radioactivity coming from the laboratory itself, the lead shield castle used for NEXT-White will be reused.

#### **Field cage**

One of the most troublesome parts to scale to a bigger detector are the components supposed to hold high voltages. Due to the higher drift length with respect to NEXT-White, a higher voltage needs to be set at the cathode. It is then expected to encounter very high electric fields locally which can cause electrical discharges. This could cripple the possibility to reach and hold the nominal voltages. Because of this the design and construction of the field cage and the high voltage feedthroughs need to be dealt with carefully.

The field cage consists mainly of a succession of 45 copper rings connected together by 12 resistor chains in order to degrade the voltage in the most uniform possible way across the inner part. The copper rings are embedded within a series of 20 HDPE struts which are also supporting 60 teflon reflector panels coated with TPB to improve light collection. The whole structure would then be wrapped in a layer of HDPE insulator. This design would reduce the amount of material used near the active volume which would translate to less radioactive background and less outgassing.

While the general design choices have been established, there are still some details that can be optimized thanks to electrostatic simulations. Because the field cage is enclosed within the inner copper shield that is electrically at ground, the field between those two elements is the one that can be problematic. Very high field regions are more likely to host an electrical breakdown while overall a high field region can produce some undesired electroluminescence light if the field is locally above the EL threshold.

An aximmetric COMSOL simulation of the field cage was done to see the impact of small changes on the field in areas of interest<sup>1</sup>. The geometry built in COMSOL assumes a simplistic toy-like cathode and EL stage because those are not expected to affect the field in the areas of interest. A map of the global potential can be seen in Figure 3.12. The material distribution is shown in the bottom image of Figure 3.13.

To minimize the unwanted light emitted outside of the active volume it is important to keep below the EL threshold in most of the area filled with xenon between the rings and the copper shield, and all of this assuming the 15 bar nominal pressure. The simulation shows, in Figure 3.14, that it can be achieved by minimizing the thickness of the HDPE insulator wrapping the field cage. Should a more drastic approach be required, the field cage diameter should be reduced, at the expense of the active volume.

In its final design, the inner diameter of the copper rings is 104.2 cm, with the teflon panels being 10 mm thick, for a total length of 140.7 cm which includes a buffer region of 26 cm. The insulator thickness was ultimately fixed to 6.35 mm. The minimal requirement being 4 mm to prevent effectively electrical breakdowns from connecting both sides.

---

<sup>1</sup>This work was done as a part of the present thesis.

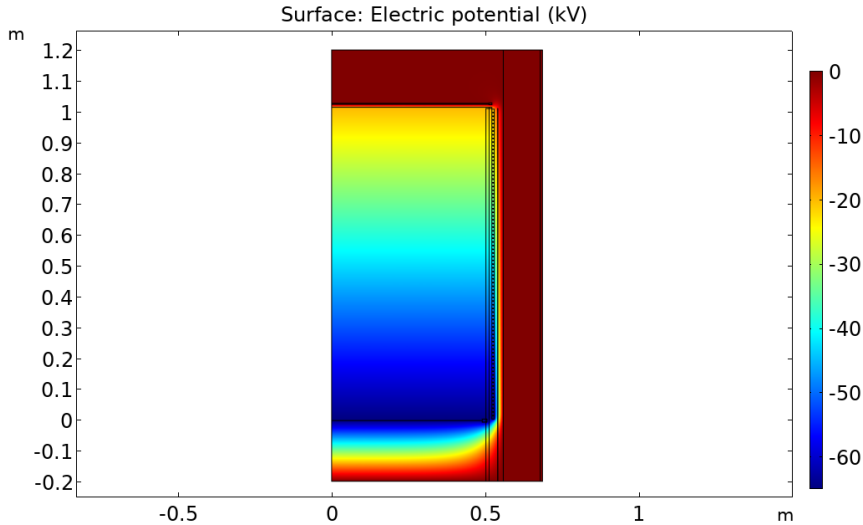


**Figure 3.12.** General 2D view of the COMSOL simulation of the electric field to study the impact design choices of the field cage. This figure corresponds to an early state of the field cage design.

A view of the final design can be found in Figure 3.15.

### Cathode and high voltage feedthroughs

The cathode high voltage feedthrough is required to deliver about 70 kV through the vessel that is at ground. To circumvent this challenge, the feedthrough will be introduced in the chamber from the anode side and will be wrapped around the field cage until reaching the cathode frame. In Figure 3.15, the feedthrough cable can be seen going around the field cage.

The cathode is a stainless steel mesh with a hexagonal pattern (hexagon sides are 5 mm) with a wire diameter of 125  $\mu\text{m}$ . These parameters ensure an optical transparency of 95%. The frame of the cathode has an inner diameter of 98.5 cm and an outer diameter of 102 cm. A picture of the cathode built and tensioned can be seen in Figure 3.16.

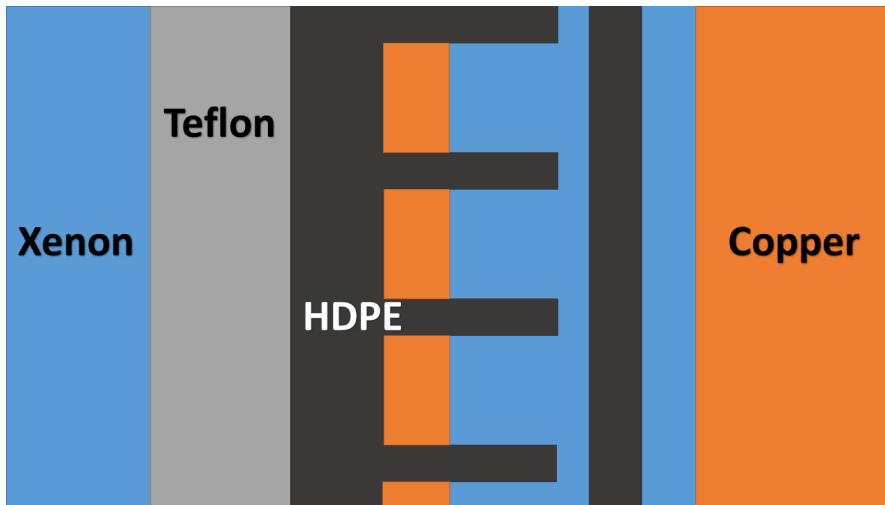


**Figure 3.13.** Material distribution in the COMSOL simulation. This shows the sector of the field cage where the HDPE struts are located (in black on the left). The insulator is also made of HDPE (in black but on the right). The copper inner shield is on the right (in orange), the copper rings are on the left in orange. The teflon reflective panels are on the side of the active volume and the rest of the image, in blue, represents the xenon gas.

### EL stage

The EL stage is perhaps the most sensitive part of the detector because the response of the detector results from the amplification of the signal there. As such, non-uniformity in the EL stage can translate to a degraded overall energy resolution and a distorted 2D response of the tracking. NEXT-White was originally running with a 5 mm EL gap; in order to improve the high voltage stability, this has been moved to 6 mm. For NEXT-100 an EL gap of 10 mm has been fixed.

The electrostatic forces applied to the mesh are expected to significantly deflect the mesh due to its increased size compared to NEXT-White. A compromise between transparency and mechanical robustness must be found but the collaboration explored a technique allowing to drastically limit the bending of a thinner mesh. The electrostatic deflection posts (ED posts) are HDPE pieces that will tension the mesh inside its surface. Thus reducing the maximum deflection the mesh

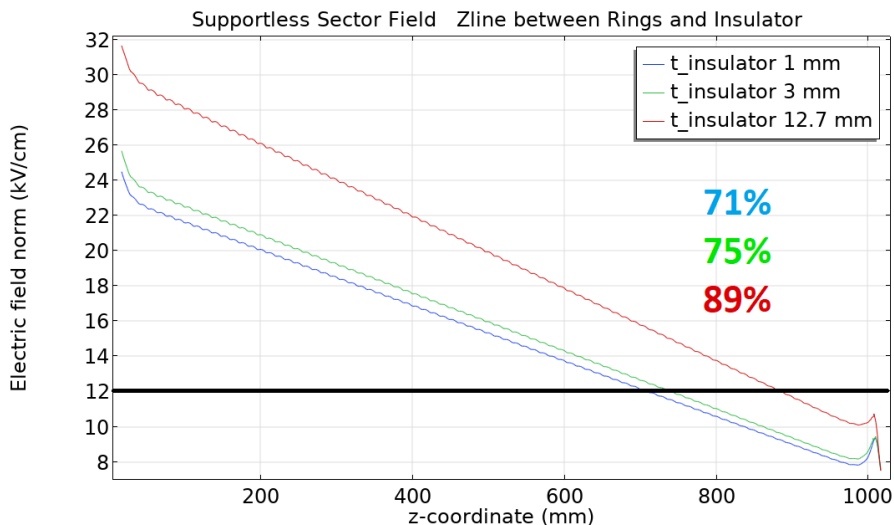


**Figure 3.14.** Norm of the electric field along a line between the field cage and the copper shield for different insulator thicknesses. The bump at the high- $z$  end is caused by the proximity of the EL structure. The black line is the threshold for electroluminescence at 15 bar in xenon. The percentages correspond to the fraction of the volume between the field cage and the insulator that is above the EL threshold.

will experience and consequently limiting the non-uniformity of the amplifying field. A drawing of the two pieces forming an ED post is shown in Figure 3.17 while the effect it can have on the bending is shown in Figure 3.18.

The EL stage being such a critical part of the detector, a contingency plan is being developed to replace the mesh with ED posts, should a failure happen. This contingency plan consists of a more traditional grid with thicker tensioned wires of stainless steel or tungsten coated with gold or platinum. With reservations concerning its radioactivity, tungsten could be more suitable than stainless steel because of its higher Young's modulus and yield strength. As such it deforms less than steel for a given applied force and its elastic regime spans a higher band which allows for it to withstand a more robust tensioning. As for gold and platinum coating they have a high work function which in principle reduces the probability of an electrical breakdown. They also

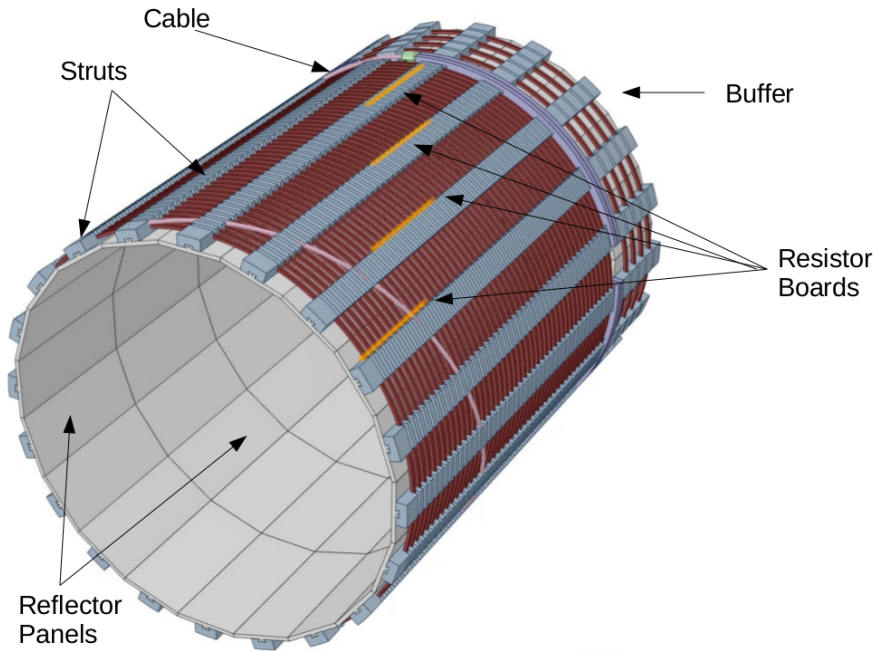


**Figure 3.15.** Drawing of the NEXT-100 field cage (left). It includes the teflon reflector panels, the HDPE struts supporting the copper rings connected by a series of resistor chain. The buffer is visible and is connected to the main part by the cathode frame. The cable providing the voltage to the cathode can also be seen wrapped around the field cage.

have higher reflectivity to VUV and short wavelength light in general which favors them over other materials.

### Tracking plane

The tracking plane of NEXT-100 will feature 56 DICE boards with 64 SiPMs each arranged in an  $8 \times 8$  matrix. The DICE boards are kapton boards embedding the SiPMs. The pitch will be increased to 1.55 cm compared to the 1 cm pitch of NEXT-White. This is because the increased number of channels leads to a volume of cables that need to fit the feedthrough. Also, unlike NEXT-White, and to reduce the amount of materials yielding background, the DICES will be covered





**Figure 3.16.** Picture of the tensioned cathode for NEXT-100. The hexagonal pattern of the grid can be seen.

with kapton only on one side instead of both sides to avoid using glue near the active volume.

### **Energy plane**

The energy plane of NEXT-100 will be composed of 60 Hamamatsu 3 inch R11410-10 PMTs for a coverage of approximately 37%. The model selected is the same that was used in NEXT-White. It has been established that most of the radioactive budget comes from the base circuit of the PMTs. For NEXT-100 a new design limiting the number of capacitors might reduce their contribution to the background index. The rest of the mechanical parts of the energy plane will remain similar,

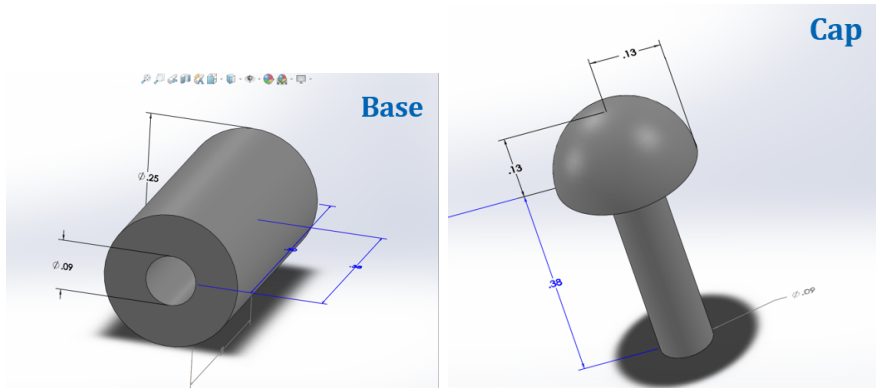


**Figure 3.17.** The two pieces forming the electrostatic deflection posts (ED posts). The base part (left) will sit between the gate mesh and the anode.

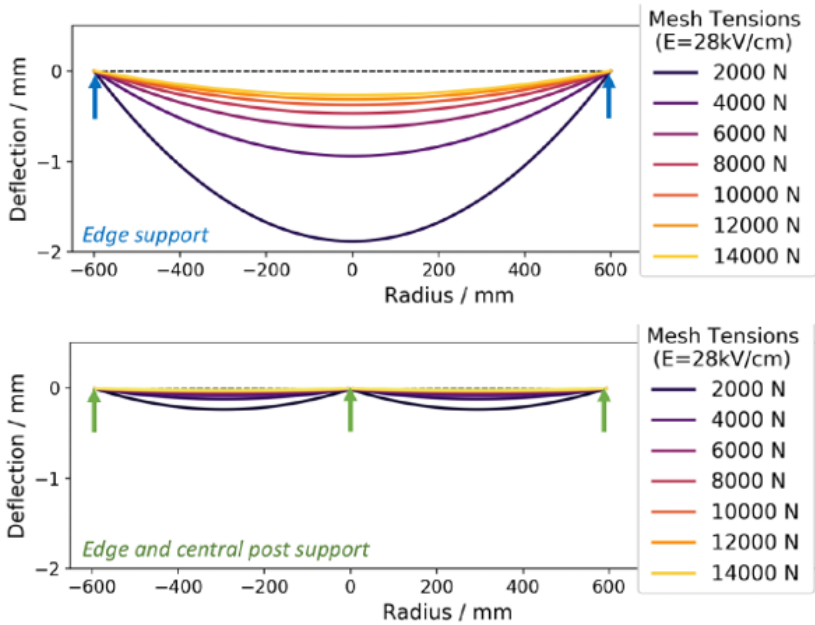


**Figure 3.18.** Numerical simulation showing the deflection of the mesh

albeit scaled up, to what they were in NEXT-White.

### Gas system

Operating the gas system of NEXT-White for a few years has taught the collaboration a few useful lessons that can be implemented on NEXT-100. The necessity to avoid dead spots in the gas flow is helped by moving the pressure vessel gas inlet behind the energy plane. As the gas outlet is behind the tracking plane it allows for a more uniform flow within the detector. It can have a positive effect on the uniformity of the electron lifetime in the active volume. Another takeaway from NEXT-White is that it can be needed to reverse the gas flow. To account for this possibility the gas system of NEXT-100 will feature a bypass system that will allow doing this without having to open the detector. A last minor change will consist of adding a number of additional gas lines to the pressure vessel. This is to improve the gas recovery time.

## 3.4 Towards the tonne scale: NEXT-HD and NEXT BOLD

In order to achieve a sensitivity covering the whole inverted mass hierarchy, the NEXT collaboration aims to reach a tonne scale and possibly beyond. Its outline to follow this plan is based on a conservative, yet highly competitive, tonne detector named NEXT-HD (High Definition) followed by a more "aggressive" design that could achieve a background-free regime: NEXT-BOLD (Barium atOm Light Detection).

### 3.4.1 NEXT-HD

NEXT-HD can be seen as the prime version of the NEXT design. It is made possible mainly thanks to the experience gained over the years in operating high pressure xenon TPCs and thanks to the current maturity achieved by the SiPM technology. The detector will be built at the LSC starting in 2026, following the operations of NEXT-100. Its purpose is to achieve a sensitivity better than  $10^{27}$  years [109].

Unlike the previous NEXT detectors, NEXT-HD will be a symmetric vertical TPC. This design makes the cathode grid the center of the detector with two anodes at the bottom and at the top of the

detector. Each anode comes with its own EL stage which defines then two back-to-back drift regions. The active volume will be a cylinder of 3 m long for 2.2 m diameter. The maximum drift length would then be 1.5 m which would obviously not degrade the topology as much as a maximum drift length of 3 m. This is one of the advantages of a symmetrical design in order to achieve a high-definition tracking.

The tracking planes will be instrumented by a number of the order of  $10^5$  SiPMs arranged with a pitch between 5 and 10 mm (which still is to be decided). The use of a low-diffusion mixture alongside the dense enough sensors array would allow for a high-definition tracking ensuring that an optimal topological background rejection is achieved. For comparison NEXT-White had 1792 SiPMs with a 10 mm pitch and NEXT-100 will have 3584 SiPMs with a 15.6 mm pitch. Accommodating the very high number of channels of NEXT-HD will require a high effort on optimizing the electronic circuits. For this purpose ASICs are being designed within the collaboration. Another of the premier benefits coming with this design, is that by removing the PMTs from the energy plane their radioactive contribution vanishes. By getting rid of the major contribution to the radioactive budget NEXT-HD would be able to reduce its background index by an order of magnitude.

But on the flip side, getting rid of the PMTs means that an alternative way to reach the same light collection for  $S1$  and for  $S2$  must be found. In order to perform a proper calibration on the fly (à la NEXT-White), it is needed to detect reliably the elusive  $S1$  signal of the point-like  $\text{Kr}^{83m}$  events which gave a total of about 10 photoelectrons per event.

For NEXT-HD the approach consists of collecting the light with a dense array of double-clad wavelength-shifting optical fibers located on the walls surrounding the active volume of the TPC. A schematic view showcasing this approach can be found in Figure 3.19. The wavelength of the VUV photons is first shifted by the TPB coating to blue light. The blue photons are then absorbed and re-emitted as green photons inside the fibers [147, 148]. The green photons are then trapped inside the fiber by total internal reflections [149]. They propagate to the end of the fiber where they are read by light sensors, most likely SiPMs, located at both ends of the fiber. Some preliminary estimations tend to give a photon detection efficiency about 2% better

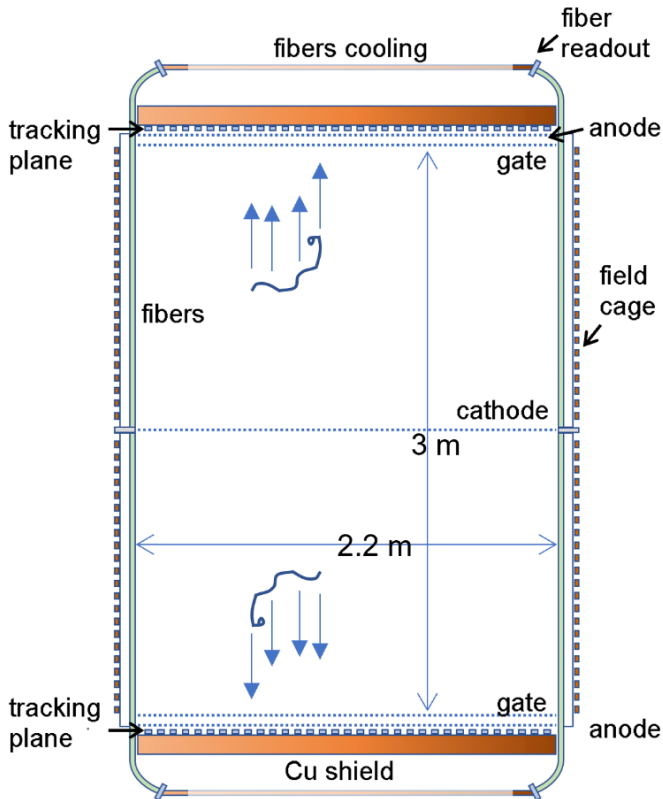


**Figure 3.19.** Schematic drawing of the working principle of the envisioned NEXT-HD detector. The two tracking planes mark the end of the two drift regions from either side of the cathode. The optical fibers are increasing the light collection.

than the one achieved in NEXT-White. If these estimations can be met in practice then this approach can lead to a calorimetric measurement with an improved energy resolution with respect to NEXT-White.

### 3.4.2 NEXT-BOLD

As experimentalists aim for a sensitivity to higher half-lives, more mass is needed coupled with even less background than the previous generation of experiments. The constant endeavour of reducing

background appears however to be increasingly challenging. But an approach based on tagging the daughter nucleus of a double beta decay can potentially lead to a background-free experiment. There is no known process other than a double beta decay that can generate a doubly charged barium cation  $Ba^{2+}$ . So a background-free detection of a neutrinoless double beta decay in a detector would appear as the conjunction of an unambiguous detection of a  $Ba^{2+}$  ion together with an event whose energy would be precisely measured to be compatible with  $Q_{\beta\beta}$ . Because of this consideration, implementing in a detector a functioning barium tagging technique together with a good enough energy resolution would ensure a background-free experiment.

Barium tagging relying on the fluorescence imaging of the atomic transitions of  $Ba^+$  has been suggested for liquid and solid xenon but appears to be impracticable for gaseous xenon due to the low recombination and the doubly charged barium being the dominant species. It has been suggested in 2015 by Dave Nygren [150] that a monolayer of fluorescent molecular indicators can reliably perform barium tagging in a high pressure xenon atmosphere. These molecules are used in Single-Molecule Fluorescence Imaging (SMFI). They change their fluorescence response to light stimulation when they capture ("chelate") a specific ion within their molecular structure. The proof-of-concept resolved individual  $Ba^{2+}$  ions on a scanning surface [151, 152]. This result was achieved in an aqueous solution with a fairly low concentration of molecular indicators. An effort has been made to identify candidate molecules suitable for operation in a dry phase like in a high pressure xenon TPC [153]. More recently a group inside the NEXT collaboration successfully engineered a molecule suitable for barium tagging in a high pressure TPC [154]. This molecule, called FBI (Fluorescent Bicolor Indicator), not only has a much brighter response in its chelated state, but its response is also done at a different wavelength which increases dramatically the separation power of the SMFI technique between the chelated and unchelated states. An illustration of this property can be seen in Figure 3.20.

Building on these promising results the NEXT collaboration aims to construct a first detector, NEXT-BOLD (Barium atOm Light Detection), capable of tagging barium ions on the fly with high accuracy. This new design would diverge to some extent from the traditional NEXT detector design. It will implement a Barium Tagging Detector that will

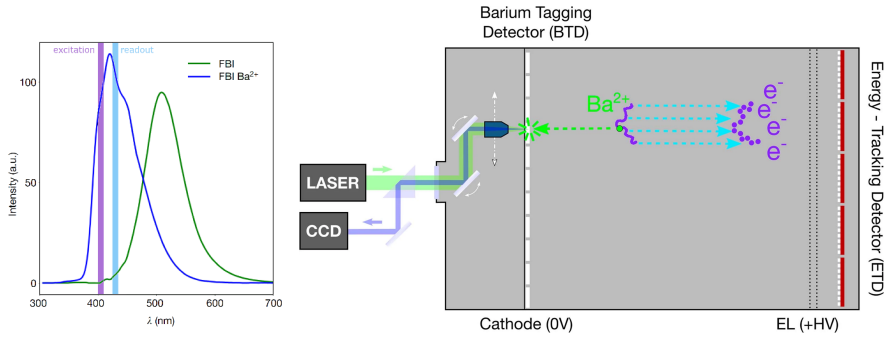


**Figure 3.20.** Different response of the FBI molecule in its chelated and unchelated state (left). Scheme showing the NEXT-BOLD concept (right) where a double beta decay in the TPC leaves a track of secondary electrons drifting towards the energy-tracking plane and a much slower drifting barium ion that can be detected by the Barium Tagging Detector. These figures are extracted from [154].

be deployed behind the cathode and consists of an array of sensors at ground potential coated with a layer of the target molecule for SMFI. These sensors will be scanned by a fast laser microscopy system, able to establish the presence of a trapped barium ion with a very high signal-to-noise ratio.

On the anode side of the chamber will be an energy-tracking plane capable of measuring the energy accurately while reconstructing the 3D topology of the events. Upon receiving a  $\beta\beta$ -like signal with an energy falling in the ROI, the Barium Tagging Detector will be set in motion, expecting to detect a barium ion within a time window defined by the drifting properties of ions in the xenon gas. This delayed coincidence between the classic  $\beta\beta$ -like signal and a barium-positive signal on the tagging system would virtually kill all radioactive backgrounds. A schematic view of this concept can be seen in Figure 3.20. Should this concept prove to be successful the NEXT collaboration would build a number of background-free modules allowing for a sensitivity better than  $10^{28}$  years.

### 3.5 Summary

In the landscape of  $0\nu\beta\beta$  searches the NEXT collaboration has been developing high pressure xenon TPCs over the last decade. The strengths of this type of detector essentially lies in an intrinsic sub-percent energy resolution at  $Q_{\beta\beta}$  and in accessing the event topology for further background rejection. The NEXT collaboration has successfully demonstrated its prowess at building and running detectors of increasing scale.

It started with two prototypes using 1 kg of xenon: NEXT-DEMO and NEXT-DBDM. These were used to validate the choice of the sensors used in the detector: PMTs for calorimetry and SiPMs for tracking. The success of the most recent prototype NEXT-White proved the validity of the design choices in terms of detector performance. Next-White paved the way for its successor, NEXT-100, that will take over after its commissioning later this year.

The collaboration aims to be competitive and relevant in the field of searching for  $0\nu\beta\beta$  decay and finding the Majorana nature of the neutrino. Currently major R&D efforts revolve around NEXT-HD and NEXT-BOLD, notably with barium tagging. The endgame for the NEXT experiment is to achieve a background-free experiment which would then be the best candidate for further exploring the normal mass hierarchy and measuring half-lives of  $10^{28}$  years and beyond.



# *Low-diffusion mixtures* 4

In a high pressure xenon TPC such as those developed by the NEXT experiment, the background rejection based on the energy measurement is greatly enhanced by a topological-based background rejection. An electron loses its energy within the active volume mostly by ionizing and exciting the ambient xenon atoms. As its energy tends to zero, its energy loss per unit of length ( $dE/dx$ ) increases and it ends up losing the remainder of its energy within a small volume due to multiple scatterings. Therefore, the topology of a single electron event features a distinct track ending with a "blob-like" structure while a two electron event features a distinct track ending with two "blobs", one for each electron. This topological difference is the tool used to distinguish a single electron background event with an energy falling in the region of interest from a double beta event.

This technique relies on the ability to correctly reconstruct and identify the topological features of the events. However, while drifting, the secondary electrons constituting a track are diffusing in all directions and this diffusion blurs the features of that track. In view of constructing a tonne-scale detector with a maximum drift length of 1.5 m, diffusion becomes a major threat to the topology reconstruction and therefore to the background rejection. That is why one of the main lines of research within the NEXT experiment was to find a suitable low-diffusion gas mixture, ie a mixture showcasing low diffusion and competitive energy resolution. An illustration of the impact of diffusion on a simulated double beta decay event is shown in Figure 4.1.

This chapter expands on the effort made by the collaboration and focuses on the proposal to use helium as an additive to xenon which is the central subject of the work developed in this thesis.

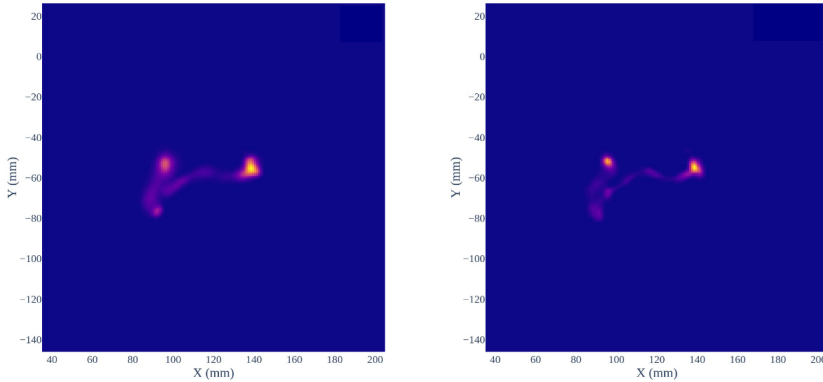


**Figure 4.1.** A simulated event reconstructed from a detector with a high-diffusion mixture on the left and with a low-diffusion mixture on the right. The end-points are unambiguously visible with the low diffusion. This figure showcases the effect diffusion can have on the topology reconstruction.

## 4.1 Microphysics of electron transport

The physics of the drift and diffusion of electrons in gas is the cornerstone of the working principle of gaseous proportional counters such as TPCs. It is fundamentally important for the NEXT experiment because the topology-based background rejection relies on the retrieved track information, which is heavily affected by the drift and diffusion of the electrons in xenon.

### 4.1.1 Transverse and longitudinal diffusion

At first approximation a swarm of secondary electrons can be described by the classical kinetic theory of gases [155]. The energy distribution of the electrons follows a Maxwellian distribution. Once an electric field is applied the root mean square (RMS) dispersion along any dimension is [156]:

$$\sigma = \sqrt{2D/v} \quad (4.1)$$

where  $D$  is the field dependent diffusion coefficient and  $v$  is the drift velocity of the electron swarm. The latter is a function of the reduced electric field, electric field over pressure, noted  $E/P$ .

This picture assumes that the electrons reach an equilibrium with the atomic gas by balancing the energy gained from the action of the electrical field with the energy lost through elastic collisions with the atoms. It is obvious that these transport parameters depend heavily on the gas used. The energy transfer happening in an elastic collision depends of the mass ratio between the two particles colliding. So assuming isotropic scattering, the averaged fractional energy loss is approximately:

$$\frac{2mM}{(m + M)^2} \quad (4.2)$$

where  $m$  is the mass of an electron and  $M$  is the mass of an atom of the gas. So we can already see that because xenon is the most massive of the noble gases that can be used in a TPC, it is the one with the highest diffusion of them all. This is very well documented experimentally [157].

It is also to be noted that the diffusion parallel to the field behaves differently than the diffusion transverse to the field [158, 159]. The reason is that the collision frequency of electron-gas is an energy dependant quantity. In most cases the collision frequency increases with energy. So an electron diffusing along the drifting direction will be ahead of the average electron of the swarm and locally have more kinetic energy which makes it go through more collisions and reduce its instantaneous velocity. On the other side, an electron lagging behind the average electron of the swarm will have less energy so it will experience less collisions allowing it to increase its instantaneous velocity from the action of the field. These two effects occurring simultaneously will tend to narrow the electron swarm and therefore effectively reduce the diffusion parallel to the electric field with respect to the thermal diffusion (which corresponds to the transverse diffusion). In the case where the collision frequency decreases with energy this effect is reversed and the longitudinal diffusion will be higher than the transverse one.

One thing to note when looking at the momentum transfer cross section is that all the noble gases heavier than neon feature a non monotonic behavior with a minimum called the Ramsauer minimum [160]. The Ramsauer minimum of xenon can be seen in Figure 4.7 belonging to Section 4.4. This non classical phenomenon is important

to consider for noble gas mixtures because at some energies the electron elastic scattering against one gas species can dominate that of the other gas.

But gaseous detectors do not all use solely noble gases. In fact, most of them use mixtures of a noble gas with molecular gases [161]. The additional degrees of freedom provided by the composite structure of the molecule allow for some specific kind of inelastic collisions to occur at low energy (between 0.1 and a few electronvolts typically) [162]. It leads the drifting electrons to have access to other channels than elastic collisions to lose their energy. With the typical energies drifting electrons have, they are most likely able to put the molecules in a vibrational or rotational state. As a result, the diffusion in molecular gases is very low compared to noble gases. The impact of molecular gas admixtures is detailed in greater depth in Section 4.3.

The electron transport properties in a gas are directly inherited from the energy distribution of the electrons. When working with gas mixtures a small change of composition can hence dramatically change the transport parameters.

#### 4.1.2 *MagBoltz and PyBoltz*

In order to simulate the electron transport properties for a given set of conditions, a handful of solutions have been made available in the past decades. The most popular computer program developed for this purpose is Magboltz developed by Steve Biagi [163].

As the electron swarm follows the Boltzmann equation, the first versions of Magboltz [164, 165] were solving it with Legendre polynomial solutions truncated to the third term to improve the drift velocity accuracy to better than 1%.

A significant change was made in 1999 to improve the simulation performance [166]. Since then, Magboltz relies on Monte-Carlo integration which has the advantage of making the accuracy solely dependant on the computation time instead of the solution used to solve the Boltzmann equation.

The Monte-Carlo method basically follows one test electron on a collision by collision basis and makes the reasonable assumption that the behavior of an electron swarm arises from the summation of the behavior of all its electrons independently. The detailed description

of the method can be found in [156] but its principle is summarised here. Given an initial position, direction and energy, an electron accelerates freely between two collisions. Once a collision occurs, by using random numbers, the program computes the new direction and its corresponding energy. The formulas to compute the direction (polar and azimuthal angles) must take into account the fact that the elastic scattering are not necessarily isotropic. The full equations can be found in the description of the Monte-Carlo method by Fraser and Mathieson. In the simplified case of isotropic scattering the polar and azimuthal angles are given respectively by

$$\begin{aligned}\theta &= \arccos(1 - 2R_\theta) \\ \phi &= 2\pi R_\phi\end{aligned}\tag{4.3}$$

where  $R_\theta$  and  $R_\phi$  are random numbers generated between 0 and 1. For noble gases all the collisions can only be elastic at the energy considered, so the fractional energy loss of an electron on a collision is:

$$(e_{pre} - e_{post})/e_{pre} = \frac{2mM(1 - \cos\theta)}{(M + m)^2}\tag{4.4}$$

where  $m$  is the electron mass,  $M$  is the atom mass, and  $e_{post}$  and  $e_{pre}$  are respectively the post and pre collision energies.

This method is very precise on paper but appears to be extremely demanding on the computation time which limits its efficiency. This is because for real gases the collision frequency  $\nu$  is velocity-dependant. Between each collision the time of free flight, noted  $t_{coll}$ , has to be computed with the following expression where  $R_t$  is a random number generated between 0 and 1:

$$\ln \left[ (1 - R_t)^{-1} \right] = \int_0^{t_{coll}} \nu(t) dt\tag{4.5}$$

The "null collision" is an artifice used to avoid computing an integral for each collision. It consists of choosing an arbitrary velocity independent collision frequency,  $\nu'$ , high enough to exceed the real collision frequency over the velocity interval of the electron between two collisions. A corresponding time of flight  $\tau$  is computed using Equation 4.5 which now does not require to compute an integral. At the time of the collision the electron has accelerated to a specific velocity  $v$ . At this

velocity the frequency of null collision is defined by  $\nu' - \nu(v)$  which is a known quantity. These null collisions leave the direction and energy of the electron unchanged. The nature of the collision (real or null) is decided stochastically: the probability of a real collision is  $\nu(v)/\nu'$  and consequently the probability of a null collision is  $1 - \nu(v)/\nu'$ , both are known quantities.

In the recent years, Magboltz has been rewritten in Python [167]. The Python version of Magboltz is named Pyboltz [168].

### 4.1.3 Degrad

Degrad is the sister software of Magboltz developed by Steve Biagi [169]. It is a Monte Carlo simulation for the interactions of minimum ionizing particles and X-rays in gaseous detectors. It runs for a given mixture, electric field and magnetic field. The primary particle (X-ray or electron), its energy and initial direction as well as the number of events to run can be selected according to the needs of the user.

The program simulates the interactions of the primary and the subsequent secondaries. After all the secondaries reach the thermalisation energy, set by the user, the program retrieves the number of excitations per energy level and the number of ionizations for each of the gas species involved and for each event. The user can access the detailed information for each event but the program also computes the Fano factor for ionizations as well as the average energy spent per ionization. Similar numbers are also computed for excitations.

For the purpose of finding a low-diffusion mixture suitable for NEXT, Degrad is a tool useful to evaluate the effect of additives on the intrinsic energy resolution of a mixture and on the primary scintillation properties of that mixture.

### 4.1.4 Garfield++

Garfield is a software originally developed in Fortran to simulate electrons drift in gaseous drift chambers [170]. It has been rebuilt in C++ by Heinrich Schindler under the name of Garfield++ in order to improve its performance and flexibility [171]. Even though Garfield++ can compute analytically the electric field in some very simple geometries, it is also possible to import electric potential field maps in

3D. These 3D field maps can be computed with third party finite element solvers such as COMSOL [172], Elmer [173] or Ansys [174]. That makes Garfield++ a powerful tool to simulate a specific and complex setup.

Garfield++ includes Magboltz which comes with the electron-atom and electron-molecule cross sections and can be used to compute the electron transport parameters for specific conditions. There are two ways to compute electron drifts in Garfield++. First by using the macroscopic transport coefficients (separately computed by Magboltz) to compute the drift lines and avalanches. In this method a step of a given length depending on the local field and the corresponding drift velocity is calculated and then a random diffusion step is sampled according to the diffusion coefficients corresponding to the local electric field.

The second method, named AvalancheMicroscopic, consists of tracking microscopically electrons on a collision by collision basis, in which case the calculation uses the relevant electron-atom (or molecule) cross section imported from Magboltz and the "null collision" method described in Section 4.1.2. This method is deemed to be more accurate but more demanding on computing power. It is also possible to retrieve much information on each real collision, such as its type (elastic, excitation, ionization, etc...), the energy pre and post collision, etc...

All of this makes Garfield++ a flexible tool that can be used to study the electroluminescent behavior of a given mixture in a given amplification setup.

## 4.2 Pure xenon

Pure xenon is logically the baseline mixture of the NEXT detectors. One of the main assets of xenon, besides the fact that its isotope 136 is a double beta emitter and a potential neutrinoless double beta emitter, is that in its gaseous form it has a Fano factor that has been measured to lie between 0.13 and 0.17. Such a low Fano factor means that the intrinsic energy resolution is better than 1% FWHM at  $Q_{\beta\beta}$ . This energy resolution is key in order to distinguish a background  $\beta\beta$  from a potential signal  $0\nu\beta\beta$  event. But as seen through the previous

chapter, the other main asset of the NEXT detector concept is the ability to reject background based on the topology of the reconstructed event. Topology reconstruction that is, as mentioned in Section 3.2.2, undermined notably by diffusion. That makes understanding the electron transport properties of xenon critical.

The high mass of a xenon atom with respect to the mass of a drifting electron makes the elastic collisions particularly inefficient to cool the electrons, that is to reduce the temperature of the electron swarm. Most measurements of the transport parameters in xenon have been made at low pressure [175–180]. The drift velocity and longitudinal diffusion have been measured before on the prototype NEXT-DEMO [115, 131] and NEXT-DBDM [133]. But the transverse diffusion, however, appeared to not be measurable on that detector. On the one hand the light spread was dominating the transverse spread of the electron cloud, given the short drift length. And on the other hand the detector's SiPMs density was too low.

In the recent years the detector NEXT-White has been running in the Canfranc Underground Laboratory (LSC). The detector is described more thoroughly in Section 3.3.3 and in the following publication [134]. It is in short a 10 kg high pressure xenon EL TPC. While NEXT-DEMO drift length was roughly 30 cm, NEXT-White features a 53 cm drift length. This makes the latter suitable to measure all the electron transport parameters in high pressure xenon, including the transverse diffusion. Part of that study [138] will be detailed in the following paragraphs<sup>1</sup>.

#### 4.2.1 Data production

In the NEXT-White detector the point-like events used to calibrate the detector response as well as to measure the transport parameters are provided by a rubidium source. The  $^{83}\text{Rd}$  decays by electron capture to  $^{83m}\text{Kr}$ . This source is commonly named a krypton source. The krypton emanates from the source in the gas flow and spreads uniformly inside the detector. It decays to its ground state with a lifetime of 1.83 hour by emitting two consecutive electrons for a total energy of 41.5 keV. This cascade is shown in Figure 4.2. At the pressure at which the detector

---

<sup>1</sup>The work done for the present thesis includes a minor contribution to this study, in the data taking, simulation work and calculation of the drift velocity.



is operated such events appear as point-like monochromatic energy deposition.

Within Run 2 of NEXT-White two data taking campaigns were done specifically to measure the transport parameters in high pressure xenon. Within these sub-runs (they will be referred to as runs) the only radioactive source used was the rubidium one that produces the krypton events described above. The first run (run A) was taken at the intermediate pressure of 7.2 bar between the 13th of September 2017 until the 19th of September 2017. The second one (run B) was taken at 9.1 bar between the 22nd of October 2017 until the 29th of October 2017.

The voltage on the gate defining the EL field was set constant at 7.0 kV for run A and 8.5 kV for run B. These voltages were chosen so as to maximize the light collected while keeping the detector in a safe running mode. These voltages set a reduced EL field of respectively 1.63 and  $1.56 \text{ kV} \cdot \text{cm}^{-1} \cdot \text{bar}^{-1}$  for run A and B. As the transport parameters are mostly a function of the drift field the data were taken for various cathode voltages ranging between 16 to 28 kV for run A and between 21.5 kV and 29.5 kV for run B. A summary of the datasets used for this measurement can be found in more details in the corresponding publication.

To evaluate the robustness of the analysis, a set of Monte-Carlo data were generated by NEXUS [181], the Geant4 [182] simulation toolkit of the NEXT collaboration.

#### 4.2.2 Data selection and reconstruction

The detector triggers on the krypton  $S_2$  signal seen by the PMTs and records the waveforms of the PMTs and SiPMs. The PMT waveforms are first deconvolved from the electronic effects before being processed by the analysis software framework of the NEXT collaboration, *Invisibles Cities (IC)* [183].

A peak finder algorithm stores the information of the  $S_1$  and  $S_2$  peaks identified according to the parameters used for each type of peak. Only the events displaying exactly 1  $S_1$  and 1  $S_2$  are kept for the analysis. An additional requirement is set which consists of having at least one SiPM collecting an amount of light distinguishable from its dark count at room temperature.

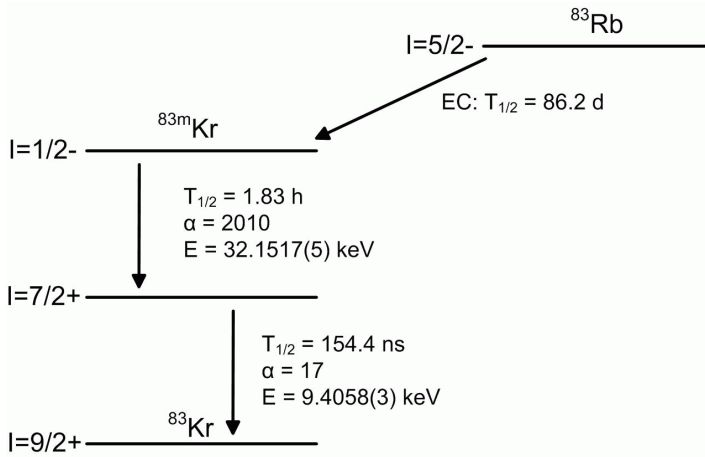


**Figure 4.2.** Scheme of the decay cascade leading to the Kr events used for point-like calibration.

Once the krypton event has been identified, its 3D position is computed. The  $x$  and  $y$  coordinates are defined as the mean of the activated SiPMs positions weighted by the integrated light they collected over the  $S2$  duration. The  $z$  position is defined by multiplying the drift velocity by the drift time. The drift velocity is obtained by measuring the drift time for events coming from the only known distance in the detector: the cathode position. And the drift time is obtained by subtracting the rising time of the  $S2$  with the one of the  $S1$ .

To ensure the quality of the dataset a radial cut of 150 mm is performed to avoid border effects. Before a cut on the energy of the events is applied, it is needed to correct the measured energy to account for the electrons being captured by impurities across their drift. The signal decreases exponentially as a function of the drift time:

$$E = E_0 e^{-t/\tau} \quad (4.6)$$

where  $\tau$  is the lifetime of the secondary electrons. The lifetime is computed for each dataset as it varies with the ever evolving purity of the gas and with the drift field. After all the selection cuts have been made only 23% of the recorded events are kept for the analysis.

### 4.2.3 Drift velocity

As mentioned above the drift velocity is fairly straightforward to obtain as it just requires measuring the drift time for a known distance. The bulk of the events producing a measurable signal happen inside the fiducial volume which is delimited by the radial cut of 150 mm in the XY plane and by the gate and cathode in the z-axis. So the maximum drift time corresponds to events originating from the cathode (in the left panel of Figure 4.3) hence the drift velocity is given by:

$$v_d = \frac{Z_{cath}}{t_{max}} \quad (4.7)$$

However since the drift time is defined as the time between the maximum of the  $S1$  and  $S2$  signals, it is necessary to twist the above expression a bit. The  $S2$  of a point-like event is the convolution of a diffusion-induced gaussian with a square function. So the maximum is reached after a time  $t_{EL/2}$  when the centroid of the electron swarm is halfway through the EL gap. Therefore the expression of the drift velocity needs to be changed to:

$$v_d = \frac{Z_{cath}}{t_{max} - t_{EL/2}} \quad (4.8)$$

Because no reliable estimation of the time  $t_{EL/2}$  can be extracted from the data, it has been evaluated by performing Magboltz simulations. Given the size of the EL gap in NEXT-NEW, 6 mm, and the drift velocity within the EL gap computed by Magboltz, the following numbers were assigned to  $t_{EL/2}$ :  $0.806 \pm 0.006 \mu s$  for run A and  $0.852 \pm 0.008 \mu s$  for run B. Together with the drift distance  $Z_{cath} = 530 \pm 2.0$  mm the drift velocity could be computed for each of the conditions spanning the data taking campaigns.

The results can be found in the right panel of Figure 4.3. A small consistent discrepancy is observed between the data and the values predicted by Magboltz, the data being on average 1.2% higher. A possible explanation might be the non uniformity of the drift field near the cathode. The field becoming significantly higher close to the wires.

An outcome of this measurement is to validate the fact that the drift velocity can consistently be expressed as a function of the reduced electric field which means that one can extrapolate the data to higher operating pressure.

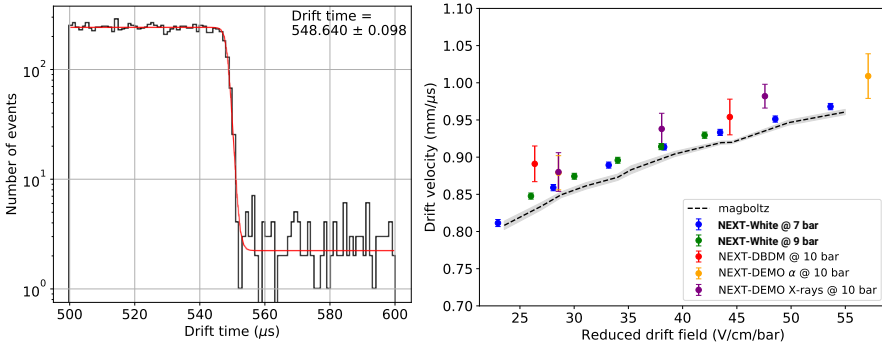


**Figure 4.3.** Drift time distribution end-point for the run at 7.2 bar and  $54 \text{ V cm}^{-1} \text{ bar}^{-1}$ . Drift velocity as a function of the reduced drift field (right). Previous works and Magboltz are also included.

#### 4.2.4 Longitudinal diffusion

The details of the analysis performed to compute the diffusion coefficients is beyond the scope of this section but is detailed in the parent publication [138]. But some context will be provided. The longitudinal diffusion is extracted from the properties of the  $S2$  signals through two different methods.

The first one consists of dividing the chamber in a set of drift time slices and computing a mean  $S2$  waveform for each of these slices over all the events selected. Each of these mean waveforms is the convolution of the diffusion spread at their given drift time with the light spread induced by the EL stage. The light spread induced by the EL can be extracted from the mean waveform corresponding to the first drift time slice. The diffusion spread can be extracted for the mean waveforms corresponding to all the drift time slices. Finally the diffusion coefficient,  $D_L$ , is retrieved from the spread equation:

$$\sigma_t^2 = \sigma_{t_0}^2 + 2 \frac{D_L}{v_d} t_{drift} \quad (4.9)$$

The other method consists of computing the gaussian spread of each  $S2$  signal and sorting them against the drift time. A linear fit is enough to retrieve the diffusion coefficient.

The resulting reduced diffusion coefficients are shown in the left panel of Figure 4.4.

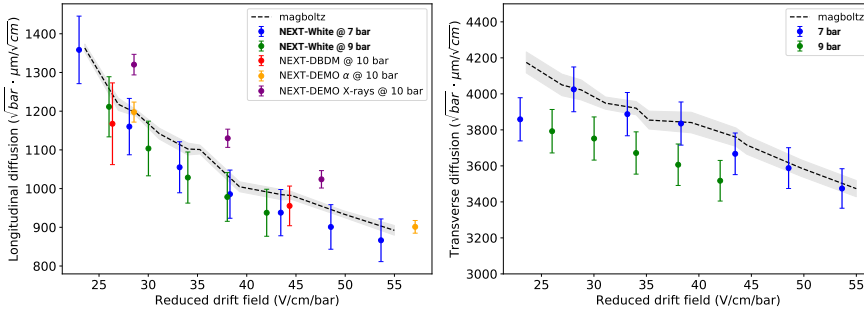


**Figure 4.4.** Reduced longitudinal diffusion (left) and reduced transverse diffusion (right) as a function of the reduced drift field. Previous works and Magboltz are also included.

#### 4.2.5 Transverse diffusion

The transverse diffusion is obtained following a method similar to the mean waveform method described above. The mean point spread function (PSF) is computed for each drift time slice and the diffusion component is isolated for the high drift time with respect to the PSF at low drift times.

The resulting reduced diffusion coefficients are shown in the right panel of Figure 4.4.

### 4.3 Molecular gas admixtures

The most straightforward solution to reduce the diffusion is to use molecular gases as dopant of the xenon. These gases are commonly used in the TPCs supposed to function at high rate, with charge amplification and where tracking is the primary goal (for example in collider experiments).

#### 4.3.1 Molecule additive impact on electron drift in EL TPC

The typical molecules used in TPCs provide two main features. The first one is that they cool the electrons very efficiently because the molecules considered have a good number of low energy rotational and vibrational degrees of freedom. The cross sections of electron collisions with methane are given as an example in Figure 4.5. Those energy

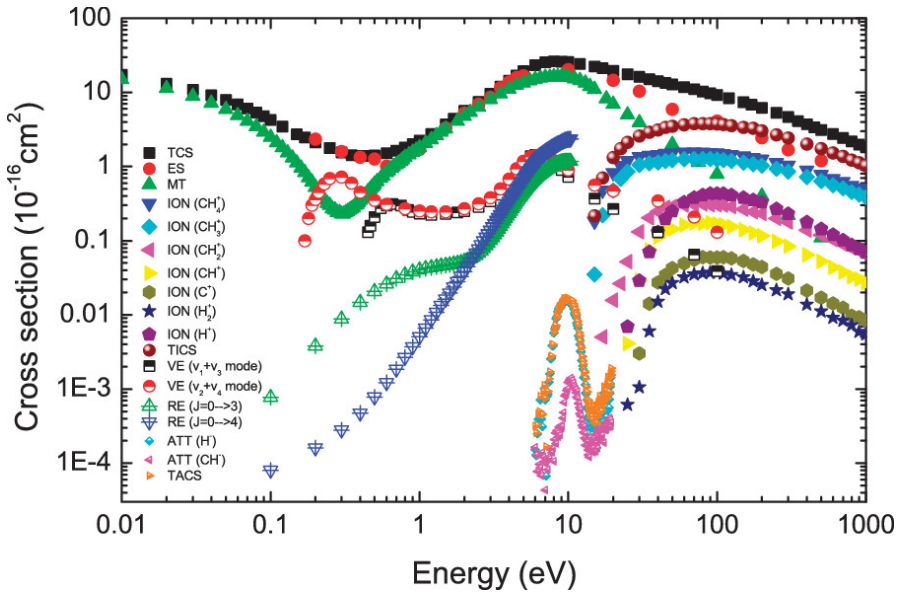


**Figure 4.5.** Summary of cross sections for electron collisions with methane. Taken from [184]. TCS - total scattering, ES - elastic scattering, MT - momentum transfer, ION - partial ionization, TICS - total ionization, VE - vibrational excitation, RE - rotational excitation, ATT - dissociative attachment, and TACS - total dissociative attachment.

levels are widely covered by the energy range of the drifting electrons in a TPC. Despite the fact that the cross section for electron-molecule elastic collisions is higher than the inelastic low energy collisions, the kinetic energy loss is much more efficient in the latter case. So overall, even a small amount of additive is enough for the energy loss process to be dominated by the inelastic collisions. This feature is a strong asset in the framework of NEXT TPCs because it results in the diffusion coefficients being close to the thermal diffusion limit.

The second feature is less of an asset for electroluminescent TPCs. In a TPC that is amplifying its signal through charge multiplication for high flux applications, the VUV light produced may trigger a lot of photoelectric effect potentially increasing the risk of high voltage breakdown, and limiting the stability of these detectors. Molecular gases are used in these TPCs partially for their VUV quenching capabilities. The VUV quenching comes from a few concurrent effects: the

cooling efficiency reduces the frequency at which the electrons gain enough energy to excite noble gas atoms, excimer quenching, photon absorption and electron attachment.

In the context of NEXT detectors where the light produced is used for tracking and calorimetry, the minimization of the quenching effect is crucial while the maximization of the cooling effect is desired.

One quick note regarding a spin-off project initiated by the NEXT Collaboration is the investigation of a mixture of xenon with trimethylamine (TMA:  $\text{N}(\text{CH}_3)_3$ ) [185]. The two form a Penning mixture in which the excited atoms of xenon can transfer their energy by ionizing the TMA molecules. This effect results in a Fano factor lower than the one of pure xenon effectively improving the energy resolution with the added benefit of a very low diffusion [186]. This however comes at the cost of the primary scintillation and secondary scintillation of xenon which make this mixture beyond the scope of this thesis.

#### 4.3.2 Molecules tested by the NEXT Collaboration

The three molecules of interest evaluated to be possible options for a low-diffusion NEXT TPC are: carbon dioxide, methane and carbon tetrafluoride ( $\text{CO}_2$ ,  $\text{CH}_4$  and  $\text{CF}_4$  respectively). Magboltz simulations show [187] that not more than 1% of admixture would be enough to lower the diffusion to near thermal level in the case of  $\text{CH}_4$ .  $\text{CO}_2$  and  $\text{CF}_4$  do not require more than a tenth of that value. Their effect on diffusion were to be expected given the arguments given in the previous section. But the impact of these gases on the light yield remains to be carefully evaluated. Simulations tend to show that fine tuning of the gas quantity could minimize the light quenching to an acceptable level [188].

Within the NEXT collaboration, the group based in the University of Coimbra in Portugal used a "driftless" Gas Proportional Scintillation Counter (GPSC) [189] to test the light yield of candidate gas mixtures.

The first study focuses on  $\text{CO}_2$  [190] while the second study added  $\text{CH}_4$  and  $\text{CF}_4$  [191]. A degradation of the light yield is seen when increasing the amount of admixture but the pattern of this degradation is not the same for  $\text{CH}_4$  and for the two others. But to identify the best admixture together with the best concentration, the study balances the

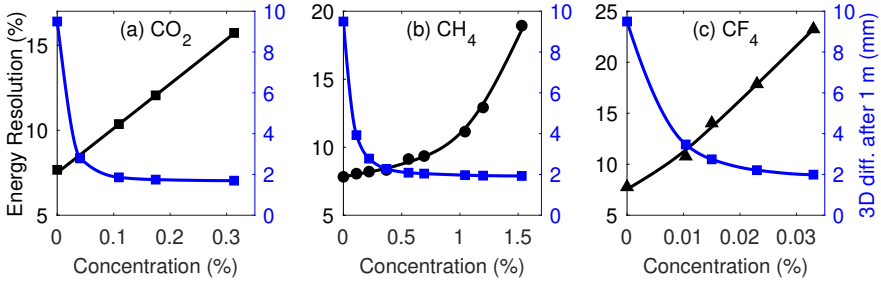


**Figure 4.6.** Energy resolution measured (black) and 3D diffusion spread after 1 m computed by Magboltz (blue) as a function of the additive concentration. The panel (a) is for CO<sub>2</sub>, (b) is for CH<sub>4</sub> and (c) is for CF<sub>4</sub>. The measurements were done with a reduced amplification field of 2.5 kV cm<sup>-1</sup> bar<sup>-1</sup> and the simulated diffusion spreads were obtained for a mixture at 10 bar and under a field of 200 V/cm. Taken from [191].

light production with the energy resolution and the expected diffusion according to Magboltz simulations shown in Figure 4.6.

The work concludes that CF<sub>4</sub> and CO<sub>2</sub> should not be favored due to the high impact the dissociative attachment has on energy resolution. It is also more complicated to monitor such a small fraction of gas in a big gas system, and self transparency to VUV light could not be assured for a CO<sub>2</sub>-Xe mixture.

For the reasons mentioned above, CH<sub>4</sub>, despite its higher excimer quenching appears to be the most favorable molecule but its quenching may also hurt the primary scintillation down to a level that could hinder the 3D reconstruction.

#### 4.4 Helium-Xenon mixtures

It has been proposed within the NEXT collaboration to mix xenon with helium [192]. Unlike the molecular gases helium is a noble gas. This has many implications regarding the two main characteristics of a TPC, namely diffusion (tracking) and light yield (energy resolution). In short it is believed that a fairly small amount of helium could drastically improve the diffusion with no trade off in terms of energy resolution. But operating a TPC with a helium-xenon (HeXe) gas mixture would also have some implications and challenges in other



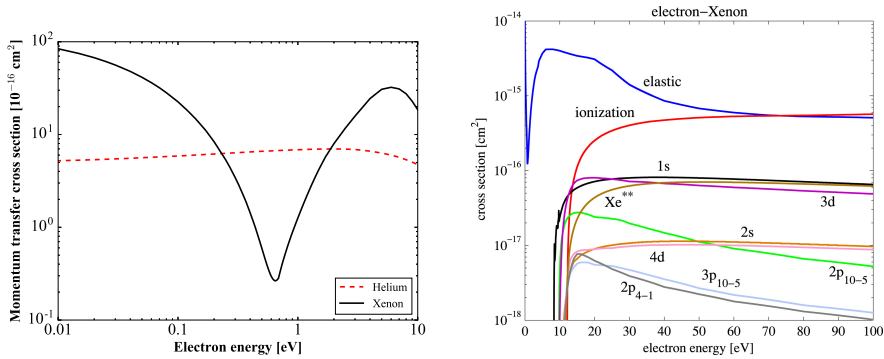


**Figure 4.7.** Electron-xenon (black line) and electron-helium (red line) elastic momentum transfer cross sections as a function of the electron energy (left). Data extracted from [193]. Simplified version of the cross sections of electron collisions with xenon for a wider energy range (right). Panel taken from [188].

areas. In the following, the HeXe mixtures will be referred to by their percentage of helium concentration.

#### 4.4.1 Diffusion and drift velocity

First of all, just like with xenon, the electrons can only interact with helium atoms through elastic collisions. When looking at Table 4.1, we see that the mean momentum transfer in helium-electron collisions is almost two orders of magnitude higher than for xenon-electron collisions. This is due to the mass of a helium atom and of an electron being that much closer than for the xenon-electron couple. The outcome is that helium-electron collisions are much more efficient at cooling the electrons than xenon-electron collisions.

However one could expect that because the xenon population dominates largely the helium population, the impact of a helium addition would be too small to be relevant. That is because naively the collision frequency depends on the density and the size of the atoms, both favoring xenon. But while the helium-electron cross section remains fairly constant between 0.01 eV and 10 eV, the xenon-electron cross section scattering features a Ramsauer minimum peaking at 0.7 eV. This can be seen by superposing the two electron-atom cross sections on the same panel as is done in the Figure 4.7. The typical

|    |                      |
|----|----------------------|
| He | $2.74 \cdot 10^{-4}$ |
| Ne | $5.44 \cdot 10^{-5}$ |
| Ar | $2.75 \cdot 10^{-5}$ |
| Kr | $1.31 \cdot 10^{-5}$ |
| Xe | $8.07 \cdot 10^{-6}$ |

**Table 4.1.** Mean fractional energy loss of electrons in collisions against noble gas atoms. Calculated using Equation 4.2.

energy of drifting electrons in NEXT TPCs extends to up to 2 eV and has a local maximum slightly below 1.5 eV as can be seen on Figure 4.8. All of these energies are where the helium-electron collisions dominate (by a maximum of an order of magnitude). Thanks to this behavior we expect that a fairly minimal addition of helium would be enough to translate to a helium-like diffusion.

As an initial work to evaluate the diffusion in these mixtures, a handful of Magboltz simulations were run. The numbers are computed for a set of conditions that has been reported to be nominal for a NEXT TPC. So the pressure was set at 15 bar and the drift field spans the typical set of values that are used in TPC from 50 V/cm up to 600 V/cm.

The diffusion coefficient is commonly given in the units of  $[m^2/s]$  but in the framework of drift chambers they are often written as units of  $[mm/\sqrt{m}]$  which corresponds to the dispersion per  $\sqrt{m}$  of electron drift and simply computed as follow:  $\sqrt{\frac{2D}{v_z}}$  where D is the diffusion coefficient in units of  $[cm^2/s]$  and  $v_z$  being the drift velocity. These are the units used in this section.

The simulations confirm that the transverse diffusion is drastically reduced in HeXe mixtures with respect to pure xenon. The evolution of the transverse diffusion coefficient with the helium concentration is shown in the left panel of Figure 4.9.

But there is a notable difference in behavior between the transverse and longitudinal diffusion as it has been detailed in Section 4.1.1. The longitudinal diffusion coefficient is heavily influenced by the electron

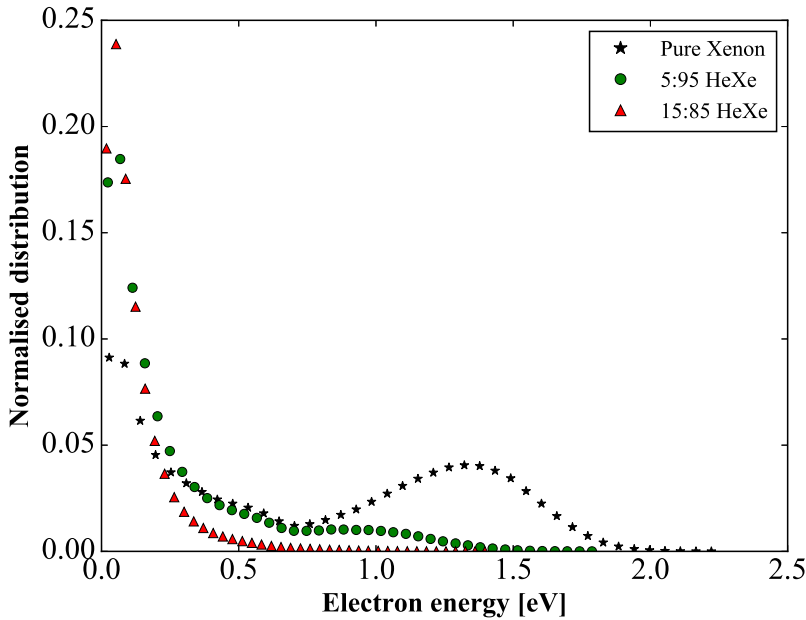


**Figure 4.8.** Normalised energy distribution of drifting electrons at 400 V/cm and 15 bar computed by Magboltz for three mixtures. Comparing the distributions in pure xenon (black) and in the 5% and 15% HeXe mixtures (green and red respectively) shows the cooling effect of helium.

energy distribution when there is a Ramsauer minimum as is the case for xenon. In short the more the energy distribution is on the left of the Ramsauer minimum (towards lower energies), the higher the longitudinal diffusion coefficient is expected to be with respect to the transverse diffusion coefficient. As a side note this is why increasing the field tends to reduce the longitudinal diffusion: it moves the energy distribution towards the right of the minimum and higher energies. But since the addition of helium also impacts the energy distribution by cluttering it on the left of the Ramsauer minimum, the longitudinal diffusion remains fairly high when compared to the transverse diffusion at the fields considered. But as can be seen on the right panel of Figure 4.9, for the typical drift fields (superior to 300 V/cm) the longitudinal diffusion remains basically unchanged

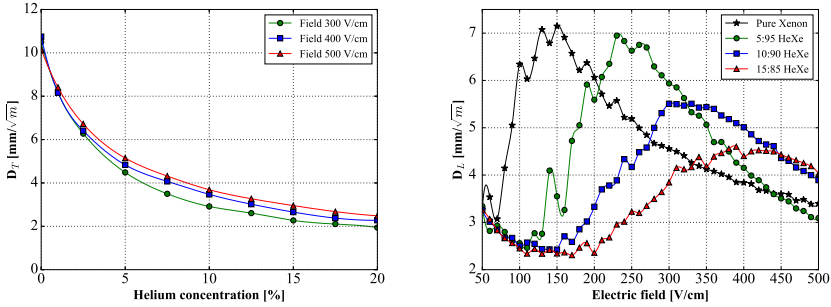


**Figure 4.9.** Transverse diffusion coefficient in HeXe mixtures as a function of the helium concentration (left) for three different electric fields. The absolute pressure remains the same across all mixtures: 15 bar. Longitudinal diffusion coefficient in pure xenon and in three HeXe mixtures as a function of the electric field (right).

with respect to pure xenon.

Regardless, a 15% HeXe mixture appears to provide a major improvement on the diffusion, reducing its transverse component 5 fold with respect to pure xenon. This HeXe mixture is therefore deemed the most promising low-diffusion mixture.

The drift velocity of the drifting electrons is not the most crucial parameter impacting the performance of the TPC. But increasing it may allow for a shorter buffer duration which could reduce the volume of data on the storage. It would also have a minor positive impact on the electron lifetime at a given gas purity level. As such, and given their simulated drift velocities that are shown in Figure 4.10, the HeXe mixtures are also appealing on that front.

A preliminary study to measure the drift velocity and the longitudinal diffusion in HeXe mixtures has been carried out by the NEXT group at University of Texas Arlington in the United States [194]. These measurements are in good agreement with simulations.

#### 4.4.2 Energy Resolution

It has been detailed in the previous chapters that the energy resolution is a central performance number for all the  $0\nu\beta\beta$  experiments. Not

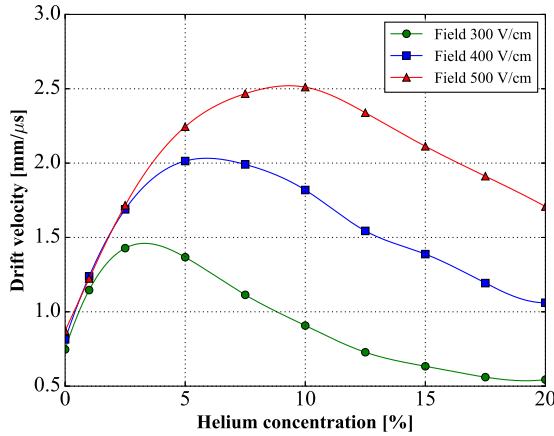


**Figure 4.10.** Drift velocity in HeXe mixtures as a function of the helium concentration for three different electric fields. The absolute pressure remains the same across all mixtures: 15 bar.

only does it reduce the size of the ROI, but it is also the only way to separate a  $0\nu\beta\beta$  candidate from a  $2\nu\beta\beta$  event.

The energy resolution of a proportional scintillation counter is the summation of different terms accounting for different phenomena: the fluctuation in the production of the charge carriers, the fluctuation in the production of EL light and the fluctuation in the light detection. Only the first two terms are specific to a transparent mixture.

### Secondary electrons production

The first term accounts for the variance in the production of secondary electrons. The variance of the ionization is given by:

$$\sigma_e^2 = \frac{FE}{w} \quad (4.10)$$

where  $F$  is the Fano factor and  $w$  is the average energy needed to produce one ionization. The combination of these two numbers defines the intrinsic limit of energy resolution for a given mixture at a given energy  $E$ . The Fano factor and the  $w$  value typically do not vary sizeably for energies higher than the binding energy of the K-shell of xenon (34 keV).

The Fano factor for pure xenon is reported broadly to be close to 0.17 while the average energy spent by a primary in an ionization is about 22 eV. In order to evaluate how these numbers evolve with an addition of helium we use the software Degrad introduced in Section 4.1.3.

Running the simulation also requires considering the potential Penning ionization transfer that can occur between an excited helium atom and a xenon atom. The Penning ionization transfer is the mechanism responsible for the Fano factor improvement and scintillation quenching of TMA-xenon mixtures mentioned in Section 4.3.1. But in the case of HeXe mixtures it is the helium that is losing its excited atom population to xenon ionizations so for a xenon based mixture the effect can be expected to be minimum. Evaluating the probability of Penning ionization to take place is not a trivial effort and no measurement has ever been made in high pressure HeXe mixture.

A few considerations can however help to make a plausible estimation. Among all the collisions between helium atoms and other noble gas atoms it is xenon that is the most likely to lead to a Penning ionization transfer per collision [195]. The lifetime of excited helium atoms is very long compared to other species: the triplet state  $2^3S_1$  lifetime has been measured to be around 131 min [196] while the singlet state  $2^1S_0$  lifetime is 19.7 ms [197]. In a high pressure HeXe chamber, for all intents and purposes, we can then expect that all the excitations of helium atoms will lead to ionizations of xenon atoms. This guess is most likely accurate given the conclusions made for argon-xenon mixtures [198] and the experiments carried on helium-neon and helium-argon mixtures [199].

The results of Degrad are shown in the Figure 4.11. Despite the conclusion of the previous paragraph and for the sake of completeness, the study was made for the two extreme cases where Penning ionization probability is set to 0 and to 1. This was done as a mean to conclude that the potential uncertainty on the Penning transfer does not affect the outcome with respect to finding a suitable low-diffusion mixture for a NEXT detector. The  $w$ -value of a HeXe mixture is bounded by its value in pure xenon, around 22 eV, and its value in pure helium, around 46 eV. The Fano factor however will slowly improve towards lower values with Penning ionization. But all in all the difference remains extremely small compared to pure xenon for the

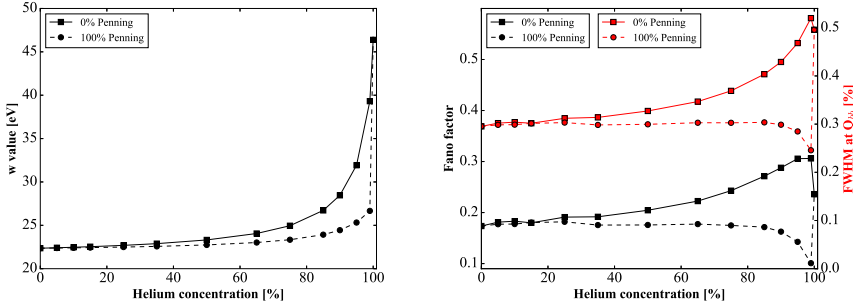


**Figure 4.11.** Average energy loss per ionization (left) and Fano factor (right) against the helium concentration in a HeXe mixture at 15 bar as computed by the Degrad in a zero field scenario. The right panel also includes in red the intrinsic energy resolution at  $Q_{\beta\beta}$ . The solid line corresponds to the extreme case where Penning transfer is disabled while the dashed line corresponds to the likely case of perfect efficiency in Penning transfer.

HeXe mixtures with up to 20% helium. These mixtures overlap those deemed to be the most efficient at lowering the diffusion according to the results shown in Section 4.4.1. Using Equation 3.6 we can compute the intrinsic resolution of the mixture which is unsurprisingly left unchanged for the mixtures of interest.

### Electroluminescence

The second phenomenon playing a role in the energy resolution is the variance induced by the way the signal is amplified. In an optical TPC such as the one used by NEXT the signal is amplified by electroluminescence (EL). Because of its low variance the energy resolution achievable is very close to the intrinsic one described previously.

In a similar fashion as the Fano factor we can define the Q-factor to measure the fluctuations of the EL process:

$$Q = \frac{\sigma_{EL}^2}{N_{EL}^2} \quad (4.11)$$

where  $N_{EL}$  is the average number of photons produced by a single electron crossing the EL stage and  $\sigma_{EL}$  is the variance of that process.

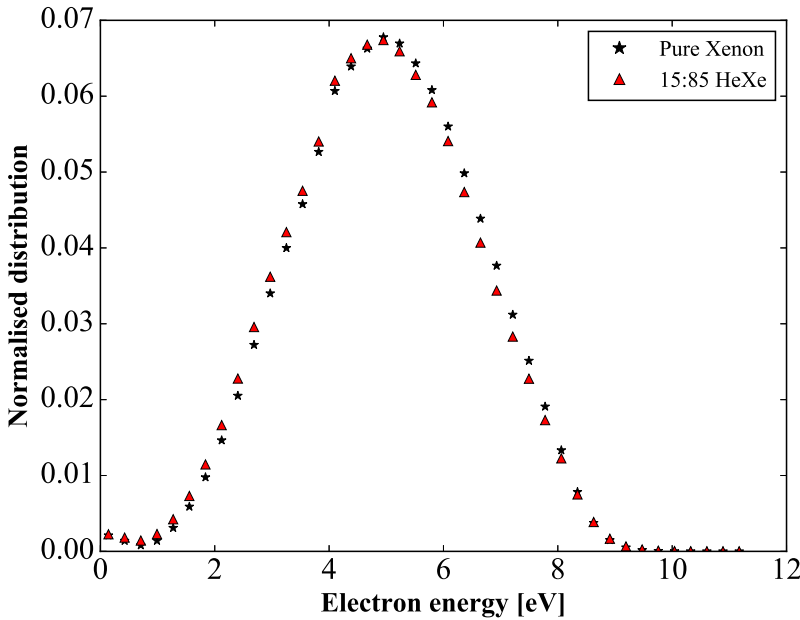


**Figure 4.12.** Normalised energy distribution of drifting electrons at a reduced field of  $2.5 \text{ kV cm}^{-1} \text{ bar}^{-1}$  ( $37.5 \text{ kV/cm}$  and  $15 \text{ bar}$ ) computed by Magboltz for pure xenon (black) and 15% HeXe (red).

The advantage of using the Q-factor as a figure of merit is that it adds up directly with the Fano factor in the energy resolution formula 3.6:

$$R_E = 2.35 \sqrt{\frac{w}{Q_{\beta\beta}} [F + Q]} \quad (4.12)$$

According to the previous equations it is obvious that to improve the energy resolution one should maximize the light yield while minimizing the variance of the EL. Studies on energy resolution for pure xenon have shown that increasing the amplifying field lowers the variance up to the certain point where some ionizations kick in [117]. Despite increasing the light yield, those ionizations also dramatically increase the variance. This is why charge amplification is not used in NEXT, it would degrade significantly the energy resolution.



Therefore we can assume that, by design, the secondary electrons never gain enough energy to ionize xenon atoms, which consequently set the maximum energy they can reach below 12.13 eV, the first ionization state of xenon. This is far below the 19.8 eV corresponding to the first excited state of helium. So in the EL amplification stage of the detector, the only way electrons ever interact with helium atoms is through elastic collisions. And if we take a look once again at the elastic cross sections of xenon and helium with electrons we can expect that for energies above 2 eV the xenon collisions are dominating the helium collisions. In the EL stage then, a HeXe mixture would behave like a xenon mixture. This is confirmed by looking at the normalised energy distribution of electrons drifting through an EL stage for pure xenon and for a 15% HeXe mixture, the comparison can be seen in Figure 4.12.

Comparing with the molecular admixtures mentioned in Section 4.3, there is no concurrent channel to lose energy except the suppressed elastic collisions with helium. We expect an extremely marginal degradation of the variance at similar conditions with respect to pure xenon. So in conclusion, these arguments hint that the energy resolution should not deteriorate by moving to a HeXe low-diffusion mixture.

A simulation model was set in order to quantify these considerations. Based on Garfield++ AvalancheMicroscopic class detailed in Section 4.1.4. We used the simple simulation model for noble gases [200] that has been used to study the energy resolution of pure xenon for a NEXT detector [117]. It assumes that, at the pressure of interest, each excitation leads to a photon being emitted. This assumption appears to be valid with an accuracy better than 5% and has the advantage of avoiding the complication of simulating the microphysics of the atomic cascade [188].

The workflow followed was to first produce one field map for each EL field considered with the COMSOL electrostatic module. Since this study only focuses on the property of the mixture itself, the COMSOL geometry is extremely simple: it consists of two blocks put together: one for the drift region and one for the EL region so the field in both blocks are perfectly uniform. Originally the EL gap was 5 mm so this study assumes that the EL block has a height of 5 mm but in the more recent design it is 10 mm. The drift block has dimensions corresponding to a maximum drift length of 1 mm. To compute the potential the

medium in both blocks is set to have a dielectric constant of 1, which can be approximated to gaseous xenon. The lateral boundaries of the block union have periodicity conditions. The voltage assigned to the top of the EL block is set to ground (anode), the voltage assigned to the boundary separating the two blocks is the one that defines the EL field and goes as  $E^* \times 5 \text{ mm} \times 15 \text{ bar}$  with a negative polarity, where  $E^*$  is the desired reduced electric field. The voltage assigned to the bottom of the drift block is set to ensure a drift field of 400 V/cm in all the field maps produced. The reduced field goes from  $1.0 \text{ kV cm}^{-1} \text{ bar}^{-1}$  up to  $5.0 \text{ kV cm}^{-1} \text{ bar}^{-1}$  with a step of  $0.25 \text{ kV cm}^{-1} \text{ bar}^{-1}$ . A mesh file is also exported, it gives the coordinates of the nodes corresponding to the potential values given in the field map file.

These files are then fed to Garfield++ which associates the desired mixture to the domains defined in the field map. The mixtures probed are the 5%, 10% and 15% HeXe mixtures as well as pure xenon at 15 bar. An electron is generated with an initial energy of 1 eV and a random initial direction in the middle of the drift region. The reason to let the electron drift for 0.5 mm before reaching the EL stage is to ensure that the electron comes into the amplification stage from a realistic drifting state. Across the drift of electrons across the EL gap, the number of excitations happening is retrieved and an histogram is filled on the fly. About 10000 electrons for each reduced field are simulated.

By showing the reduced light yield, expressed in the number of photons produced per (electron cm bar) against the reduced electric field one can see (in the left panel of Figure 4.13) that the amplification parameter (the slope of the fitted curve) remains fairly constant among the different mixtures. However the higher the amount of helium the higher the threshold becomes (the reduced field for which the fitted curve crosses the  $x$ -axis). This is most likely due to the residual cooling effect of helium as well and marginally to the lower partial pressure of xenon since the total pressure remains the same. This will be tested in the following section by simply running a configuration where the partial pressure of xenon is 15 bar in a 15% HeXe mixture making the total pressure 17.65 bar.

On the front of the variance of the light produced by EL, there is a similar effect: the Q-factor degrades with the percentage of helium (right panel in Figure 4.13). This is because the elastic collisions of helium, while suppressed, still compete with the excitation collisions.

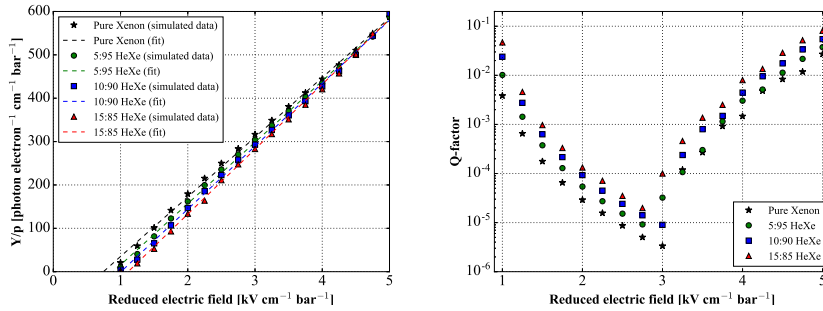


**Figure 4.13.** Reduced EL yield,  $Y/p$ , against the reduced electric field  $E/P$  (left). The points are obtained from the Garfield++ simulation and the dashed lines correspond to linear fits. Q-factor against the reduced electric field (right). The Q-factor is the quantitative definition of the yield fluctuation as defined in Equation 4.11.

The behavior of the Q-factor features two regimes: in the first one for the lower values of the reduced electric field it is decreasing. This is because the amount of light emitted increases so the relative variance goes down. This translates to a linear increase of the light yield. Above roughly  $2.75\text{--}3\text{ kV cm}^{-1}\text{ bar}^{-1}$  the Q-factor starts to increase. This is due to the probability that an ionization happens becoming non-zero. When an ionization happens there is much more light produced for this electron which increases the variance of the process. From that point, the increase of light yield is not linear anymore. This is shown in Figure 4.14 where the light production is compared between the linear regime and the non-linear regime. The Figure 4.14 also shows how the numbers were extracted from the simulation to produce the results shown in Figure 4.13.

But overall the Q-factor remains very small compared to the Fano factor. Therefore the changes in the energy resolution between all these mixtures is influenced mostly by the intrinsic fluctuations of the production of the charge carriers, not the ones of the light yield. And these changes of energy resolution are nearly indistinguishable from one another. As a conclusion it appears as though that HeXe mixtures retain the very competitive energy resolution coming with pure xenon. It must be noted that due to the higher threshold of HeXe mixtures,

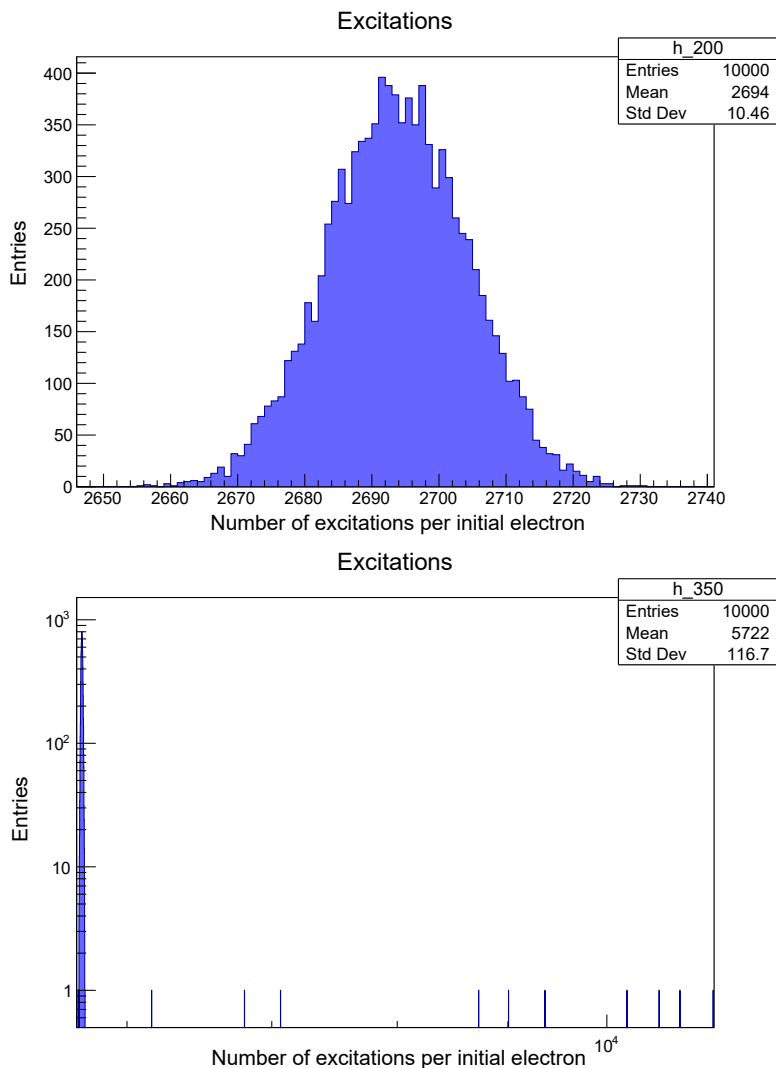


**Figure 4.14.** Histograms filled with the number of excitations per initial electron simulated with Garfield++. Both images were obtained in a pure xenon simulation with a gap of 10 mm, the result for the reduced light yield is consistent with the simulations done for a gap of 5 mm. The top panel shows the excitation histogram for a reduced field of  $2 \text{ kV cm}^{-1} \text{ bar}^{-1}$  as an example corresponding to the linear regime. On the bottom panel the reduced field is  $3.5 \text{ kV cm}^{-1} \text{ bar}^{-1}$  (the scale of both axes is logarithmic).

running at a low reduced EL field would have a noticeable negative impact on energy resolution, due to lack of light.

A preliminary study has been performed by the NEXT group based in Coimbra, Portugal [201]. They used the same setup to measure the EL and energy resolution for 10%, 20% and 30% HeXe mixtures. The results they got confirm the higher threshold of HeXe mixtures with respect to pure xenon but on the other hand their results show a degradation of the light yield that is less than the value expected from the the simulations above. This discrepancy may be due to the photosensors being sensitive to neutral bremsstrahlung emission [202]. All in all those experimental results strengthen the case of HeXe mixtures as a suitable low-diffusion possibility for neutrinoless double beta searches.

#### 4.4.3 Primary scintillation

The conclusion of the two previous sections is that HeXe mixtures appear to be a promising low-diffusion gas mixture that would retain the quality of the energy resolution that can be achieved in pure xenon. But there are a few other areas where the HeXe mixtures should be compared to pure xenon to ensure its full capability.

The primary scintillation in a TPC is necessary to trigger on an event and to "project the time" in order to fully reconstruct an event in three dimensions. It has been mentioned in Section 4.3 that some gas mixtures are quenching this primary scintillation to the extent where the 3D reconstruction is not possible or severely hindered.

To evaluate the effect of helium on xenon scintillation we can exploit the Degrad simulations performed to evaluate the Fano factor. In the previous section we were looking at the ionization numbers but Degrad also provides the detailed numbers of every excited state populations for the different gas species. Here again, the two cases including or not the Penning transfer are simulated. While keeping in mind that it is extremely likely for the 100% Penning transfer efficiency to be accurate.

The xenon scintillation probability is defined as the amount of xenon atoms scintillating in the mixture with respect to this number in pure xenon. The number of xenon atoms scintillating is counted differently depending on the assumption of the Penning transfer efficiency.

In the most likely case where its efficiency is 100%, the number of xenon atoms scintillating would be only equal to the number of xenon excitations, the helium excitations being transferred to ionizations as in a helium-argon mixture [199]. In the extreme case where the Penning transfer is disabled, it would be assumed that the excited helium atoms would transfer their energy to xenon by leaving them in an excited state, ultimately leading to xenon scintillation. This effect corresponds to what is seen on helium-neon mixtures [199] where excited helium is very unlikely to ionize neon atoms due to a much higher ionization potential. Any other possibility would lie in-between these extremes. The results are shown in Figure 4.15.

As in Section 4.4.2, the numbers show that the HeXe mixtures we consider diverge very little from the pure xenon, irrespective of the behavior of the Penning transfer. As long as the concentration of helium does not exceed 20%, the expected loss of scintillation remains within 3% of the one of pure xenon. The so-called krypton events are the low energy point-like events used to calibrate the detector [137]. Being the tiniest light signal used in a NEXT detector, their  $S1$  sets the constraint on the primary scintillation requirements and a degradation of 3% is not enough to kill their detection potential.

A study of the scintillation properties of binary noble gas mixtures show that the scintillation of mixtures based on helium are heavily affected by minute concentration of a heavier noble gas [203]. This has been specifically studied for a HeXe mixtures containing up to 90% of helium [204].

#### 4.4.4 Photosensors and helium atmosphere

The current state of the art to design optical TPCs such as the NEXT ones is to use photomultipliers (PMTs) to collect the light of both the  $S1$  and the  $S2$ . The  $S1$  are used as a trigger and to measure the  $z$  coordinate of the event while the  $S2$  are used to do the calorimetry and the track reconstruction. So far only PMTs can measure reliably the  $S1$  and precisely the  $S2$ .

But as we have seen that HeXe mixtures are very promising low-diffusion mixtures, one has to remember that helium is a dangerous hazard for PMTs [205]. The volume of the PMTs containing the photocathode and the dynodes require a very good level of vacuum. The

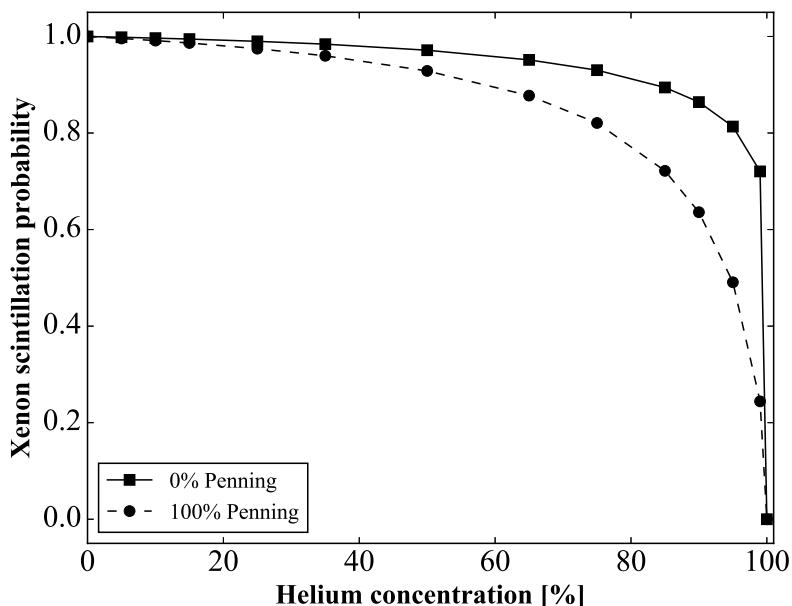


**Figure 4.15.** Scintillation probability of xenon against the helium concentration in a HeXe mixture at 15 bar as computed by the Degrad in a zero field scenario. The solid line corresponds to the extreme case where Penning transfer is disabled while the dashed line corresponds to the likely case of perfect efficiency in Penning transfer.

amplified electron between the dynodes can ionize the gaseous impurities and lead to afterpulses or even electrical breakdown, permanently damaging the phototube. A concentration of  $10^{-2}$  or  $10^{-1}$  mbar can make a PMT unusable. Helium is such a specific threat because it is the gas which is most likely to permeate the glass window of the PMTs. The highest grade of glass optically-wise, pure fused silica, is actually the most permeable to helium [206]. This is due to the holes in the amorphous structure of the glass that allow the very small atom of helium to diffuse very easily. It has been shown that the chemical composition of the glass can alter this effect [207]. Glass impurities fill the holes in the structure hence lowering its permeability to helium. Some glass such as borosilicate or soda-lime glass could theoretically

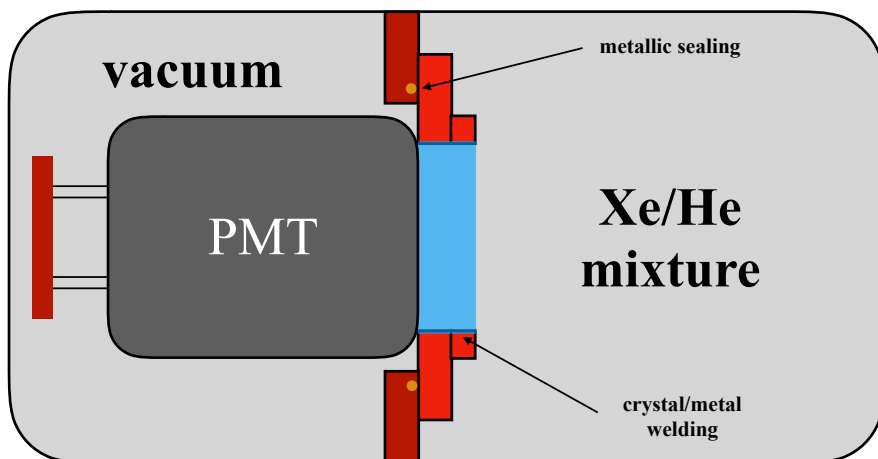


**Figure 4.16.** Scheme for the operation of PMTs in a helium-rich atmosphere. The PMT is looking into the active volume through a crystalline quartz/sapphire window that is coated with a wavelength shifter to maximize the light transmission. The crystal is welded to a metallic frame that can easily be mounted in a flange with a metallic sealing, avoiding helium diffusion into the PMT volume.

withstand an atmosphere of 1 bar of helium for hundreds of days.

A way to operate PMTs safely close to an atmosphere of helium consists of shielding them behind crystalline optical windows. The structure of those crystals is redundant and it has been shown that their permeability to helium is so small that it is only noticeable at a geological time scale [208]. Two crystals are commonly grown to form windows with very good optical and mechanical performances: crystalline quartz and sapphire. Theoretical calculations demonstrate the incapability of helium atoms in their ground state and singlet state  $2^1S_0$  to diffuse through crystalline quartz [209]. Sapphire however is a crystal that has a similar structure to that of hematite. The diffusion of helium through hematite has been the subject of a specific measurement [210]. This study extrapolates a diffusion coefficient at room temperature of  $10^{-26}$  cm<sup>2</sup>/s. This value is about twenty orders of magnitude below the diffusion coefficients corresponding to the glasses mentioned above. In conclusion, both crystalline quartz and sapphire are able to shield PMTs from helium atoms.



In NEXT-White the Hammamatsu PMTs were not able to withstand high pressures so to protect them they were shielded behind a sapphire window. The challenge to operate a detector with a HeXe atmosphere is to find a sealing method that would be totally helium proof. Metal-to-metal sealants are believed to be able to provide enough tightness to avoid helium contamination of the PMT side. A scheme for this principle is shown in Figure 4.16.

Ultimately the first tonne-scale module that the NEXT collaboration is aiming to build, NEXT-HD, would definitely remove the PMTs from its design as detailed in Section 3.4.1. NEXT-HD would be a symmetrical TPC where both ends would feature an energy-tracking plane able to perform both functions thanks to a competitive array of SiPMs working in concert with an array of optical fibers around the bulk of the detection medium in order to improve the light collection efficiency. A way to improve the performance of the SiPMs, notably to make them sensitive to the  $S1$  level of light, is to cool them down so as to lower their electronic noise. These are work-in-progress and are presently beyond the scope of this thesis.

## 4.5 HeXe mixtures at constant target mass

It has been shown that HeXe mixtures can provide low diffusion that do not come at the cost of energy resolution, as is seen with molecular admixtures. However, unlike these molecular admixtures, the amount of helium to mix with xenon is substantial, about 15%. If the design constrains work with a mixture at 15 bar this implies reducing the xenon quantity within the mixture, hence reducing the target mass: the number of  $^{136}$ -xenon atoms. A balance of benefit-cost can be done to see if the advantage gained by reducing the background overcomes the loss of target mass in terms of the sensitivity defined in Equation 2.13.

But from a realistic perspective, and due to the high cost of isotopic enrichment, the amount of  $^{136}$ -enriched xenon should be one of the limiting factors of an experiment. As such one should aim to use all the enriched xenon available and thereafter optimize the background index of the experiment. If the baseline assumption is that a detector can be operated with 15 bar of pure xenon, then one can perform

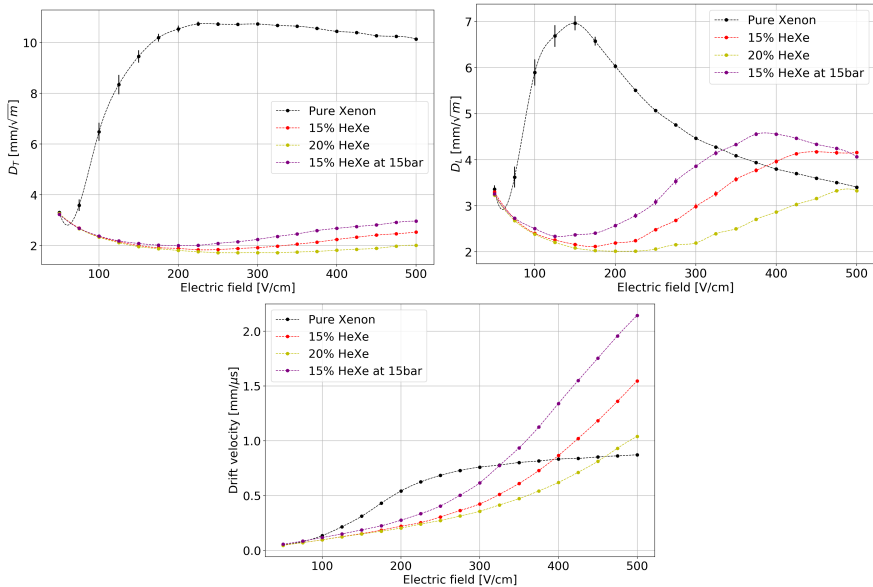


**Figure 4.17.** Transverse diffusion (top left), longitudinal diffusion (top right) and drift velocity (bottom) against the drift field. The mixtures labeled 15% HeXe and 20% HeXe are simulated at 17.65 and 18.75 bar respectively ensuring that the partial pressure of xenon remains 15 bar.

the same study as in the previous section albeit keeping the partial pressure of xenon at 15 bar across the different HeXe mixtures.

Considering a 15% HeXe mixture with a partial pressure of xenon at 15 bar means a total pressure of about 17.65 bar. The transverse diffusion and the longitudinal diffusion calculated by Magboltz are shown in Figure 4.17. It appears that the diffusion in the 15% HeXe mixture at 17.65 bar is noticeably lower than the one simulated for a HeXe mixture at 15 bar. This additional improvement is notably more pronounced for the longitudinal diffusion. These simulations also show that the drift velocity is close to that of pure xenon at a field around 400 V/cm.

On the side of the Fano factor, the  $w$ -value and the primary scintillation probability described in Section 4.4.3, the simulations done with Degrad do not show any meaningful change. One can however evaluate how the size of the tracks evolve for these different mixtures.

A figure of merit that can be used is the 3D dispersion of the electrons within the track. This value has been calculated for 5000 double beta decay events simulated through Degrad by retrieving the position of all the thermalised electrons.

In order to exclude the satellites skewing the estimation of the size of the main track, secondary effects such as Bremsstrahlung were excluded. The distributions of the 3D dispersion for pure xenon and the 15% HeXe mixture at 17.65 bar are shown in Figure 4.18. As expected the tracks get significantly longer by moving from pure xenon at 15 bar to 15% HeXe at 15 bar. This increase, of about 19%, is due to the very low stopping power of the helium that is replacing the xenon. But surprisingly, by keeping the same density of xenon and adding some helium to reach a 15% HeXe mixture, the tracks also get very marginally longer, the increase being of just 1% according to the simulation.

Finally a light simulation following the exact same procedure as the one described in Section 4.4.2 was performed. The same panels as in the previous study were produced except that the light yield is shown as the absolute light yield. They are shown in Figure 4.19. The reduced light yield is characteristic of the mixture studied, but the parameter that enters in the energy resolution formula is the absolute yield.

There is, as expected, no substantial difference in the behavior of the 15% HeXe mixtures at 15 bar and at 17.65 bar: the reduced light yield remains nearly identical at a given reduced electric field. But because they are not at the same pressure, the absolute light yield improves faster in the mixture at 17.65 bar. As such the reduction of the light yield with respect to pure xenon is extreme at low reduced field but the situation improves rapidly if one can achieve a higher reduced field.

## 4.6 Summary

The drift of electrons in gases is a mechanism that is the cornerstone of the working principle of a TPC. It is particularly crucial for the NEXT experiment to have an in-depth understanding of it in order to evaluate the potential of its background rejection based on topology

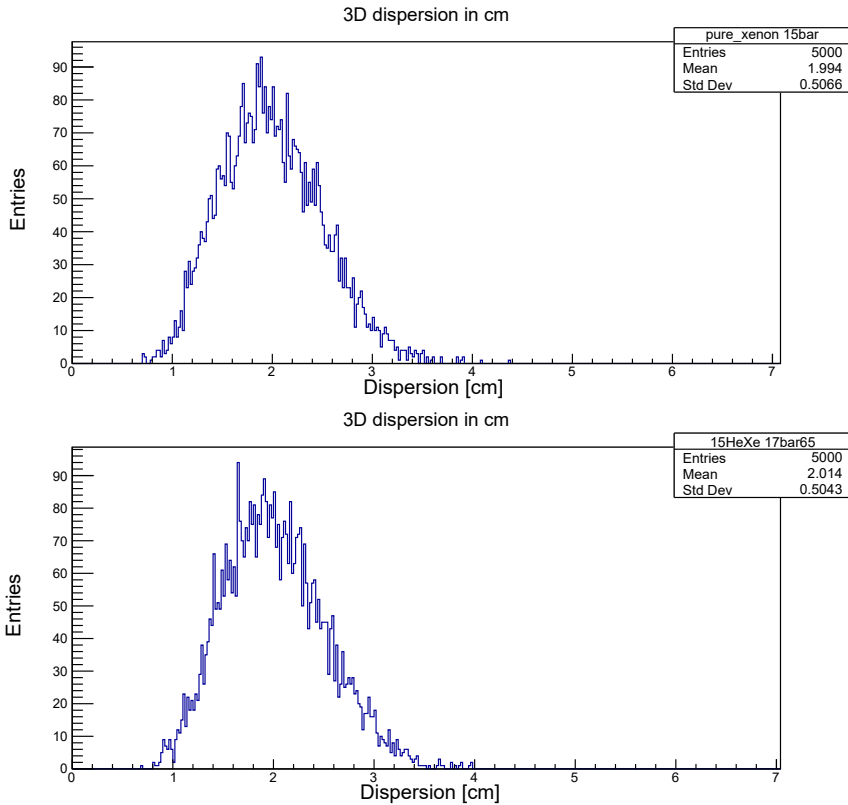


**Figure 4.18.** Histograms of the 3D dispersion of ionization tracks for pure xenon at 15 bar (top) and for 15 HeXe at 17.65 bar (bottom).

reconstruction, which when associated with its sub-percent energy resolution makes it a very competitive technology for the upcoming generation of  $0\nu\beta\beta$  experiments.

The mechanisms that are governing the diffusion of an electron swarm drifting in gas were described as well as the parameters that affect it in order to lower the diffusion and therefore improve the detector performance. The current state of knowledge experimentally gathered by the NEXT collaboration regarding the transport parameters of electrons in high pressure xenon has been presented. The results obtained within the collaboration regarding some proposed low-diffusion mixtures containing minute concentration of molecular

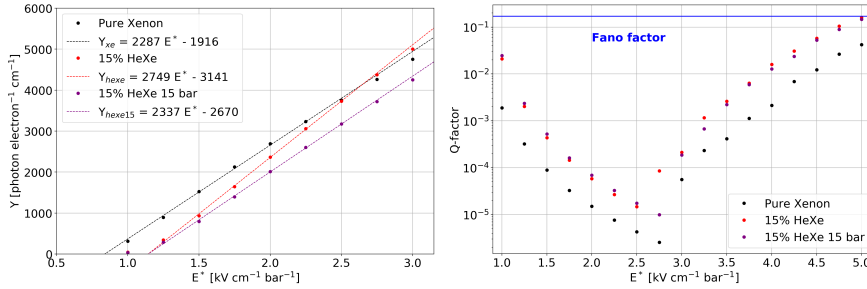


**Figure 4.19.** EL yield, noted  $Y$ , against the reduced electric field noted  $E^*$  (left). The fits are performed only on the points belonging to the linear regime. Q-factor against the reduced electric field (right), the Fano factor that it adds with in the energy resolution expression is also shown.

gases were also mentioned.

But most crucially it has been shown that a helium-xenon mixture is a very promising low-diffusion mixture. Its low diffusion would enable a good topological reconstruction for forthcoming detectors that would not come at the cost of energy resolution or other key assets that working with pure xenon brings. The only concern of losing target mass is alleviated by using a helium-xenon mixture at constant partial pressure of xenon.



# The NEXT-DEMO++ *5* detector

The NEXT-DEMO detector was built at the Instituto de Física Corpuscular (IFIC) in Valencia, Spain. The detector itself was a Time Projection Chamber (TPC) operated from November 2010 until 2016. It successfully validated the SOFT concept developed by the NEXT collaboration for  $0\nu\beta\beta$  searches. To do so it mainly achieved demonstration of a competitive energy resolution [131] and the capability of reconstructing tracks with a tracking plane instrumented with SiPMs [132]. NEXT-DEMO was then decommissioned, after helping the collaboration to acquire the necessary know-how to operate larger detectors. It gave its status of being NEXT's flagship detector to NEXT-White.

In 2018 the detector was revived and modernized under a new name: NEXT-DEMO++. Its main objectives were set to study low-diffusion mixtures and to become a testing ground for the upcoming NEXT-100 detector.

## 5.1 Gas system and pressure vessel

### 5.1.1 *Pressure vessel*

The pressure vessel used for NEXT-DEMO++ is the same that was used for NEXT-DEMO and was certified for 10 bar operation. It consists of a stainless steel (grade 304L) cylindrical shell with a 30 cm diameter and a 60 cm length. The thickness of the walls are 3 mm. It features numerous CF40 ports on its side. They were established in order to allow radioactive sources to be located close to the active volume. On top of the vessels there are three ports (CF130, CF67 and CF80), the central one is sealed while the two others are used to deliver high voltages to the cathode and to the gate. This part is welded to CF



**Figure 5.1.** General view of the detector NEXT-DEMO++ inside the clean room. The gas system can be seen on the background. Below the table supporting the detector are located the high voltage power supplies and the turbomolecular pump.

flanges at its ends.

The detector is "closed" by two stainless steel end-caps that are mounted directly on the cylindrical part. Almost all sealings are ensured by copper gaskets. The two end-caps are installed on a rail system that allows for a safer and easier mounting. Because they host the energy plane and the tracking plane they are manufactured differently to optimize the sensors electronics.

### 5.1.2 Gas system

The gas system is designed to pressurize the detector with the chosen mixture, to recirculate the gas through the purifiers, to recover the gas (in the case of xenon by cryo-recovery) and to pump the system to the



best achievable vacuum.

The gas recirculation during normal operation is necessary to purify it from electronegative impurities such as O<sub>2</sub> and CO<sub>2</sub> that hinder the secondary electron lifetime. The chemical purifier used is a SAES PS4-MT50-R-535 hot getter [211] and the membrane compressor is a discontinued model manufactured by SERA [212].

The gas bottles (xenon, argon and helium) are connected to the gas system through pressure regulators, allowing for a smooth and precise filling. The recovery of the xenon in its bottle is done by immersing the bottle in a liquid nitrogen bath. The temperature of the liquid nitrogen (approximately 77 K) is far below the solidification point of xenon leading the xenon to solidify in the bottle which acts as a xenon pump on the whole gas system.

The gas system is composed of two types of gas lines: those that are expected to withstand the nominal pressure of roughly 10 bar and those that are not. The first kind of lines are referred to as "pressure lines" and the second as "vacuum lines". Both kinds of lines connect the vessel to the rest of the gas system. The gas flow can be controlled by opening and closing pressure valves mounted at many key points of the gas system as can be seen on the scheme in Figure 5.2.

The purpose of the vacuum lines is to reduce the contamination of other gases and substances (oxygen, nitrogen, water, oils, etc.) trapped inside the detector, the pipes and inside the detector's materials. The experience gathered from the operations of previous TPCs shows that the quality of the vacuum reached before filling the detector has a major impact on the gas purity later on. The main reason behind this is that all the materials inside the detectors contribute to a virtual volume that is filled when the detector is pressurized. To achieve a high gas purity it is required to expunge the maximum amount of impurities from this virtual volume as it showcases a "memory" of when the detector was last filled with air. It is therefore a source of contamination of the gas.

The vacuum is obtained thanks to a turbomolecular pump mounted below the vessel. Its inlet is directly connected to the vessel through a CF100 port at the bottom of the vessel. In order to protect the pump and the vacuum lines from the pressure side in normal conditions, the CF100 port is closed by a guillotine valve. The level of vacuum is measured by a couple of vacuum gauges (VG) and its composition

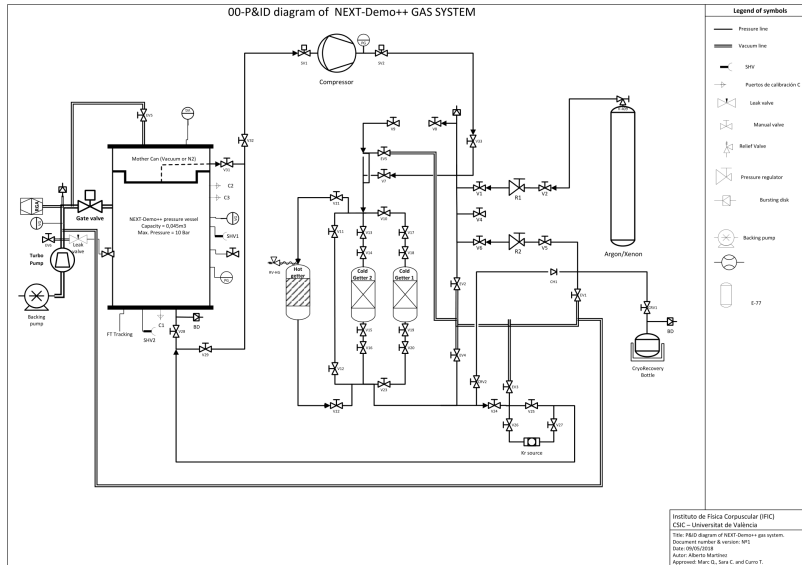


**Figure 5.2.** Diagram of the gas system of NEXT-DEMO++. The valve label EV stands for Evacuation Valve; they connect to the vacuum lines. The valve label CRV stands for Cryo-Recovery Valve; they connect the gas system to the cryo-bottle of xenon. The Rb/Kr source for point-like events is represented at the bottom right of the diagram.

is sampled by a Residual Gas Analyzer (RGA) that is mounted near the inlet of the turbomolecular pump. A vacuum gauge is located in the same volume as the RGA to make sure reliably that the vacuum is not a hazard for the RGA's hot filament. A leak valve connects the vessel to the vacuum lines in order to evaluate the gas composition that is in the detector. The pressure is measured by pressure gauges (PG) located in two spots: inside the vessel and inside the compressor volume.

The safety of the gas system is handled by bursting disks in specific locations. They are able to withstand a pressure up to 12 bar.

It is needed to mention here that, as for NEXT-White, a rubidium source is embedded in the gas system to produce point-like monochromatic energy depositions inside the active volume for calibration. A

section of the gas system contains the source that is in direct contact with the gas flow. The source produces krypton atoms that emanate directly into the gas and are circulated through the detector. A section of the gas system contains the source that is in direct contact with the gas flow. This small section can be closed to the rest of the gas system or opened thanks to two valves shown in Figure 5.2. Due to its short lifetime, the activity induced by the source inside the detector extinguishes within a few hours after the source is closed.

## 5.2 TPC main components

At the root of an EL TPC such as NEXT-DEMO++ there is a drift region and an amplification region. These regions are delimited by field shaping conductors: the cathode, the gate, the anode and the field cage. These conductors define the boundary conditions necessary to create the electric fields associated with the drift and amplification regions. Because the secondary electron collection plane is very close to the tracking plane, which is at ground, the voltages in the chamber are set with a negative polarity.

### 5.2.1 Field cage

The field cage has the purpose of ensuring that the detection medium, where interactions occur, is kept under a uniform electric field. The action of this field drives the secondary electrons to the amplification stage. The uniformity of the field is a necessity to not deform the topology of the events recorded and avoid electron loss to the walls of the vessel.

The field cage is divided in two sections: the drift section (or active volume) between the cathode and the gate and the buffer section between the cathode and the energy plane. The drift section has a length of 310 mm and the buffer has a length of 117 mm. The latter is in place to degrade progressively the field on that side of the detector towards the energy plane that is electrically grounded.

The field cage is made of aluminum rings: 4 on the buffer side and 19 on the drift side. The inner diameter of the rings is 235 mm. They are held together by HDPE pillars following the same design that was

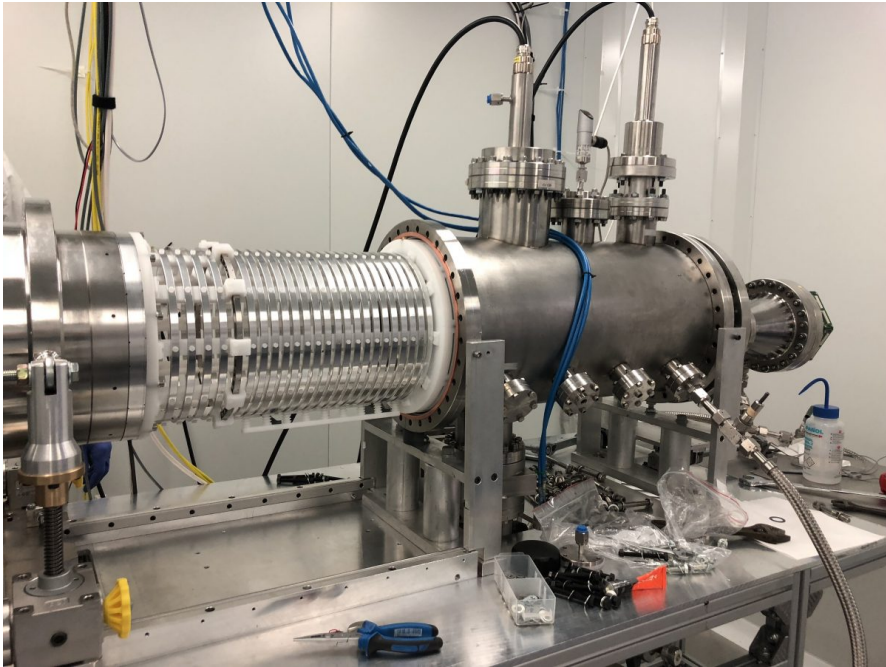


**Figure 5.3.** Field cage of NEXT-DEMO++ assembled, fixed to the energy plane and about to be slid inside the pressure vessel.

selected for NEXT-100 field cage (detailed in Section 3.3.4 of Chapter 3). Pictures of the field cage are shown in Figure 5.3 and Figure 5.4.

The potential of the cathode is linearly degraded through the field cage by using two resistor chains connecting the rings together. The resistor chain for the drift section is made of 20 resistors connected in series for a total resistance of  $10\text{ G}\Omega$ . The resistor chain for the buffer section is made of 9 resistors connected in parallel-series for a total resistance of  $4.5\text{ G}\Omega$ . The two resistor chains are shown in Figure 5.4.

### 5.2.2 Cathode

The cathode of NEXT-DEMO++ is a grid of parallel stainless steel wires that is shown in Figure 5.5. The wires go through a stainless steel frame that has an inner diameter of 226 mm. The wires are tensioned manually while being screwed to the frame. This frame also

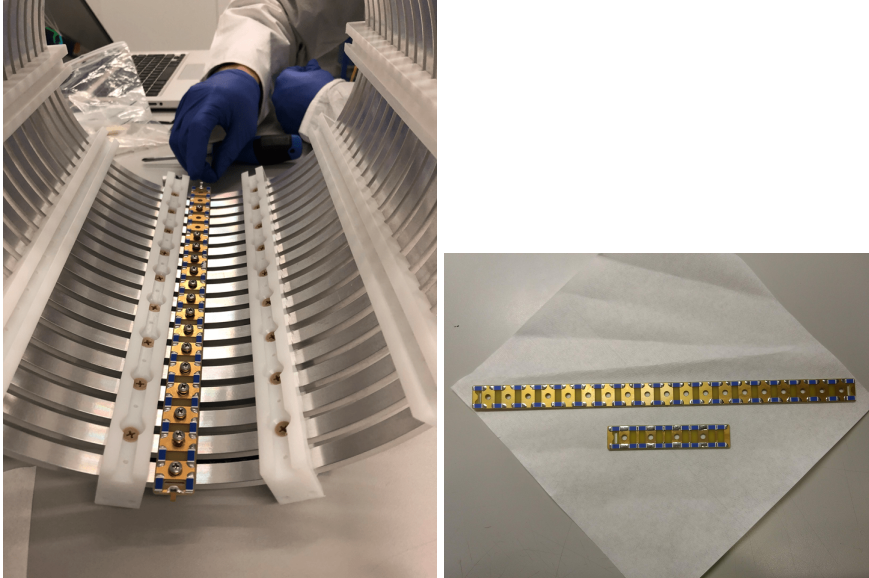


**Figure 5.4.** Drift section of the field cage (left) showing the resistor chain being screwed to the rings. The two resistor chains (right) used in NEXT-DEMO++, the longer one for the drift section and the other one for the buffer.

bridges the electrical contact between the wires and the high voltage feedthrough. The wires have a diameter of  $177.8 \mu\text{m}$  and the pitch separating them is  $17.4 \text{ mm}$ .

These dimensions provide an excellent optical transparency of the grid. But an electrostatic simulation shows that this design also results in a significant field leakage that needs to be accounted for when estimating the drift field corresponding to a given set of voltages. For example when the gate is at  $10.5 \text{ kV}$  and the cathode at  $23.5 \text{ kV}$ , the field is reduced by  $16\%$  with respect to the value extrapolated from the voltage difference ( $351 \text{ V/cm}$  instead of  $419 \text{ V/cm}$ ). Figure 5.6 shows the result of these simulations.

### 5.2.3 Gate and anode

The EL region is located between the gate and the anode. The gate is a stainless steel mesh that is tensioned by a frame made of two stainless



**Figure 5.5.** Cathode frame mounted on the buffer section of the field cage (left). The tensioned stainless steel wires can also be seen. Mesh frame embedded in its HDPE support (center). The mesh, being too thin, can not be seen on the picture. Anode plate housed in its HDPE support (right). On that picture the anode plate is mounted on the field cage which is inside the pressure vessel.

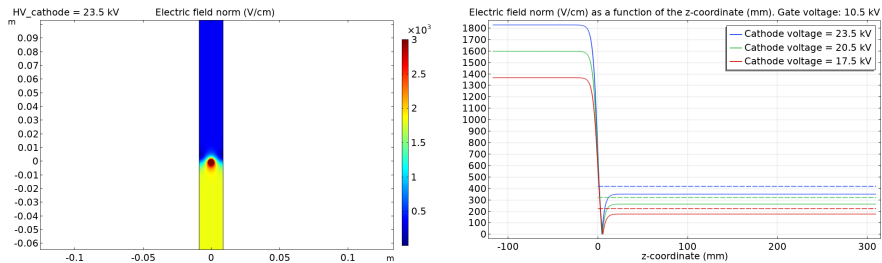


**Figure 5.6.** Electric field in NEXT-DEMO++. The full lines correspond to the simulated norm of the electric field in the chamber and the dashed lines represent that value extrapolated from the voltage difference. The drift region extends over the positive values of  $z$  and the buffer over the negative values.

steel parts pressed and screwed together. The frame holding the gate has an inner diameter of 191 mm. Just like for the cathode this frame bridges the gap between the mesh and the high voltage feedthrough.

The anode in the first iteration of NEXT-DEMO++ followed the same design as that of NEXT-White. A transparent plate coated primarily with indium tin oxide (ITO) and secondarily with TPB. The ITO coating allowed electrical connection of the surface of the plate to the tracking plane set at ground. The plate has a diameter of 255 mm and a thickness of 3 mm. It was made of a low iron glass that has optical properties not significantly far from fused silica at a fraction of its price.

The gate and the anode were enclosed in their own HDPE frame, they are shown in Figure 5.5. These two frames were then screwed together setting the EL gap to be of 10 mm. This assembly was fixed at the extremity of the field cage.

In the ulterior iteration of NEXT-DEMO++, the anode plate was replaced by another mesh electrically set at ground as a mean to improve the light transmission between the active volume and the tracking plane. The EL gap was reduced to 5 mm to reduce the light spread over the  $z$ -direction.

As said before, one of the purposes behind the construction of NEXT-DEMO++ is to be a test bench for different possible implementations of the EL region. To replicate the conditions of NEXT-White, the first iteration was a solid anode and a mesh gate. Then a combination of two meshes was tested. This work is still ongoing and will be followed by testing the possible EL designs for NEXT-100 mentioned in Section 3.3.4.

#### 5.2.4 High voltage feedthroughs

The feedthroughs used to provide the voltages to the gate and to the cathode follow the same designs as those used in NEXT-White. The cathode feedthrough is the one that most risks an electrical breakdown since the electric fields near it are the highest within the whole vessel. The conic shape of the HDPE insulator is aligned with the local field lines, thus avoiding charge accumulation. The gate feedthrough is much more straightforward because the fields are not as problematic in its vicinity. Pictures of both feedthroughs are shown in Figure 5.7.



**Figure 5.7.** High voltage feedthroughs operated in NEXT-White. The one connected to the cathode is on the left and the one connected to the gate is on the right. Those used for NEXT-DEMO++ were built following the exact same design.

### 5.2.5 Light tube

The light tube surrounds the active volume. It has the purpose of improving the light collection by reflecting the light emitted in the active volume until it reaches a light sensor. By improving the light collection the light tube is important to get the energy resolution of the TPC as close as possible to its intrinsic energy resolution.

In the same fashion as for NEXT-100 the HDPE pillars mentioned earlier hold 20 reflecting teflon panels: 10 for the drift side and 10 for the buffer side. All of these panels have a thickness of 8 mm balancing the maximum of reflectivity for the minimum space taken in the active volume. All of these reflecting panels have been coated with TPB to improve the light collection since the reflectivity of teflon at the peak emission wavelength of TPB is close to 97% [213].

The coating was performed by vacuum evaporation which gives the best homogeneous resulting TPB layer. A picture of some of the panels fixed inside the evaporator is shown in Figure 5.8, they are shown mounted on the field cage in Figure 5.9. The evaporation consists of establishing a very good vacuum before heating the TPB located in a crucible open to the chamber. The evaporated TPB deposits on the surfaces fixed on a disk on the other side of the vessel. This disk is rotating in order to ensure homogeneous coating.





**Figure 5.8.** Evaporator during operation (left) and installation of the teflon panels in the rotating disk of the evaporator prior to operation (right). The evaporator was used through the courtesy of the neutrino group of the University of Manchester.

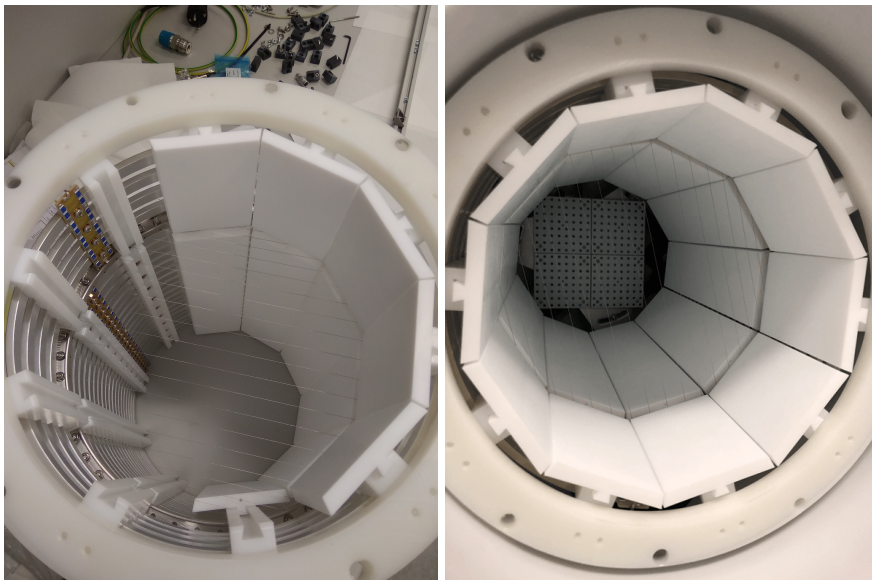


**Figure 5.9.** Teflon panels being installed on the assembled field cage.

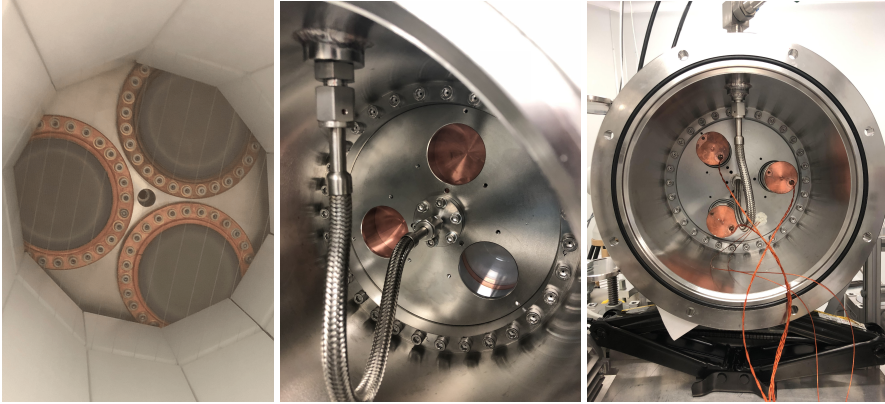


**Figure 5.10.** Picture of the energy plane seen through the field cage (left). The cathode grid can be noticed on the foreground. Picture of the setup for the leak test of the sealings between the PMTs and the energy plane end-cap (middle). Same point of view with the three connected PMTs before closing the energy plane.

## 5.3 Energy plane

### 5.3.1 Description and mechanical design

The energy plane is performing the calorimetry measurement as well as detecting the prompt  $S1$  signal required for the 3D reconstruction. It consists of 3 Hamamatsu R11410-10 PMTs, the same model chosen for NEXT-White and NEXT-100 for its performance and radiopurity [214]. The photocathode coverage of the energy plane, which can be seen in the left image of Figure 5.10, is 33%.

The volume enclosing the PMTs inside one of the detector's end-caps is kept at vacuum to keep the electronics of the PMTs in their working condition. To keep the PMTs away from an accidental helium leak through the vacuum lines of the gas system, this volume is independent from the gas system and is pumped separately.

Since those PMTs can not withstand high pressure, each one of them is located behind a sapphire window that is welded to a copper frame. To maximize the light transmission the PMT's fused silica window is connected to a sapphire window by a silicone gel (Nusil LS1-3252). As mentioned in Section 4.4 of the previous chapter, metallic

sealings are required to operate the PMTs safely in order to study HeXe mixtures.

The copper frames are therefore sealed on the stainless steel plate of the energy plane by the metallic seals Helicoflex [215]. Their tightness to helium was tested in the absence of PMTs by measuring the helium leak rate of the pressure vessel pressurized with 10 bar of helium to the energy plane volume kept at vacuum. Using an elastomer seal would translate to a measured leak rate of  $10^{-7}$  mbar L s<sup>-1</sup> while the helicoflex seal would lead to a leak rate below the detection threshold of the helium detector. A picture of the leak test is shown in the right image of Figure 5.10.

The side of the window exposed to the xenon atmosphere is coated by spin coating with poly(3,4-ethylenedioxythiophene) (PEDOT). It is an electrically resistive and transparent coating. It allows to electrically connect the window surface to the nearby copper plate at ground, hence obtaining a more uniform electric field in front of the window.

In addition to the PEDOT coating, the windows are coated with a thin layer of TPB to improve the light collection efficiency of the detector. The TPB was deposited by vacuum evaporation as for the teflon panels of the light tube described previously in Section 5.2.5.

### 5.3.2 Electronics

The PMTs used being the same as in NEXT-White their electronics is built in the same fashion [136]. The base circuit of the PMTs, which is shown in the left image of Figure 5.11, consists of 19 resistors of different resistances and 7 capacitors, 3 of them having a capacitance of 1.5  $\mu$ F and 4 having a capacitance of 4.7  $\mu$ F. The right image of Figure 5.11 shows how the base circuit is installed on a kapton board by soldering it to its 18 pins, the epoxy layer ensures protection against electrical breakdowns.

Because the PMT cathodes are electrically grounded the anode must be kept at a high voltage. This design choice simplifies the mechanical coupling of the PMTs to the energy plane which is also grounded but requires the anode's output to be AC coupled. Decoupling the signal from the high voltage thanks to a capacitor introduces a high pass filter. Its effect on the signal is not detailed here (it is

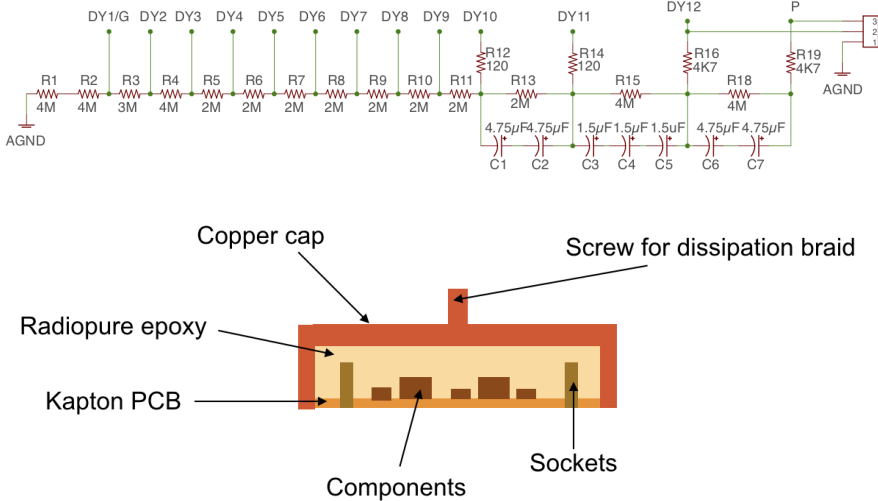


**Figure 5.11.** High voltage feedthroughs operated in NEXT-White. The one connected to the cathode is on the left picture and the one connected to the gate is on the right picture. Those used for NEXT-DEMO++ were built following the exact same design.

explained in [136]) but that effect is automatically software-corrected by what is called the baseline reconstruction algorithm (BLR).

## 5.4 Tracking plane

### 5.4.1 Description

The tracking plane is collecting the  $S_2$  signal on a dense array of SiPMs. The spatial information of the  $S_2$  recorded enables the topology reconstruction.

In NEXT-DEMO++ the SiPMs are of the model used in NEXT-White: SensL C-Series MicroFC-10035-SMT-GP [216]. These sensors have an active area of  $1 \times 1 \text{ mm}^2$ , they are made of 576  $35 \text{ }\mu\text{m}$  microcells. The SiPMs are arrayed on a kapton board (DICE board) as an  $8 \times 8$  matrix with a pitch of 1 cm which can be seen in the right image of Figure 5.9 and in Figure 5.12. The tracking plane is made of 4 DICE boards resulting in a total of 256 SiPMs. Each one of these DICE boards

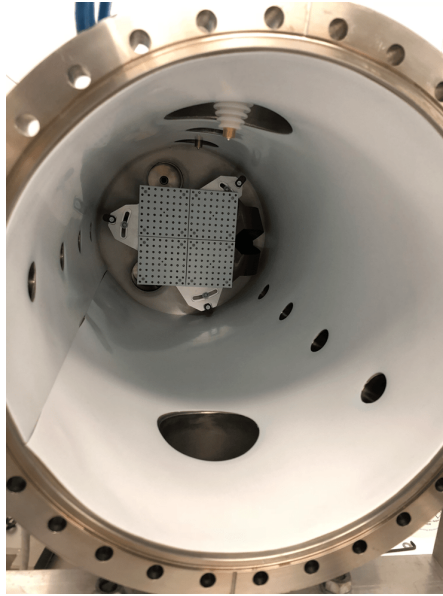


**Figure 5.12.** The tracking plane seen through the vessel in the absence of the field cage. The insulator layer wrapping the field cage covers the walls of the pressure vessel; the high voltage feedthroughs can be seen on the top of the image.

has a side of 79 mm. The DICE boards are covered with PTFE masks to improve the light collection in the detector. The tracking plane was originally placed 3 mm away from the anode plate.

A number of other tracking plane configurations have been tested with a two meshes amplification stage. These configurations were changing the thickness of the PTFE masks, the presence of a 250  $\mu\text{m}$  transparent TPB coated membrane in front of the SiPMs, the distance between the tracking plane and the anode. Another sensor from the manufacturer Hamamatsu was also tested: the model MPPC S13372-1350TE.

#### 5.4.2 Electronics

The DICE board where the SiPMs are connected is a flexible kapton circuit that has a trace of 100  $\mu\text{m}$  width with a 0.5 mm pitch. In NEXT-

White this cable takes the signal to an inner cable, also made of kapton. But in NEXT-DEMO++ the absence of an inner copper shield and the smaller number of channels does not require this extra inner cable. The DICE boards take their signal directly outside of the pressure vessel through the FR4 feedthrough of the tracking plane. At the end of the kapton cable, the signal is divided between 4 cables of 51 wires each of which feeds the cables to the Front End Boards that perform the digitization. More information can be found in [135].

## 5.5 Data Acquisition System

### 5.5.1 Hardware

The Data Acquisition System (DAQ) of NEXT-DEMO++ is a reduced version of that of NEXT-White [217], to take into account the smaller number of sensors. It follows the SRS-ATCA standard, the Scalable Readout System ported to the Advanced Telecommunications Computing Architecture. This was developed between 2011 and 2014 by a collaboration between the RD51 collaboration, the NEXT collaboration and IFIN-HH Bucharest [218,219]. An ATCA blade houses two interconnected FPGA (Xilinx Virtex-6 XC6VLX240T-1ff1156), two mezzanine slots, two event buffers, and I/O interfaces (Gigabit Ethernet and NIM trigger signals), which consequently allows one ATCA to house two FEC cards [218].

The DAQ system is divided into three parts: the energy plane (3 PMTs), the tracking plane (256 SiPMs spread over 4 DICE boards with each DICE board being connected to a Front End Board, FEB [220]) and the trigger. NEXT-DEMO++ therefore uses two ATCA translating to three FEC modules: one for the trigger module, one for the energy plane module and one for the tracking plane module. They communicate between each other by a DTC link (Data, Trigger, Clock and Control [221]). Figure 5.13 shows a diagram of that structure.

In running mode, data are recorded continuously to a circular buffer. When the trigger [222] finds a signal fitting the preset conditions fixed by the operator (called a *shifter*), the data are framed and sent to a local data concentrator (LDC) which sends merged sub-events to a global data concentrator (GDC) that leaves the raw events files ready to be processed. In NEXT-DEMO++ two LDCs and only one

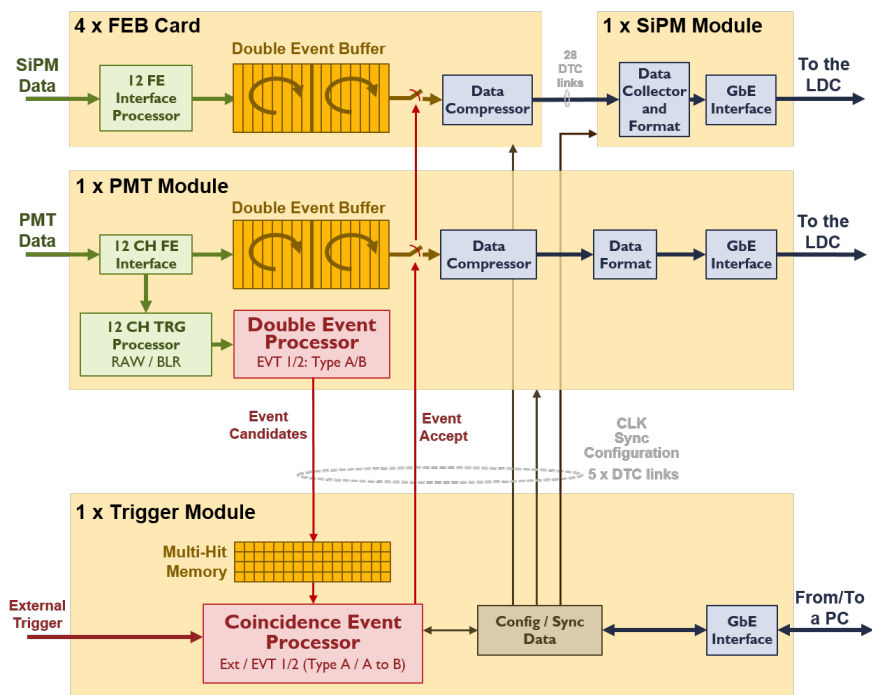
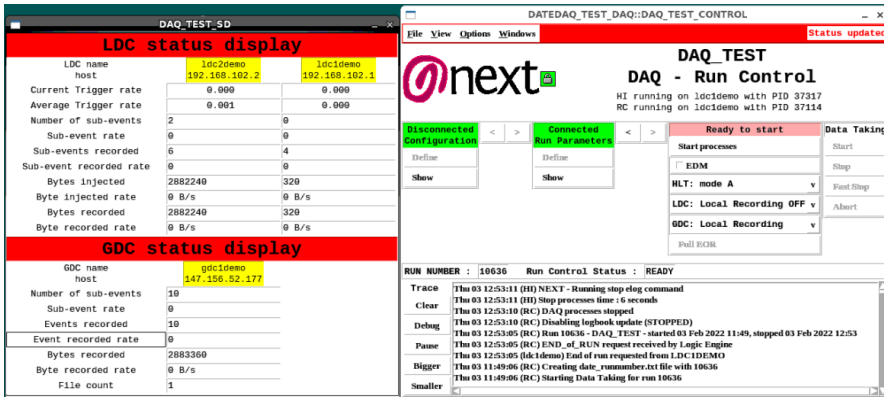


Figure 5.13. DAQ structure of NEXT-DEMO++.

GDC are used. The system has been updated to accommodate the need for constant calibration of the detector by adding a dual trigger configuration. The trigger 1 is dedicated to the events required to perform the krypton calibration while trigger 2 targets higher energy events. The trigger can also handle an external trigger that is used in NEXT-DEMO++ exclusively for calibration purposes which will be described in the next section.

### 5.5.2 Software

The software DATE was developed for the ALICE experiment at CERN [223] and has been used by NEXT-White since 2016. DATE was designed to handle the data produced in parallel by different subsystems of a detector such as the tracking and energy planes of a NEXT-type detector. The data taking is organized by runs that are



**Figure 5.14.** Main control (right) and monitoring (left) windows of DATE for NEXT-DEMO++.

started manually by a *shifter*. Figure 5.14 shows a screenshot of the windows used for monitoring and managing the data taking.

DATE is used in conjunction with an application developed by the NEXT collaboration. Written in Java, it configures the trigger and sends control commands to the FEC cards.

## 5.6 Sensors calibration

The procedure to calibrate the sensors follows the same procedure that was developed for NEXT-White.

### 5.6.1 PMTs

The PMTs, despite having the same base circuit, give a slightly different response to the same light input. Regular calibrations are required to equalize their response and to verify their stability over time.

The light for PMT calibration is provided by an LED embedded in the tracking plane, facing the PMTs, that is pulsed with a period of  $50 \mu\text{s}$ . The readout is triggered automatically at a 25 Hz frequency with a buffer window of  $800 \mu\text{s}$ . The duration of the run is made sufficient to gather a few thousands of triggers. The operation is repeated for a set of light levels emitted by the LED in order to cover the single



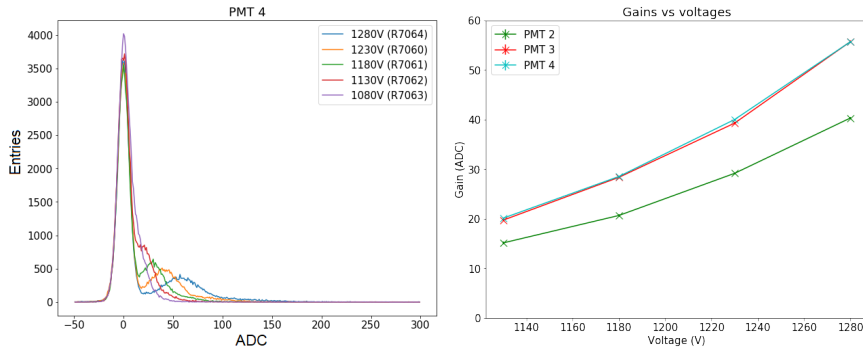


**Figure 5.15.** Spectra for PMT 4 (the PMTs are labelled 2, 3 and 4) at different operating voltages (left). The right panel shows the gain of the three PMTs as a function of the operating voltage (right).

photon detected regime per PMT. Using the different runs taken allow disentangling the PMTs response from the light output of the LED.

The data taken are then processed to remove the pedestal and to integrate the signal over the time bins corresponding to the LED emitting light as well as  $2 \mu\text{s}$  before. The spectrum that can be retrieved from these runs shows the contribution mainly of 0 photoelectron and 1 photoelectron, with the small contributions for 2 and more photoelectrons. An example of these spectra obtained for one of the PMTs of NEXT-DEMO++ can be seen in Figure 5.15. For each one of the PMTs the gaussian fit to the single photoelectron contribution defines the gain of the PMT. The gain of the PMTs of NEXT-DEMO++ spanning the range of advised operating voltages is shown in the right panel of Figure 5.15. A gain too high can lead to saturation of the PMTs, therefore it is chosen according to the light levels expected.

### 5.6.2 SiPMs

The procedure to calibrate the SiPMs requires first to check their connectivity i.e. to verify that they are operational. To do so, electronic noise of the SiPMs is retrieved without biasing the sensors. These data are compared with those taken with the bias voltage on (dark current run). This comparison allows determination of whether or not a SiPM is faulty. An example of the spectra resulting from these two types of

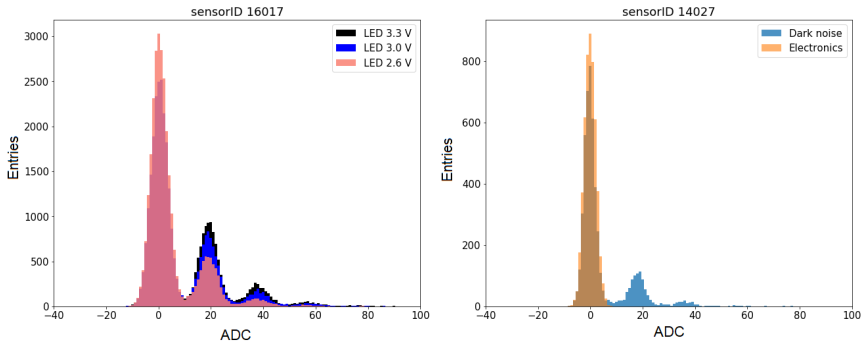


**Figure 5.16.** Spectra for a SiPM exposed to different light levels resulting from different LED voltages (left). Dark noise and electronics noise for a noisy SiPM (right).

calibration runs is shown in Figure 5.16.

Then, similarly as for the PMTs, a LED enclosed within the energy plane is pulsed and data are taken using only the SiPMs with an autotrigger. The data from the SiPMs are processed in a similar fashion as the PMTs: the baseline is calculated and the signal is integrated over  $2 \mu\text{s}$  starting at the trigger time. This procedure of integration was selected to compromise between the necessity to capture all the light and to avoid integrating over the high level of noise that some SiPMs feature. The spectra generated then allow extraction of the gain defined as the gap between the pedestal and the single photoelectron contribution. An example of these spectra is shown in Figure 5.16.

### 5.6.3 Calibration database

When the gain factors have been calculated for each sensor's channel they are added to a database. Thereafter they are used to set the signal recorded by each channel on a same scale before further processing the data. The database also allows quick verification of the stability overtime of the sensors.

## 5.7 Slow controls

A number of LabVIEW programs monitor and control the main systems of the detector. They were originally developed for NEXT-White and were subsequently adapted for NEXT-DEMO++. A lot of functions are automated, mostly those dealing with the immediate safety of the detector components.

The slow control **HHV** deals with the voltages applied to both the gate and the cathode by controlling directly the high voltage power supply. The *shifter* inputs solely the desired voltages (the values are written as positive but the voltages are delivered with a negative polarity nonetheless). The response to an electrical breakdown (commonly named spark) is to make one attempt to recover automatically the nominal voltage. Should this attempt fail the power supplies are turned off to prevent any damage on the sensors' electronics.

The slow control **PMT** is responsible for monitoring the voltage and current consumption of the three PMTs. The slow control **PWR** fulfills roughly the same task for the tracking plane by monitoring the bias voltages for the SiPMs and their current consumption and temperature. This slow control also controls the sensors front-end power supplies. In both slow controls the *shifter* can possibly turn on or turn off the sensors as well as selecting their working condition.

The slow control **GAS** is the last one used in NEXT-DEMO++. It reads out the pressure and vacuum gauges installed on the gas system as described in Section 5.1.2. It controls directly the status of the compressor. If the pressure drops below a preset level the compressor is automatically stopped and a notification alarm is sent to the *shifter*.

A set of screenshots of these slow control programs are shown in Figure 5.17.

## 5.8 Geant4 simulation of NEXT-DEMO++

A Geant4 simulation of NEXT-DEMO++ has been developed for the latest configuration of NEXT-DEMO++ in the same way it was done for NEXT-White and NEXT-100. Visualisation of the detector's geometry is shown in Figure 5.18. The simulation is built with the framework developed by the NEXT collaboration: NEXUS [181].



**Figure 5.17.** Main window of the slow control programs managing the high voltage (top left), the gas system (top right), the PMTs voltages (bottom left) and the SiPMs voltages and sensors front end electronics (bottom right).

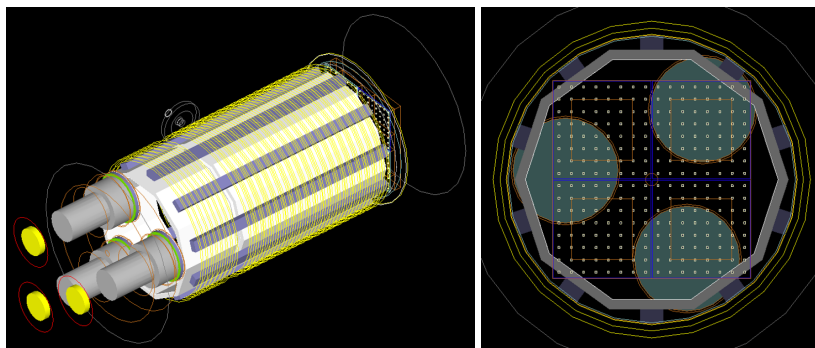


**Figure 5.18.** General view of the detector (left). View from behind the tracking plane (right).

## 5.9 Summary of NEXT-DEMO++ operation

The detector was commissioned in Summer 2019 and has been operated successfully since then. Its first activity was to compare pure xenon with a 15% HeXe mixture before testing different tracking plane designs for NEXT-100.

### 5.9.1 Helium-xenon separation challenge

In its first operation the detector was operated with the intent to measure the transport parameter in xenon and in helium-xenon mixtures. For this, the only radioactive source used was the rubidium source providing the point like  $^{83m}\text{Kr}$  events. An unexpected challenge regarding helium-xenon separation prevented study of the total range of HeXe mixtures scheduled.

A standard cryo-recovery of xenon is shown in Figure 5.19. In the pure xenon case the pressure drops to zero. Actually there are a few millibars of xenon left in the chamber ( $<10$  mbar) that can not be recovered, after a while the outgassing of the materials inside the detector raise this leftover to about 150-200 mbar. Another cycle of recovery is then performed before pumping out the remaining leftover.

It was expected that separating the helium from xenon would be trivial [192]. The wide gap between the boiling point of helium (4.22 K) and the melting point of xenon (161.4 K) was thought to be enough for freezing all the xenon at the temperature of liquid nitrogen. The pressure in the system would drop and stabilize at a pressure corresponding to the remaining quasi-pure helium atmosphere, with a partial pressure of xenon at the level of a few millibars. This remaining atmosphere would be just pumped out, effectively separating the helium from the xenon.

However it came as a surprise during the initial HeXe operation that the cryo-recovery would end up with the pressure stabilizing at a value significantly higher than expected: roughly 1.8 bar instead of the 1.4 bar corresponding to the partial pressure of helium. The remaining atmosphere therefore contained a HeXe mixture with a significant fraction of xenon. An example of this is shown in Figure 5.20.

As pumping out the gas mixture leftover did not improve the situation, it seemed that even a tiny amount of helium was enough

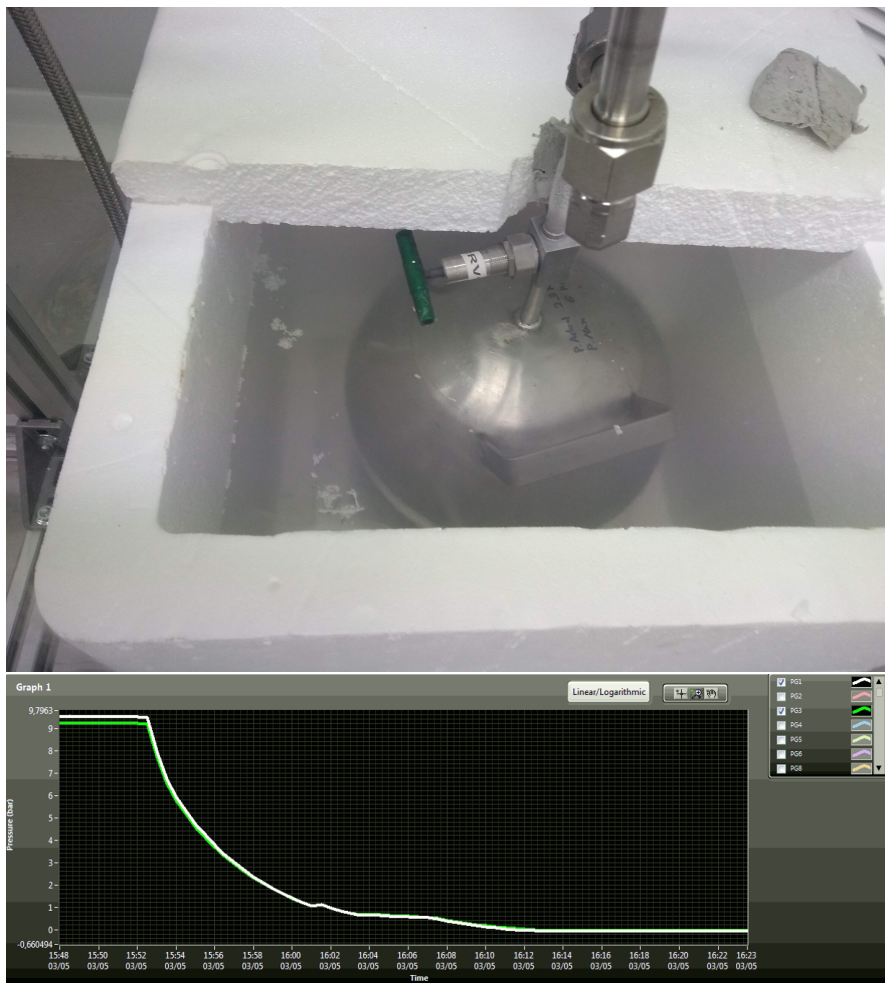


**Figure 5.19.** Bottle of xenon immersed in a liquid nitrogen bath during a recovery operation (top). Pressure in the gas system throughout the cryo-recovery of pure xenon (bottom). The two lines correspond to the pressure measured at two different spots of the gas system. Their values are not identical because the gauges are not of the same model.

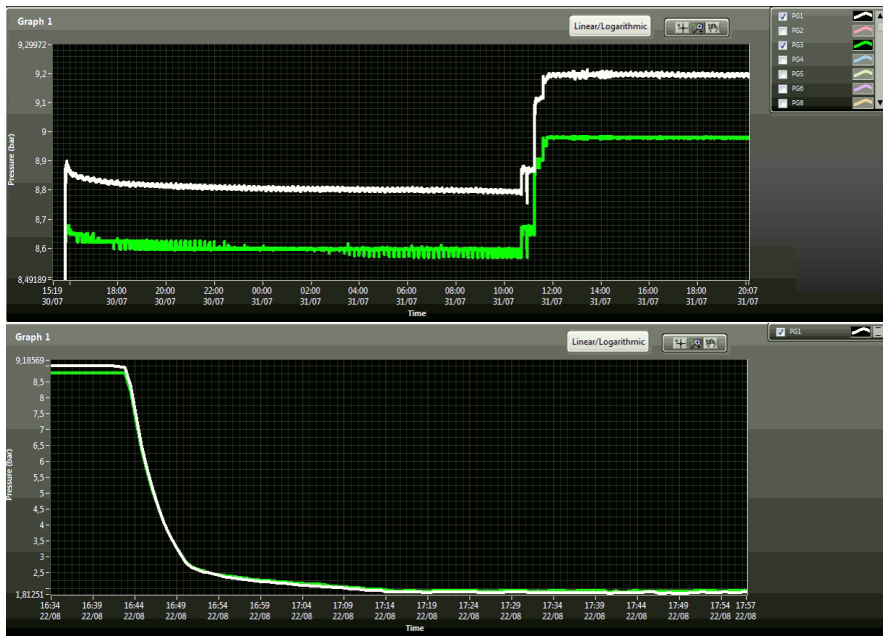


**Figure 5.20.** Total pressure in the gas system during the addition of helium to a pure xenon mixture (top), the partial pressure of helium is about 0.4 bar. Pressure drop during the attempt at recovering the xenon (bottom), the pressure stabilizes at 1.8 bar.

to impair the cryo-recovery. A number of tests performed such as immersing gas pipes in liquid nitrogen showed that adding more surfaces at the temperature of liquid nitrogen improved the xenon recovery. Ultimately adding an extra cryo-bottle of xenon, as shown in Figure 5.21, allowed the system to have a residual pressure of a few hundreds millibars.

No final conclusions could have been made. Further tests would have been necessary to establish an efficient xenon recovery system in presence of helium. But the cost of xenon and the planned operations of NEXT-DEMO++ did not allow it: the detector requiring pure xenon for the following studies.

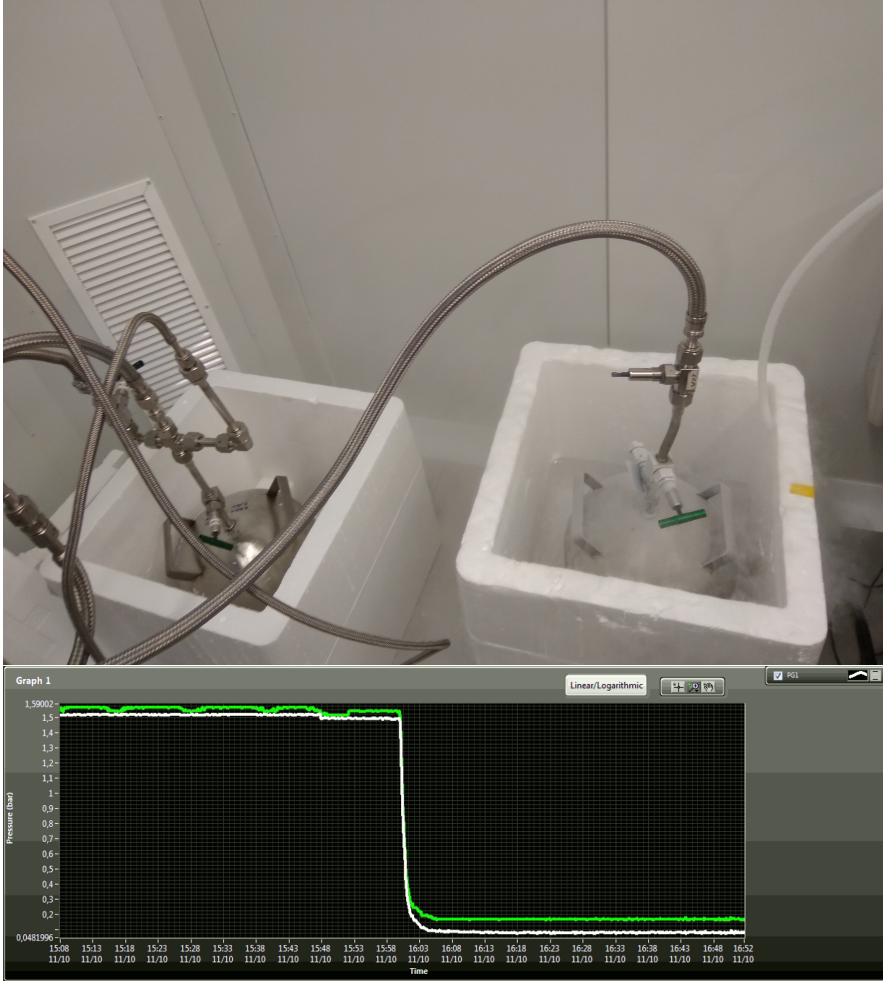


**Figure 5.21.** Bottle of xenon immersed in a liquid nitrogen bath during a recovery operation (top). Pressure in the gas system throughout the cryo-recovery of pure xenon (bottom). In the latter image, the starting pressure is lower than before due to pumping out some gas in an earlier test.



# 6 Characterization of a Helium-Xenon mixture

The NEXT-DEMO++ detector described in the previous chapter is the ideal tool to characterize different mixtures and assess their full potential as low-diffusion mixtures for the future of the NEXT experiment. The helium-xenon (HeXe) mixtures proposed in Section 4.4 were partly the reason behind the construction of NEXT-DEMO++. Its first run was dedicated to perform a systematic study of HeXe mixtures but, due to the issue mentioned in the previous chapter with the recovery of xenon in presence of helium, only a comparison between pure xenon and a 15% HeXe mixture could be achieved.

## 6.1 Datasets and data selection

### 6.1.1 Datasets and run conditions

The only data available were preliminary runs taken to test the procedure of data taking and the corresponding analysis. These runs were performed with the detector running in normal conditions. That means very close to the running conditions of NEXT-White, which was being operated at the same moment.

In order to measure the electron transport parameters a similar method that was used for NEXT-White [138] with krypton-events was implemented. A rubidium-83 source was embedded in the gas system, it decays to  $^{83m}\text{Kr}$ . These emanate from the source directly in the gas system and are distributed uniformly within the active volume of the detector. The  $^{83m}\text{Kr}$  decays to its ground state through two consecutive electron conversions. The rate of those two decays can be approximated to the one of the first decay (1.83 h) due to the second rate being much faster: 154.4 ns. These two decays release 41.56 keV

which leads to a point-like energy deposition, given the high pressure of the gas.

Once the detector was assembled and its gas system and sensors were certified the detector was filled with pure xenon at roughly 9.1 bar. During the whole operation the temperature was maintained constant at 19 °C. At this pressure the voltage on the gate was set to 11.5 kV which defined an EL field of 11.5 kV/cm translating to a reduced field of  $1.26 \text{ kV cm}^{-1} \text{ bar}^{-1}$ . The cathode was set to 26 kV which would translate to a drift field of 468 V/cm. However, in Section 5.2.2 of the previous chapter related to the cathode of NEXT-DEMO++ it was shown that there is a substantial field leakage between the drift region and the buffer region. According to the COMSOL simulation described there, the drift field that can be assumed for these conditions in the detector is 392 V/cm. In addition the field becomes uniform 2 cm away from the cathode.

After the data were taken the xenon was recovered successfully. The detector was then filled again with xenon up to 7.7 bar; the helium was added thereafter to form a 15% HeXe mixture at 9.1 bar. The same gate and cathode voltages were applied. The conditions of the detector for the two runs are summarised in Table 6.1. In the following, the pure xenon run will be referred to as the *xenon* run and the HeXe run will be referred to as the *helium* run.

| Parameters       | Value                                      |
|------------------|--|
| Pressure         | 9.1 bar                                    |
| $V_{gate}$       | -11.5 kV                                   |
| EL gap           | 10 mm                                      |
| EL reduced field | $1.26 \text{ kV cm}^{-1} \text{ bar}^{-1}$ |
| $V_{cathode}$    | -26 kV                                     |
| Drift length     | 31 cm                                      |
| Drift field      | 392 V/cm                                   |

**Table 6.1.** Detector conditions for the two datasets.

### 6.1.2 Data reconstruction and selection

#### Reconstruction

The data acquisition system was configured to trigger on events that include the Kr-events. Once an  $S2$  signal matching the pre-defined requirements is found, the system records the PMTs and the SiPMs waveforms. The time window for data taking is  $800\ \mu\text{s}$  and the  $S2$  that triggered the system starts in the middle of the time window.

The waveforms are processed using the Python framework *Invisibles Cities* (IC) developed by the NEXT collaboration [183]. To begin, the PMTs waveforms are deconvolved from the electronic effects induced by the PMT base circuits. The PMT signals are then converted to photoelectrons (pes) using the conversion factors obtained with the calibration runs, following a process described in Section 5.6 of the previous chapter. An example of a PMT waveform showcasing an  $S1$  and an  $S2$  peak is given in Figure 6.1. The calibrated waveforms of the PMTs are summed together before applying a threshold of 2 photoelectrons. Finally the SiPM waveforms are processed similarly to the PMT waveforms using the calibration runs dedicated to the SiPMs. It should also be mentioned that the time of the waveforms for both kind of sensors are synchronized; in order to have an  $S2$  coincident signal bin-to-bin between the waveforms of the PMTs and those of the SiPMs, the former are rebinned to match the sampling of the latter:  $1\ \mu\text{s}$  (originally the sampling is of 25 ns).

A peak finder algorithm then goes over every waveform; it is tuned to look for small  $S1$ -like signals in the first half of each waveform and for  $S2$  signals on the other half. The information regarding these peaks are mapping the response of the energy plane and of the tracking plane; they are stored in a new set of files. This procedure allows reducing the amount of data to be processed thereafter by only keeping the information of interest ie those about the peaks.

The second algorithm used for the reconstruction is specifically tuned for reconstructing point-like energy depositions such as the Kr-events from the files previously generated. A first selection is performed at this level: only events featuring exactly one  $S1$  and one  $S2$  are selected. Each combination of  $S1$  and  $S2$  signals stored at the previous stage are sorted according to a filter selecting events with

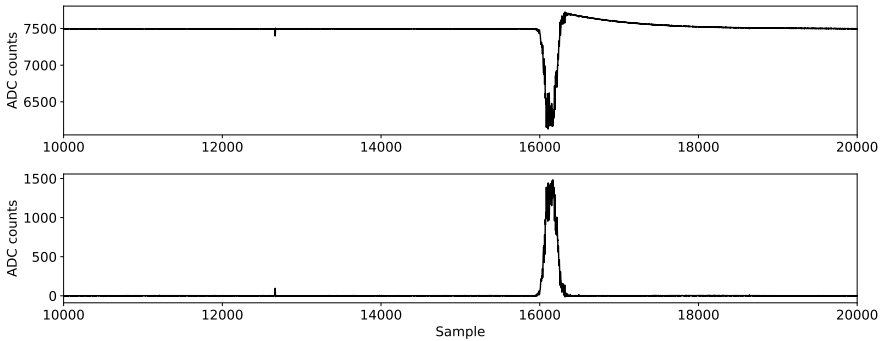


**Figure 6.1.** The top panel shows a raw waveform as recorded directly from the PMTs during the *xenon* run. The bottom panel shows the same waveform after it has been deconvolved and the PMTs calibrated. The *S1* is clearly visible on the left of the waveform and the *S2* on the right. Both waveforms shown are a summation of the waveforms recorded by the three PMTs.

given properties.

The energy of an event is computed as the time-summed amplitude of the *S2* peak. The  $x$  and  $y$  positions of a point-like event are computed as the charge-weighted average of the SiPMs positions; to avoid biasing the reconstruction with the dark noise of the SiPMs, only the SiPMs recording a minimum of 5 pes in the time window are accounted for. The drift time,  $t$ , is defined as the time elapsed between the maximum of the *S1* peak and the maximum of the *S2* peak. The longitudinal position,  $z$ , can simply be retrieved by multiplying the time coordinate with the drift velocity, once the latter is known. Finally the algorithm also computes and stores the standard deviation of the SiPM signal over the  $x$  and  $y$  dimensions as well as that of the PMT signal over the  $z$  dimension.

### Selecting the krypton events

As the study on the electron transport properties relies on the point-like Kr-events distributed across the active volume, it is necessary to apply a set of selections on each dataset to only retain the events of interest. In the following, the "charge" refers to the signal collected by the SiPMs, while the "energy" refers to the *S2* signal collected by the

PMTs.

It has been clearly established in NEXT-White that the detector response is not homogeneous on the X-Y plane. This is mostly pronounced on the outer layers of the active volume where border effects degrade dramatically the energy resolution [137]. In order to keep only the core of the detector, a radial cut of 40 mm is first applied. The border effects on the energy measurement can be seen in the top panels of Figure 6.2.

A second cut is performed on the charge integrated by the SiPMs corresponding to the S2. One can expect a correlation between the charge collected by the SiPMs and by the PMTs. This is seen in the middle panels of Figure 6.2. The *xenon* data were selected for a total charge collected by the SiPMs between 125 pes and 325 pes, while the *helium* data were selected between 17 pes and 120 pes.

Furthermore an additional requirement of more than one SiPM activated appeared to be necessary to remove poorly reconstructed events from the *helium* dataset. This is because the charge collected by SiPMs in the *helium* run was much smaller, some outlier events could make the previous cut with just one SiPM activated. Applying this cut on the *xenon* data has no effect.

After the data-quality selections have been applied, a clean energy spectrum appears, it can be seen for both the *xenon* run and for the *helium* run in the bottom panels of Figure 6.2. The same Kr energy peak corresponding to an energy deposition of 41.56 keV is observed at a very different scale of light collected between the two mixtures; this will be expanded upon in Section 6.4.

One can notice two peaks appearing at energies smaller than the Kr peak, they correspond to the X-rays from the K/L shells of xenon [131]. An additional cut on the S2 energy to select the Kr peak ensures that the events are overwhelmingly Kr events from now on. This selection for the *xenon* data is between 4500 pes and 5300 pes and between 1500 pes and 1900 pes for the *helium* data.

Foreshadowing the calculation of the drift velocity, there is a final cut on the data corresponding to a maximum drift time. The COMSOL simulations have shown that the field is poorly uniform within 2 mm from the cathode. In order to get rid of the events originating from this region its position is converted to an upper value of the drift time allowed by using the measured drift velocity. Thus a maximum drift

time cut is established for the *xenon* data of 305  $\mu\text{s}$  and of 97  $\mu\text{s}$  for the *helium* data. This last cut was applied after calculating the drift velocity, it does not apply to the work described in Section 6.3.

A summary of the data selection can be found in Table 6.2.

| Cut                           | <i>Xenon</i> run | <i>Helium</i> run |
|-------------------------------|------------------|-------------------|
| 1 S1 1 S2                     | 1862784 (100%)   | 2361243 (100%)    |
| Radial cut (<40 mm)           | 368775 (19.8%)   | 534856 (22.7%)    |
| S2 charge cut                 | 250412 (13.4%)   | 214146 (9.1%)     |
| Number of SiPM activated (>1) | 250412 (13.4%)   | 213413 (9%)       |
| Kr peak selection             | 226857 (12.2%)   | 182063 (7.7%)     |
| Maximum drift time            | 201873 (10.8%)   | 159442 (6.8%)     |

**Table 6.2.** Efficiency of the data selection. The number of events surviving each cuts are reported.

## 6.2 S1 comparison

It is possible from the reconstructed events to study and compare the main characteristic of the *S1* signal for both runs. In other words the relative difference of primary scintillation yield can be assessed from looking at the detected light from the primary scintillation.

Both distributions feature a somewhat positive skewness: a skewed gaussian is fitted to the data to retrieve the characteristics of the distributions and compare them between the two runs. The histograms with their best fit restricted to the bins around the peaks (between 3 and 15 pes) are shown in Figure 6.3.

The two distributions look alike, the positions of their peak are compatible with each other<sup>1</sup> which means that there is no indication of any change of the *S1* light yield between the two mixtures. This observed similarity holds true when comparing the *S1* from both runs coming from the same section of the active volume.

This is a confirmation of the conclusions given in Section 4.4.3: the light yield of the *S1* in pure xenon and in a 15% HeXe mixture remains

<sup>1</sup>The parameter  $\mu$  of the skewed gaussian fit is the central location of the distribution; the value where the center of the peak is can be evaluated numerically.

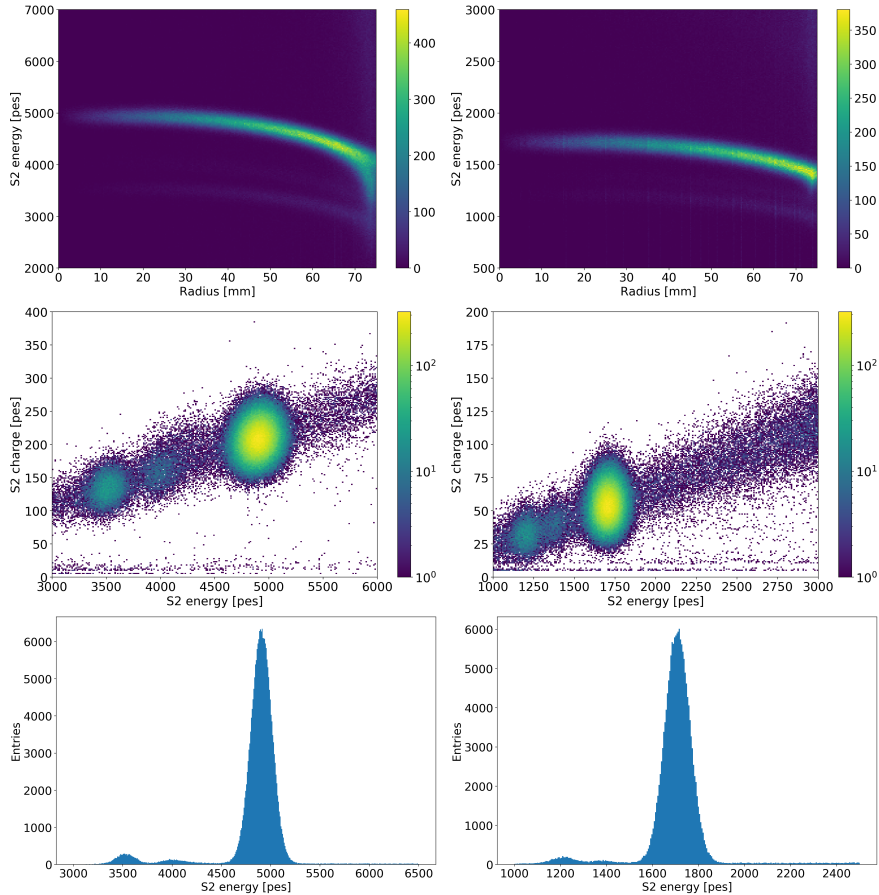


**Figure 6.2.** Panels showing how the data were selected. The left panels refer to the *xenon* run while the right panels refer to the *helium* run. The top panels are the histograms of the S2 energy versus the radial position. The cut at 40 mm removes the border effects. The middle panels show the histograms of the S2 energy versus the S2 charge collected by the SiPMs. The bottom panels show the raw energy spectra after all the cuts have been made. The two X-rays peaks can be seen below the Kr peak.

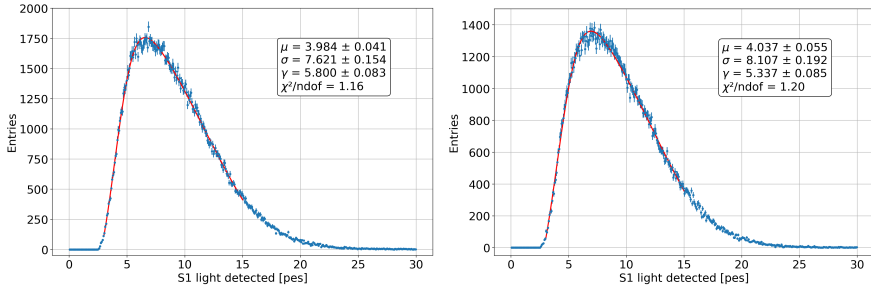


**Figure 6.3.** Panels showing the distribution of the light detected for  $S1$  peaks. The left panel refers to the *xenon* run while the right panel refers to the *helium* run. The best fit restricted to the region between 3 and 15 pes is shown in both cases with the parameters of the fit. For clarity the amplitude and the constant of the model used are not shown as they only depend of the binning chosen.

nearly equal. This result is particularly important considering that during normal operation, the smallest signal that a NEXT-like detector has to be sensitive to is the  $S1$  of Kr events. Being sensitive to them is a requirement to ensure that the optimal calibration procedure of the detector can be followed.

### 6.3 Drift velocity

Calculating the drift velocity from the data is straightforward. It requires associating events at a given drift time with a known distance of reference within the chamber. Due to the nature of the TPC, events happening beyond the cathode can not be detected: their secondary electrons would not drift towards the amplification stage and produce an  $S2$ . That makes the cathode the origin of the events with the maximum drift time recorded, the latter being noted  $Dt_{max}$ . So the drift velocity is simply:

$$v_d = \frac{Z_{cathode}}{Dt_{max}} \quad (6.1)$$

However, the reconstruction algorithm calculates for each event the drift time as the time difference between the maximum amplitude of both its  $S1$  and its  $S2$ . Therefore it accounts for a time during which the secondary electrons are drifting in the amplification stage at a



much higher field than that of the drift region. On the one hand the electron swarm of point-like Kr events arrive at the EL gap spread along the  $z$  direction due to the diffusion, this effect is gaussian. On the other hand the electroluminescence yield per unit of length at a given reduced field is constant. Therefore the  $S2$  signal of a Kr events can be seen as the convolution of a gaussian distribution with a square distribution. The maximum amplitude of the signal is then expected to happen when the centroid of the swarm has crossed half of the EL gap. This duration is noted in this section  $t_{EL/2}$ . Equation 6.1 becomes:

$$v_d = \frac{Z_{cathode}}{Dt_{max} - t_{EL/2}} \quad (6.2)$$

With  $t_{EL/2}$  being evaluated from the drift velocity in the EL that is computed by Magboltz for both runs. The outcome of these simulations gives  $t_{EL/2} = 1.864 \pm 0.032 \mu s$  for the *xenon* run and  $t_{EL/2} = 1.494 \pm 0.017 \mu s$  for the *helium* run. The cathode distance from the gate is  $Z_{cathode} = 310 \pm 2.0$  mm.

To finally retrieve the maximum drift time  $Dt_{max}$  from the data, a histogram of the events sorted by their drift time was made. The function that was fitted to this histogram is a logistic function:

$$f(x) = \frac{A}{1 + \exp^{-k(x-\mu)}} + B \quad (6.3)$$

The parameter  $\mu$  of the best fit is a measurement of the value of  $Dt_{max}$  while B represents the events misreconstructed with a drift time higher than the maximum drift time. This happens because of the time window being too large with respect to the maximum drift time: some small peaks are misidentified as an  $S1$  due to the algorithm settings being too loose. Removing these events that have a misidentified  $S1$  is an added reason for performing the cut on the maximum drift time described in Section 6.1.2. The best fit applied to the data sorted by their drift time for both runs is shown in Figure 6.4. The results are summarised in Table 6.3.

The values computed by Magboltz are also added as a reference. However, an imperfect evaluation of the conditions inside the detector introduces an uncertainty on the parameters for which Magboltz is run. The pressure in the vessel is ever changing due to the gases filling

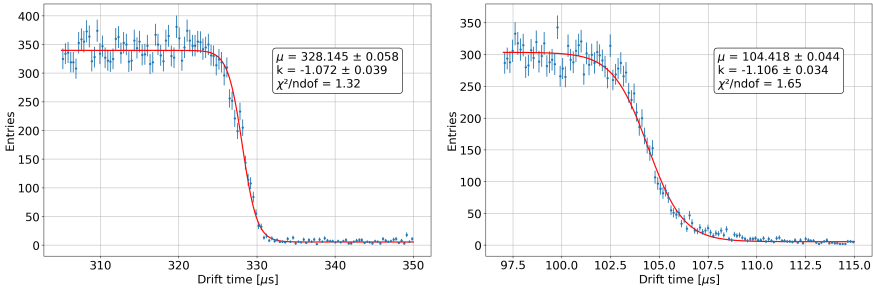


**Figure 6.4.** Panels showing the distribution of the events according to their reconstructed drift time. The left panel refers to the *xenon* run while the right panel refers to the *helium* run. The best fit is shown in both case with the parameters of the fit.

the virtual volume mentioned in Section 5.1.2. For the NEXT-White detector it takes a few weeks for the pressure to stabilize. Adding helium to the mix makes things more complex due to the difference of behavior between the two gases.

Considering the inaccuracy of filling the detector using manual pressure regulators, a typical uncertainty of  $\pm 0.1$  bar was assumed on the total pressure and in the case of the HeXe mixture an additional inaccuracy of  $\pm 0.1$  bar on the helium partial pressure was also assumed which translates to the fraction of helium being in-between 14% and 16%.

| Quantity                                   | <i>Xenon</i> run    | <i>Helium</i> run   |
|--|---------------------|---------------------|
| Maximum drift time [ $\mu\text{s}$ ]       | $328.145 \pm 0.058$ | $104.418 \pm 0.044$ |
| Drift velocity [ $\text{mm}/\mu\text{s}$ ] | $0.950 \pm 0.006$   | $3.012 \pm 0.020$   |
| Magboltz                                   | $0.914 \pm 0.003$   | $2.903 \pm 0.55$    |

**Table 6.3.** Measured maximum drift time for both runs and the corresponding drift velocity calculated. The drift velocity computed by Magboltz are added.

## 6.4 Energy resolution

The Kr peak obtained after the cuts gives an option to measure energy resolution for both runs and to measure the relative difference of light detected between the two mixtures. The energy resolution corresponds to the energy released by the  $^{83m}\text{Kr}$  decaying in the active volume: 41.56 keV. By performing a gaussian fit to the Kr peak for both runs, the light detected for the Kr peak can be extracted as the mean of the peak and the energy resolution is expressed as the Full Width Half Maximum (FWHM) of the peak. The raw energy resolutions are reported in Table 6.4. It is possible to easily refine these values by correcting the energy of each event to account for the electron lifetime.

### 6.4.1 Lifetime correction

It has been mentioned in Section 3.2.2 that the secondary electrons while drifting are facing the risk to get caught by electronegative impurities such as  $\text{O}_2$ . This effect is modeled by an exponential law:

$$N(t) = N_0 \exp(-t/\tau) \quad (6.4)$$

where  $N(t)$  is the number of drifting electrons after a drifting time  $t$ ,  $N_0$  is the initial number of secondary electrons produced and  $\tau$  is the electron lifetime. This loss of electrons distorts the energy reconstructed, the effect is more pronounced the higher is the drift time. To calculate the lifetime, the mean of the  $S2$  peak is computed at different drift times by fitting a gaussian to all the local Kr peaks. An exponential fit is then performed to these points distribution of the  $S2$  energy against the drift time as seen in Figure 6.5.

Once the lifetime has been retrieved, the energy of each event is corrected by the inverse function of the exponential law quoted in Equation 6.4. The values that have been measured are:  $\tau_{Xe} = 23.82 \pm 0.44$  ms and  $\tau_{\text{HeXe}} = 6.43 \pm 0.28$  ms. The lifetime is much higher for the *xenon* run because the xenon used in the detector has been used by the first iteration of NEXT-DEMO and kept in storage until then, therefore it went through many cycles of purification unlike the helium used for the HeXe mixture. The latter comes from a regular commercial helium bottle with a higher concentration of impurities.

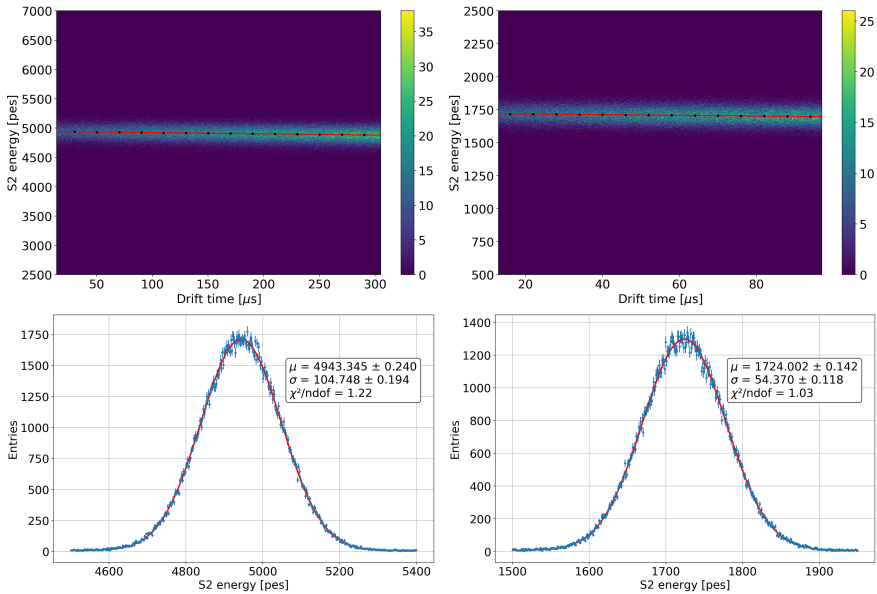


**Figure 6.5.** The top panels show how the lifetime is extracted for both runs by performing an exponential fit to the means of the Kr peak for various time slices of the chamber. The bottom panels show the gaussian fit to the lifetime-corrected Kr peaks. The left panels are for the *xenon* run and the right ones for the *helium* run.

With the corrected spectra, the same gaussian fit as before can be performed to retrieve the central peak value (light detected) and the corresponding energy resolution. The spectra and their corresponding fits can be seen in Figure 6.5. The results are reported in Table 6.4.

Because the parameters of the detector are identical between the two runs, the relative difference of light detected between them can be directly compared with the simulated light yield difference. The light yields simulated are also added to Table 6.4. It is to be noted that the difference observed is less than the one predicted by the simulations. This discrepancy might be due to some inaccuracy in the evaluation of the physical conditions inside the chamber (pressure sensors, field leakage etc...). This observation however adds to that made in the study [201].

An extended version of the energy resolution formula given in

| Quantity                                       | Xenon run   | Helium run  |
|--|-------------|-------------|
| Light detected [pes]                           | 4943        | 1724 (-65%) |
| Light yield [pes/e <sup>-</sup> ] (Garfield++) | 586         | 167 (-71%)  |
| Raw energy resolution at 41.56 keV             | 5.05 ± 0.02 | 7.46 ± 0.04 |
| Corrected energy resolution                    | 4.99 ± 0.02 | 7.42 ± 0.04 |

**Table 6.4.** Averaged light detected and energy resolution for both runs. The energy resolutions are given as the FWHM of the peak in percentage. The light yield is estimated from the Garfield++ simulations described in Section 4.4.2.

Equation 4.12 gives [117]:

$$R_E = 2.35 \sqrt{\frac{w}{E_{decay}} [F + Q] + \frac{1}{N_{dec}} \left( 1 + \frac{\sigma_q^2}{G_q^2} \right)} \quad (6.5)$$

where  $N_{dec}$  is the number of photons per event being converted to photoelectrons by the photocathodes of the PMTs. The contribution of the Q-factor is negligible before the Fano factor for the mixtures studied [192,201]. Because the term  $\sigma_q/G_q$  is characteristic of the PMT response, it remains constant from one run to the other. This formula shows the effect the light yield has on the energy resolution. For the HeXe mixture to match the energy resolution in xenon the number of photons collected by the photocathode per event must be optimized. This can be done by achieving a higher amplification field, as predicted in [192] and verified experimentally in [201], which goes hand in hand with an optimized light collection.

## 6.5 Longitudinal diffusion

The diffusion along the electric field, the longitudinal diffusion, behaves differently than the transverse diffusion due to the action of the electric field on the electron swarm. This has been detailed in Section 4.1.1. Moreover, in the detector, the signature of the longitudinal diffusion is of a different nature than that of the transverse diffusion. This is because the electron swarm of point-like events are widened due to diffusion while drifting. The more it drifts the wider it becomes

which has the consequence of increasing the time it takes to cross the EL stage and therefore results in a wider S2 peak. recorded by the PMTs.

It was mentioned in Section 6.3 that the S2 peak can be approximated to a convolution of a square distribution (due to the crossing of the EL stage) with a gaussian distribution (due to diffusion). Thus the RMS computed for every PMT waveform can be reasonably approximated to the standard deviation of the gaussian component of the S2, assuming it dominates the spread due to the size of the EL gap. The RMS is computed by the reconstruction algorithm used on the data.

The diffusion coefficient  $D_L$  is defined by the following equation:

$$\sigma_L^2(t_{drift}) = S_L^2 + 2D_L t_{drift} \quad (6.6)$$

where  $\sigma_L^2$  is the mean longitudinal spread observed after a drift time  $t_{drift}$  and  $S_L^2$  is the mean longitudinal spread induced by the extension of the EL stage. However in the data, the RMS of S2 peaks are quantities homogeneous to time and are expressed in  $\mu s$ . Thus, when applying Equation 6.6 to the data,  $\sigma_L^2$  becomes actually homogeneous to a time squared while the diffusion coefficient in the equation, noted D, can then be related to the actual longitudinal diffusion coefficient by the relation:

$$D_L = Dv_d^2 \quad (6.7)$$

where  $v_d$  is the drift velocity measured in Section 6.3.

In order to compute the diffusion, the chamber is first divided in a number of time slices. Each time slice corresponds to a range of drift time for the events it contains. The slicing is of 20  $\mu s$  for the *xenon* run and of 6  $\mu s$  for the *helium* so that the slices have a similar size over the  $z$  direction. The detector is therefore divided in 14 time slices. In each one of these time slices, the mean time spread of the S2 signal must be computed. To do so, a skewed gaussian fit is applied to the distribution of events according to their S2 time spread (the time RMS squared). Only the data points above 10% of the peak height are selected for the fit. The reason for the skew observed in the time spread distribution comes from the fluctuation of the spread within the time slice. It might also partly be due to the longitudinal diffusion that happens inside the EL stage. While not very pronounced it gives a positive skewness to the RMS of the S2 peak distribution. An example of the fit obtained

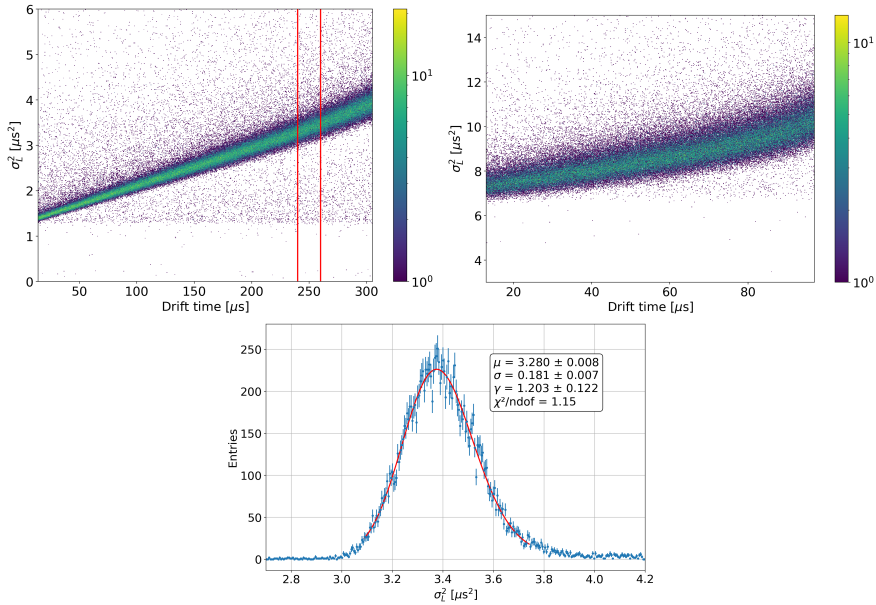


**Figure 6.6.** The top panels show histograms of the time spread versus the drift time for *xenon* (left) and *helium* (right) the scale is logarithmic. Below is an example of a fit done to a time slice highlighted between red vertical lines on the top left panel.

for a time slice is shown in Figure 6.6. The mean time spread is taken as the value below the peak which is retrieved numerically. The error associated is that of the center of the distribution  $\mu$ .

Additional to the mean time spread, the corresponding mean drift times of the slices are also computed. Indeed, within a time slice the distribution of events is not centered around the middle of the time bin. That stems from the fact that the number of events per unit of drift time increases with the drift time. This behavior is due to the *S1* signal being more likely to be detected when it happens close to the PMTs, hence at high drift time.

A linear fit is finally performed to model the dependency of the diffusion spread with the drift time, as is given in Equation 6.6. The fit is done accounting for a bit more than the last third of the chamber, in other words, it accounts for the last six points. Not only is it to ensure that the time spread of the *S2* observed is dominated by the diffusion,

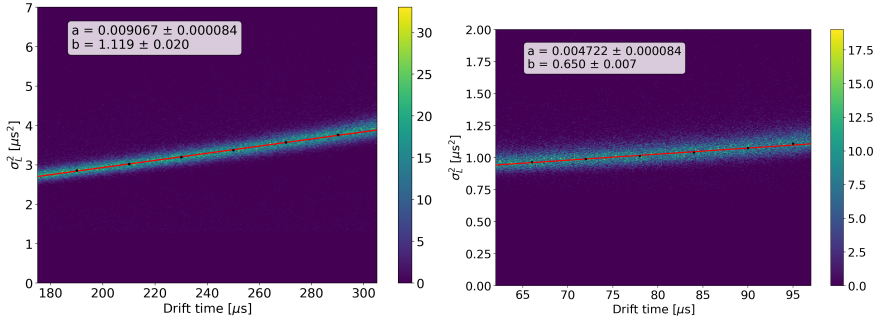


**Figure 6.7.** Panels showing the linear fit (in red) on the data to retrieve the longitudinal diffusion coefficients. The left panel is for *xenon* and the right one for *helium*.

it also corresponds to the slices containing the most statistics. The final fit for both *xenon* and *helium* are shown in Figure 6.7.

After converting the parameters of the fit, the longitudinal diffusion coefficients are obtained. They are reported in Table 6.5 where they can be compared to the values predicted by Magboltz. The reduced diffusion coefficient, noted  $D_{L*}$  allows direct comparison between results taken at different pressure and electric field, it is computed according to the following formula<sup>2</sup>

$$D_{L*} = \sqrt{1000 \frac{293[K]}{T} \frac{2D_L P}{v_d}} \quad (6.8)$$

The sizeable discrepancy between the value measured for the *xenon* data and the corresponding Magboltz prediction is not fully understood. It can be conjectured that due to the diffusion being low, the gaussian spread is not reflected in the RMS of the  $S2$  well enough; it remains perturbed by the light spread induced by the size of the EL gap, even at high drift. However the reduced diffusion coefficient obtained appears compatible with the previous measurement achieved in high pressure xenon [138].

<sup>2</sup>The parameters in the expression are expressed in the units in which they are reported in the present chapter.



| Quantity   | Xenon run      | Helium run      |
|--|----------------|-----------------|
| $D_L$ [cm <sup>2</sup> /s]                                     | 40.915 ± 0.896 | 214.188 ± 6.660 |
| $D_L^*$ [ $\sqrt{\text{bar}}$ $\mu\text{m}/\sqrt{\text{cm}}$ ] | 886 ± 17       | 1134 ± 26       |
| Magboltz   | 69.72 ± 0.42   | 233.0 ± 8.4     |

**Table 6.5.** Measured longitudinal diffusion coefficient for both runs. The reduced coefficient is calculated according to the formula

## 6.6 Transverse diffusion

The transverse diffusion is widening the electron swarm along the  $x$  and  $y$  directions and thus the PMTs are not sensitive to it. It affects the response of the tracking plane sensors. In NEXT-DEMO++ the SiPMs of the tracking plane are separated from each other by a pitch of 1 cm. This granularity has been high enough to measure the transverse diffusion previously on NEXT-White in pure xenon at high pressure.

### 6.6.1 Point Spread Functions

Throughout the endeavour of measuring the transverse diffusion coefficient it is required to compute the average Point Spread Function (PSF) of Kr events for various time slices of the chamber. The reconstructed data used in the previous sections do not have the necessary detailed information of the tracking plane response to the Kr events. The data resulting from the peak finder algorithm are processed through another reconstruction algorithm in lieu of the one focusing specifically on point-like events.

A SiPM is considered activated if it collects a level of light above a specified threshold. For each event, the algorithm is processing every activated SiPM signal corresponding to an  $S_2$  signal into what is labeled a *hit*. Each *hit* contains the information about the  $x$  and  $y$  positions of an activated SiPM and the charge it collected. They also include the energy reconstructed by the energy plane and the total charge collected by the tracking plane for that event. The same cuts applied to the data reconstructed with the first algorithm described in Section 6.1.2 are also applied here: only the Kr events selected

previously are reconstructed as a collection of *hits*. Thus only the Kr events are used for computing the PSFs.

As for the longitudinal diffusion measurement, the chamber is divided in time slices. The slicing chosen for *xenon* is the same as before: 20  $\mu\text{s}$ . However the one for *helium* has been slightly increased to 7.5  $\mu\text{s}$  to increase the amount of events per slice.

The PSF corresponding to each time slice is an average of the PSFs of all the events within that time slice. For each event the charge collected by each *hit* is normalised by the total charge collected for that event. The relative position of the SiPM of each *hit* with respect to the reconstructed  $x$ - $y$  position of the event is weighted with its normalised charge collected and filled in a 2D histogram with a bin (pixel) size of 1  $\text{mm}^2$ . The PSF of an event is built by repeating the aforementioned procedure for every *hit*.

Comparing the PSFs built for a time slice at a low drift time and at a high drift time shows the effect of the transverse diffusion on the electron swarm. By comparing this effect between the *xenon* data and the *helium* data one can see clearly that the transverse diffusion is considerably reduced in the HeXe mixture. This comparison is shown in Figure 6.8.

### 6.6.2 Transverse coefficient measurement

The transverse diffusion coefficient,  $D_T$ , is defined in the same manner as the longitudinal diffusion coefficient:

$$\sigma_T^2(t_{drift}) = S_T^2 + 2D_T t_{drift} \quad (6.9)$$

The transverse spread has to be extracted from the PSFs.

Each PSF has a spread over the  $x$  direction and a spread over the  $y$  direction. In principle there is no difference between them. The approach chosen is to compute the spread along  $x$  and  $y$  independently. The global transverse spread being an average of the two. In addition, since the origin of the X-Y plane on which the PSFs are projected adjoins the four central pixels, each 1D profile of the PSF is slightly off-axis by 0.5 mm given the pixel size. So there again, two spreads are computed along each direction: for the central pixels with a positive coordinate and for the central pixels with a negative coordinate. These

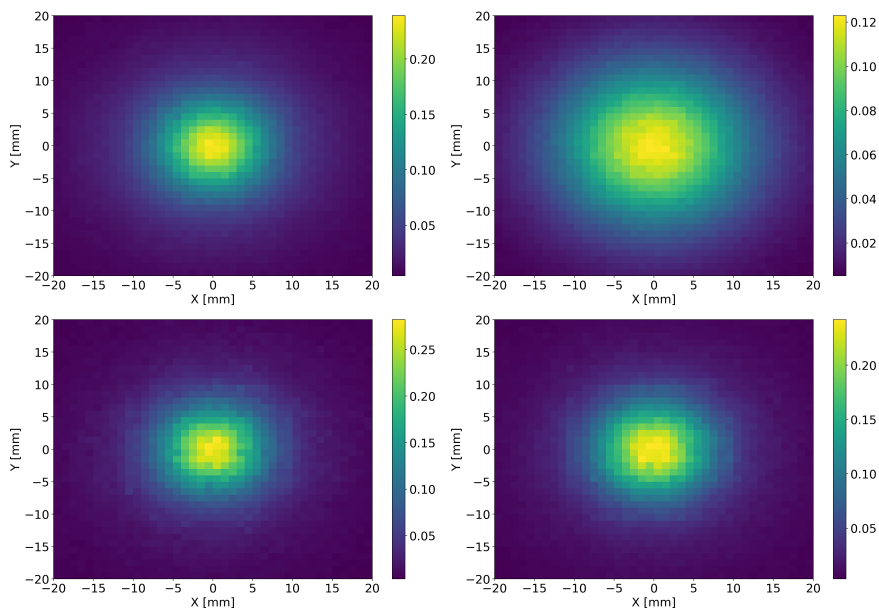


**Figure 6.8.** Panels showing the effect of the transverse diffusion on the PSFs in pure xenon and in a HeXe mixture. The top panels are PSFs of the *xenon* data and the bottom panels are PSFs of the *helium* data. The left ones correspond to low drift events and the right ones correspond to high drift events.

two spreads are averaged to get the spread along the corresponding direction.

Each PSF arises from two convolved effects: on the one hand it results from the interception of light emitted isotropically from a point-like source by a plane at a given distance; on the other hand this point-like source is widened by diffusion. The first effect is described by a Cauchy-Lorentz distribution and the second by a gaussian distribution. Thus the PSFs observed can be described on a 1D profile by the convolution of the two distributions: a Voigt profile.

The Cauchy-Lorentz scale is calculated by finding the best fit for the first time slice profiles. The fits to the PSF profiles for all the other time slices is done with that parameter constrained to the value calculated. The two gaussian spreads for each time slice, along the  $x$  and  $y$  directions are obtained from the resulting best fits to the profiles

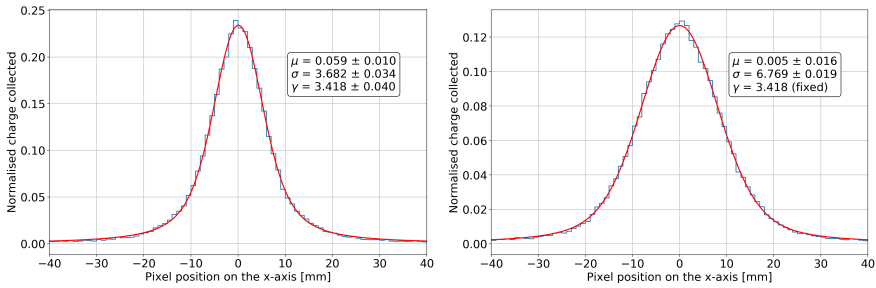


**Figure 6.9.** Examples of the Voigt profile best fit to the profiles of the PSFs. These examples are from the *xenon* data: the left panel is for the lowest drift PSF (average drift time of  $35 \mu\text{s}$ ) and the right panel is for a high drift PSF ( $275 \mu\text{s}$ ). For the lowest drift PSF the Cauchy-Lorentz scale factor is left free. Its numerical evaluation is used as a constraint for the subsequent fits.

considered. Two fits are shown in Figure 6.9 as an example of the procedure.

As for the longitudinal diffusion, the mean drift time of each time slice is computed and a linear fit is then performed to model the dependency of the diffusion spread with the drift time given in Equation 6.9. The resulting linear fits to the data are shown in Figure 6.10 and the measured diffusion coefficients are reported together with the Magboltz results in Table 6.6. The reduced transverse coefficients are also computed in the same manner as was done previously.

The results given for *xenon* seem very in line with the Magboltz expectation proving the validity of the procedure. But the results given for the *helium* data do not show the same consistency. They also feature a sizeable discrepancy between the spreads computed along the  $x$  and  $y$  directions hinting that the PSF reconstruction suffered from the two main hinderances of the *helium* dataset. Firstly, according to Table 6.2 it contains about 20% fewer events than the *xenon* dataset; secondly, it can be seen in Figure 6.2 that the light collected by the SiPMs per Kr event is greatly reduced compared to the *xenon* run.

Notwithstanding, the diffusion measured for the HeXe mixture shows a significant reduction factor between 2 and 3 with respect to pure xenon. While expected it remains the first measurement of the transverse diffusion in a HeXe mixture and confirms the HeXe mixture as a serious low-diffusion mixture for a NEXT-like detector.

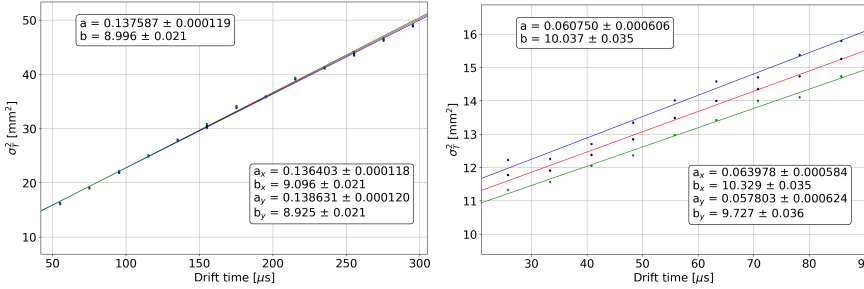


**Figure 6.10.** Panels showing the linear fit (in red) on the data to retrieve the transverse diffusion coefficients. The left panel is for *xenon* and the right one for *helium*. The data points and linear fits corresponding to the *x* and *y* responses are shown respectively in blue and green, their best fit values are also reported.

| Quantity   | <i>Xenon</i> run    | <i>Helium</i> run   |
|--|---------------------|---------------------|
| $D_T$ [cm <sup>2</sup> /s]                                       | $687.935 \pm 0.596$ | $303.749 \pm 3.028$ |
| $D_{T^*}$ [ $\sqrt{\text{bar}}$ $\mu\text{m}/\sqrt{\text{cm}}$ ] | $3637 \pm 33$       | $1357 \pm 19$       |
| Magboltz   | $697.45 \pm 3.05$   | $247.1 \pm 28.1$    |

**Table 6.6.** Measured transverse diffusion coefficient for both runs.

## 6.7 Summary

The detector NEXT-DEMO++ was used to study a 15% HeXe mixture at 9.1 bar and to compare its properties to pure xenon at the same pressure. The study was performed relying on the point-like energy depositions coming from the decay of  $^{83m}\text{Kr}$  and distributed uniformly within the active volume of the detector.

The properties of the *S1* of the HeXe mixture were extremely similar to the properties of the *S1* in pure xenon. This was the behavior expected and confirms that HeXe mixtures would have the same sensitivity to the *S1* signal as xenon.

The energy resolution measured on the Kr peak at 41.56 keV showed a mild degradation in HeXe. Despite that the light yield behavior between xenon and HeXe mixtures has been shown numerically [192] and experimentally [201] to be nearly the same, there is a

higher EL threshold in HeXe. Thus, an amplification field too low leads to a sizeable relative drop of the light produced, which is consistent with the observation and degrades the energy resolution.


The electron transport parameters were also evaluated. The drift velocity in HeXe was measured to be much higher than that of pure xenon and very well in line with the expected value given by Magboltz. It should not be concluded that the drift velocity in HeXe is systematically that high compared to pure xenon: under the typical range of drift field and pressure at which NEXT detectors are operated the drift velocity of HeXe mixtures is fairly variable.

The longitudinal diffusion was also evaluated by using the variation of the time spread of the S2 signal with the drift time. The diffusion was observed to be higher in HeXe than in xenon, but that is not worrisome as this was expected for a 15% HeXe mixture at 9.1 bar. A 15% HeXe mixture at 15 or 17.65 bar would have a much lower longitudinal diffusion.

Finally, the transverse diffusion in a HeXe mixture was measured at high pressure and compared to that of pure xenon for the first time. Within the range of conditions in NEXT detectors the transverse diffusion is more of an intrinsic property of a given mixture. It has been measured to be between two and three times lower in a 15% HeXe mixture than in pure xenon, which is again in very good agreement with the predictions.

This study was performed for preliminary runs of what was supposed to be a systematic study of HeXe mixtures. Notwithstanding, the strength of this result validates the approach of using a HeXe mixture as a competitive low-diffusion mixture for  $0\nu\beta\beta$  searches in  $^{136}\text{Xe}$ . A few key requirements still need to be achieved regarding the helium-xenon separation, a stable and high enough amplification field associated with an optimized light collection efficiency.

# Conclusions and prospects



The neutrino is an elementary particle of the standard model of particle physics. With the discovery of the neutrino oscillations, about twenty years ago, came the proof that neutrinos do have a mass. The mass of the neutrino is beyond reach of the cutting edge experiments, at the time at which these lines are written. Notwithstanding, this discovery makes the neutrino a potential window towards new physics beyond the standard model. To explain the origin of the neutrino mass, the most elegant mechanism involves the neutrino being a Majorana particle (explained in Chapter 1). A Majorana neutrino in conjunction with a CP violation in the leptonic sector could also provide a mechanism explaining the matter-antimatter asymmetry observed in the early universe.

The experimental signature of a Majorana neutrino could be observed realistically only as a special mode of a double beta decay. The double beta decay is a rare decay that has been observed for numerous nuclides. In a classical fashion, a double beta decay consists of a nuclide changing its atomic number by two units while emitting two electrons and two antineutrinos. Should the neutrino be a Majorana particle, a zero-neutrino mode would be allowed, violating the lepton number by two units. Thus, observing unambiguously a neutrinoless double beta decay would be a direct proof of the Majorana nature of the neutrino (described in Chapter 2).

A number of experiments have chased this elusive decay during the last decades. So far they all met a null signal. These experiments span a large number of detection techniques for a wide variety of potential double beta emitters, a number of them were presented in Chapter 2. The community is currently working on a few experiments aiming for a sensitivity to a zero-neutrino mode with a half-life of  $10^{27}$

years and beyond. The flagships of the next generation are LEGEND (on  $^{76}\text{Ge}$ ), CUPID (on  $^{100}\text{Mo}$ ) and nEXO (on  $^{136}\text{Xe}$ ).

The NEXT experiment has been developing high pressure xenon TPCs over the past decade. This technological choice provides two main attractive features. The first one is a sub-percent energy resolution. The energy resolution reduces the size of the energy region of interest and therefore the background coming from external events as well as from the two-neutrino mode of the double beta decay. The second crucial asset is the possibility to reconstruct the topology of the events occurring inside the detector due to the extended nature of the tracks. This topology reconstruction serves as a powerful tool for rejecting further background.

The most recent detector operated by the collaboration, NEXT-White, met all the expectations that were put to it. It demonstrated with 10 kg of enriched-xenon a sub-percent energy resolution at the Q-value of the double beta decay and it proved the power of the topology-based background rejection. Its stable operation validated the technological choices made and allowed it to make its own measurement of the two-neutrino mode.

Its successor, NEXT-100, is currently under construction. It will operate, as its name suggests, with 100 kg of xenon and aim at providing a competitive half-life limit on the neutrinoless double beta decay of  $^{136}\text{Xe}$ . The challenge of building such a large detector lies partly in its critical electrical components that shape the electric fields inside the TPC. Electrostatic simulations of the field cage was performed and described in Chapter 3.

The main hinderance that gaseous xenon, as a detection medium, brings to a TPC is its natural high diffusion to drifting electrons. This high diffusion harms the topological reconstruction and therefore harms the background rejection that is a crucial feature of the technology. Chapter 4 presented the line of search within the collaboration to alleviate this issue. This chapter includes the proposal to use helium as an additive to xenon in order to lower the diffusion which is the central subject of the work developed in this thesis. A number of simulations were performed to assess the potential of a helium-xenon mixture mainly in terms of diffusion and energy resolution. While other mixtures lower the diffusion at the cost of key features that xenon brings, the helium-xenon (HeXe) mixtures appears capable of



lowering substantially the diffusion at a very low cost.

Having been identified as a very promising low-diffusion mixture, HeXe mixtures were set to be tested within the collaboration. Chapter 5 describes thoroughly the prototype NEXT-DEMO++ that was built with the primary goal to confirm that an optical TPC can be operated with a HeXe mixture without harming the helium-sensitive photomultipliers. The second goal of NEXT-DEMO++ was to measure the electron transport properties of HeXe mixtures.

The characterisation of a HeXe mixture was therefore performed and compared to a reference pure xenon mixture. This study is covered extensively in Chapter 6. The most notable result is a first measurement of the transverse diffusion coefficient in a 15% HeXe mixture confirming experimentally a reduction factor between two and three with respect to pure xenon.

The NEXT collaboration is already designing its first tonne-scale detector, NEXT-HD that will be built at the LSC starting in 2026. This detector is designed in a way that will allow it to be operated with a low-diffusion HeXe mixture. It has been seen that for the energy resolution of a HeXe mixture to be competitive with that of pure xenon the conditions are a high amplification field as well as an optimized light collection efficiency. These are two important lines of research of the NEXT-HD program. The investigation involves using optical fibers surrounding the active volume for the energy measurement and a new design for the EL stage that would avoid electrostatic deflections while allowing for a stable higher amplification field.



# Bibliography

- [1] J Chadwick. Intensitätsverteilung im magnetischen Spectrum der  $\beta$ -Strahlen von radium B + C. *Verhandl. Dtsc. Phys. Ges.*, 16:383, 1914.
- [2] Charles Drummond Ellis, W. A. Wooster, and Ernest Rutherford. The average energy of disintegration of radium E. *Proceedings of the Royal Society of London. Series A, Containing Papers of a Mathematical and Physical Character*, 117(776):109–123, 1927.
- [3] W. Pauli. Dear radioactive ladies and gentlemen. *Phys. Today*, 31N9:27, 1978.
- [4] Fred L. Wilson. Fermi's theory of beta decay. *American Journal of Physics*, 36(12):1150–1160, 1968.
- [5] F. Joliot and I. Curie. Artificial production of a new kind of radio-element. *Nature*, 133(3354):201–202, Feb 1934.
- [6] H. Bethe and R. Peierls. The "Neutrino". *Nature*, 133(3362):532–532, Apr 1934.
- [7] B. Pontecorvo. Inverse beta process. *Camb. Monogr. Part. Phys. Nucl. Phys. Cosmol.*, 1:25–31, 1991.
- [8] Raymond Davis. Attempt to Detect the Antineutrinos from a Nuclear Reactor by the  $\text{Cl}^{37}(\bar{\nu}, e^-)\text{A}^{37}$  Reaction. *Phys. Rev.*, 97:766–769, Feb 1955.
- [9] C. L. Cowan, F. Reines, F. B. Harrison, H. W. Kruse, and A. D. McGuire. Detection of the free neutrino: a confirmation. *Science*, 124(3212):103–104, 1956.

- [10] Frederick Reines and Clyde L. Cowan, jr. The neutrino. *Nature*, 178(4531):446–449, Sep 1956.
- [11] J. Csikai. Photographic evidence for the existence of the neutrino. *Il Nuovo Cimento (1955-1965)*, 5(4):1011–1012, Apr 1957.
- [12] G. Danby, J-M. Gaillard, K. Goulianos, L. M. Lederman, N. Mistry, M. Schwartz, and J. Steinberger. Observation of high-energy neutrino reactions and the existence of two kinds of neutrinos. *Phys. Rev. Lett.*, 9:36–44, Jul 1962.
- [13] M. L. Perl et al. Evidence for anomalous lepton production in  $e^+ - e^-$  annihilation. *Phys. Rev. Lett.*, 35:1489–1492, Dec 1975.
- [14] M. L. Perl et al. Properties of the proposed  $\tau$  charged lepton. *Physics Letters B*, 70(4):487–490, 1977.
- [15] K. Kodama et al. Observation of tau neutrino interactions. *Physics Letters B*, 504(3):218–224, 2001.
- [16] D. Decamp et al. Determination of the number of light neutrino species. *Physics Letters B*, 231(4):519–529, 1989.
- [17] John N. Bahcall. Solar neutrinos. I. theoretical. *Phys. Rev. Lett.*, 12:300–302, Mar 1964.
- [18] Raymond Davis. Solar neutrinos. II. experimental. *Phys. Rev. Lett.*, 12:303–305, Mar 1964.
- [19] Raymond Davis, Don S. Harmer, and Kenneth C. Hoffman. Search for neutrinos from the sun. *Phys. Rev. Lett.*, 20:1205–1209, May 1968.
- [20] Neutrino flux from sun is lower than expected. *Physics Today*, 21(3):73–73, 1968.
- [21] K. S. Hirata et al. Observation of  $^8\text{B}$  solar neutrinos in the Kamiokande-II detector. *Phys. Rev. Lett.*, 63:16–19, Jul 1989.
- [22] P. Anselmann et al. Solar neutrinos observed by GALLEX at Gran Sasso. *Physics Letters B*, 285(4):376–389, 1992.

- [23] J.N. Abdurashitov et al. Results from SAGE (the russian-american gallium solar neutrino experiment). *Physics Letters B*, 328(1):234–248, 1994.
- [24] IN2P3. History of the neutrino, accessed 14 November 2021. <https://neutrino-history.in2p3.fr/solar-neutrinos/>.
- [25] V. Gribov and B. Pontecorvo. Neutrino astronomy and lepton charge. *Physics Letters B*, 28(7):493–496, 1969.
- [26] Ziro Maki, Masami Nakagawa, and Shoichi Sakata. Remarks on the Unified Model of Elementary Particles. *Progress of Theoretical Physics*, 28(5):870–880, 11 1962.
- [27] B. Pontecorvo. Neutrino experiments and the problem of conservation of leptonic charge. *Soviet Physics JETP*, 26(5):984–988, 1968.
- [28] L. Wolfenstein. Neutrino oscillations in matter. *Phys. Rev. D*, 17:2369–2374, May 1978.
- [29] S. P. Mikheyev and A. Yu. Smirnov. Resonant amplification of  $\nu$  oscillations in matter and solar-neutrino spectroscopy. *Il Nuovo Cimento C*, 9(1):17–26, Jan 1986.
- [30] Y. Fukuda et al. Measurements of the solar neutrino flux from Super-Kamiokande’s first 300 days. *Phys. Rev. Lett.*, 81:1158–1162, Aug 1998.
- [31] T. Kajita. Atmospheric neutrino results from Super-Kamiokande & Kamiokande - evidence for  $\nu_\mu$  oscillations, Talk at Neutrino 1998. <http://www-sk.icrr.u-tokyo.ac.jp/nu98/scan/index.html>.
- [32] Q. R. Ahmad et al. Measurement of the rate of  $\nu_e + d \rightarrow p + p + e^-$  interactions produced by  $^8\text{B}$  solar neutrinos at the Sudbury Neutrino Observatory. *Phys. Rev. Lett.*, 87:071301, Jul 2001.
- [33] Q. R. et al. Ahmad. Direct evidence for neutrino flavor transformation from neutral-current interactions in the Sudbury Neutrino Observatory. *Phys. Rev. Lett.*, 89:011301, Jun 2002.

- [34] B. Pontecorvo. Inverse beta processes and nonconservation of lepton charge. *Sov. Phys. JETP*, 7:172–173, 1958. [Zh. Eksp. Teor. Fiz.34,247(1957)].
- [35] P. F. de Salas, D. V. Forero, S. Gariazzo, P. Martínez-Miravé, O. Mena, C. A. Ternes, M. Tórtola, and J. W. F. Valle. 2020 global reassessment of the neutrino oscillation picture. *Journal of High Energy Physics*, 2021(2):71, Feb 2021.
- [36] Alejandro Segarra. *Breaking of Discrete Symmetries and Global Lepton Number in Neutrino Physics*. PhD thesis, IFIC, 2019.
- [37] F. Perrin. *Comptes rendus* 197, 1625 (1933).
- [38] Emil J. Konopinski.  $h^3$  and the mass of the neutrino. *Phys. Rev.*, 72:518–519, Sep 1947.
- [39] S. C. Curran, J. Angus, and A. L. Cockroft. The beta-spectrum of tritium. *Phys. Rev.*, 76:853–854, Sep 1949.
- [40] G. C. Hanna and B. Pontecorvo. The  $\beta$ -Spectrum of  $H^3$ . *Phys. Rev.*, 75:983–984, Mar 1949.
- [41] Donald R. Hamilton, W. Parker Alford, and Leonard Gross. Upper limits on the neutrino mass from the tritium beta spectrum. *Phys. Rev.*, 92:1521–1525, Dec 1953.
- [42] Karl-Erik Bergkvist. A high-luminosity, high-resolution study of the end-point behaviour of the tritium  $\beta$ -spectrum (i). basic experimental procedure and analysis with regard to neutrino mass and neutrino degeneracy. *Nuclear Physics B*, 39:317–370, 1972.
- [43] M. Fritschi, E. Holzschuh, W. Kündig, J.W. Petersen, R.E. Pixley, and H. Stüssi. An upper limit for the mass of  $\psi_{3/2}$  from tritium  $\beta$ -decay. *Physics Letters B*, 173(4):485–489, 1986.
- [44] V.M Lobashev et al. Direct search for mass of neutrino and anomaly in the tritium beta-spectrum. *Physics Letters B*, 460(1):227–235, 1999.

- [45] M. Aker et al. Direct neutrino-mass measurement with sub-electronvolt sensitivity. *Nature Physics*, 18(2):160–166, Feb 2022.
- [46] David Lorca Galindo. *SiPM based tracking for detector calibration in NEXT*. PhD thesis, U. Valencia, 2015.
- [47] K. Assamagan et al. Measurement of the muon momentum in pion decay at rest using a surface muon beam. *Physics Letters B*, 335(2):231–236, 1994.
- [48] R. Barate et al. and ALEPH Collaboration. An upper limit on the  $\tau$  neutrino mass from three- and five-prong tau decays. *The European Physical Journal C - Particles and Fields*, 2(3):395–406, Apr 1998.
- [49] David N. Spergel and John N. Bahcall. The mass of the electron neutrino: Monte Carlo studies of SN 1987A observations. *Physics Letters B*, 200(3):366–372, 1988.
- [50] Thomas J. Loredo and Donald Q. Lamb. Bayesian analysis of neutrinos observed from supernova SN 1987A. *Phys. Rev. D*, 65:063002, Feb 2002.
- [51] P.A. Zyla et al. Review of Particle Physics. *PTEP*, 2020(8):083C01, 2020.
- [52] Ettore Majorana. Teoria simmetrica dell'elettrone e del positrone. *Il Nuovo Cimento (1924-1942)*, 14(4):171, Sep 2008.
- [53] Sacha Davidson, Enrico Nardi, and Yosef Nir. Leptogenesis. *Physics Reports*, 466(4):105–177, 2008.
- [54] M. Goeppert-Mayer. Double beta-disintegration. *Phys. Rev.*, 48:512–516, Sep 1935.
- [55] T. Kirsten, O. A. Schaeffer, E. Norton, and R. W. Stoenner. Experimental Evidence for the Double-Beta Decay of  $\text{Te}^{130}$ . *Phys. Rev. Lett.*, 20:1300–1303, Jun 1968.
- [56] S. R. Elliott, A. A. Hahn, and M. K. Moe. Direct evidence for two-neutrino double-beta decay in  $^{82}\text{Se}$ . *Phys. Rev. Lett.*, 59:2020–2023, Nov 1987.

- [57] K.A. Olive. Review of particle physics. 40(10):100001, oct 2016.
- [58] R. Arnold et al. Measurement of the double-beta decay half-life and search for the neutrinoless double-beta decay of  $^{48}\text{Ca}$  with the NEMO-3 detector. *Phys. Rev. D*, 93:112008, Jun 2016.
- [59] C. Alduino et al. Measurement of the two-neutrino double-beta decay half-life of  $^{130}\text{Te}$  with the CUORE-0 experiment. *The European Physical Journal C*, 77(1):13, Jan 2017.
- [60] W. H. Furry. On transition probabilities in double beta-disintegration. *Phys. Rev.*, 56:1184–1193, Dec 1939.
- [61] E. Aprile et al. Observation of two-neutrino double electron capture in  $^{124}\text{Xe}$  with XENON1T. *Nature*, 568(7753):532–535, Apr 2019.
- [62] Julian Heeck and Werner Rodejohann. Neutrinoless quadruple beta decay. 103(3):32001, aug 2013.
- [63] Martin Hirsch, Rahul Srivastava, and José W.F. Valle. Can one ever prove that neutrinos are Dirac particles? *Physics Letters B*, 781:302–305, 2018.
- [64] R. Arnold et al. Search for neutrinoless quadruple- $\beta$  decay of  $^{150}\text{Nd}$  with the NEMO-3 detector. *Phys. Rev. Lett.*, 119:041801, Jul 2017.
- [65] J. Schechter and J. W. F. Valle. Neutrinoless double- $\beta$  decay in  $\text{SU}(2) \times \text{U}(1)$  theories. *Phys. Rev. D*, 25:2951–2954, Jun 1982.
- [66] Michael Duerr, Manfred Lindner, and Alexander Merle. On the quantitative impact of the Schechter-Valle theorem. *Journal of High Energy Physics*, 2011(6):91, Jun 2011.
- [67] Masaru Doi, Tsuneyuki Kotani, and Eiichi Takasugi. Double Beta Decay and Majorana Neutrino. *Progress of Theoretical Physics Supplement*, 83:1–175, 03 1985.
- [68] J. Kotila and F. Iachello. Phase-space factors for double- $\beta$  decay. *Phys. Rev. C*, 85:034316, Mar 2012.



- [69] Sabin Stoica and Mihail Mirea. Phase space factors for double-beta decays. *Frontiers in Physics*, 7:12, 2019.
- [70] J. Menéndez, A. Poves, E. Caurier, and F. Nowacki. Disassembling the nuclear matrix elements of the neutrinoless  $\beta\beta$  decay. *Nuclear Physics A*, 818(3):139–151, 2009.
- [71] Fedor Šimkovic, Vadim Rodin, Amand Faessler, and Petr Vogel.  $0\nu\beta\beta$  and  $2\nu\beta\beta$  nuclear matrix elements, quasiparticle random-phase approximation, and isospin symmetry restoration. *Phys. Rev. C*, 87:045501, Apr 2013.
- [72] Juhani Hyvärinen and Jouni Suhonen. Nuclear matrix elements for  $0\nu\beta\beta$  decays with light or heavy majorana-neutrino exchange. *Phys. Rev. C*, 91:024613, Feb 2015.
- [73] J. Barea, J. Kotila, and F. Iachello.  $0\nu\beta\beta$  and  $2\nu\beta\beta$  nuclear matrix elements in the interacting boson model with isospin restoration. *Phys. Rev. C*, 91:034304, Mar 2015.
- [74] Nuria López Vaquero, Tomás R. Rodríguez, and J. Luis Egido. Shape and pairing fluctuation effects on neutrinoless double beta decay nuclear matrix elements. *Phys. Rev. Lett.*, 111:142501, Sep 2013.
- [75] L. S. Song, J. M. Yao, P. Ring, and J. Meng. Nuclear matrix element of neutrinoless double- $\beta$  decay: Relativity and short-range correlations. *Phys. Rev. C*, 95:024305, Feb 2017.
- [76] Werner Rodejohann. Neutrino-less double beta decay and particle physics. *International Journal of Modern Physics E*, 20(09):1833–1930, 2011.
- [77] Andrei Neacsu, Vasile Alin Sevestrean, and Sabin Stoica. Brief review of the results regarding the possible underlying mechanisms driving the neutrinoless double beta decay. *Frontiers in Physics*, 9:241, 2021.
- [78] J.J Gómez-Cadenas, J Martín-Albo, M Sorel, P Ferrario, F Monrabal, J Muñoz, P Novella, and A Poves. Sense and sensitivity of double beta decay experiments. *Journal of Cosmology and Astroparticle Physics*, 2011(06):007–007, jun 2011.

- [79] Steven R. Elliott and Petr Vogel. Double beta decay. *Annual Review of Nuclear and Particle Science*, 52(1):115–151, 2002.
- [80] Javier Menéndez. Double beta decay matrix elements, July 2020.
- [81] Michelle J. Dolinski, Alan W.P. Poon, and Werner Rodejohann. Neutrinoless double-beta decay: Status and prospects. *Annual Review of Nuclear and Particle Science*, 69(1):219–251, 2019.
- [82] A. Bettini. The world deep underground laboratories. *The European Physical Journal Plus*, 127(9):114, Sep 2012.
- [83] Alessandro Bettini. New underground laboratories: Europe, Asia and the Americas. *Physics of the Dark Universe*, 4:36–40, 2014. DARK TAUP2013.
- [84] M. K. Moe. Detection of neutrinoless double-beta decay. *Phys. Rev. C*, 44:R931–R934, Sep 1991.
- [85] M. Agostini et al. Final results of GERDA on the search for neutrinoless double- $\beta$  decay. *Phys. Rev. Lett.*, 125:252502, Dec 2020.
- [86] D. Q. Adams et al. Improved limit on neutrinoless double-beta decay in  $^{130}\text{Te}$  with CUORE. *Phys. Rev. Lett.*, 124:122501, Mar 2020.
- [87] G. Anton et al. Search for neutrinoless double- $\beta$  decay with the complete EXO-200 dataset. *Phys. Rev. Lett.*, 123:161802, Oct 2019.
- [88] M. Agostini et al. Searching for neutrinoless double beta decay with GERDA. *Journal of Physics: Conference Series*, 1342:012005, Jan 2020.
- [89] E.W. Hoppe et al. Reduction of radioactive backgrounds in electroformed copper for ultra-sensitive radiation detectors. *Nuclear Instruments and Methods in Physics Research Section A: Accelerators, Spectrometers, Detectors and Associated Equipment*, 764:116–121, 2014.

- [90] S. I. Alvis et al. Search for neutrinoless double- $\beta$  decay in  $^{76}\text{Ge}$  with 26 kg yr of exposure from the Majorana Demonstrator. *Phys. Rev. C*, 100:025501, Aug 2019.
- [91] Davide Chiesa. The CUORE experiment at LNGS. In *18th Lomonosov Conference on Elementary Particle Physics*, pages 90–93, 2019.
- [92] J. B. Albert et al. Search for majorana neutrinos with the first two years of EXO-200 data. *Nature*, 510(7504):229–234, Jun 2014.
- [93] N. Ackerman et al. Observation of two-neutrino double-beta decay in  $^{136}\text{Xe}$  with the EXO-200 detector. *Phys. Rev. Lett.*, 107:212501, Nov 2011.
- [94] J. B. Albert et al. Improved measurement of the  $2\nu\beta\beta$  half-life of  $^{136}\text{Xe}$  with the EXO-200 detector. *Phys. Rev. C*, 89:015502, Jan 2014.
- [95] J. B. Albert et al. Searches for double beta decay of  $^{134}\text{Xe}$  with EXO-200. *Phys. Rev. D*, 96:092001, Nov 2017.
- [96] M Auger et al. The EXO-200 detector, part I: detector design and construction. *Journal of Instrumentation*, 7(05):P05010–P05010, may 2012.
- [97] Junpei Shirai for the KamLAND-Zen Collaboration. Results and future plans for the KamLAND-Zen experiment. *Journal of Physics: Conference Series*, 888:012031, sep 2017.
- [98] Yoshihito Gando on behalf of the KamLAND-Zen collaboration. First results of KamLAND-Zen 800. *Journal of Physics: Conference Series*, 1468(1):012142, feb 2020.
- [99] Zen Collaboration. First search for the Majorana nature of neutrinos in the inverted mass ordering region with KamLAND-Zen. *arXiv*, 2022.
- [100] A. Gando et al. Measurement of the double- $\beta$  decay half-life of  $^{136}\text{Xe}$  with the KamLAND-Zen experiment. *Phys. Rev. C*, 85:045504, Apr 2012.

- [101] V. Albanese et al. The SNO+ experiment. *Journal of Instrumentation*, 16(08):P08059, aug 2021.
- [102] S. Ajimura et al. Low background measurement in CANDLES-III for studying the neutrinoless double beta decay of  $^{48}\text{Ca}$ . *Phys. Rev. D*, 103:092008, May 2021.
- [103] T. Kishimoto, K. Matsuoka, T. Fukumoto, and S. Umehara. Calcium isotope enrichment by means of multi-channel counter-current electrophoresis for the study of particle and nuclear physics. *Progress of Theoretical and Experimental Physics*, 2015(3), 03 2015. 033D03.
- [104] R. Arnold et al. Probing new physics models of neutrinoless double beta decay with SuperNEMO. *The European Physical Journal C*, 70(4):927–943, Dec 2010.
- [105] Yoann Kermaidic. GERDA, Majorana and LEGEND - towards a background-free ton-scale Ge76 experiment, July 2020.
- [106] N. Abgrall et al. LEGEND-1000 Preconceptual Design Report, 2021.
- [107] The CUPID Interest Group. CUPID pre-CDR, 2019.
- [108] J. B. Albert et al. Sensitivity and discovery potential of the proposed nEXO experiment to neutrinoless double- $\beta$  decay. *Phys. Rev. C*, 97:065503, Jun 2018.
- [109] C. Adams et al. Sensitivity of a tonne-scale NEXT detector for neutrinoless double-beta decay searches. *Journal of High Energy Physics*, 2021(8):164, Aug 2021.
- [110] D. R. Nygren. A time projection chamber. PEP-198, 1975.
- [111] Jay N. Marx and David R. Nygren. The Time Projection Chamber. *Physics Today*, 31(10):46–53, 1978.
- [112] R. Luescher et al. Search for  $\beta\beta$  decay in  $^{136}\text{Xe}$ : new results from the Gotthard experiment. *Physics Letters B*, 434(3):407–414, 1998.

- [113] David Nygren. High-pressure xenon gas electroluminescent TPC for  $0\nu\beta\beta$ -decay search. *Nuclear Instruments and Methods in Physics Research Section A: Accelerators, Spectrometers, Detectors and Associated Equipment*, 603(3):337–348, 2009.
- [114] Matthew Redshaw, Elizabeth Wingfield, Joseph McDaniel, and Edmund G. Myers. Mass and Double-Beta-Decay  $Q$  Value of  $^{136}\text{Xe}$ . *Phys. Rev. Lett.*, 98:053003, Feb 2007.
- [115] V Álvarez et al. Ionization and scintillation response of high-pressure xenon gas to alpha particles. *Journal of Instrumentation*, 8(05):P05025–P05025, may 2013.
- [116] R.L. Platzman. Total ionization in gases by high-energy particles: An appraisal of our understanding. *The International Journal of Applied Radiation and Isotopes*, 10(2):116–127, 1961.
- [117] C A B Oliveira, M Sorel, J Martin-Albo, J J Gómez-Cadenas, A L Ferreira, and J F C A Veloso. Energy resolution studies for NEXT. *Journal of Instrumentation*, 6(05):P05007–P05007, may 2011.
- [118] C M B Monteiro et al. Secondary scintillation yield in pure xenon. *Journal of Instrumentation*, 2(05):P05001–P05001, may 2007.
- [119] Christopher Benson, Gabriel D. Orebi Gann, and Victor Gehman. Measurements of the intrinsic quantum efficiency and absorption length of tetraphenyl butadiene thin films in the vacuum ultraviolet regime. *The European Physical Journal C*, 78(4):329, Apr 2018.
- [120] V.M. Gehman et al. Fluorescence efficiency and visible re-emission spectrum of tetraphenyl butadiene films at extreme ultraviolet wavelengths. *Nuclear Instruments and Methods in Physics Research Section A: Accelerators, Spectrometers, Detectors and Associated Equipment*, 654(1):116–121, 2011.
- [121] U. Fano. Ionization yield of radiations. II. the fluctuations of the number of ions. *Phys. Rev.*, 72:26–29, Jul 1947.
- [122] A.J.P.L. Policarpo et al. Detection of soft X-rays with a xenon proportional scintillation counter. *Nuclear Instruments and Methods*, 118(1):221–226, 1974.

- [123] Heikki Sipilä. Energy resolution of the proportional counter. *Nuclear Instruments and Methods*, 133(2):251–252, 1976.
- [124] D.F. Anderson, T.T. Hamilton, W.H.-M. Ku, and R. Novick. A large area, gas scintillation proportional counter. *Nuclear Instruments and Methods*, 163(1):125–134, 1979.
- [125] T. H. V. T. Dias et al. Full-energy absorption of x-ray energies near the Xe L- and K-photoionization thresholds in xenon gas detectors: Simulation and experimental results. *Journal of Applied Physics*, 82(6):2742–2753, 1997.
- [126] Aleksey Bolotnikov and Brian Ramsey. The spectroscopic properties of high-pressure xenon. *Nuclear Instruments and Methods in Physics Research Section A: Accelerators, Spectrometers, Detectors and Associated Equipment*, 396(3):360–370, 1997.
- [127] *Noble Fluids as Detector Media*, chapter 2, pages 7–32. John Wiley & Sons, Ltd, 2006.
- [128] Hamamatsu Photonics. Photomultiplier tube r7378a, 2004. <https://www.hamamatsu.com/>.
- [129] V. Álvarez et al. Initial results of NEXT-DEMO, a large-scale prototype of the NEXT-100 experiment. *Journal of Instrumentation*, 8(04):P04002–P04002, apr 2013.
- [130] V. Álvarez et al. Operation and first results of the NEXT-DEMO prototype using a silicon photomultiplier tracking array. *Journal of Instrumentation*, 8(09):P09011–P09011, sep 2013.
- [131] D. Lorca et al. Characterisation of NEXT-DEMO using xenon  $K_{\alpha}$ X-rays. *Journal of Instrumentation*, 9(10):P10007–P10007, oct 2014.
- [132] P. Ferrario et al. First proof of topological signature in the high pressure xenon gas TPC with electroluminescence amplification for the NEXT experiment. *Journal of High Energy Physics*, 2016(1):104, Jan 2016.

- [133] V. Álvarez et al. Near-intrinsic energy resolution for 30-662keV gamma rays in a high pressure xenon electroluminescent TPC. *Nuclear Instruments and Methods in Physics Research Section A: Accelerators, Spectrometers, Detectors and Associated Equipment*, 708:101–114, 2013.
- [134] F. Monrabal et al. The NEXT White (NEW) detector. *Journal of Instrumentation*, 13(12):P12010–P12010, dec 2018.
- [135] J. Rodríguez, J. Toledo, R. Esteve, D. Lorca, and F. Monrabal. The front-end electronics for the 1.8-kchannel SiPM tracking plane in the NEW detector. *Journal of Instrumentation*, 10(01):C01025–C01025, jan 2015.
- [136] V. Álvarez, V. Herrero-Bosch, R. Esteve, A. Laing, J. Rodríguez, M. Querol, F. Monrabal, J.F. Toledo, and J.J. Gómez-Cadenas. The electronics of the energy plane of the NEXT-White detector. *Nuclear Instruments and Methods in Physics Research Section A: Accelerators, Spectrometers, Detectors and Associated Equipment*, 917:68–76, 2019.
- [137] G. Martínez-Lema et al. Calibration of the NEXT-White detector using 83mKr decays. *Journal of Instrumentation*, 13(10):P10014–P10014, oct 2018.
- [138] A. Simón et al. Electron drift properties in high pressure gaseous xenon. *Journal of Instrumentation*, 13(07):P07013–P07013, jul 2018.
- [139] P. Novella et al. Measurement of radon-induced backgrounds in the next double beta decay experiment. *Journal of High Energy Physics*, 2018(10):112, Oct 2018.
- [140] J. Renner et al. Energy calibration of the NEXT-White detector with 1% resolution near  $Q\beta\beta$  of  $^{136}\text{Xe}$ . *Journal of High Energy Physics*, 2019(10):230, Oct 2019.
- [141] P. Novella et al. Radiogenic backgrounds in the next double beta decay experiment. *Journal of High Energy Physics*, 2019(10):51, Oct 2019.

- [142] P. Novella et al. Measurement of the  $^{136}\text{Xe}$  two-neutrino double beta decay half-life via direct background subtraction in NEXT. 2021.
- [143] P. Ferrario et al. Demonstration of the event identification capabilities of the NEXT-White detector. *Journal of High Energy Physics*, 2019(10):52, Oct 2019.
- [144] A. Simón et al. Boosting background suppression in the NEXT experiment through Richardson-Lucy deconvolution. *Journal of High Energy Physics*, 2021(7):146, Jul 2021.
- [145] NEXT Collaboration. The NEXT-100 experiment for neutrinoless double beta decay searches (Conceptual Design Report), 2011.
- [146] V. Álvarez et al. NEXT-100 technical design report (TDR). executive summary. *Journal of Instrumentation*, 7(06):T06001–T06001, jun 2012.
- [147] A Pla-Dalmau, G.W Foster, and G Zhang. Coumarins as wavelength shifters in polystyrene. *Nuclear Instruments and Methods in Physics Research Section A: Accelerators, Spectrometers, Detectors and Associated Equipment*, 361(1):192–196, 1995.
- [148] R. B. Pahlka, G. Elpers, J. Huang, K. Lang, and M. Proga. Spectral characterization and modeling of wavelength-shifting fibers, 2019.
- [149] E.C. Dukes, P.J. Farris, R.C. Group, T. Lam, Y. Oksuzian, and D. Shooltz. Performance of wavelength-shifting fibers for the Mu2e cosmic ray veto detector. *Journal of Instrumentation*, 13(12):P12028–P12028, dec 2018.
- [150] David R Nygren. Detecting the barium daughter in  $^{136}\text{Xe}$   $0-\nu\beta\beta$  decay using single-molecule fluorescence imaging techniques. *Journal of Physics: Conference Series*, 650:012002, nov 2015.
- [151] B.J.P. Jones, A.D. McDonald, and D.R. Nygren. Single molecule fluorescence imaging as a technique for barium tagging in neutrinoless double beta decay. *Journal of Instrumentation*, 11(12):P12011–P12011, dec 2016.



- [152] A. D. McDonald et al. Demonstration of single-barium-ion sensitivity for neutrinoless double-beta decay using single-molecule fluorescence imaging. *Phys. Rev. Lett.*, 120:132504, Mar 2018.
- [153] P. Thapa, I. Arnquist, N. Byrnes, A. A. Denisenko, F. W. Foss, B. J. P. Jones, A. D. McDonald, D. R. Nygren, and K. Woodruff. Barium chemosensors with dry-phase fluorescence for neutrinoless double beta decay. *Scientific Reports*, 9(1):15097, Oct 2019.
- [154] Iván et al. Rivilla. Fluorescent bicolour sensor for low-background neutrinoless double  $\beta$  decay experiments. *Nature*, 583(7814):48–54, Jul 2020.
- [155] L. G. H. Huxley. Free path formulae for the coefficient of diffusion  $D$  and velocity of drift  $W$  of ions and electrons in gases. *Australian Journal of Physics*, 13(3):578–583, 1960.
- [156] G.W. Fraser and E. Mathieson. Monte Carlo calculation of electron transport coefficients in counting gas mixtures: I. Argon-methane mixtures. *Nuclear Instruments and Methods in Physics Research Section A: Accelerators, Spectrometers, Detectors and Associated Equipment*, 247(3):544–565, 1986.
- [157] Anna Peisert and Fabio Sauli. *Drift and diffusion of electrons in gases: a compilation (with an introduction to the use of computing programs)*. CERN Yellow Reports: Monographs. CERN, Geneva, 1984.
- [158] James H. Parker and John J. Lowke. Theory of electron diffusion parallel to electric fields. i. theory. *Phys. Rev.*, 181:290–301, May 1969.
- [159] H R Skullerud. Longitudinal diffusion of electrons in electrostatic fields in gases. *Journal of Physics B: Atomic and Molecular Physics*, 2(6):696–705, jun 1969.
- [160] Stephen G. Kukolich. Demonstration of the Ramsauer-Townsend effect in a Xenon Thyatron. *American Journal of Physics*, 36(8):701–703, 1968.

- [161] D. Attié. TPC review. *Nuclear Instruments and Methods in Physics Research Section A: Accelerators, Spectrometers, Detectors and Associated Equipment*, 598(1):89–93, 2009. Instrumentation for Colliding Beam Physics.
- [162] Michael F. Modest. Chapter 10 - radiative properties of molecular gases. In Michael F. Modest, editor, *Radiative Heat Transfer (Second Edition)*, pages 288–360. Academic Press, Burlington, second edition edition, 2003.
- [163] Stephen Biagi. Magboltz, accessed 30 January 2022. <https://magboltz.web.cern.ch/magboltz/>.
- [164] S. F. Biagi. Accurate solution of the Boltzmann transport equation. *Nuclear Instruments and Methods in Physics Research, Section A*, 273(2/3):533–535, Dec 1988.
- [165] S.F. Biagi. A multiterm Boltzmann analysis of drift velocity, diffusion, gain and magnetic-field effects in argon-methane-water-vapour mixtures. *Nuclear Instruments and Methods in Physics Research Section A: Accelerators, Spectrometers, Detectors and Associated Equipment*, 283(3):716–722, 1989.
- [166] S.F. Biagi. Monte Carlo simulation of electron drift and diffusion in counting gases under the influence of electric and magnetic fields. *Nuclear Instruments and Methods in Physics Research Section A: Accelerators, Spectrometers, Detectors and Associated Equipment*, 421(1):234–240, 1999.
- [167] B. Al Atoum, S.F. Biagi, D. González-Díaz, B.J.P. Jones, and A.D. McDonald. Electron transport in gaseous detectors with a Python-based Monte Carlo simulation code. *Computer Physics Communications*, 254:107357, 2020.
- [168] B. Al Atoum, S.F. Biagi, D. González-Díaz, B.J.P. Jones, and A.D. McDonald. Pyboltz, accessed 30 January 2022. <https://github.com/UTA-REST/PyBoltz>.
- [169] Stephen Biagi. Degrad, accessed 30 January 2022. <https://degrad.web.cern.ch/degrad/>.

- [170] Rob Veenhof. Garfield, accessed 30 January 2022. <https://garfield.web.cern.ch/garfield/>.
- [171] Heinrich Schindler and Rob Veenhof. Garfield++, accessed 30 January 2022. <https://garfieldpp.web.cern.ch/garfieldpp/>.
- [172] Comsol, accessed 30 January 2022. <https://www.comsol.com/>.
- [173] Elmer, accessed 30 January 2022. <http://www.elmerfem.org/>.
- [174] Ansys, accessed 30 January 2022. <https://www.ansys.com/>.
- [175] J. L. Pack, R. E. Voshall, and A. V. Phelps. Drift velocities of slow electrons in krypton, xenon, deuterium, carbon monoxide, carbon dioxide, water vapor, nitrous oxide, and ammonia. *Phys. Rev.*, 127:2084–2089, Sep 1962.
- [176] J. L. Pack, R. E. Voshall, A. V. Phelps, and L. E. Kline. Longitudinal electron diffusion coefficients in gases: Noble gases. *Journal of Applied Physics*, 71(11):5363–5371, 1992.
- [177] T Koizumi, E Shirakawa, and I Ogawa. Momentum transfer cross sections for low-energy electrons in krypton and xenon from characteristic energies. *Journal of Physics B: Atomic and Molecular Physics*, 19(15):2331–2342, aug 1986.
- [178] J. C. Bowe. Drift velocity of electrons in nitrogen, helium, neon, argon, krypton, and xenon. *Phys. Rev.*, 117:1411–1415, Mar 1960.
- [179] E. L. Patrick, M. L. Andrews, and A. Garscadden. Electron drift velocities in xenon and xenon-nitrogen gas mixtures. *Applied Physics Letters*, 59(25):3239–3240, 1991.
- [180] W. N. English and G. C. Hanna. Grid ionization chamber measurements of electron drift velocities in gas mixtures. *Canadian Journal of Physics*, 31(5):768–797, 1953.
- [181] NEXT Collaboration. Nexus, accessed 30 January 2022. <https://github.com/next-exp/nexus>.

- [182] S. Agostinelli et al. Geant4 - a simulation toolkit. *Nuclear Instruments and Methods in Physics Research Section A: Accelerators, Spectrometers, Detectors and Associated Equipment*, 506(3):250–303, 2003.
- [183] NEXT Collaboration. Invisibles Cities (IC), accessed 30 January 2022. <https://github.com/next-exp/IC>.
- [184] Mi-Young Song, Jung-Sik Yoon, Hyuck Cho, Yukikazu Itikawa, Grzegorz P. Karwasz, Viatcheslav Kokoouline, Yoshiharu Nakamura, and Jonathan Tennyson. Cross sections for electron collisions with methane. *Journal of Physical and Chemical Reference Data*, 44(2):023101, 2015.
- [185] Diego González-Díaz et al. Accurate  $\gamma$  and MeV-electron track reconstruction with an ultra-low diffusion Xenon/TMA TPC at 10atm. *Nuclear Instruments and Methods in Physics Research Section A: Accelerators, Spectrometers, Detectors and Associated Equipment*, 804:8–24, 2015.
- [186] David Nygren. Can the "intrinsic" energy resolution in xenon be surpassed? *Journal of Physics: Conference Series*, 309:012006, aug 2011.
- [187] C.D.R. Azevedo et al. An homeopathic cure to pure xenon large diffusion. *Journal of Instrumentation*, 11(02):C02007–C02007, feb 2016.
- [188] C.D.R. Azevedo et al. Microscopic simulation of xenon-based optical tpcs in the presence of molecular additives. *Nuclear Instruments and Methods in Physics Research Section A: Accelerators, Spectrometers, Detectors and Associated Equipment*, 877:157–172, 2018.
- [189] P. C. P. S. Simões, J. M. F. dos Santos, and C. A. N. Conde. Driftless gas proportional scintillation counter pulse analysis using digital processing techniques. *X-Ray Spectrometry*, 30(5):342–347, 2001.

- [190] C.A.O. Henriques et al. Secondary scintillation yield of xenon with sub-percent levels of CO<sub>2</sub> additive for rare-event detection. *Physics Letters B*, 773:663–671, 2017.
- [191] C. A. O. Henriques. Electroluminescence tpcs at the thermal diffusion limit. *Journal of High Energy Physics*, 2019(1):27, Jan 2019.
- [192] R. Felkai et al. Helium-Xenon mixtures to improve the topological signature in high pressure gas xenon TPCs. *Nuclear Instruments and Methods in Physics Research Section A: Accelerators, Spectrometers, Detectors and Associated Equipment*, 905:82–90, 2018.
- [193] *Interactions of Photons and Electrons with Molecules*. Y. Itikawa (ed.) , Springer-Verlag Berlin Heidelberg, 2003.
- [194] A.D. McDonald et al. Electron drift and longitudinal diffusion in high pressure xenon-helium gas mixtures. *Journal of Instrumentation*, 14(08):P08009–P08009, aug 2019.
- [195] K L Bell, A Dalgarno, and A E Kingston. Penning ionization by metastable helium atoms. *Journal of Physics B: Atomic and Molecular Physics*, 1(1):18–22, jan 1968.
- [196] S. S. Hodgman, R. G. Dall, L. J. Byron, K. G. H. Baldwin, S. J. Buckman, and A. G. Truscott. Metastable helium: A new determination of the longest atomic excited-state lifetime. *Phys. Rev. Lett.*, 103:053002, Jul 2009.
- [197] Robert S. Van Dyck, Charles E. Johnson, and Howard A. Shugart. Radiative lifetime of the 2<sup>1</sup>S<sub>0</sub> metastable state of helium. *Phys. Rev. A*, 4:1327–1336, Oct 1971.
- [198] Ö Şahin, İ Tapan, E N Özmutlu, and R Veenhof. Penning transfer in argon-based gas mixtures. *Journal of Instrumentation*, 5(05):P05002–P05002, may 2010.
- [199] Shinzou Kubota, Tan Takahashi, and Tadayoshi Doke. Mechanism of scintillation of helium, helium-argon, and helium-neon gas mixtures excited by alpha particles. *Phys. Rev.*, 165:225–230, Jan 1968.

- [200] C.A.B. Oliveira, H. Schindler, R.J. Veenhof, S. Biagi, C.M.B. Monteiro, J.M.F. dos Santos, A.L. Ferreira, and J.F.C.A. Veloso. A simulation toolkit for electroluminescence assessment in rare event experiments. *Physics Letters B*, 703(3):217–222, 2011.
- [201] A. F. M. Fernandes et al. Low-diffusion Xe-He gas mixtures for rare-event detection: electroluminescence yield. *Journal of High Energy Physics*, 2020(4):34, Apr 2020.
- [202] C. A. O. Henriques et al. Neutral bremsstrahlung emission in xenon unveiled. *Phys. Rev. X*, 12:021005, Apr 2022.
- [203] J.A. Northrop and Judith C. Gursky. Relative scintillation efficiencies of noble gas mixtures. *Nuclear Instruments*, 3(4):207–212, 1958.
- [204] Kiwamu Saito, Shinichi Sasaki, Hiroko Tawara, Toshiya Sanami, and Eido Shibamura. Study of scintillation in helium mixed with xenon to develop thermal neutron detectors. *Nuclear Instruments and Methods in Physics Research Section A: Accelerators, Spectrometers, Detectors and Associated Equipment*, 581(1):119–122, 2007. VCI 2007.
- [205] J.R. Incandela et al. The performance of photomultipliers exposed to helium. *Nuclear Instruments and Methods in Physics Research Section A: Accelerators, Spectrometers, Detectors and Associated Equipment*, 269(1):237–245, 1988.
- [206] Francis J. Norton. Helium diffusion through glass. *Journal of the American Ceramic Society*, 36(3):90–96, 1953.
- [207] V. O. Altemose. Helium diffusion through glass. *Journal of Applied Physics*, 32(7):1309–1316, 1961.
- [208] Ethan F. Baxter. Diffusion of Noble Gases in Minerals. *Reviews in Mineralogy and Geochemistry*, 72(1):509–557, 01 2010.
- [209] E. Kalashnikov, I. Tolstikhin, B. Lehmann, and B. Pevzner. Helium transport along lattice channels in crystalline quartz. *Journal of Physics and Chemistry of Solids*, 64(11):2293–2300, 2003.

- [210] Hans J. Lippolt, Rolf S. Wernicke, and Werner Boschmann. 4he diffusion in specular hematite. *Physics and Chemistry of Minerals*, 20(6):415–418, Dec 1993.
- [211] Now Entegris, formerly SAES Pure Gas. Heated Getter Gas Purifiers PS4-MT50-R. <https://www.entegris.com/>.
- [212] SERA. <https://www.sera-web.com/>.
- [213] V Boccone et al. Development of wavelength shifter coated reflectors for the ArDM argon dark matter detector. *Journal of Instrumentation*, 4(06):P06001–P06001, jun 2009.
- [214] K. Lung et al. Characterization of the Hamamatsu R11410-10 3-in. photomultiplier tube for liquid xenon dark matter direct detection experiments. *Nuclear Instruments and Methods in Physics Research Section A: Accelerators, Spectrometers, Detectors and Associated Equipment*, 696:32–39, 2012.
- [215] Technetics Group. Helicoflex resilient metal seal. <https://technetics.com/products/helicoflex-metal-resilient-seal/>.
- [216] Now Onsemi, Formerly SensL. C-Series MicroFC-10035-SMT-GP. <https://www.onsemi.com/>.
- [217] R. Esteve, J. Toledo, J. Rodríguez, M. Querol, and V. Álvarez. Readout and data acquisition in the NEXT-NEW detector based on SRS-ATCA. *Journal of Instrumentation*, 11(01):C01008–C01008, jan 2016.
- [218] J. Toledo, H. Muller, R. Esteve, J. M. Monzó, A. Tarazona, and S. Martoiu. The Front-End Concentrator card for the RD51 Scalable Readout System. *Journal of Instrumentation*, 6(11):C11028–C11028, Nov 2011.
- [219] S Martoiu, H Muller, A Tarazona, and J Toledo. Development of the scalable readout system for micro-pattern gas detectors and other applications. *Journal of Instrumentation*, 8(03):C03015–C03015, mar 2013.

- [220] J. Rodríguez, J. Toledo, R. Esteve, D. Lorca, and F. Monrabal. The front-end electronics for the 1.8-kchannel SiPM tracking plane in the NEW detector. *Journal of Instrumentation*, 10(01):C01025–C01025, jan 2015.
- [221] A Tarazona, K Gnanvo, S Martoiu, H Muller, and J Toledo. A point-to-point link for data, trigger, clock and control over copper or fibre. *Journal of Instrumentation*, 9(06):T06004–T06004, jun 2014.
- [222] Raúl Esteve Bosch et al. The Event Detection System in the NEXT-White Detector. *Sensors*, 21(2), 2021.
- [223] F. Carena et al. The ALICE data acquisition system. *Nuclear Instruments and Methods in Physics Research Section A: Accelerators, Spectrometers, Detectors and Associated Equipment*, 741:130–162, 2014.